

NORTHWESTERN UNIVERSITY

Atomic Scale Structure-Chemistry Relationships at Oxide Catalyst Surfaces and Interfaces

A DISSERTATION

SUBMITTED TO THE GRADUATE SCHOOL
IN PARTIAL FULFILLMENT OF THE REQUIREMENTS

for the degree

DOCTOR OF PHILOSOPHY

Field of Materials Science and Engineering

By

Martin E. McBriarty

EVANSTON, ILLINOIS

December 2014

© Copyright by Martin E. McBriarty 2014

All Rights Reserved

ABSTRACT

Atomic Scale Structure-Chemistry Relationships at Oxide Catalyst Surfaces and Interfaces

Martin E. McBriarty

Oxide catalysts are integral to chemical production, fuel refining, and the removal of environmental pollutants. However, the atomic-scale phenomena which lead to the useful reactive properties of catalyst materials are not sufficiently understood. In this work, the tools of surface and interface science and electronic structure theory are applied to investigate the structure and chemical properties of catalytically active particles and ultrathin films supported on oxide single crystals. These studies focus on structure-property relationships in vanadium oxide, tungsten oxide, and mixed V-W oxides on the surfaces of α -Al₂O₃ and α -Fe₂O₃ (0001)-oriented single crystal substrates, two materials with nearly identical crystal structures but drastically different chemical properties. *In situ* synchrotron X-ray standing wave (XSW) measurements are sensitive to changes in the atomic-scale geometry of single crystal model catalyst surfaces through chemical reaction cycles, while X-ray photoelectron spectroscopy (XPS) reveals corresponding chemical changes. Experimental results agree with theoretical calculations of surface structures, allowing for detailed electronic structure investigations and predictions of surface chemical phenomena. The surface configurations and oxidation states of V and W are found to depend on the coverage of each, and reversible structural shifts accompany chemical state changes through reduction-oxidation cycles. Substrate-dependent effects suggest how the choice of oxide support material may affect catalytic behavior. Additionally, the structure and chemistry of W deposited on α -Fe₂O₃

nanopowders is studied using X-ray absorption fine structure (XAFS) measurements in an attempt to bridge single crystal surface studies with real catalysts. These investigations of catalytically active material surfaces can inform the rational design of new catalysts for more efficient and sustainable chemistry.

Approved

Professor Michael J. Bedzyk
Department of Materials Science and Engineering
Northwestern University
Evanston, Illinois

Final Examination Committee
Prof. Michael J. Bedzyk, Chair
Prof. Donald E. Ellis
Prof. Mark C. Hersam
Prof. Laurence D. Marks
Prof. Peter C. Stair

Acknowledgements

This document would not exist without the fantastic guidance I have received from Prof. Michael Bedzyk and Prof. Donald Ellis. As a new grad student in the autumn of 2008, I deliberated over taking an experimental or computational path through my materials science studies. Mike offered a joint project with Don on model catalyst surfaces, giving me the best of both worlds while opening my eyes to the incredibly interesting world of surfaces and interfaces. For the past six years, Mike has provided unparalleled experimental guidance while giving me the freedom to carve out my own research path, and working with Don developed in me a deeper appreciation for the magic of electronic structure and the physical underpinnings of chemistry.

I am grateful for the time and support of my committee members. Prof. Mark Hersam has been a professional guide and mentor, and his courses and discussions always challenge me to think more deeply. Through our interactions in ICEP and the Hilliard symposium, Prof. Laurence Marks has given excellent advice; his suggestions manifest themselves throughout this document. Prof. Peter Stair has guided me through the field of catalysis, either through insightful conversations or his leadership and contributions to ever-enriching ICEP events.

My colleagues in the Bedzyk and Ellis groups have all supported me in their own ways. Early on, I was shown the ropes by Dr. Steve Christensen, Prof. Yuan-Chieh Tseng, Dr. Phillip Lin, Dr. Vaibhav Kohli, Dr. Jeff Klug, and Dr. Dan Wells. Dr. Paul Dalach was my UNIX guru, and it was a pleasure to set up and build servers with him. I'm fortunate to have worked closely with rising stars in the Bedzyk group: Li Zeng, an excellent partner at the beamline; Bor-Rong Chen, whose interests in structure-property relationships in catalysis have led to lots of insightful discussion; Liane Moreau, our resident XAFS expert; and Gavin Campbell, who has been invaluable in

developing software for XSW analysis. I'm also grateful for my interactions with Dr. Sven Stoltz, Dr. Sumit Kewalramani, Dr. Curtis Leung, Dr. Guena Evmenenko, Dr. Parasmani Rajput, Dr. Sudeshna Chattopadhyay, Dr. John Okasinski, I-Cheng Tung, Xiao Chen, Changrui Gao, Kurinji Krishnamoorthy, Stephanie Moffitt, Boris Harutyunyan, Jeremy Harris, Prof. Lukasz Koscielski, and Chris Engelhardt.

Above all, I was fortunate (and still am) to have excellent mentors in Dr. Zhenxing Feng and Dr. Jon Emery. Zhenxing is a scientist of exceptional enthusiasm and dedication, and through our collaborations he helped define the scope of my work. Over countless hours at APS Sectors 5 and 33, Zhenxing taught me how to work a beamline. Jon has been a mentor and friend since I came into the Bedzyk group. He is an excellent teacher, never turning down a question that probes the breadth and depth of his knowledge of X-ray physics. I'm fortunate for the discussions and collaborations I've had with Jon – our beamtime at the European Synchrotron Research Facility and subsequent foray to CERN (for the announcement of the Higgs boson discovery, no less!) were unforgettable.

Early on in my time with the group, Mike mentioned a collaboration between Northwestern's Institute for Catalysis in Energy Processes and the UniCat research cluster in Berlin. Roughly two years (and one Fulbright fellowship) later, I was on a plane to Berlin to work with Prof. Hajo Freund at the Fritz Haber Institute. While that work on metal-supported ultrathin ZnO films is not covered in this document, my time at the FHI has been crucial to my development as a scientist. I am grateful to my collaborators and mentors in Berlin, especially Prof. Irene Groot, Dr. Jorge Anibal Boscoboinik, Dr. Yulia Martynova, and our group leader, Dr. Shamil Shaikhutdinov. I'm glad to have shared a project with Bo-Hong Liu, and it was a delight to host him at Northwestern

and Argonne earlier this year. My time in Berlin would not have been anywhere near as pleasant or productive without Hilary Bown's friendship and willingness to help me navigate German culture, bureaucracy, and grocery shopping.

I have spent many hours working at Advanced Photon Source beamlines 5-BM-D and 5-ID-C with the diligent and insightful guidance of Denis Keane and Qing Ma. Denis is a saint – his patient and methodical approach to optimizing the beamline (and saving experiments) is impressive, especially at 3 AM. In a pinch, Jim Rix, Mike Guise, and Steve Weigand have all gone out of their way to help me at Sector 5. I am also grateful to Zhan Zhang, whose patience rivals Denis Keane's, for keeping things going at 33-ID-D, and for Trudy Bolin's assistance at Sector 9.

At Northwestern, I have received assistance in user facilities from Gajendra Shekhawat, Xinqi Chen, Carla Shute, and Bruce Buchholz. I'm especially grateful for Jerry Carsello's help, expertise, and conversation in the Jerome B. Cohen X-ray Diffraction Facility.

I might not have gone on to Northwestern without the guidance and mentorship of Prof. Jacob Jones, with whom I worked at the University of Florida. Jacob has remained my professional mentor and loudest cheerleader. My former research mentors Dr. Bohdan Andraka, Prof. Yang Shao-Horn, and Prof. Peter Searson have all guided me toward where I am today.

I must also acknowledge my colleagues from my incoming class at Northwestern for their friendship and support, especially Justin Connell, George Fraley, Anthony Johnson, and Evan Laprade. The Northwestern Curling Club has been a wonderful diversion through the Chicago winters, yielding friends and acquaintances across the Midwest and beyond. I'd also like to acknowledge Emily Sutherlin, the MS Word sorceress who helped get this document in shape.

Finally, I am grateful to my parents, Denis and Michele McBriarty, for raising me to be curious, confident, and diligent, and for providing me with ample opportunities for education and enrichment. I'm grateful to my sister, Sondra Hallman, for a friendship that matures along with us, and my nephew, Lucian, for whom the world's opportunities are wide open.

Ellen Lekostaj has been and continues to be a phenomenal companion. Through her encouragement and support, she has put almost as much effort into this document as I have, and I am eternally grateful. As we paddle on, I'm excited to see what's around the bend for us.

This research was supported in part by the Chemical Sciences, Geosciences and Biosciences Division, Office of Basic Energy Sciences, Office of Science, US Department of Energy, Grant No. DE-FG02-03ER15457, at the Institute for Catalysis in Energy Processes at Northwestern University. Equipment support was received from the Initiative for Sustainability and Energy at Northwestern University. This material is partially based upon work supported by the National Science Foundation Graduate Research Fellowship under Grant No. DGE-0824162. Use of the APS at Argonne National Laboratory was supported by the DOE-BES under Contract No. W-31-109-ENG-38. DND-CAT is supported in part by the State of Illinois. This work made use of the Northwestern University Atomic- and Nanoscale Characterization Experimental Center (NUANCE, NIFTI, Keck-II) and the J.B.Cohen X-Ray Diffraction Facility supported by the MRSEC program of the National Science Foundation (DMR-1121262) at the Materials Research Center of Northwestern University. Graphics for DFT-derived figures were prepared using XCrySDen (<http://www.xcrysden.org>) or VESTA (<http://jp-minerals.org/vesta/en/>) software.

For Ellen,
looking forward

Table of Contents

1. Introduction.....	27
1.1 Motivation: The Role of Catalysis	27
1.2 Principles of the Study of Catalysis	30
1.3 The Selective Catalytic Reduction of Nitric Oxides	32
1.4 Model Oxide Supports for Heterogeneous Catalysis: α -Fe ₂ O ₃ and α -Al ₂ O ₃	34
1.5 Outline.....	38
2. Methods.....	41
2.1 Statistically Averaging Methods	41
2.1.1 Introduction to X-rays.....	41
2.1.2 Kinematical X-ray scattering	44
2.1.3 Dynamical X-ray diffraction and the X-ray Standing Wave technique.....	46
2.1.4 X-ray standing waves.....	50
2.1.5 X-ray photoemission and spectroscopy: XPS, XRF, and XAFS	54
2.2 Local probe imaging: atomic force microscopy.....	59
2.3 Sample preparation: atomic layer deposition	60
2.4 Theoretical methods	61
2.4.1 Self-consistent field (Hartree-Fock) method	61

	11
2.4.2 Density functional theory.....	62
2.4.3 Electronic structure and chemical analysis.....	64
3. Structural and Chemical Behavior of Low Coverage $\text{WO}_x / \alpha\text{-Fe}_2\text{O}_3$ Single Crystals and Nanopowders.....	68
3.1 Introduction: Model Catalysis Studies on $\alpha\text{-Fe}_2\text{O}_3$ (Hematite).....	68
3.2 Oxidized and reduced states of $\text{WO}_x / \alpha\text{-Fe}_2\text{O}_3$: a theoretical investigation.....	70
3.2.1 Methods.....	70
3.2.2 Results.....	74
3.2.3 Comparison with experimental results.....	113
3.3 Structure and Chemistry of $\text{WO}_x / \alpha\text{-Fe}_2\text{O}_3$ Nanopowders.....	118
3.3.1 Methods.....	119
3.3.2 Results.....	121
3.3.3 Discussion.....	133
3.4 Conclusions.....	136
4. V-W Interactions on the $\alpha\text{-Al}_2\text{O}_3$ (0001) Surface.....	138
4.1 Introduction: V and W in heterogeneous catalysis.....	138
4.2 Methods.....	140
4.3 Results.....	148
4.3.1 Experiment.....	148

	12
4.3.2 Theory	166
4.4 Discussion	189
4.5 Conclusions	194
5. VO _X for NO _X -SCR: Effect of WO _X addition and substrate chemistry	195
5.1 Introduction	195
5.2 Methods	199
5.3 Results	200
5.3.1 0.5 ML V / O-terminated α -Al ₂ O ₃ (0001)	200
5.3.2 0.5 ML V / O-terminated α -Al ₂ O ₃ (0001): NH ₃ adsorption	214
5.3.3 0.25 ML V + 0.25 ML W / O-terminated α -Al ₂ O ₃ (0001)	219
5.3.4 0.25 ML V + 0.25 ML W / O-terminated α -Al ₂ O ₃ : NH ₃ adsorption	228
5.3.5 0.5 ML V / O-terminated α -Fe ₂ O ₃ (0001)	233
5.3.6 0.5 ML V / O-terminated α -Fe ₂ O ₃ (0001): NH ₃ adsorption	244
5.4 Discussion	248
5.4.1 Effect of W on V chemistry	248
5.4.2 Substrate effects on V chemistry	249
5.5 Conclusions	252
6. Conclusions: Cation-Cation Interactions on Oxide Catalyst Surfaces	254
6.1 Summary	254

6.2	Future directions in surface and interface studies of oxide catalysts	256
6.2.1	<i>In situ</i> and <i>operando</i> studies of model catalysts	256
6.2.2	Simulation of the V/W/TiO ₂ surface.....	257
6.2.3	Reaction pathway calculation and <i>ab initio</i> thermodynamics	258
6.2.4	Structural characterization of real catalysts: zeolites.....	259
	References.....	260
	Appendix A: Introduction to DFT Calculations in VASP	281
	Getting started.....	281
	The input files: INCAR, POTCAR, POSCAR, and KPOINTS.....	283
	INCAR.....	283
	POTCAR	290
	POSCAR	290
	KPOINTS.....	292
	Choice of functional.....	293
	Composing the slab.....	296
	Running VASP and achieving convergence	297
	The output files: WAVECAR, CONTCAR, OUTCAR, CHGCAR, DOSCAR	299
	WAVECAR.....	299
	CONTCAR.....	299

	14
OUTCAR	299
CHGCAR	301
DOSCAR	301
References	302
Appendix B: XSW Measurements on α -Al ₂ O ₃ Substrates	305
References	315

List of Figures

Figure 1.1: Schematic reactivity curves along a reaction coordinate for an exothermic reaction in the presence or absence of a catalyst.	29
Figure 1.2: Top and side views of the calculated Al-terminated α -Al ₂ O ₃ (0001) surface.....	37
Figure 2.1: Calculated Si (220) Bragg reflectivity (rocking curve) and phase ν of the E-field amplitude ratio for an incident beam energy of 7 keV.	49
Figure 2.2: Calculated fluorescence yields of perfectly coherent surface atoms at the Si (220) reflection condition at 7 keV, with calculated reflectivity for reference.	52
Figure 2.3: Schematic of the electron levels of an atom; a photoemission event caused by an incident X-ray, wherein a photoelectron is ejected and a core hole is created; and a relaxation event leading to the emission of a fluorescent photon.....	55
Figure 3.1: Side (1 1 -2 0) and top (0 0 0 1) views of the relaxed O-terminated hematite (0001) supercell slab used as a starting point for calculations.	72
Figure 3.2: Atom-projected partial densities of states (PDOS) for surface and near-surface atoms on clean O-terminated and Fe-terminated hematite.....	76
Figure 3.3: Three-, four-, and six-fold coordinated $\frac{1}{2}$ ML W O-terminated structures representing 0, $\frac{1}{3}$ and 1 ML coadsorbed oxygen.	82
Figure 3.4: Atom-projected PDOS for W _A , W _B , and O' _A W _A on O-terminated hematite.	84
Figure 3.5: Side view and top view of a volume-rendered valence electron density map of $\frac{1}{2}$ ML W _A adsorbed on O-terminated hematite (0001) surface.	87
Figure 3.6: Four- and six-fold coordinated $\frac{1}{2}$ ML W hydroxylated surfaces.	89

Figure 3.7: PDOS of surface and near-surface atoms of HO' _A W _A ($\frac{1}{3}$ ML OH) on O-terminated hematite (0001).	90
Figure 3.8: Side views of three-, four-, and six-fold coordinated 1 ML W representing $\frac{1}{3}$, $\frac{2}{3}$, and 1 ML coadsorbed oxygen.....	94
Figure 3.9: PDOS for surface and near-surface atoms of 1 ML W _A W _B on O-terminated hematite.	97
Figure 3.10: Side views of $\frac{1}{2}$ ML W representing 0, $\frac{1}{3}$, $\frac{2}{3}$, and 1 ML coadsorbed oxygen with additional surface Fe.	101
Figure 3.11: PDOS for surface and near-surface atoms of the O' ₂ W _B Fe _A and O' ₃ W _B Fe _A structures on Fe-terminated (0001) hematite.....	104
Figure 3.12: Convex hull analysis of relative surface energies for several W / α -Fe ₂ O ₃ (0001) surface structures.	110
Figure 3.13: Proposed structures for oxidized and reduced sub-ML W / α -Fe ₂ O ₃ (0001) by comparison of theoretical models to experimental results.....	116
Figure 3.14: Schematic and corresponding photograph of the XAFS setup at APS beamline 5-BM-D.	121
Figure 3.15: XRD patterns of HNPs deposited with 18.8 % w/w WO _x coverage.	123
Figure 3.16: TEM micrographs of W-coated HNPs with a coverage of 4.3% w/w WO _x	124
Figure 3.17: TEM micrographs of W-coated HNPs with a coverage of 0.29% w/w WO _x	124
Figure 3.18: W 4f XP spectra fits (calibrated to the adventitious C 1s peak) for 3.4% w/w WO _x deposited on HNPs.....	125

Figure 3.19: Phase-uncorrected W radial distribution functions (RDFs) derived from EXAFS scans for samples with different WO _x loadings	131
Figure 3.20: XANES and differential XANES spectra for the four reported states of the sample with 2.43% w/w WO _x coverage	132
Figure 4.1: Perspective view of the Be dome mini-chamber mounted on the kappa-geometry diffractometer at APS beamline 5-ID-C.	145
Figure 4.2: Top (0 0 0 1) and side (1 1 -2 0) views of the relaxed Al-terminated α -Al ₂ O ₃ surface supercell.	147
Figure 4.3: AFM images of sample MV	150
Figure 4.4: AFM images of sample MW	151
Figure 4.5: AFM images of sample VW1	152
Figure 4.6: AFM images of sample VW2.....	153
Figure 4.7: XPS survey scans for the four samples referred to in this chapter.	154
Figure 4.8: O 1s – V 2p XP spectra for samples MV, VW1, and VW2.	157
Figure 4.9: W 4f XP spectra for samples MW, VW1, and VW2.....	159
Figure 4.10: XRF spectra of 0.6 ML W / 1.0 ML V / α -Al ₂ O ₃ (0001) sample in the as-deposited condition in open air and in the oxidized condition under a Be dome.	161
Figure 4.11: α -Al ₂ O ₃ (006) XSW yield fits and a typical fitted reflectivity curve for W and V on samples MW, MV, VW1, and VW2.....	162
Figure 4.12: Convex hull analysis of the calculated 0.5 ML W / α -Al ₂ O ₃ (0001) structures....	168
Figure 4.13: PDOS and band-projected charge densities for V, terminal O species, and H in the V _B -O(OH) and V _B -O ₂ structures on Al-terminated α -Al ₂ O ₃ (0001).	177

Figure 4.14: PDOS and band-projected charge densities for V, terminal O species, and H in the $V_B\text{-(OH)}_3$, $V_B\text{-O(OH)}_2$, and $V_B\text{-O}_2\text{OH}$ structures on Al-terminated $\alpha\text{-Al}_2\text{O}_3$ (0001).	178
Figure 4.15: Structures and W, V, terminal O, and H partial densities of states (PDOS) for the fully oxidized $W_B\text{Al}_A\text{-O}_3$ and $W/\text{Al}_2\text{O}_3$ -supported $V_C\text{-O}_2\text{OH}$ structures	187
Figure 4.16: W, V, terminal O, and H PDOS and band-projected charge density maps for the $W/\text{Al}_2\text{O}_3$ -supported $V_C\text{-(OH)}_3$ and $V_C\text{-O(OH)}_2$ structures	188
Figure 5.1: Top (0001) views of V_{A12} (monomers); V_{A1B1} (dimers); and V_{A2B1} (polymers).....	201
Figure 5.2: Top (0001) views of $V_{A12}\text{-O}_{A12}$; $V_{A12}\text{-O}_{A1}(\text{OH})_{A2}$; and $V_{A12}\text{-(OH)}_{A12}$	204
Figure 5.3: V atom-projected partial densities of states (PDOS) for relaxed structures of V monomers on sapphire	205
Figure 5.4: Band-projected partial charge densities for $V_{A12}\text{-O}_{A1}(\text{OH})_{A2}$	206
Figure 5.5: Charge difference maps for the reactions $V_{A12}\text{-O}_{A12} \rightarrow V_{A12}\text{-O}_{A1}(\text{OH})_{A2}$; $V_{A12}\text{-O}_{A1}(\text{OH})_{A2} \rightarrow V_{A12}\text{-(OH)}_{A12}$; $V_{A12}\text{-O}_{A12} \rightarrow V_{A12}\text{-(OH)}_{A12}$	208
Figure 5.6: Top (0001) views of: $V_{A1B1}\text{-O}_{br}$; $V_{A2B1}\text{-O}_{br}$; $V_{A12}\text{-O}_{A12}$; $V_{A1B1}\text{-O}_{A1B1}$; $V_{A2B1}\text{-O}_{A2B1}$; $V_{A2B1}\text{-O}_{2br}$	210
Figure 5.7: Top (0001) views of: $V_{A12}\text{-O}_{A1}(\text{OH})_{A2}$; $V_{A1B1}\text{-O}_{A1}(\text{OH})_{B1}$; $V_{A1B1}\text{-O}_{br}(\text{OH})_{A1}$; $V_{A2B1}\text{-O}_{B1}(\text{OH})_{A2}$; $V_{A2B1}\text{-O}_{br}(\text{OH})_{A2}$; $V_{A2B1}\text{-O}_{br}(\text{OH})_{B1}$	211
Figure 5.8: Top (0001) views of: $V_{A12}\text{-(OH)}_{A12}$; $V_{A1B1}\text{-(OH)}_{A1B1}$; $V_{A2B1}\text{-(OH)}_{A2B1}$; $V_{A1B1}\text{-O}_{br}(\text{OH})_{A1B1}$; $V_{A2B1}\text{-O}_{br}(\text{OH})_{A2B1}$	213
Figure 5.9: Side (1 1 -2 0) and top (0001) views of relaxed structures of NH_3 adsorbed on: $V_{A12}\text{-O}_{A1}(\text{OH})_{A2}$; $V_{A1B1}\text{-O}_{A1}(\text{OH})_{B1}$; $V_{A2B1}\text{-O}_{br}(\text{OH})_{B1}$	217

Figure 5.10: NH_n PDOS and V difference PDOS for the relaxed structure of NH_3 adsorbed on the $\text{V}_{\text{A}12}\text{-O}_{\text{A}1}(\text{OH})_{\text{A}2}$ and $\text{V}_{\text{A}2\text{B}1}\text{-O}_{\text{br}}(\text{OH})_{\text{B}1}\text{-(NH}_3\text{)}_{\text{B}1}$ surfaces	218
Figure 5.11: Top (0001) views of: $\text{W}_{\text{A}1}\text{V}_{\text{A}2}$; $\text{W}_{\text{A}1}\text{V}_{\text{B}1}$; $\text{W}_{\text{B}1}\text{V}_{\text{A}1}$; $\text{W}_{\text{A}2}\text{V}_{\text{B}1}$; $\text{W}_{\text{B}1}\text{V}_{\text{A}2}$	220
Figure 5.12: Top (0001) views of: $\text{W}_{\text{A}1}\text{V}_{\text{B}1}\text{-O}_{\text{br}}$; $\text{W}_{\text{B}1}\text{V}_{\text{A}1}\text{-O}_{\text{br}}$; $\text{W}_{\text{A}2}\text{V}_{\text{B}1}\text{-O}_{\text{br}}$; $\text{W}_{\text{B}1}\text{V}_{\text{A}2}\text{-O}_{\text{br}}$; $\text{W}_{\text{A}1}\text{V}_{\text{A}2}\text{-O}_{\text{A}12}$; $\text{W}_{\text{A}1}\text{V}_{\text{B}1}\text{-O}_{\text{A}1\text{B}1}$; $\text{W}_{\text{B}1}\text{V}_{\text{A}1}\text{-O}_{\text{A}1\text{B}1}$; $\text{W}_{\text{A}2}\text{V}_{\text{B}1}\text{-O}_{\text{A}2\text{B}1}$; $\text{W}_{\text{B}1}\text{V}_{\text{A}2}\text{-O}_{\text{A}2\text{B}1}$	223
Figure 5.13: Top (0001) views of: $\text{W}_{\text{A}1}\text{V}_{\text{A}2}\text{-O}_{\text{A}1}(\text{OH})_{\text{A}2}$; $\text{W}_{\text{A}1}\text{V}_{\text{B}1}\text{-O}_{\text{A}1}(\text{OH})_{\text{B}1}$; $\text{W}_{\text{B}1}\text{V}_{\text{A}1}\text{-O}_{\text{B}1}(\text{OH})_{\text{A}1}$; $\text{W}_{\text{A}2}\text{V}_{\text{B}1}\text{-O}_{\text{A}2}(\text{OH})_{\text{B}1}$; $\text{W}_{\text{B}1}\text{V}_{\text{A}2}\text{-O}_{\text{B}1}(\text{OH})_{\text{A}2}$	224
Figure 5.14: Top (0001) views of: $\text{W}_{\text{A}1}\text{V}_{\text{A}2}\text{-O}_{\text{A}2}(\text{OH})_{2\text{A}1}$; $\text{W}_{\text{A}1}\text{V}_{\text{B}1}\text{-O}_{\text{B}1}(\text{OH})_{2\text{A}1}$; $\text{W}_{\text{B}1}\text{V}_{\text{A}1}\text{-O}_{\text{A}1}(\text{OH})_{2\text{B}1}$; $\text{W}_{\text{A}2}\text{V}_{\text{B}1}\text{-O}_{\text{B}1}(\text{OH})_{2\text{A}2}$; $\text{W}_{\text{B}1}\text{V}_{\text{A}2}\text{-O}_{\text{A}2}(\text{OH})_{2\text{B}1}$	226
Figure 5.15: Top (0001) views of: $\text{W}_{\text{A}1}\text{V}_{\text{A}2}\text{-O}_{\text{A}12}(\text{OH})_{\text{A}1}$; $\text{W}_{\text{A}1}\text{V}_{\text{B}1}\text{-O}_{\text{A}1\text{B}1}(\text{OH})_{\text{A}1}$; $\text{W}_{\text{B}1}\text{V}_{\text{A}1}\text{-O}_{\text{A}1\text{B}1}(\text{OH})_{\text{B}1}$; $\text{W}_{\text{A}2}\text{V}_{\text{B}1}\text{-O}_{\text{A}2\text{B}1}(\text{OH})_{\text{A}2}$; $\text{W}_{\text{B}1}\text{V}_{\text{A}2}\text{-O}_{\text{A}2\text{B}1}(\text{OH})_{\text{B}1}$	227
Figure 5.16: Side (1 1 -2 0) and top (0001) views of relaxed structures of NH_3 adsorbed on $\text{W}_{\text{A}1}\text{V}_{\text{A}2}\text{-O}_{\text{A}12}(\text{OH})_{\text{A}1}$ and $\text{W}_{\text{A}1}\text{V}_{\text{B}1}\text{-O}_{\text{A}1\text{B}1}(\text{OH})_{\text{A}1}\text{-(NH}_3\text{)}_{\text{A}1}$	229
Figure 5.17: Side (1 1 -2 0) and top (0001) views of relaxed structures of NH_3 adsorbed on $\text{W}_{\text{A}1}\text{V}_{\text{A}2}\text{-O}_{\text{A}2}(\text{OH})_{2\text{A}1}$ and $\text{W}_{\text{A}2}\text{V}_{\text{B}1}\text{-O}_{\text{B}1}(\text{OH})_{2\text{A}2}$	231
Figure 5.18: Charge density difference maps for NH_3 adsorption onto the $\text{W}_{\text{A}1}\text{V}_{\text{A}2}\text{-O}_{\text{A}2}(\text{OH})_{2\text{A}1}$ and $\text{W}_{\text{A}2}\text{V}_{\text{B}1}\text{-O}_{\text{B}1}(\text{OH})_{2\text{A}2}$ structures.	233
Figure 5.19: NH_n PDOS and W,V difference PDOS for the relaxed structure of NH_3 adsorbed on the $\text{W}_{\text{A}1}\text{V}_{\text{A}2}\text{-O}_{\text{A}2}(\text{OH})_{2\text{A}1}$ and $\text{W}_{\text{A}2}\text{V}_{\text{B}1}\text{-O}_{\text{B}1}(\text{OH})_{2\text{A}2}$ structures	234
Figure 5.20: Top (0001) views of the hematite-supported monomer structures $\text{V}_{\text{A}12}\text{-O}_{\text{A}12}$; $\text{V}_{\text{A}12}\text{-O}_{\text{A}1}(\text{OH})_{\text{A}2}$; and $\text{V}_{\text{A}12}\text{-(OH)}_{\text{A}12}$	234
Figure 5.21: Spin-polarized V PDOS for $\text{V}_{\text{A}12}\text{-O}_{\text{A}12}$; $\text{V}_{\text{A}12}\text{-O}_{\text{A}1}(\text{OH})_{\text{A}2}$; $\text{V}_{\text{A}12}\text{-(OH)}_{\text{A}12}$	237

Figure 5.22: Charge difference maps for reactions on the hematite surface: $V_{A12-O_{A12}} \rightarrow V_{A12-O_{A1}(OH)_{A2}}$; $V_{A12-O_{A1}(OH)_{A2}} \rightarrow V_{A12-(OH)_{A12}}$; $V_{A12-O_{A12}} \rightarrow V_{A12-(OH)_{A12}}$	238
Figure 5.23: Top (0001) views of hematite-supported structures: $V_{A1B1-O_{br}}$; $V_{A2B1-O_{br}}$; $V_{A12-O_{A12}}$; $V_{A1B1-O_{A1B1}}$; $V_{A2B1-O_{A2B1}}$; $V_{A2B1-O_{2br}}$	241
Figure 5.24: Top (0001) views of hematite-supported structures: $V_{A12-O_{A1}(OH)_{A2}}$; $V_{A1B1-O_{A1}(OH)_{B1}}$; $V_{A1B1-O_{br}(OH)_{A1}}$; $V_{A2B1-O_{A2}(OH)_{B1}}$; $V_{A2B1-O_{B1}(OH)_{A2}}$; $V_{A2B1-O_{br}(OH)_{B1}}$; $V_{A2B1-O_{br}(OH)_{A2}}$	242
Figure 5.25: Top (0001) views of hematite-supported structures: $V_{A12-(OH)_{A12}}$; $V_{A1B1-(OH)_{A1B1}}$; $V_{A2B1-(OH)_{A2B1}}$; $V_{A1B1-O_{br}(OH)_{A1B1}}$; $V_{A2B1-O_{br}(OH)_{A2B1}}$	244
Figure 5.26: Side (1 1 -2 0) and top (0001) views of relaxed structures of NH_3 adsorbed on: $V_{A12-O_{A1}(OH)_{A2}}$, $V_{A1B1-O_{br}(OH)_{A1}}$, and $V_{A2B1-O_{B1}(OH)_{A2}}$	246
Figure 5.27: Spin-polarized V PDOS for hematite-supported structures $V_{A2B1-O_{B1}(OH)_{A2}}$ and $V_{A2B1-O_{B1}(OH)_{A2}(NH_3)_{A2}}$	247
Figure B.1: Comparison of $\alpha-Al_2O_3$ and $\alpha-Fe_2O_3$ (006) rocking curves.....	306
Figure B.2: Comparison of the crystal structures and dynamical diffraction effects through the (006) reflection condition for sapphire and hematite.....	307
Figure B.3: Calculated $\alpha-Al_2O_3$ (006) rocking curves and reflected wave phases as well as fluorescence yields for different coherent positions P_{006} relative to the center of the Al_2 plane	308
Figure B.4: Atomic and ionic form factors for Al and O.....	310
Figure B.5: Sapphire (006) rocking curves at 13 keV beam energy calculated using ionic (Al^{3+} , O^{2-}) and atomic (Al^0 , O^0) form factors.....	311
Figure B.6: Schematic of the optics setup for $\alpha-Al_2O_3$ (006) XSW measurements	313

List of Tables

Table 2.1: Integrated Bader charge for bulk cations in DFT-relaxed structures.....	66
Table 2.2: Calculated bond valence sums for bulk cations in DFT-relaxed structures.....	67
Table 3.1: Comparison of surface and near-surface layer relaxations in the z direction for hematite (0001) surface configurations	74
Table 3.2: Calculated interlayer distances R_L (Å) for various W and O adsorption scenarios on hematite (0001).	77
Table 3.3: Interatomic distances R_{ij} (Å) for half-monolayer W deposited on O_3^- - and Fe-terminated hematite (0001) surfaces.	79
Table 3.4: Comparison of chemical characteristics of bulk WO_3 and WO_2 and different configurations of $\frac{1}{2}$ ML W atop the O-terminated α - Fe_2O_3 (0001) surface.....	81
Table 3.5: Chemical details for hydroxylated $\frac{1}{2}$ ML W on O-terminated hematite (0001).....	89
Table 3.6: Chemical details for $\frac{1}{2}$ ML W on O-terminated hematite (0001) with one, two, or three surface O vacancies (O_v).	92
Table 3.7: Chemical details for 1 ML W on O-terminated hematite (0001).	95
Table 3.8: Chemical details for $\frac{1}{2}$ ML W with 0 or 1 adsorbed O atoms per Fe-terminated hematite (0001) cell	99
Table 3.9: Chemical details for $\frac{1}{2}$ ML W with 2 or 3 adsorbed O atoms per Fe-terminated hematite (0001) cell	100
Table 3.10: Chemical details for $\frac{1}{2}$ ML W with 1, 2, or 3 adsorbed hydroxyl groups per Fe-terminated hematite (0001) cell	106

Table 3.11: Chemical details for $\frac{1}{2}$ ML W on Fe-terminated hematite (0001) with one, two, or three surface O vacancies (O_v).....	108
Table 3.12: Comparison of converged electronic energies (in eV) of selected relaxed configurations converged with the PW91+ U method.....	112
Table 3.13: Comparison of W A- and B-site z displacements above the bulk-like O_3 plane derived from XSW experiments with selected energetically favored DFT-calculated configurations ...	115
Table 3.14: ALD parameters used for WO_x deposition on hematite nanopowders.....	119
Table 3.15: Annealing conditions for hematite nanopowder samples coated by ALD with different coverages of WO_x	125
Table 3.16: Best-fit parameters for unconstrained fits of EXAFS spectra for several loadings of WO_x on hematite nanopowders.....	129
Table 3.17: Best-fit parameters for constrained fits ($\sigma^2 = 0.001$) of EXAFS spectra for several loadings of WO_x on hematite nanopowders.....	130
Table 4.1: Comparison of interlayer relaxations between the α - Al_2O_3 (0001) supercell used in this work and previously published experimental and theoretical data.....	147
Table 4.2: Coverage of atomic layer deposited V and W on the four α - Al_2O_3 (0001) samples referred to in this work.....	149
Table 4.3: Fitted O $1s$ – V $2p_{3/2}$ binding energy differences (BEDs) for V-deposited samples after oxidation and reduction.....	157
Table 4.4: Fitted W $4f_{7/2}$ binding energies for W-deposited samples after oxidation and reduction, calibrated to the C $1s$ peak.....	158

Table 4.5: Fitted W $4f_{7/2}$ binding energies for W-deposited samples after oxidation and reduction, calibrated to the Al $2p$ peak.	159
Table 4.6: XSW-derived coherent fractions (f) and coherent positions (P) for the (006) crystal reflections in oxidized, reduced, and re-oxidized conditions.	164
Table 4.7: XSW-derived coherent fractions (f) and coherent positions (P) for the (006) crystal reflections, with average values for separate oxidized cases.	165
Table 4.8: Relative differences in converged supercell energy for $\frac{1}{2}$ ML W / Al-terminated α -Al ₂ O ₃ (0001).	167
Table 4.9: Structural and chemical information for low-energy $\frac{1}{2}$ ML W structures and coordination environments atop the Al-terminated α -Al ₂ O ₃ (0001) surface supercell.	169
Table 4.10: Relative differences in converged supercell energy for $\frac{1}{2}$ ML V / O-terminated α -Al ₂ O ₃ (0001).	171
Table 4.11: Structural and chemical information for low-energy $\frac{1}{2}$ ML V structures and coordination environments atop the O-terminated α -Al ₂ O ₃ (0001) surface supercell.	171
Table 4.12: Calculated total supercell binding energy differences (eV) for different coordination environments of V atop an Al-terminated cell.	172
Table 4.13: Structural and chemical information for low-energy $\frac{1}{2}$ ML V structures and coordination environments atop the Al-terminated α -Al ₂ O ₃ (0001) surface supercell.	173
Table 4.14: Average O Bader charges in different coordinating environments for $\frac{1}{2}$ ML V and W on stable Al-terminated α -Al ₂ O ₃ (0001) surfaces.	175
Table 4.15: Structural and chemical information for low-energy 1 ML V structures and coordination environments atop the O-terminated α -Al ₂ O ₃ (0001) surface supercell.	180

Table 4.16: Structural and chemical information for low-energy 0.25 ML V structures and coordination environments atop the Al-terminated α -Al ₂ O ₃ (0001) 2x2 surface supercell.	181
Table 4.17: Calculated total supercell binding energy differences for different coordination environments of V atop a fully O-terminated W _B Al _A cell.....	183
Table 4.18: Structural and electronic parameters for V atop a fully O-terminated Al _A W _B cell.	184
Table 4.19: Average O Bader charges of surface structures described in Table 4.18 , including the value from bulk α -Al ₂ O ₃ for comparison.	187
Table 5.1: Structural and chemical information for reduced ½ ML V structures and coordination environments atop the O-terminated (2x1) α -Al ₂ O ₃ (0001) surface supercell.....	201
Table 5.2: Structural and chemical information for ½ ML monomer V structures on the (0001) sapphire surface	203
Table 5.3: Structural and chemical information for ½ ML V structures on the (0001) sapphire surface with one or two additional O ligands.	210
Table 5.4: Structural and chemical information for ½ ML V structures on the (0001) sapphire surface with one additional O and one OH ligands.	212
Table 5.5: Structural and chemical information for ½ ML V structures on the (0001) sapphire surface with two additional OH ligands, as well as one additional O and two OH ligands	213
Table 5.6: Structural and chemical information for ½ ML V structures on the (0001) sapphire surface with one additional O and one OH ligands as well as one adsorbed NH ₃ molecule.....	216
Table 5.7: Structural and chemical information for ¼ ML V and ¼ ML W structures on the (0001) sapphire surface with no additional ligands.....	220

Table 5.8: Structural and chemical information for $\frac{1}{4}$ ML V and $\frac{1}{4}$ ML W structures on the (0001) sapphire surface with one or two additional O ligands.....	222
Table 5.9: Structural and chemical information for $\frac{1}{4}$ ML V and $\frac{1}{4}$ ML W structures on the (0001) sapphire surface with one additional O and one OH ligands.....	223
Table 5.10: Structural and chemical information for $\frac{1}{4}$ ML V and $\frac{1}{4}$ ML W structures on the (0001) sapphire surface with one additional O and two OH ligands.....	225
Table 5.11: Structural and chemical information for $\frac{1}{4}$ ML V and $\frac{1}{4}$ ML W structures on the (0001) sapphire surface with two additional O and one OH ligands.....	227
Table 5.12: Structural and chemical information for $\frac{1}{4}$ ML V and $\frac{1}{4}$ ML W structures on the (0001) sapphire surface with two additional O and one OH ligands as well as one adsorbed NH_3 molecule.	228
Table 5.13: Structural and chemical information for $\frac{1}{4}$ ML V and $\frac{1}{4}$ ML W structures on the (0001) sapphire surface with one additional O and two OH ligands as well as one adsorbed NH_3 molecule.	230
Table 5.14: Structural and chemical information for $\frac{1}{2}$ ML V monomer structures on the (0001) hematite surface	235
Table 5.15: Structural and chemical information for $\frac{1}{2}$ ML V structures on the (0001) hematite surface with one or two additional oxygen ligands.	241
Table 5.16: Structural and chemical information for $\frac{1}{2}$ ML V structures on the (0001) hematite surface with one additional oxygen and one hydroxyl ligands.....	242
Table 5.17: Structural and chemical information for $\frac{1}{2}$ ML V structures on the (0001) hematite surface with two additional hydroxyl ligands.	243

Table 5.18: Structural and chemical information for $\frac{1}{2}$ ML V structures on the (0001) hematite surface with one additional oxygen and one hydroxyl ligands, as well as one adsorbed NH_3 molecule.....	245
Table 5.19: Bader charges on O atoms in the V-O coordination environment for 0.5 ML V monomers.....	250
Table B.1: Selected calculated parameters of the $\alpha\text{-Al}_2\text{O}_3$ (006) reflection at an incident beam energy of 13 keV.....	312

1. Introduction

1.1 Motivation: The Role of Catalysis

Just before the turn of the 19th century, Thomas Malthus wrote in *An Essay on the Principle of Population*,

“Famine seems to be the last, the most dreadful resource of nature. The power of population is so superior to the power of the earth to produce subsistence for man, that premature death must in some shape or other visit the human race. ... [G]igantic inevitable famine stalks in the rear, and with one mighty blow levels the population with the food of the world.”[1]

This “Malthusian catastrophe” was predicted as the result of rapid population growth far exceeding food production. Of course, Malthus was not counting on the tremendous advances in technology and automation that would come over the following two centuries which would allow the population to grow from fewer than 1 billion in 1800 to over 7 billion today[2].

The largest advance that allowed the population to continue growing through the past century was the production of synthetic reactive nitrogen, a component of agricultural fertilizers[3]. Prior to the 20th century, reactive nitrogen was mined from exhaustible natural sources such as Peruvian guano. Despite the ubiquity of non-reactive N₂ in our atmosphere, there was no practical synthetic route to fixing N₂ into useful forms. However, in the first decade of the 20th century, Fritz Haber developed a relatively inexpensive route to reacting atmospheric N₂ with H₂ to form ammonia[4]. Haber’s trick was to compress the elemental gases in the presence of Fe, which dramatically

increased the rate of NH_3 production. Fe remains the catalyst at the heart of the Haber-Bosch process, so named after Carl Bosch adapted Haber's process to the industrial scale.

Today, the global chemical industry depends critically on catalysts[5]. Nearly every chemical and chemical-derived product, from polymers to pharmaceuticals to fertilizers, requires a catalyst at some point in its production. The multi-billion-dollar catalysis industry is extremely competitive, as new catalysts can drastically reduce the operating costs and feedstock requirements for large-scale chemical reactions. Catalysts are crucial in the energy sector for cracking larger molecules from crude oil into smaller ones for use as fuels, and so advances in catalysis can help us make the most efficient use of non-renewable fuels. Environmental catalysis is also used for pollution mitigation. Automotive catalytic converters oxidize CO to CO_2 and reduce smog-causing nitric oxides to harmless N_2 , and similar reactions take place on industrial smokestacks.

A catalyst increases the rate of a chemical reaction by providing a chemical pathway with a low activation energy barrier. That is, the reaction pathway is modified to reduce the "rate-limiting step". Two possible pathways for a hypothetical exothermic reaction are shown in **Figure 1.1**, with the reaction coordinate proceeding from reactants (on the left) to products (on the right). Although the difference in free energies ΔG between the reactants and products is negative, some activation energy barrier E_a prevents the reaction from occurring spontaneously. The pathway taken by the reactants in a homogeneous gas- or liquid-phase reaction might look like **Figure 1.1 (A)**, which has a large activation energy barrier. **Figure 1.1 (B)** shows the effect of a catalyst on this barrier. The highest energy barrier E'_a is much lower than E_a , and therefore the rate-limiting step will proceed much faster over the catalyst.

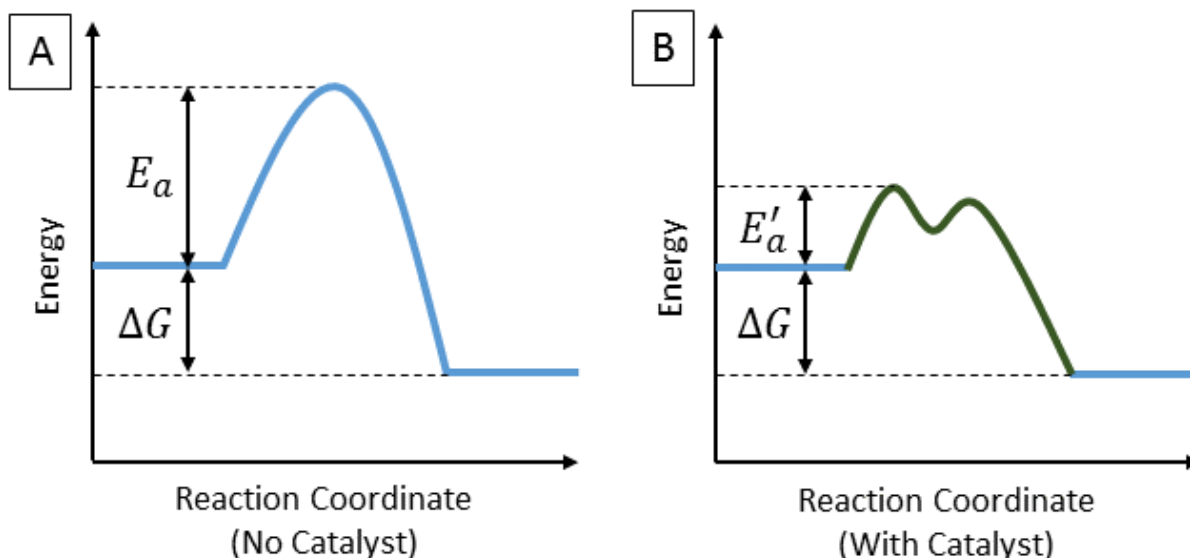


Figure 1.1: Schematic reactivity curves along a reaction coordinate for an exothermic reaction. (A) Homogeneous gas- or liquid-phase reaction; (B) reaction in the presence of a catalyst.

To illustrate why the activation energy barrier changes, imagine N_2 and H_2 molecules reacting in a sealed container to form ammonia. In order for a reaction to take place, the molecules must be near each other in the proper stoichiometry (three H_2 molecules and one N_2 molecule), and the extremely strong N-N triple bond must be somehow destabilized. To achieve a reasonable reaction rate, the pressure and temperature must be raised to extreme conditions to bring the molecules together and increase the likelihood of spontaneous destabilization of the N-N bond. This heating and pressurization requires an enormous amount of external energy input. Adding a reactive material surface, such as Haber's iron, provides sites at which a higher density of molecules might be present, and transition states might be stabilized at the surface. In the presence of this material surface, the reaction therefore proceeds differently than it would in the gas. Not only does the material provide anchoring sites for atoms, molecules, and transition states, but the material itself

can donate or accept electrons, destabilizing bonds or “activating” otherwise stable molecules. This improved reactivity at the solid-gas or solid-liquid interface is *heterogeneous catalysis*.

For the most of the past century or so of directed catalyst development, chemists and chemical engineers have taken a “top-down” approach; that is, through chemical intuition and a lot of trial and error, new catalysts were developed to speed up existing reactions or catalyze new ones. In recent decades, however, the field has turned towards a “bottom-up” approach of rational catalyst design from first principles[6-10]. By using the physical and chemical insight developed over the past century in chemistry, chemical physics, and materials science, catalysts may be designed towards specific reactions, with high activity and selectivity. A careful selection of materials and processing parameters would result in a high distribution of catalytically active sites tailored towards one particular product. This dream of a rationally designed catalyst has been realized in a few cases, such as the development of NiFe alloys for the conversion of CO and CO₂ to methane[8]. Thus, there is clearly motivation to study the fundamental behavior of catalysts at the atomic scale in order to understand the structure and function of catalytically active sites.

1.2 Principles of the Study of Catalysis

From a materials science perspective, solid catalysts are structurally complex. These materials typically consist of metal or metal oxide nanoparticles supported on oxide substrates such as porous silica, zeolites, or metal oxide powders. Individually, the catalyst and support particles span a range of shapes and sizes, and they feature a variety of surface defects and a great deal of crystallographic inhomogeneity. When combined, interfacial effects between the catalyst and support must also be considered. Under reaction conditions, the catalyst surface may support a variety of physisorbed and chemisorbed species on a myriad of surface sites. While catalysis

research focuses on defining and understanding the sites on the catalyst surface that are most responsible for their useful behavior, the complexities of real catalysts nearly preclude a complete, atomic-scale characterization of catalyst active sites, especially under reaction conditions.

One widely used solution to this problem is the “surface and interface science” approach to catalysis[11]. In this approach, the catalyst is simplified from an ensemble of 3-dimensional particles to a single 2-dimensional surface. This drastically reduces the structural complexity and makes the problem accessible to the tools of surface and interface science, by which surface structures can be solved with atomic resolution. The behavior of catalysts can therefore be studied under simplified conditions which allow for the observation of the fundamental physical-chemical phenomena that underlie their properties. For example, the deeper mechanisms of the Haber-Bosch process were not well understood for almost 70 years until Gerhard Ertl, using the recently-introduced tools of surface science, elucidated them by studying the interaction of N_2 , H_2 , and NH_3 on Fe single crystal surfaces[12]. Additionally, Ertl revealed that K, a “promoter” used to improve the catalyst activity in the industrial Haber-Bosch process, strengthens the adsorption of N_2 onto Fe surface and weakens the binding of NH_3 , substantially improving the reaction rate. Of course, the surface and interface science approach does not completely represent the nuances of the real system due to the “materials gap” and “pressure gap” between surface studies in vacuum and the real material under high pressure. However, these methods enable the extraction of meaningful insight about the mechanisms governing the behavior of the real system[13].

The primary methods of surface and interface science may be broken down into two classes: *local probe* and *surface averaging*. Local probe methods specific to surface and interface science include scanning probe microscopies (SPM) such as scanning tunneling microscopy (STM),

atomic force microscopy (AFM), and Kelvin probe force microscopy (KPFM). Electron microscopies are widely employed as well. These methods yield images of the surface structure from nanometer to sub-Ångström length scales. While they can provide local atomic-scale insight, revealing features such as defects, they only provide views of small areas on the surface, and the resolution of atomic positions in the surface normal direction is limited. Surface averaging methods, including X-ray and electron scattering, provide results averaged over a larger (micron- to millimeter-scale) portion of the surface. The combined signal from enormous ensembles of atoms provides sensitivity to structural details and minority species that is not achievable at smaller scales. Surface stoichiometry and chemical states can be determined by X-ray and electron spectroscopies, while X-ray scattering from surfaces can provide ensemble-averaged measurements of atomic position with sub-Ångström resolution. These two families of characterization tools are clearly complementary, and taken together they can provide a view of the entire surface at several length scales, especially when paired with first-principles theoretical calculations.

1.3 The Selective Catalytic Reduction of Nitric Oxides

As mentioned above, catalysts are tremendously important for chemical production and fuel processing. However, they are also widely used for environmental protection and remediation, such as the oxidation of poisonous CO to CO₂ and the reduction of nitric oxides (NO_x) to harmless N₂. NO_x are environmental pollutants which are produced in power plants, incinerators, and various industrial processes, composing up to several thousand parts per million (by volume) of the waste gases[14]. Unmitigated, these pollutants contribute to the formation of smog and acid rain. The formation mechanisms of NO_x include the oxidation of nitrogen contained in fuel such

as coal or oil; the fixation of atmospheric N₂ at high temperatures; and the oxidation of HCN, an intermediate formed by the reaction of hydrocarbons with nitrogen radicals[15].

Among several strategies of reducing NO_x output, selective catalytic reduction (SCR) with ammonia is the most efficient process, with 98 – 99% NO_x removal[5, 14]. The reaction can be written as



This reaction typically takes place over a vanadium oxide (VO_x) catalyst dispersed on an anatase TiO₂ support. Vanadium is a very versatile catalyst[16], and in this reaction, vanadium is proposed to have two synergistic roles[17]. Some V species provide Brønsted acid sites for NH₃ adsorption, and the resulting ammonium cation transfers a proton to a nearby redox V site. This reduces the redox site, activating it to bind NO and interact with the NH₃ to form N₂.

The nature of the catalytically active V species in NO_x-SCR and other reactions is under consistent study. VO_x can take different oligomeric forms on the surface, ranging from isolated monomers to crystalline species such as V₂O₅, and the morphology of VO_x has consequences for the chemical behavior of the catalyst[18-23]. The oxide substrate upon which VO_x is deposited (referred to as the “support” in most catalysis literature) plays a significant role in the reactivity of VO_x as well[19, 24-27]. The addition of W to VO_x catalysts for NO_x-SCR is known to significantly improve the catalytic activity, although the mechanism of this promotion effect is still not clear[28-31]. We are therefore interested in the dependence of catalytic behavior on the chemistry of the substrate and the influence of co-catalysts. For oxides, this approach can be summarized as a study of cation-cation interactions mediated by oxygen or adsorbates.

1.4 Model Oxide Supports for Heterogeneous Catalysis: α -Fe₂O₃ and α -Al₂O₃

Industrial catalysts for NO_x-SCR consist of V and W species dispersed on anatase TiO₂, a reducible oxide. Our group has investigated the structures of V and W at different coverages and under different chemical conditions on rutile α -TiO₂[32-35], culminating in a recent study exploring mixed V-W species on the α -TiO₂ (110) surface[36]. In order to search for more general trends in the support-dependent behavior of V and W, two oxide substrates were chosen for investigation because of their similar structure but drastically different chemical properties: α -Fe₂O₃ (hematite) and α -Al₂O₃ (sapphire). These sesquioxides both have the corundum structure which is shared with other metal oxides including Cr₂O₃, V₂O₃, and reduced titania Ti₂O₃[37, 38].

Hematite is a semiconductor with a bandgap of roughly 2 eV. This earth abundant mineral, a primary component of rust, is of interest for several applications because of its stability and low cost. Hematite shows useful photocatalytic properties due to its absorption of visible light and has therefore attracted interest as a photoanode to derive H₂ from water[39, 40] or alcohols[41]. Its surface reactivity has also stimulated interest in hematite as a gas sensor[42]. Because of its ubiquity and properties, hematite is the subject of many fundamental environmental and geochemical studies[43-45].

Sapphire, the most stable isomorph of Al₂O₃, is a highly ionic wide-bandgap insulator with excellent lattice thermal conductivity. Large, high-quality single crystals of sapphire can be grown. Sapphire is used as a substrate for optical devices such as LEDs[46], and natural α -Al₂O₃ crystals with color center dopants are prized as sapphire and ruby gemstones. Its high strength makes it attractive for scratch-resistant digital displays[47]. Sapphire surfaces are of interest for

geochemical studies, often alongside hematite[43-45]. Alternative Al_2O_3 structures known as “transition aluminas”, mainly $\gamma\text{-Al}_2\text{O}_3$ but also δ -, κ -, χ -, or $\theta\text{-Al}_2\text{O}_3$, are used as high-surface-area catalyst support materials. Unlike the distorted Al-O octahedra that make up the corundum structure, transition aluminas contain tetrahedrally coordinated cations and surface sites that contribute to their activity as acid catalysts[48, 49]. They have less ionic character than sapphire[50], making them more chemically active in real catalytic reactions. Despite the interest of transition aluminas in the catalyst community, $\alpha\text{-Al}_2\text{O}_3$ is intended to be an “inert” support in this work to contrast with hematite.

The corundum lattice is hexagonal and centrosymmetric, with a unit cell consisting of six oxygen layers flanked by metal cations along the (0001) direction. The ionic stacking sequence is Tasker Type 2, with each stacked $[\text{cation}]_2\text{O}_3$ unit having a total dipole moment of zero[51]. There are three possible bulk-like corundum (0001) surface terminations: O_3 , $[\text{cation}]\text{-O}_3$, or $[\text{cation}]\text{-}[\text{cation}]\text{-O}_3$. The $[\text{cation}]\text{-O}_3$ termination is the only nonpolar option, and it has been shown to be the stable surface for $\alpha\text{-Al}_2\text{O}_3$ (0001) in vacuum[52] as well as for transition metal corundum oxides, typically with corresponding inward relaxations of the terminal metal cation[38]. Under non-vacuum conditions, however, the oxygen-terminated surface may be stable. The $\alpha\text{-Al}_2\text{O}_3$ (0001) surface is fully O-terminated in the presence of water[53], although the surface polarization may be compensated by hydroxyl groups. Likewise, O_3 -terminated $\alpha\text{-Fe}_2\text{O}_3$ (0001) is observed at high O_2 chemical potentials[54, 55]. Other hematite surface phases exist uniquely or coexist with the O_3 -terminated surface, depending on the methods used and conditions studied; these include Fe termination[54-56], ferryl groups[57-59], and Fe-rich phases at or just below the surface[60,

61]. Hydroxylated α -Fe₂O₃ (0001) surfaces have also been predicted and observed upon exposure to water[40, 62, 63].

The surface and interface science approach to materials research typically requires that a single crystal surface is as close as possible to an ideal surface termination, usually a plane of low Miller index. However, on a real crystal surface, defects will always be present at some concentration. For example, a crystal may be cut at a small miscut angle deviating from the crystal plane of interest. If the ideal crystal termination is otherwise stable, then the crystal surface will have a step density that increases with miscut angle. This is sometimes done intentionally, especially for metals, resulting in a vicinal surface which can have unique structural and chemical properties that model real, defect-rich materials[64]. However, for the studies reported herein, we assume that the step density of our oxide crystal surfaces (~ 0.03 step nm⁻¹, corresponding terrace widths of 30 nm or larger) is sufficiently low to ignore step edge effects in our statistically averaging measurements. For most of this work, I will focus on the (0001) surface terminations of these crystals. The structure of the α -Al₂O₃ (0001) surface is shown in **Figure 1.2**. This is a theoretically calculated structure which agrees well with previously published results[52, 65], as is discussed in **Chapter 4**. The bulk corundum crystal structure is framed by triangular O planes with octahedral sites in between. The cations occupy two of the three available octahedral interstitial sites in each layer, leaving a vacancy in one site. The cation positions are staggered so as to reduce cation-cation repulsion in the structure. The bulk corundum unit cell is hexagonal and consists of six [cation]₂O₃ layers stacked in the *c* direction. Experimentally measured lattice parameters for α -Fe₂O₃ are $a = b = 5.0345$ Å, $c = 13.749$ Å and for α -Al₂O₃ are $a = b = 4.7589$ Å, $c = 12.991$ Å[37].

If the (0001) surface is truncated just above the oxygen layer, then three empty half-octahedral sites will remain on the surface. In this work, the sites are labeled A, B, and C, with the A and B sites corresponding to a continuation of the bulk cationic structure and the C site representing the normally unfilled octahedral site. The case shown below is considered to be singly Al-terminated, with Al in the A site above the surface O_3 plane. The structure of the Fe-terminated $\alpha\text{-Fe}_2\text{O}_3$ (0001) surface is similar.

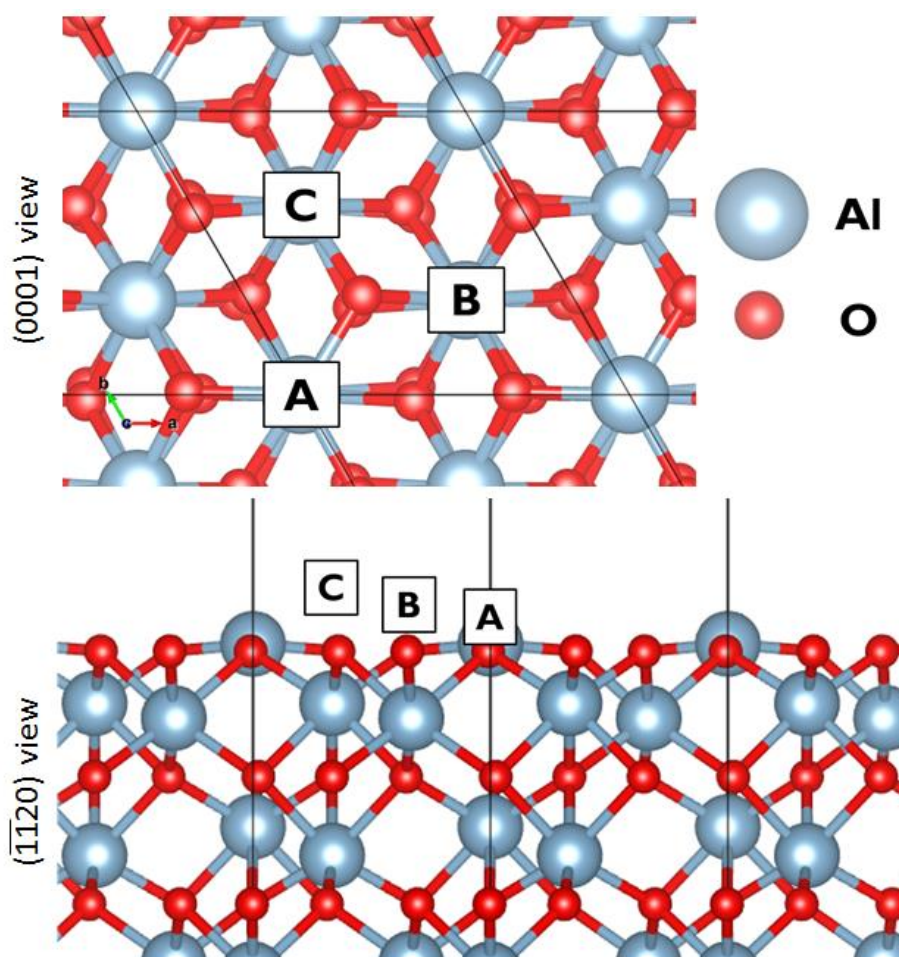


Figure 1.2: Top and side views of the calculated Al-terminated $\alpha\text{-Al}_2\text{O}_3$ (0001) surface. A, B, and C high symmetry surface cation sites are labeled and will be referred to in the text. Black lines indicate the bulk unit cell boundaries in the a and b directions. One unit cell consists of six Al_2O_3 units stacked in the c direction.

1.5 Outline

In this document, I explore the interactions between components of oxide catalysts under simplified model conditions. This work focuses on planar model catalysts that are compositionally related to those in use today, but the cases studied are also excellent models for studying the fundamental chemical physics of catalysis. Ultrathin films (on the order of monolayers or less) of catalytically active materials, namely oxides of V and W, are grown on single crystal substrates and studied with a suite of tools, including *in situ* synchrotron X-ray, scanning probe, and ultra-high vacuum surface science methods. Theoretical calculations are also employed to refine experimentally derived models and provide further insight into the electronic mechanisms underlying the real materials' behavior. These methods are discussed in **Chapter 2**.

In **Chapter 3**, I introduce prior experimental results which lay the groundwork for my studies on the V-W system, including the work of Feng *et al.*[66] on tungsten oxide (WO_x) atop $\alpha\text{-Fe}_2\text{O}_3$ (hematite) single crystal surfaces. This is followed by theoretical results which explain the experimental data, providing information to which the experimental methods are not sensitive. The redox-induced transition between the oxidized and reduced phases, which involves the movement of cations into different symmetry-inequivalent surface sites, is explained as a consequence of two stable terminations of the hematite (0001) surface. I also present results from studies on $\text{WO}_x/\alpha\text{-Fe}_2\text{O}_3$ nanopowders for comparison with the model catalyst results in an attempt to bridge the “materials gap” between single crystal surfaces and real catalysts.

Chapter 4 includes a detailed experimental and theoretical study of V, W, and mixed V-W oxides on the $\alpha\text{-Al}_2\text{O}_3$ (0001) surface. While transition aluminas are frequently used in catalysis, I consider sapphire to be a mostly-inert “stage” upon which the interactions between V and W may

be studied. V is found to undergo a redox-reversible coherent-incoherent transition similar to that observed previously on α -TiO₂ (110)[33]. On its own, sapphire-supported W is very stable as W⁶⁺, largely unaffected by a reducing environment. However, in the presence of nearby V, W will reduce to a lower oxidation state. DFT modeling confirms that the presence of V affects the *d*-states of nearby W, suggesting a mechanism of V-W catalytic synergy.

To date, the experimental work in the Bedzyk group's catalysis studies have only involved redox reactions in H₂ and O₂ (with the exception of Dr. Zhenxing Feng's use of cyclohexane over V / TiO₂[35]). This is due to the difficulty of performing *in situ* experimental studies with reactants such as NH₃ or NO, important components of the NO-SCR reaction. In **Chapter 5**, I approach this problem using density functional theory, studying the interaction of NH₃ with oxide-supported V and W *in silico*. The stability of different VO_x structures (monomers, dimers, and longer oligomers) on α -Al₂O₃ (0001) is calculated for different chemical conditions, and structural and chemical effects on NH₃ adsorption are explored. The system is then modified either by replacing some V with W or by switching the support to α -Fe₂O₃ (0001). In both of these cases, the interaction of NH₃ with the surface is stronger than for V / α -Al₂O₃ (0001).

This work concludes with a view forward in **Chapter 6**. Future projects along the lines of this work are proposed, as well as new challenges which might be undertaken as our experimental capabilities improve. Two appendices are provided to aid in future investigations. **Appendix A** provides a "how-to" guide to DFT using VASP software. This is intended to provide some familiarity with VASP, *ab initio* calculations in general, and the UNIX environment in which calculations are set up and executed. **Appendix B** covers challenges in the dynamical X-ray diffraction of sapphire crystals. Due to the extremely narrow rocking curves of this electron-light

material, special care must be taken in XSW measurements and optical setups. Some surprising consequences of the low electron density of Al are also documented.

2. Methods

As mentioned in **Chapter 1**, the methods of surface and interface science may be divided into two classes: *surface averaging* and *local probe*. Each set of approaches has advantages and disadvantages, but they are highly complementary. In this chapter, I discuss the use of statistically averaging X-ray methods for the characterization of surfaces and interfaces. The theory of X-ray scattering and spectroscopy of materials is also described in detail. Local probe methods, namely atomic force microscopy (AFM), will also be presented. Finally, I discuss theoretical methods, namely density functional theory (DFT), which provides structural, electronic, and energetic information about the materials studied in this dissertation.

2.1 Statistically Averaging Methods

2.1.1 Introduction to X-rays

Since Röntgen's discovery of X-rays in 1895, we have used this radiation for probing matter that is invisible to us. Anyone who has broken a bone knows how X-rays reveal the structure of matter that is buried beneath other matter. However, in materials science, we use the ability of X-rays to probe length scales well beyond the visible. While the penetrating power of X-rays through bulk materials is useful in many aspects of materials science, in this document I will mostly focus on the latter use: X-ray scattering and spectroscopy to study phenomena at the scale of atoms. Mathematical descriptions and derivations in this section are derived from Refs. [67-69].

Electromagnetic radiation with wavelengths of $0.1 - 100 \text{ \AA}$ makes up the X-ray spectrum, with wavelengths of $0.1 - 2 \text{ \AA}$ defined as "hard" X-rays and $2 - 100 \text{ \AA}$ called "soft" X-rays. Because their wavelength is on the order of the spacing between atoms and molecules in solids and liquids,

we can use the scattering of X-rays to learn about the structure of condensed matter. Additionally, these wavelengths correspond to the characteristic energies that bind core-shell electrons to their atoms. The absorption of X-rays at characteristic wavelengths (and the corresponding emission of X-rays or electrons) enables X-ray spectroscopies that probe the chemistry of materials.

X-rays, as with any electromagnetic radiation, can be described as a temporally oscillating electric field \mathbf{E} propagating along the wavevector \mathbf{k} with an electric field amplitude E_0 pointing in the $\hat{\mathbf{e}}$ polarization direction as described by

$$\mathbf{E}(\mathbf{r}, t) = \hat{\mathbf{e}} E_0 e^{i(\mathbf{k} \cdot \mathbf{r} - \omega t)} \quad (2.1)$$

where \mathbf{r} is the position vector, ω is the frequency of the radiation, and t is the time. \mathbf{k} is related to the wavelength λ of the radiation by $\mathbf{k} = \frac{2\pi}{\lambda} \hat{\mathbf{u}}$, where $\hat{\mathbf{u}}$ is the unit vector of propagation of the X-ray. The intensity of this field, which can be measured by counting the number of photons to pass through a given area over time, is proportional to $|\mathbf{E}|^2$. This demonstrates a well-known problem with X-ray measurements: if we are limited to measuring the intensity of an X-ray wave, then we lose any information relating to its phase.

To understand the scattering of X-rays from materials, we must start by defining the scattering of X-rays from the particles that compose them. Consider the fraction of X-ray intensity elastically scattered by a particle with charge q and mass m , which is measured at a point a distance R_0 from the particle and angle 2θ from the incident radiation:

$$\frac{I}{I_0} = \frac{q^4}{R_0^2 m^2 c^2} P \quad (2.2)$$

where $\frac{I}{I_0}$ is the ratio of scattered intensity to the intensity of radiation incident on the particle, c is the vacuum speed of light, and P is the polarization factor. In the case of unpolarized incident light, $P = \frac{1+\cos^2 2\theta}{2}$. For polarized X-rays, this factor depends on the scattering direction relative to the polarization and will be discussed later. Since the ratio of the mass of atomic nuclei to electrons is on the order of 10^4 , nuclear scattering can be neglected, and we only consider scattering from electrons. In the case of X-rays scattered from electrons, this is referred to as Thomson scattering. We can then consider the elastic scattering of X-rays from an ensemble of electrons, namely the electron cloud of an atom. As Thomson scattering from one electron suggests, X-ray scattering from an atom will not be isotropic, but rather will depend on the angle between the incident beam and the point of measurement of the scattered beam. We therefore discuss scattering in terms of the scattering vector (or momentum transfer vector)

$$\mathbf{Q} = \mathbf{k} - \mathbf{k}' \quad (2.3)$$

where \mathbf{k} and \mathbf{k}' represent the incident and scattered X-ray wavevectors which are separated by an angle 2θ . Since $\mathbf{k} = \frac{2\pi}{\lambda} \hat{\mathbf{u}}$, the magnitudes $|\mathbf{k}| = \frac{2\pi}{\lambda}$ and $|\mathbf{Q}| = \frac{4\pi}{\lambda} \sin \theta$. As we will see, it is often more convenient to discuss X-ray scattering in momentum space, i.e. reciprocal space, instead of real space.

The atomic form factor $f^0(\mathbf{Q})$ takes into account the scattering from all electrons in an atom:

$$f^0(\mathbf{Q}) = \int \rho(\mathbf{r}) e^{i\mathbf{Q}\cdot\mathbf{r}} d\mathbf{r} \quad (2.4)$$

where $\rho(\mathbf{r})$ is the electron density of the atom at a point \mathbf{r} . The value of the form factor is the atomic number Z of the atom at $\mathbf{Q} = 0$ but decreases monotonically at higher \mathbf{Q} . We see that the

form factor is proportional to the Fourier transform of the real-space electron density, and this is generally true beyond a single atom. The absorption of X-rays by the atom, as well as resonant effects near absorption edges, are accounted for in the complete atomic scattering factor

$$f(\mathbf{Q}, \lambda) = f^0(\mathbf{Q}) + f'(\lambda) + if''(\lambda). \quad (2.5)$$

$f'(\lambda)$ and $f''(\lambda)$ account for wavelength-dependent “anomalous” scattering near absorption edges and absorption effects, respectively.

2.1.2 Kinematical X-ray scattering

In an ensemble of atoms, such as a crystal, scattered X-rays will interfere with each other. Since a crystal is composed of planes of atoms, coherent addition of X-rays resulting in intense reflection from the crystal will only occur at particular geometries. Here, we assume that X-rays are relatively non-interacting and will only scatter once in the crystal. The scattering of electromagnetic radiation by a crystal is described by the structure factor $F(\mathbf{Q}, \lambda)$, which builds on the atomic form factor by accounting for the position of multiple atoms in space. The structure factor over a volume of material, F_V , is written as

$$F_V(\mathbf{Q}, \lambda) = \sum_{\mathbf{r}_j} f_j(\mathbf{Q}, \lambda) e^{i\mathbf{Q} \cdot \mathbf{r}_j} \sum_{\mathbf{R}_n} e^{i\mathbf{Q} \cdot \mathbf{R}_n} \quad (2.6)$$

where the first sum represents the structure factor $F(\mathbf{Q}, \lambda)$ for one repeating unit of matter, such as a crystal unit cell, and the second sum accounts for all these units in the volume under X-ray illumination. The intensity of scattered X-rays is proportional to the square of the modulus of the structure factor. If we consider a 3-dimensional crystal of finite dimensions $N_1 N_2 N_3$, where N is the number of unit cells in a particular direction, and $\mathbf{R}_n = n_1 \mathbf{a} + n_2 \mathbf{b} + n_3 \mathbf{c}$, where n are integers and \mathbf{a} , \mathbf{b} , and \mathbf{c} are the crystallographic directional vectors, then the second sum becomes

$$\sum_{n_1=0}^{N_1-1} e^{i\mathbf{Q}\cdot(n_1\mathbf{a})} \sum_{n_2=0}^{N_2-1} e^{i\mathbf{Q}\cdot(n_2\mathbf{b})} \sum_{n_3=0}^{N_3-1} e^{i\mathbf{Q}\cdot(n_3\mathbf{c})} \quad (2.7)$$

Each component of this sum is a geometrical series

$$\sum_{n=0}^{N-1} e^{i\mathbf{Q}\cdot(n\mathbf{a})} = \frac{e^{i\mathbf{Q}\cdot(N\mathbf{a})}}{e^{i\mathbf{Q}\cdot\mathbf{a}}} \quad (2.8)$$

Taken together, the square of the modulus of these sums can be expressed as

$$\frac{\sin^2(\frac{1}{2}N_1\mathbf{Q}\cdot\mathbf{a})}{\sin^2(\frac{1}{2}\mathbf{Q}\cdot\mathbf{a})} \frac{\sin^2(\frac{1}{2}N_2\mathbf{Q}\cdot\mathbf{b})}{\sin^2(\frac{1}{2}\mathbf{Q}\cdot\mathbf{b})} \frac{\sin^2(\frac{1}{2}N_3\mathbf{Q}\cdot\mathbf{c})}{\sin^2(\frac{1}{2}\mathbf{Q}\cdot\mathbf{c})} \quad (2.9)$$

The intensity of X-rays scattered by the crystal then becomes

$$I(\mathbf{Q}, \lambda) = |F_V(\mathbf{Q}, \lambda)|^2 = \left| \sum_{\mathbf{r}_j} f_j(\mathbf{Q}, \lambda) e^{i\mathbf{Q}\cdot\mathbf{r}_j} \right|^2 \frac{\sin^2(\frac{1}{2}N_1\mathbf{Q}\cdot\mathbf{a})}{\sin^2(\frac{1}{2}\mathbf{Q}\cdot\mathbf{a})} \frac{\sin^2(\frac{1}{2}N_2\mathbf{Q}\cdot\mathbf{b})}{\sin^2(\frac{1}{2}\mathbf{Q}\cdot\mathbf{b})} \frac{\sin^2(\frac{1}{2}N_3\mathbf{Q}\cdot\mathbf{c})}{\sin^2(\frac{1}{2}\mathbf{Q}\cdot\mathbf{c})} \quad (2.10)$$

From this formulation, we see that for large values of $N_1N_2N_3$, the intensity will approach zero except when the so-called Laue conditions

$$\mathbf{Q}\cdot\mathbf{a} = 2\pi h, \quad \mathbf{Q}\cdot\mathbf{b} = 2\pi k, \quad \mathbf{Q}\cdot\mathbf{c} = 2\pi l \quad (2.11)$$

are satisfied; here we refer to the Miller indices hkl . This is a principal tenet of X-ray crystallography, since diffracting planes of crystals will result in intense reflections only at particular values of \mathbf{Q} . Since the intensity of the reflection will be in part proportional to the unit

cell structure factor, the pattern of diffracted intensity from a crystal can be used to solve its structure.

As the structure factor is related to the Fourier transform of the real-space distribution of scattering matter, it is convenient to visualize X-ray interactions in reciprocal (or momentum) space. By this concept, each set of hkl planes collapses into a point at $\mathbf{H} = h\mathbf{a}^* + k\mathbf{b}^* + l\mathbf{c}^*$ with the reciprocal lattice vectors defined as

$$\mathbf{a}^* = 2\pi \frac{\mathbf{b} \times \mathbf{c}}{\mathbf{a} \cdot (\mathbf{b} \times \mathbf{c})}, \quad \mathbf{b}^* = 2\pi \frac{\mathbf{c} \times \mathbf{a}}{\mathbf{a} \cdot (\mathbf{b} \times \mathbf{c})}, \quad \mathbf{c}^* = 2\pi \frac{\mathbf{a} \times \mathbf{b}}{\mathbf{a} \cdot (\mathbf{b} \times \mathbf{c})} \quad (2.12)$$

At these points, $|\mathbf{H}| = \frac{2\pi}{d_{hkl}}$, where d_{hkl} is the spacing between hkl planes. When $\mathbf{Q} = \mathbf{H}$, these reciprocal-space points coincide with large values of the structure factor, which is experimentally analogous to moving a crystal into a diffracting condition and placing a detector in the path of the diffracted beam. This is illustrated by recalling that $|\mathbf{Q}| = \frac{4\pi}{\lambda} \sin \theta$, so at a Laue condition

$$|\mathbf{H}| = \frac{2\pi}{d_{hkl}} = |\mathbf{Q}| = \frac{4\pi}{\lambda} \sin \theta$$

$$\lambda = 2d_{hkl} \sin \theta_B \quad (2.13)$$

where θ_B is the Bragg angle of the hkl reflection. **Equation 2.13** is known as Bragg's Law.

2.1.3 Dynamical X-ray diffraction and the X-ray Standing Wave technique

The above discussion assumes that X-rays only scatter once in the crystal. However, in the case of highly perfect single crystals, frequent multiple scattering events result in nearly perfect X-ray reflection. This phenomenon is described by solving Maxwell's equations for electromagnetic waves in a 3-dimensional periodic dielectric medium[70-73]. In the case of diffraction from a

crystal in which the polarization vectors of the incident and diffracted X-ray radiation point in the same direction (σ -polarization), the behavior in the region of X-ray reflectivity near a Laue condition is described in terms of the complex angular coordinate

$$\eta = \frac{b\Delta\theta \sin(2\theta_B) + \frac{1}{2}\Gamma F_0(1-b)}{\Gamma\sqrt{|b|}\sqrt{F_{\mathbf{H}}F_{\bar{\mathbf{H}}}}} \quad (2.14)$$

where the constant $\Gamma = \frac{r_e\lambda^2}{\pi V_C}$, V_C is the crystal unit cell volume, the classical electron radius $r_e = 2.818 \times 10^{-5} \text{ \AA}$, and b is the crystal asymmetry factor

$$b = -\frac{\sin(\theta_B - \phi)}{\sin(\theta_B + \phi)} \quad (2.15)$$

where ϕ is the miscut angle between the diffracting planes and the physical surface of the crystal. $F_{\mathbf{H}}$ and $F_{\bar{\mathbf{H}}}$ are the unit cell structure factors at the Laue conditions $\mathbf{H} = hkl$ and $\bar{\mathbf{H}} = -\mathbf{H} = \bar{h}\bar{k}\bar{l}$, and F_0 is the structure factor at $hkl = 0,0,0$ (the forward scattering condition). Note that the structure factor may be broken down into real and imaginary components:

$$F_{\mathbf{H}} = F'_{\mathbf{H}} + iF''_{\mathbf{H}} \quad (2.16)$$

The region in which the real component of the complex angular coordinate $\eta' < -1$ is called the β branch, and the region $\eta' > +1$ is the α branch. As the crystal is rotated from $\eta = +1$ to $\eta = -1$ (corresponding to an increase in θ), the crystal passes through the Bragg bandgap between the two branches in which total external reflection occurs. The electric field amplitude ratio between the diffracted (E_H) and incident (E_0) electromagnetic waves through this transition is

$$\frac{E_{\mathbf{H}}}{E_0} = -\sqrt{|b|} \sqrt{\frac{F_{\mathbf{H}}}{F_{\bar{\mathbf{H}}}}} (\eta \pm \sqrt{\eta^2 - 1}) \quad (2.17)$$

In the β branch, the right-most side of the equation is $(\eta + \sqrt{\eta^2 - 1})$, whereas it is $(\eta - \sqrt{\eta^2 - 1})$ elsewhere. There is a significant imaginary component to $\frac{E_{\mathbf{H}}}{E_0}$ when $|\eta| < 1$, corresponding to the Bragg bandgap which connects the α branch and β branch. This solution satisfies the boundary condition imposed by conservation of energy; otherwise, the energy exiting the crystal in the diffracted wave would be larger than that transferred into the crystal by the incident wave. The measured reflectivity R is normalized to the incident beam intensity and is the square of the electric field amplitude ratio:

$$R = \frac{I_{\mathbf{H}}}{I_0} = \left| \frac{E_{\mathbf{H}}}{E_0} \right|^2 \quad (2.18)$$

The theoretical rocking curve of the (220) reflection of a symmetrically cut Si crystal at an X-ray beam energy of 7 keV is shown in **Figure 2.1**.

One consequence of this phenomenon is that the reflection (known as the Darwin curve or rocking curve) has a finite angular width

$$\omega = \Delta\theta_{\eta=-1} - \Delta\theta_{\eta=+1} = \frac{2\Gamma \sqrt{F'_{\mathbf{H}}F'_{\bar{\mathbf{H}}} + F_0''^2 - F''_{\mathbf{H}}F''_{\bar{\mathbf{H}}}}}{\sqrt{|b|} \sin 2\theta_B} \quad (2.19)$$

In the hard X-ray regime, rocking curve widths are typically on the order of $0.0001^\circ - 0.001^\circ$ ($2 - 20 \mu\text{rad}$). This is an obvious departure from kinematical theory, which predicts an infinitesimally narrow rocking curve for an infinite perfect crystal. Additionally, due to refraction of X-rays at the crystal surface, the center of the rocking curve is offset from the nominal Bragg angle by

$$\Delta\theta_{\eta=0} = \frac{\Gamma F'_0}{\sin 2\theta_B} \frac{1 + |b|}{2|b|} \quad (2.20)$$

While the amplitude of E_H is relatively large as the crystal moves from the α branch to the β branch, there is also a shift in the phase of E_H by $-\pi$. On the low-angle side of the rocking curve, E_H and E_0 are out of phase with each other on the diffraction planes, whereas they are in phase on the high-angle side. This phase shift occurs through the Bragg bandgap, and it is the foundation of the X-ray standing wave (XSW) technique[73-75]. The position of the diffraction planes as defined above has been derived in terms of the XSW phase shift[76].

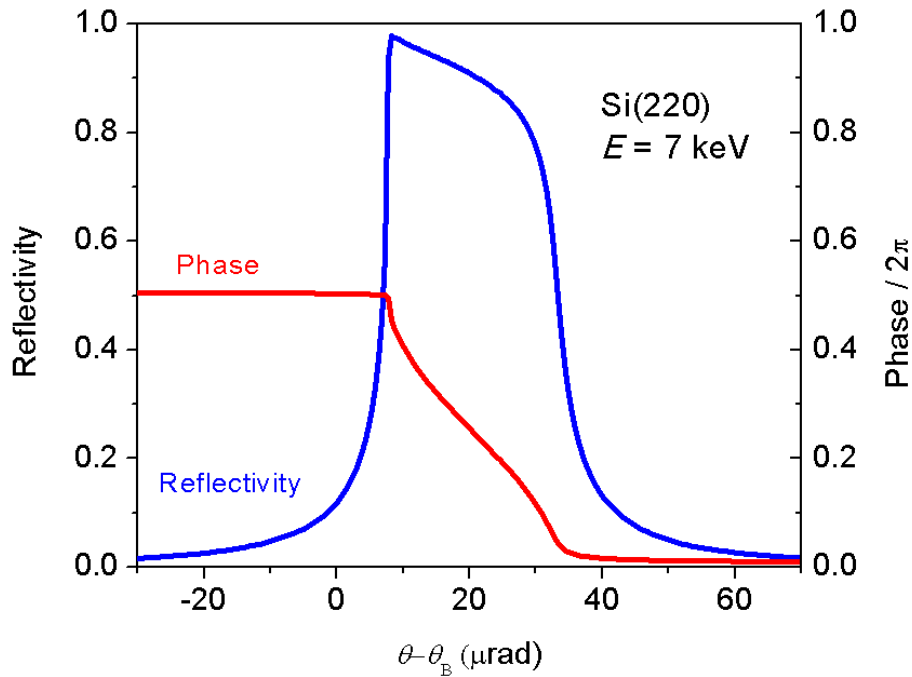


Figure 2.1: Calculated Si (220) Bragg reflectivity (rocking curve) $\left|\frac{E_H}{E_0}\right|^2$ and phase ν of the E-field amplitude ratio $\frac{E_H}{E_0}$ for an incident beam energy of 7 keV. The relative phase shift of π radians is independent of the choice of unit cell origin relative to the atomic positions in the crystal structure. This particular absolute phase setting corresponds to a selection of the unit cell origin to coincide with a Si (220) atomic plane.

2.1.4 X-ray standing waves

In the region above the crystal, the superposition of all contributions to the local electric field near a reflection at \mathbf{H} results in a total electric field intensity (normalized to the incident plane wave intensity) of

$$I(\theta, \mathbf{r}) = 1 + R(\theta) + 2\sqrt{R(\theta)} \cos(v(\theta) - \mathbf{H} \cdot \mathbf{r}) \quad (2.21)$$

The first and second terms come from E_0 and E_H , respectively. The interference of E_H and E_0 near the surface of the crystal results in an additional standing wave field which is parallel to the diffracting crystal planes. The period of the standing wave is equal to $d_{hkl} = \frac{2\pi}{|\mathbf{H}|}$, which is the d -spacing of the diffracting crystal planes, and the phase v changes through the Bragg bandgap as described above. Below the surface of the crystal, the intensity in **Equation 2.21** is multiplied by an absorption term $e^{-\mu_z(\theta)z}$, where μ_z is the effective linear absorption coefficient, which includes an extinction effect, and z is the depth into the crystal from the surface[77].

As the crystal is rotated through the rocking curve and phase of the outgoing wave shifts, the phase of the standing wave will also shift by $-\pi$. Because the standing wave is independent of time, this corresponds to an inward spatial shift of the high-intensity standing wave antinodes by $\frac{1}{2}$ of the period, i.e. $\frac{1}{2}d_{hkl}$. This shift moves the XSW antinodes in the crystal into the diffraction planes on the high-angle side of the rocking curve from the planes $\frac{1}{2}d_{hkl}$ in the direction out of the crystal face on the low-angle side[76]. (As a consequence, the high-angle side of the rocking curve typically suffers a reduction in intensity as seen in **Figure 2.1**, as the high electron density planes are usually stronger X-ray absorbers.) The atoms near the surface are therefore subjected to

substantial changes in the local electric field intensity, and their X-ray photoemission is proportional to these intensity changes. (The details of X-ray photoemission and its consequences are discussed in the following section.) X-ray photoemission or fluorescence of near-surface atoms can therefore be used as a near-field “phase detector” of the XSW phase shift. The X-ray fluorescence yield $Y_{\mathbf{H}}$ of a particular atomic surface species near a reflection condition \mathbf{H} , normalized to the “off-Bragg” fluorescence yield Y_{OB} far from the reflection condition, is

$$\frac{Y_{\mathbf{H}}}{Y_{\text{OB}}} = 1 + R_{\mathbf{H}} + 2\sqrt{R_{\mathbf{H}}}f_{\mathbf{H}}\cos(v - 2\pi P_{\mathbf{H}}) \quad (2.22)$$

where $f_{\mathbf{H}}$ is the “coherent fraction”, or fraction of atoms that are in a particular “coherent position” $P_{\mathbf{H}}$ relative to the reflecting crystal planes. Some examples of the expected $Y_{\mathbf{H}}$ for perfectly coherent ($f_{\mathbf{H}} = 1$) surface species at several different values of coherent position is shown in **Figure 2.2**. There is clearly a large change in the symmetry of the fluorescence yield for small changes in the coherent position. In the example case of the Si (220) reflection, the coherent positions are varied in increments of 0.2, corresponding to $0.2 * d_{\text{Si}(220)} = 0.38 \text{ \AA}$. Thus, by measuring the fluorescence yield and reflectivity and fitting for $f_{\mathbf{H}}$ and $P_{\mathbf{H}}$, XSWs can be used to identify the position of surface or near-surface atoms with sub-Ångström precision, so long as they are well-ordered in the direction normal to the scattering planes.

The coherent fraction and position of a particular near-surface species derived from an XSW measurement at \mathbf{H} can be considered as \mathbf{H}^{th} -order Fourier amplitude and phase components, respectively, of an atomic density distribution $\rho(\mathbf{r})$ for a particular near-surface species[75]. By measuring $f_{\mathbf{H}}$ and $P_{\mathbf{H}}$ at several different reflection conditions, an accurate density distribution can be resolved by the Fourier summation

$$\rho(\mathbf{r}) = \rho_0 \sum_{\mathbf{H}} f_{\mathbf{H}} \exp[-i(\mathbf{H} \cdot \mathbf{r} - 2\pi P_{\mathbf{H}})] \quad (2.23)$$

Atomic density maps derived this way can be used to pinpoint particular high-symmetry occupation sites for surface species or bulk impurities. They can also be used to inform models for fitting multiple occupation sites, since two symmetry-inequivalent sites may be impossible to resolve at particular \mathbf{H} conditions.

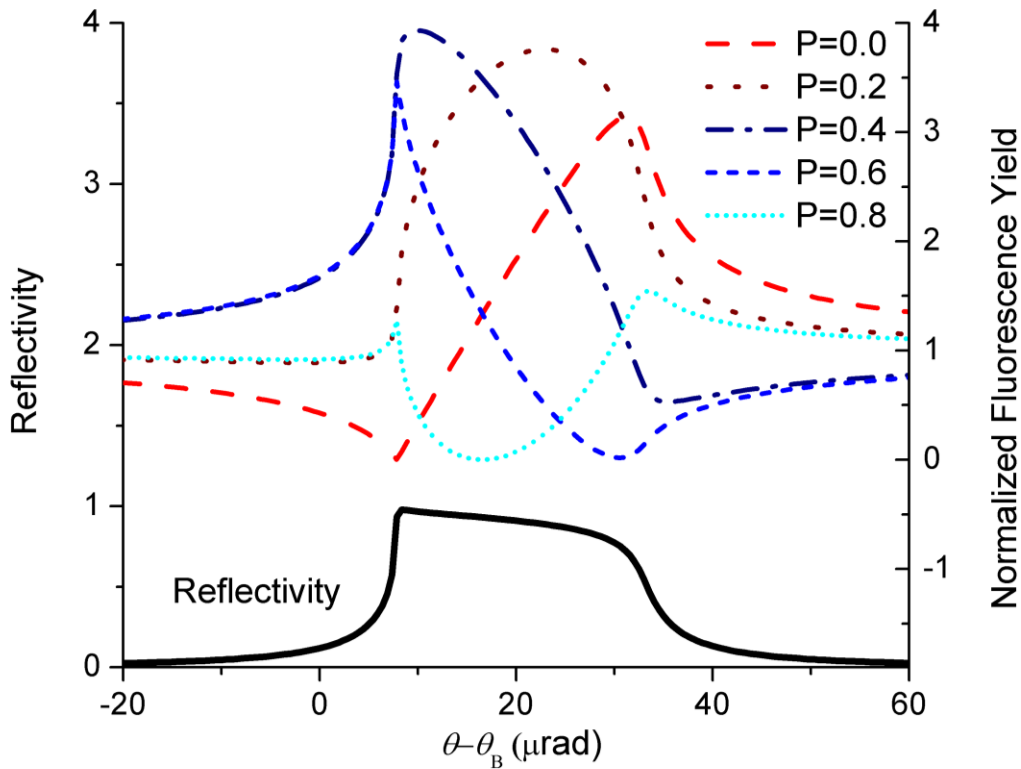


Figure 2.2: Calculated fluorescence yields $Y_{\mathbf{H}}$ of perfectly coherent surface atoms ($f_{\mathbf{H}} = 1$) at the Si (220) reflection condition at 7 keV, with calculated reflectivity for reference. The coherent position of 0.0 corresponds to the planes of high Si density.

XSW results are fitted using SWAM (Standing Wave Analysis for MATLAB) software (version 4.2) as developed in the Bedzyk group by G.P. Campbell, J.D. Emery[68], Z. Feng[78], and J.-C.

Lin[79]. SWAM is based on SWAN[80], its Fortran-based predecessor developed by L. Cheng and A.E. Escudro. Compared to SWAN, SWAM is more accessible and robust, and it models experimental conditions more accurately. XSW data are interpreted first by fitting the experimentally measured rocking curve (RC) with a curve calculated by dynamical diffraction theory. The theoretical RC used for fitting is obtained by convoluting calculated RCs for the sample reflection as well as the emission function of the upstream optics. A Gaussian curve may be incorporated into the convolution in order to account for crystal mosaic effects or other sources of experimental broadening. Additionally, the properties of multiple optical components are explicitly taken into account (as opposed to convolution with a single theoretical optic RC in SWAN). The angular narrowing of the emission function from detuned multiple-crystal optics[81] can be calculated and accounted for in XSW fits. In the case of XSW on α -Al₂O₃, as reported in **Chapter 4**, this detuning factor becomes important for accurately fitting crystal reflections which are narrower than the emission functions from a single monochromator crystals. Using RC fits, the XSW-induced fluorescence yields are fit using **Equation 2.22**.

The experimental RC is fit using detuning parameters that are consistent with the degree of detuning between two channel-cut Si(220) optics. Gaussian smearing parameters are then chosen such that a qualitatively good fit is obtained and the theoretical rocking curve (without smearing) has a maximum reflectivity roughly equal to that expected for a perfect single crystal. Two fits are typically performed with different degrees of Gaussian smearing, and these are both used to calculate f_H , P_H , and Y_{OB} . The reported results are an average of results from the two fits, with larger uncertainties calculated accordingly.

2.1.5 X-ray photoemission and spectroscopy: XPS, XRF, and XAFS

In a free atom, electrons occupy orbitals of discrete energy. Upon excitation by radiation at or above this energy, there is a probability for the electron to be ejected from the atom into the vacuum. This photoelectric effect is key to X-ray spectroscopy, as by probing the energy of these orbitals or observing the effect of photoemission in a material, we can learn the chemical identity, chemical state, and coordination environment of its atoms.

The core electrons in an atom of an element such as a transition metal are shown schematically in **Figure 2.3(A)**. These energy levels correspond to electron binding energies that are specific to each element. In **Figure 2.3(B)**, an incident photon causes an excitation in an atom resulting in the ejection of an electron from the $1s$ orbital (K shell). The removal of a core-shell electron leaves an unstable core hole, and an electron from a higher shell moves into this hole (**Figure 2.3(C)**). The energy gained in this process can be transferred to a fluorescent photon (as shown) or an Auger electron. The probability of an excitation event causing fluorescence or an Auger event depends on the atomic number Z ; the probability of fluorescence increases with increasing Z [82]. These three types of ejected particles – a photoelectron, a fluorescent photon, or an Auger electron – can all be detected and their energies measured, and from this information the composition or chemical details of their parent atom can be obtained.

X-ray photoelectron spectroscopy (XPS) is perhaps the most powerful technique for non-destructive compositional and chemical analysis of surfaces. Samples are exposed to an X-ray beam (typically from an Al, Mg, or synchrotron source), which excites core-shell photoelectrons. These are collected by an energy-dispersive spectrometer, such as a hemispherical analyzer or a cylindrical mirror analyzer. Because of the short mean-free path length of photoelectrons in matter,

XPS is typically performed in an ultra-high vacuum (UHV) chamber at pressures below 10^{-7} mbar; however, ambient pressure XPS is becoming widely accessible for *in situ* studies at pressures up to 1 mbar or so[83].

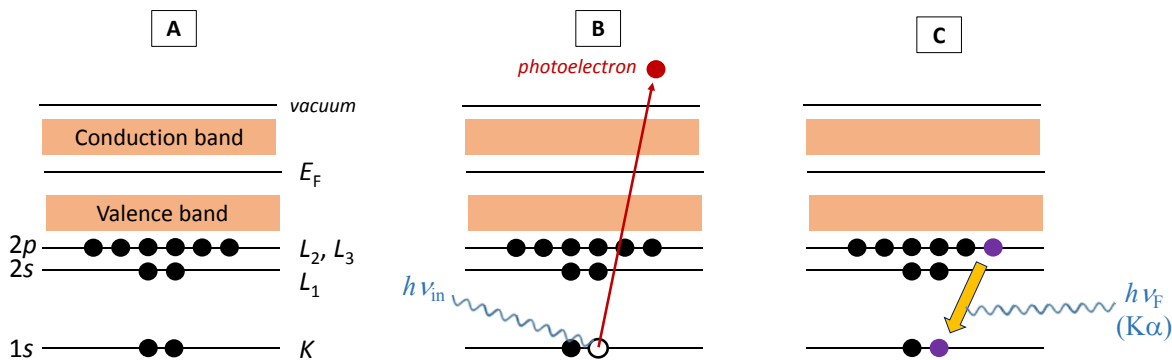


Figure 2.3: Schematic of (A) the electron levels of an atom, with the core electrons shown as black dots occupying the levels; (B) a photoemission event caused by an incident X-ray with energy $h\nu_{in}$, wherein a photoelectron is ejected and a $1s$ core hole is created; and (C) a $2p - 1s$ relaxation event leading to the emission of a $K\alpha$ fluorescent photon.

The kinetic energy E_k of a photoelectron excited by X-rays depends on the binding energy of the electron E_b and the X-ray energy $h\nu$. By conservation of energy, E_b is calculated as:

$$E_b = h\nu - E_k - \phi \quad (2.24)$$

The work function ϕ accounts for kinetic energy lost in the electron analyzer. Every orbital of every atom has a particular binding energy that can be used to “fingerprint” the presence of an atomic species. The photoelectron signal of a species in a material surface is broadened due to the core-hole lifetime, final state effects, sample charging, phonon structure, and instrumental resolution, resulting in a peak width of ~ 1 eV on a laboratory instrument[84-86]. All orbitals beyond the s orbital may demonstrate spin-orbit splitting into doublets. The chemical state of the species can also shift the binding energy by several eV from the electron binding energy in a

neutral atom. A core electron in a positively charged metal cation, for example, will experience less charge screening by other electrons than it would in a neutral atom, resulting in a higher binding energy. Thus, specific binding energy shifts indicate differences in charge state. While XPS has good chemical sensitivity, it can only detect photoelectrons emitted from the top few nanometers of material due to the short mean-free path length of photoelectrons.

The emitted X-ray fluorescence (XRF) energy is the difference in energy between the inner shell containing the core hole and the outer shell from which an electron moves into it. Both electron shells involved in this transition are affected similarly by changes in charge screening due to different valence states, so the energy of the emitted fluorescent photon does not change substantially with a change in the atomic charge unless the outer shell is near the Fermi level. This is often a moot point, as the energy resolution of most energy-dispersive X-ray detectors is on the order of 100 eV or more and therefore insensitive to shifts of a few eV. However, as X-rays interact very weakly with matter, XRF can be used to detect the composition of surfaces and interfaces in gaseous, liquid, or other *in situ* environments of interest. XRF can also be used to accurately quantify the composition of a surface by comparison with a calibrated standard sample; this is discussed in detail in **Chapter 4**.

When the energy of an incident X-ray is tuned to an absorption edge of an element in a material, photoelectrons are generated, and the X-ray absorption of the material increases dramatically. Features in the X-ray absorption spectrum below, at, and above this absorption edge compose the X-ray absorption fine structure (XAFS). The X-ray absorption spectrum within a few tens of eV of the absorption energy is referred to as the X-ray absorption near-edge structure (XANES) or near-edge X-ray absorption fine structure (NEXAFS) region. At higher energies (~50 eV above

the absorption edge), oscillations in the X-ray absorption spectrum emerge which make up the extended X-ray absorption fine structure (EXAFS)[87-91].

The XANES region encodes chemical properties and local symmetries of the absorbing atom. As with XPS, charge screening effects cause a change in the binding energy of the core electrons, with more positive oxidation states resulting in higher absorption edges. At incident photon energies just above the absorption edge, a “white line” indicates transitions from core levels to unoccupied states above the Fermi level. In some cases, such as at the Au L₃ edge, the white line is nearly nonexistent as there are almost no unoccupied levels in the uppermost *d*-states for low-energy photoelectrons to move into. As the photoelectron energy increases, low-energy photoelectrons interact strongly within the local coordination environment around the absorbing atom. Resonances with multiple photoelectron scattering events in this energy region are visible as changes in the X-ray absorption of the sample. Additionally, features at energies *below* the main absorption edge (“pre-edge” features) indicate bound states with transitions that are not allowed by dipole selection rules (such as $1s \rightarrow 3d$ for transition metals) but occur due to local symmetry effects.

The EXAFS region encodes local structural information that extends out to within ~ 6 Å of an absorbing atom. An emitted photoelectron can be thought of as an outgoing wave from the absorbing atom with a wavevector k :

$$k = \sqrt{\frac{2m_e(E - E_0)}{\hbar^2}} \approx \sqrt{0.2625(E - E_0)} \quad (2.25)$$

Here, k is in units of Å⁻¹, m_e is the electron mass, \hbar is Planck’s constant, E is the incident X-ray energy (in eV), and E_0 is the absorption edge energy (in eV). As the energy of the X-ray impinging

on a sample increases, so does k . In a condensed phase such as a solid, the emitted photoelectron wave scatters (with a phase shift) from nearby atoms. The backscattered photoelectron wave interferes with the emitted wave, causing a change in the X-ray absorption of the sample. As k increases, the photoelectron wavelength changes, and thus oscillations emerge in the X-ray absorption spectrum. Single- and multiple-scattering events contribute to this pattern, with each backscattering photoelectron path contributing. Analysis of EXAFS spectra can therefore reveal information about the local structure of a material, whether crystalline or amorphous[89].

To make sense of the EXAFS spectrum, the first step is to extract the fine-structure function

$$\chi(k) = \frac{\mu(k) - \mu_0(k)}{\Delta\mu_0(k)} \quad (2.26)$$

where $\mu(k)$ is the measured X-ray absorption coefficient, $\mu_0(k)$ is a fitted background function, and $\Delta\mu_0(k)$ is the change in absorption coefficient at the absorption edge. $\chi(k)$ can be inverse-Fourier transformed into real space, resulting in a radial distribution function[89]. However, this function does not provide accurate bond lengths as it does not take into account the phase shift of the photoelectron wave upon scattering, and it also includes multiple-scattering contributions that may give rise to extra features corresponding to a single coordination shell. For quantitative analysis, $\chi(k)$ is fit to the “EXAFS equation”[88]:

$$\chi(k) = \sum_i \frac{N_i f_i(k)^2 e^{-2k^2\sigma_j^2}}{kR_i^2} \sin(2kR_i + \delta_i(k)) \quad (2.27)$$

Here, the contributions of several different scattering paths are summed. N is the number of neighboring atoms with a particular scattering path of distance R from the absorbing atom, σ^2 accounts for structural and thermal disorder, and $\delta(k)$ and $f(k)$ define the phase shift and

attenuation due to scattering. Fitting EXAFS spectra can therefore yield information about the bond length and coordination number of a species of interest, such as a dispersed catalyst metal or oxide[5]. EXAFS spectra may be fit using FEFF software[92-94] as implemented in the Demeter package[95].

2.2 Local probe imaging: atomic force microscopy

Statistically averaging methods are complemented by local probe measurements which give real-space images of nanoscale phenomena. Scanning probe microscopy (SPM) is particularly well-suited to surface studies as it involves an interaction of a narrow tip with the surface, yielding spatially-resolved information about the surface. The SPM family includes atomic force microscopy (AFM), scanning tunneling microscopy (STM), Kelvin probe force microscopy (KPFM), magnetic force microscopy (MFM), and a variety of other methods which provide topographic, electronic, thermal, magnetic, mechanical, and chemical information at the nanometer or atomic scale[96].

AFM is one of the most robust and widely-used SPM methods. It involves a direct physical interaction between the surface and a hard, extremely sharp tip (with curvature on the order of nanometers) at the end of a cantilever[97]. The movement of the tip in the surface-normal direction causes deflections in the cantilever which are measured using a laser reflected from the cantilever into a split photodiode detector. In contact-mode AFM, the tip is rastered across the surface and is deflected by surface features. Because the tip “drags” along the surface, this type of measurement is potentially locally destructive. Tapping-mode AFM addresses this issue by oscillating the cantilever near some resonance frequency and measuring the modulation of the oscillation amplitude as the tip is rastered across the surface. This results in a much softer interaction of the

tip with the surface, preserving surface features and retaining the integrity of the tip[5]. In non-contact (NC) AFM, the tip is kept further from the sample surface, and the interaction between the tip and surface is measured as a modulation in the frequency of cantilever oscillation. NC-AFM is the preferred technique for atomic-resolution surface science studies in vacuum[97]. In this work, all AFM images were collected in tapping mode.

2.3 Sample preparation: atomic layer deposition

Atomic layer deposition (ALD) is a relatively low-temperature process for the controlled deposition of conformal thin films[98-100]. In ALD, two reactants (labeled here as A and B) are dosed over the substrate in series. Reactants are chosen such that when a surface is covered in A, it will not continue to react with A but will react strongly with B; likewise, the B-terminated surface will interact readily with A but not B. This results in a self-limiting growth pattern by which one atomic layer of material can be grown at a time. A typical example of an ALD reaction is that of trimethylaluminum (TMA) and H₂O. TMA reacts readily with a hydroxylated surface, releasing methane to form a partially methylated aluminum oxide overlayer. Subsequent dosing with H₂O removes the remaining methyl ligands and hydroxylates the surface, which can then react again with TMA to form another Al layer. By this description, ALD ostensibly yields one atomic layer of the material of interest per A-B cycle; however, the characteristics of real film growth, particularly in the initial nucleation steps, are much more complicated[101].

Although a variety of growth methods are available for coating single crystal substrates with metals or metal oxides, ALD is unique in that it can be applied to materials of any arbitrary form. Thus, we use ALD to move one step closer to bridging the “materials gap” between single crystal model surfaces and real powder catalysts. Two A-B reactions are used for ALD growth in this

work: WF_6 and Si_2H_6 for W growth[102], performed by J. Elam's group at Argonne National Laboratory, and vanadium oxytriisopropoxide / H_2O for V growth, performed by T. Drake in P. Stair's group at Northwestern. Details of ALD for each case are given in the **Methods** sections of the following chapters.

2.4 Theoretical methods

With computational capabilities ever increasing, theoretical methods become applicable to larger ensembles of simulated atoms. Within the framework of density functional theory (DFT), known material properties have been explained, and new materials have been developed from first principles. Structures calculated by methods such as plane-wave DFT are amenable to comparison with statistically averaging measurements such as X-ray diffraction. The details of these methods are described below. This section is largely derived from Ref. [103].

2.4.1 Self-consistent field (Hartree-Fock) method

Since its development, quantum mechanics has suffered from the difficulty of explicitly solving for the energy of any system of more than one electron. For large systems such as those found in real materials, more efficient methods of approximating the solutions to the multi-electron Schrödinger equation were needed. For many years, the most widely-used approximation was the Hartree-Fock method, also known as the self-consistent field (SCF) method. In SCF calculations, the multi-electron system is modeled on a basis set of orthogonal one-electron hydrogen-like Slater orbitals. Linear combination of atomic orbitals (LCAO) is then used to provide the initial trial electron wavefunctions. The energy of the Slater determinant wavefunction, which is the antisymmetrized product of all the wavefunctions of the system, is then iteratively minimized using the variational principle. This results in the one-electron Fock operator, which accounts for

the total electronic kinetic energy and all Coulombic attractions and repulsions between nuclei and electrons. The Fock operator can be used to calculate chemical and physical properties of the system since it encompasses the calculated wavefunctions of all electrons in the system. However, in reducing a system of electrons to a one-electron wavefunction, it completely neglects electron-electron correlation effects, and it is relatively computationally inefficient.

2.4.2 Density functional theory

Density functional theory (DFT) has become a useful tool in materials research, and particularly to the study of catalysis, because it can be applied to both structural and chemical problems. Through iterative electronic and atomic relaxations, the ground state (zero Kelvin) structure of a set of atoms can be determined, and the electron densities may be projected onto atomic orbitals for analysis of spatial electron densities and atom-specific partial densities of states (PDOS).

At the heart of DFT is the Hohenberg-Kohn theorem, which states that the ground state density of a system of many interacting electrons corresponds to a unique external potential $v(\mathbf{r})$, and that there exists a unique ground state electron density that corresponds to a minimization of the total energy[104]. This energy E_v is a functional of the electron density $n(\mathbf{r})$:

$$E_v[n] = \int v(\mathbf{r})n(\mathbf{r})d\mathbf{r} + F[n], \quad (2.28)$$

where $F[n]$ is a functional that accounts for the kinetic energy of the electrons and electron-electron interactions. Within the latter component of $F[n]$ lies the well-known intractable problem of multiple interacting bodies. However, the Kohn-Sham ansatz replaces the model of interacting particles with one of non-interacting particles, which can be solved[105]. Electron-electron

interactions are accounted for in an exchange-correlation energy $E_{xc}[n]$. By using an accurate formulation of $E_{xc}[n]$, the ground state energy E_v can be calculated.

Several approximations for $E_{xc}[n]$ exist today, with varying degrees of complexity[106, 107]. The simplest version is the local density approximation (LDA), in which $E_{xc}[n]$ is calculated as

$$E_{xc}^{LDA}[n] = \int d^3r n(\mathbf{r}) \epsilon_{xc}^{hom}(n(\mathbf{r})), \quad (2.29)$$

where $\epsilon_{xc}^{hom}(n(\mathbf{r}))$ is the exchange-correlation energy density calculated for a homogeneous electron gas with the same charge density as at point \mathbf{r} . This can be generalized into a spin-polarized form (LSDA) by replacing $\epsilon_{xc}^{hom}(n(\mathbf{r}))$ with a function of separate spin-up and spin-down electron densities. L(S)DA is sufficient for many calculations but can be improved by considering the gradient of the electron density as well:

$$E_{xc}^{GGA}[n] = \int d^3r n(\mathbf{r}) \epsilon_{xc}^{hom}(n(\mathbf{r})) F_{xc}(n(\mathbf{r}), |\nabla n(\mathbf{r})|, \dots) \quad (2.30)$$

Here, F_{xc} is a dimensionless functional of multiple terms in the gradient expansion of $n(\mathbf{r})$. Several different GGA functionals exist, and the inclusion of more terms in F_{xc} such as the orbital kinetic energy density $\tau_{\sigma}(\mathbf{r})$ or the Laplacian $\nabla^2 n(\mathbf{r})$ yields meta-GGA functionals. Using Hartree-Fock methods, the exact exchange energy can be calculated and blended with other exchange-correlation approximations in hybrid functionals. Several approaches exist for dealing with strongly correlated electrons as well, such as the $+U$ method which is discussed in **Section 3.2.2.9**.

In materials studies, DFT employs a basis set of atomic orbitals, Gaussian functions, or plane waves. The plane-wave method is ideally suited to periodic structures such as crystals and their surfaces. Valence electron wavefunctions are modeled as combinations of plane waves of different

energies, and a cutoff energy (typically on the order of a few hundred eV) is selected to optimize the precision of the calculations while reducing the number of plane waves that must be generated. Ionic core pseudopotentials can be used to efficiently model the core electrons which are not typically involved in interatomic interactions. However, all-electron calculations are sometimes preferred if core electron states are of interest.

For this work, plane-wave DFT as implemented in the *Vienna Ab Initio Simulation Package* (VASP) code[108-111] was used. Atoms are described by "frozen" core pseudopotentials and valence electron wavefunctions. A projector augmented wave (PAW) scheme[112] was employed to smoothen the core potential, improving the efficiency of calculations and enabling the use of a 400 eV cutoff energy. The PW91 GGA functional[113] was used for all calculations; details about the choice of functional are given in **Appendix A**. Surface supercells with periodic boundary conditions constituted "slabs" of atoms separated by regions of vacuum space. These supercells were designed with an initial guess of atomic positions, and the atoms were then relaxed using iterative quasi-Newtonian[114] or conjugate-gradient methods. k -point meshes were calculated by the method of Monkhorst and Pack[115].

2.4.3 Electronic structure and chemical analysis

DFT results in a slowly varying electron density which encompasses all the nuclei in the system. It is therefore not immediately obvious which electrons "belong" to which nuclei. In order to compare DFT results with formal charges widely referred to in chemistry, some type of partitioning is needed. In this work, three different measures are used to quantify the interaction between the catalytically active surface metal cations and the oxygen anions coordinating them. The first, the Wigner-Seitz charge (Q_{ws}), is measured by projecting the electron density onto a

sphere of radius R_{WS} surrounding the atom center. R_{WS} values are selected such that Q_{WS} is roughly equal to the expected formal charge of the cation as well as to fill the volume of the surface supercell. In this work, R_{WS} values are 0.7 Å for H, 0.8 Å for Al, V, and N, 0.9 Å for W, and 1.6 Å for O. The Wigner-Seitz method is sensitive to changes in orbital populations, although as is shown in **Chapter 3**, the effect is subtle.

An alternative *ab initio* measure of charge distribution is the Bader method as implemented by Henkelman et al.[116]. The Bader method divides the relaxed electron density along zero-flux surfaces and assigns the partitioned charge to the atomic center within the partition. By this method, the degree of ionic or covalent character of metal-oxygen bonds can be estimated, as shared charge will appear as less localized electron density (and therefore as a lower-than-expected cationic charge). The presence of a point between atoms at which the gradient of the electron density is zero, called a bond critical point, indicates the presence of a bond, and the electron density at this point correlates with the bond order or strength[117]. Bond critical points provide a topological basis for the identification of weak interactions such as hydrogen bonds[118].

Integrated cationic Bader charges derived from DFT-relaxed bulk structures of V_2O_3 , VO_2 , V_2O_5 , WO_3 , WO_2 , and bulk α - Al_2O_3 and α - Fe_2O_3 are given in **Table 2.1**. For tungsten, we find that the Bader charges yield roughly one-half of the formal ionic charge. For example, for W^{6+} and W^{4+} from DFT-relaxed bulk WO_3 and WO_2 , the calculated Bader charges are 3.03 and 2.12, respectively, and this relationship can be used to derive chemical insight for surface W species. However, Bader charge partitioning shows more limited use for V, with a charge spread of less than 0.4 e between V^{3+} and V^{5+} . For sapphire, Al shows a Bader charge of 3.00 e , corresponding to a complete lack of valence charge density in the Bader volume enclosing the Al core. This is

consistent with expectations for sapphire, which is highly ionic. The cation-anion interactions in hematite are more covalent, resulting in an intermediate Bader charge of about $1.6 e$.

Oxidation state	V	W	Al	Fe
3+	1.80		3.00	1.60 – 1.64
4+	2.12	2.12		
5+	2.19			
6+		3.03		

Table 2.1: Integrated charge within Bader volumes for bulk cations in DFT-relaxed structures.

Independent of charge density, one can derive some insight on the bonding from structural data. The valence of a metal cation, for example, is analogous to the nominal “formal charge” and can be calculated from the bond distances between a metal atom and its coordinating ligands[119, 120]. The contribution of each metal-ligand bond to the valence can be added up, giving a bond valence sum (BVS) for the ion. While this method was originally developed as a tool for bulk inorganic chemistry, it has recently been proven as an effective predictor of surface structure stability by comparing the BVS of surface ions with their bulk-like counterparts[121, 122]. The BVS for a particular atom is defined as the following:

$$V = \sum_{i=1}^n \exp\left(\frac{l_0 - l_i}{b}\right) \quad (2.31)$$

where l_i signifies the bond lengths of interest (such as metal-oxygen bonds), and l_0 and b are derived from fits to bulk materials. In this work, bond valence sums are calculated using values fit for several oxidation states of vanadium[123], tungsten[124], aluminum, and iron[125].

BVS calculations were performed for the same bulk structures documented in **Table 2.1**, and results are shown in **Table 2.2**. For V_2O_3 , there is a range of valences depending on which symmetry-inequivalent cation is selected. As expected, the BVS values are in close quantitative

agreement with the oxidation state for most of the cations of interest. In particular, the result for Al^{3+} is very close to the expected bulk-like value of 3.00; however, the valence of Fe^{3+} is significantly underpredicted, suggesting that the lattice parameter for hematite is somewhat overpredicted. This will be addressed in the interpretation of results in **Chapters 3 and 5**.

Oxidation state	V	W	Al	Fe
3+	3.03 – 3.32		3.01	2.91
4+	4.00	3.39	--	--
5+	4.80	--	--	--
6+	--	5.79	--	--

Table 2.2: Calculated bond valence sums for bulk cations in DFT-relaxed structures. BVS parameters are from published data, as mentioned in the text.

Further chemical information can be found through densities of states (DOS) calculations. In a VASP calculation, the total DOS of the supercell is calculated, and partial densities of states (PDOS) are projected onto the Wigner-Seitz spheres corresponding to each atomic orbital. Atomic PDOS plots reveal the occupied and unoccupied states around each atom and can be used to extract information about surface or interface atomic species *vs.* bulk species. Band-projected charge densities can be calculated for selected regions of the DOS, providing a real-space image of localized electronic states. Practical details of these methods are discussed in **Appendix A**.

3. Structural and Chemical Behavior of Low Coverage WO_x / α - Fe_2O_3 Single Crystals and Nanopowders

The Bedzyk group's approach to catalysis involves the precise observation of changes in model catalyst surface structures. In 2009, Dr. Zhenxing Feng and colleagues published work that showed a redox-reversible movement of sub-ML tungsten cations on the α - Fe_2O_3 (hematite) (0001) surface with corresponding chemical state changes[66]. The aims of this chapter are to: (1) elucidate the details of this transition using theoretical tools, and (2) attempt to bridge the single-crystal results with real catalysts. DFT-derived models are proposed for the oxidized and reduced states observed experimentally[126], and the structure and chemistry of WO_x supported on α - Fe_2O_3 nanopowders is investigated.

3.1 Introduction: Model Catalysis Studies on α - Fe_2O_3 (Hematite)

Low-coverage layers of transition metals or their oxides atop oxide substrates of different compositions are of interest as catalysts for a myriad of industrial and environmental applications[16, 127]. For oxide-supported heterogeneous catalysts, the catalytic selectivity and activity for specific reactions is defined by the composition of both the oxide substrate and the metal or metal oxide overlayer and the structure of the interface. In particular, the atomic and electronic structure of surface active sites must be well defined in order to understand the catalytic mechanism and for the rational design of catalytic reaction pathways[128].

In previous work[129, 130], density functional theory (DFT) has been combined with surface-sensitive X-ray techniques to characterize monolayer and sub-monolayer coverage vanadium

oxide (VO_x) on $\alpha\text{-Fe}_2\text{O}_3$ (hematite) (0001) surfaces under relevant chemical conditions. X-ray photoelectron spectroscopy (XPS) was employed to probe chemical changes when the surface was subjected to oxidizing and reducing conditions[131]. X-ray standing wave (XSW) imaging provided a sub-atomic-scale map of V positions relative to the hematite lattice under the same chemical conditions. Each of these methods revealed that chemically induced changes in the surface structure were reversible, indicating that the reaction could proceed over several redox cycles without changing substantially. With the use of the same experimental methods, the structure and chemical properties of an acid catalyst[132], tungsten oxide (WO_x) atop the hematite (0001) surface, have recently been elucidated[66].

While XSW reveals the positions of metal cations at the surface with respect to bulk cation positions, it is not possible to resolve the configuration of surface oxygen atoms and substrate cations in most cases. These details of surface stoichiometry and reconstruction are necessary to understand the chemical mechanisms underpinning catalysis and the contributions of both W and Fe, which provide acid sites for catalytic reactions[133-135]. For example, mixed W-Fe catalysts are considered for use in heavy gas oil hydrotreatment needed for the purification of hydrocarbon fuels[135, 136]. Also, both WO_x and $\alpha\text{-Fe}_2\text{O}_3$ are earth-abundant semiconductors of interest for their properties as environmental photocatalysts[137, 138] and their potential for so-called “water splitting” reactions for hydrogen production[139-142]. Oxides of W and Fe even show synergistic effects in photocatalysis due to their ideal alignment of the conduction band of WO_3 with electron trap states in Fe_2O_3 [143, 144]. Despite this growing interest, the atomic-scale interactions between the two metals which lead to desirable activity and selectivity remain essentially unknown.

In this work, we use DFT to explore several proposed surface structures under both “dry” and hydroxylated conditions. Self-consistent structural relaxations were carried out, followed by detailed density of states (DOS) calculations, for $\frac{1}{2}$ ML W coverage on O- and Fe-terminated hematite (0001), revealing the consequences of varying O coordination, hydroxylation, and surface O vacancies on the surface structure and chemical properties. Full ML coverage of W is also investigated. After surveying different surface terminations and coordinations, models are proposed to explain experimental XSW and XPS results.

In order to address the “materials gap” between single crystal model catalyst surfaces and real, structurally complex catalysts, the structure and chemical behavior of W supported on hematite nanopowders was investigated experimentally. Structural details from EXAFS spectra are interpreted in light of theoretical results, but we also show important differences in the chemical characteristics of low-coverage WO_x on single crystal vs. nanopowder supports.

3.2 Oxidized and reduced states of WO_x / $\alpha\text{-Fe}_2\text{O}_3$: a theoretical investigation

3.2.1 Methods

The *Vienna Ab Initio Simulation Package* (VASP) was used to perform spin-polarized periodic slab DFT calculations with plane-wave basis sets[108-112]. The interactions between ionic core pseudopotentials and valence electrons were modeled using the projector augmented wave (PAW) method[112] and corrected with the spin-polarized generalized gradient exchange-correlation approximation (GGA) as developed by Perdew and Wang (PW91)[113]. While PW91 and other gradient-corrected methods show systematic errors with respect to binding energy, bond lengths, and magnetic properties, they are typically more accurate than the local spin density approximation

(LSDA) for these aspects[113, 145, 146]. $4 \times 4 \times 1$ k -point meshes generated by the method of Monkhorst and Pack[115] were used for all structural relaxations and densities of states (DOS) calculations; test cases using $6 \times 6 \times 1$ and $8 \times 8 \times 1$ k -point meshes yielded similar results as for $4 \times 4 \times 1$.

Periodic supercells were constructed by decorating the surface of a 1×1 (0001) hematite slab with W, O, and H atoms to represent surface structures under oxidizing or reducing chemical environments. The surface cell shown in **Figure 3.1** is a relaxed O-terminated hematite surface cell containing 19 atoms. This stoichiometry is the “base” upon which additional atoms (including Fe, W, and their ligands) are adsorbed. The bottom 4 atomic layers ($\text{Fe-O}_3\text{-Fe}_2\text{-O}_3$) were held rigid to enforce bulk boundary conditions, while all other atoms were allowed to relax via a quasi-Newtonian method or conjugate-gradient algorithm[114]. The slab is based on the hematite unit cell with a bulk Fe BVS of 2.91 as given in **Table 2.1**, which is close to the expected value of 3. The two symmetrically inequivalent low-energy surface cation sites, denoted A and B, correspond to bulk-like cation positions. The third surface site, labeled C, sits directly above a near-surface substrate cation and is unlikely to be occupied. When labeling cations throughout the cell, we consider lines A, B, and C perpendicular to the surface and passing through the corresponding surface sites. Fe atoms occupying sites along these lines are denoted Fe_A , Fe_B , and Fe_C herein, and the same scheme is used for W (W_A , W_B). Placing W in either the A or B site on a 1×1 surface cell constitutes 0.5 monolayer (ML) coverage; a full ML is considered to be both sites filled. The mixed-ML case corresponds to W occupying one site and Fe in the opposite site, e.g. Fe_A , W_B . For adsorbed O atoms, subscripts indicate the surface site from which O is nearly vertically displaced, *i.e.* O_A , O_B ; O_s denotes a crystal surface-layer atom. The stacking sequence of the ideal O-terminated surface is $\text{O}_3\text{-Fe}_C\text{Fe}_B\text{-O}_3\text{-Fe}_A\text{Fe}_C\text{-O}_3\text{-Fe}_A\text{Fe}_B\text{...}$. The antiferromagnetic spin structure is

initialized with both Fe atoms in each Fe_2 layer having the same spin (with a magnitude of $3 \mu_B$), as has been determined to be the correct antiferromagnetic ordering for hematite[57, 147].

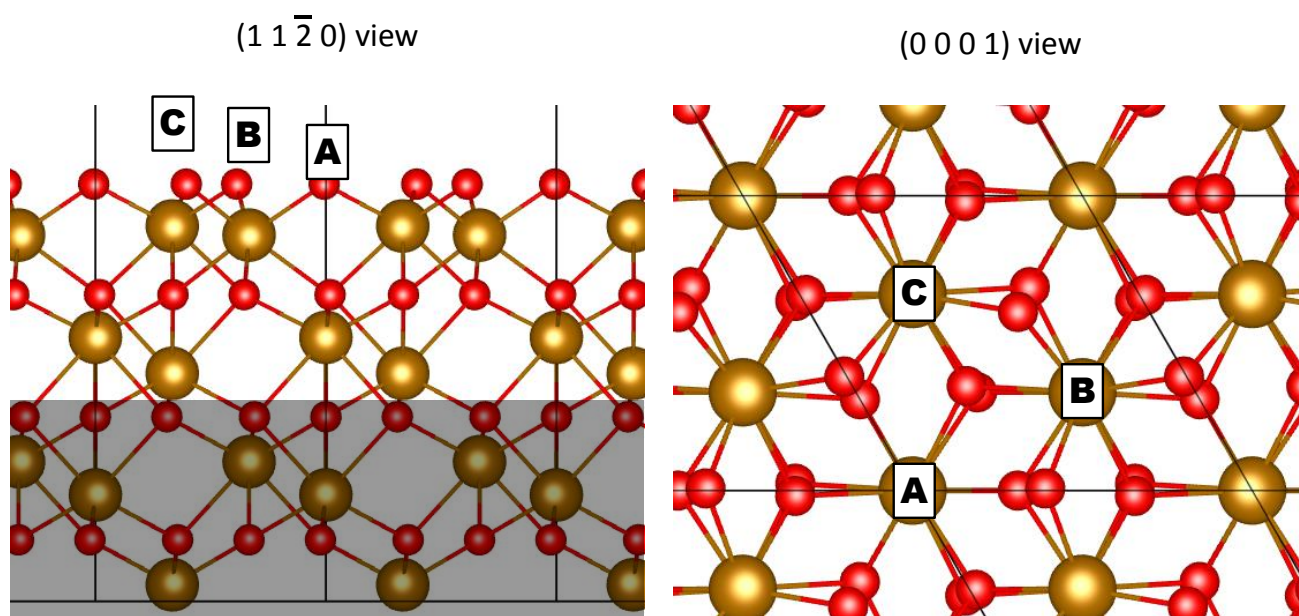


Figure 3.1: Side $(1\ 1\ \bar{2}\ 0)$ and top $(0\ 0\ 0\ 1)$ views of the relaxed O-terminated hematite (0001) supercell slab used as a starting point for the calculations reported herein. The atoms under the gray rectangle are fixed to maintain bulk-like boundary conditions, whereas all other atoms are allowed to relax. Fe and O atoms are represented by large gold and small red spheres, respectively.

After structural relaxation, the chemical properties of each atom were assessed using three complementary methods. Electron density was integrated over spherical volumes of variable radius R_S centered at atomic lattice positions, generating so-called Wigner-Seitz (WS) charges. This density was further projected onto the occupation of site-specific s , p , and d valence shells, allowing the calculation of the total density of states (DOS) of the surface cell and orbitally weighted partial densities of states (PDOS) for individual atoms. R_S values were chosen by adjusting empirical ionic radii so that the (typically overlapping) atomic volumes add approximately to the unit cell volume. In this work, R_S values were fixed at 1.6 \AA for O, 0.9 \AA for

Fe and W, and 0.7 Å for H. The Bader method and bond valence sums, described in **Chapter 2**, were also employed to analyze the ionicity and valence of Fe and W.

In XP spectra, shifts of ~1-2 eV in core-shell energy levels indicate changes in the degree of oxidation in metals. The XP shifts of the W 4f core-level doublet observed by Feng *et al.*[66] for sub-ML WO_x / α -Fe₂O₃ (0001) are consistent with conventional interpretations of W⁵⁺ and W⁶⁺ states. (W⁴⁺ was not observed in these experiments.) Excitations of core-level states create strong localized perturbations in the ground state potential which are reflected in spectral properties, including energy level shifts and wave-function distortions. Local perturbations are not easily treated in periodic band structure methods, however, as interference between localized holes in neighboring cells influences calculated results. While large supercells can in principle resolve this problem, localized molecular cluster models are an attractive alternative. The molecular orbital description used in this approach provides an intuitive chemical interpretation of the hole-induced atomic-state changes around the excitation site. Localized-state embedded cluster methods[148] were employed herein for interpreting theoretical results in light of XP spectra. Several cluster models, based on the ground state periodic structures, were studied.

Spectroscopic transition energies, which are rigorously differences in *total energy* between initial and final states, can be quantitatively approximated in the Slater transition state (TS) scheme as the differences between one-electron energies, defined by the TS Hamiltonian[149]. In its simplest form the TS Hamiltonian is derived by an expansion of the total energy in a Taylor series of the orbital occupation numbers as $H^* = (H_i + H_f)/2$, i.e., the average of initial and final state Hamiltonians. This procedure is easily implemented in Hartree-Fock and DFT codes, and it is used

in the present work to model shifts in W $4f$ XP spectra. Our non-relativistic calculations do not account for spin-orbit splitting, but they provide a good approximation of binding energy shifts due to changes in charge screening upon changing the coordination environment of W.

3.2.2 Results

The interlayer spacings of clean hematite surfaces with different oxygen coverages calculated by the model used herein are in good agreement with previously calculated data by Bergermayer *et al.*[57] and Jin *et al.*[129], as shown in **Table 3.1**. This comparison and previous studies using the same methods on vanadium oxide-terminated hematite surfaces[129, 130] lend confidence to the computational procedures used in this work.

Surface Layers	I: O ₃ -Fe			II: Fe _A -I			III: O' _A Fe _A -I	
	I ^(a)	I ^(b)	I ^(c)	II ^(a)	II ^(b)	II ^(c)	III ^(a)	III ^(c)
O _{3t} [/O _{1t}]-Fe _{At}							+87.4	+88.6
O _{3t} -Fe _{Bt}	-4.9	-5.8	-6.7					
Fe _{Bt} -Fe _{At}	-78.4	-73.0	-72.7					
Fe _{At} -O _{3s}	+34.7	+30.6	+32.7	-51.3	-59.4	-53.6	-18.8	-18.3
O _{3s} -Fe _{Cs}	-7.1	+4.5		+6.4	+5.8	+7.6	+4.6	+6.0
Fe _{Cs} -Fe _{Bs}	+17.4			-31.7	-46.0	-38.4	-50.7	-58.9
Fe _{Bs} -O _{3s-1}	-3.5			+13.1	+9.7	+14.7	+18.8	+18.8

(a) After Ref. 26 (b) After Ref. 4 (c) Present work

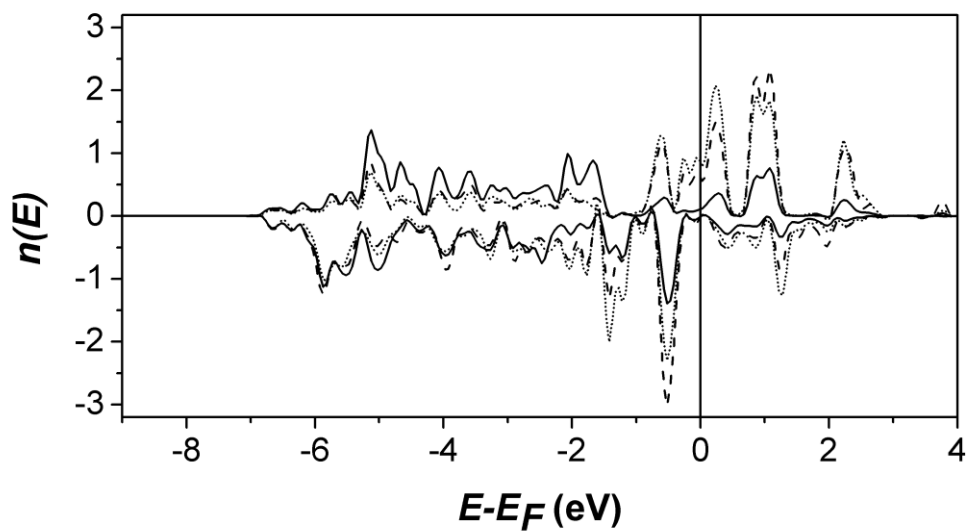
Table 3.1: Comparison of surface and near-surface layer relaxations in the z direction (% , relative to bulk) for clean O- and Fe-terminated hematite (0001) surface configurations and with $\frac{1}{3}$ ML coadsorbed oxygen on the Fe-terminated surface. Subscripts indicate the cation lattice position (A, B, C) or anion occupation number of the plane (3) as well as the layer: t (terminal), s (surface), or s-1 (sub-surface). I denotes the oxygen terminated surface; O' denotes coadsorbed oxygen.

The partial densities of states (PDOS) in **Figure 3.2** show the very different energy landscapes of the clean O- vs. Fe-terminated hematite (0001) surfaces. These are the ground-state surfaces

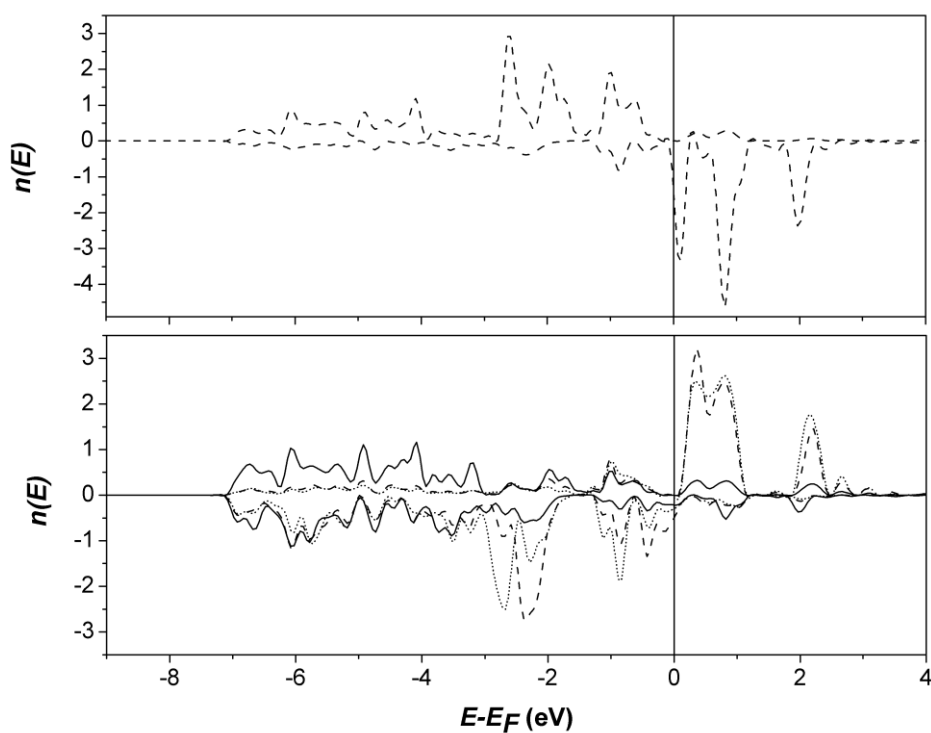
expressed under different oxidizing conditions as proposed by Wang *et al.* [54] In the former case, the O *sp* valence band of width ~ 7 eV dominates, showing strong ionic-covalent mixture from subsurface Fe_B and Fe_C sites which induce a small net magnetism. This phenomenon is in agreement with theoretical results for the (0001) hematite surface obtained by different methods in Ref. [54]. In the latter case, strong magnetic features of the Fe_A terminal layer are evident in occupied states within 3 eV of the Fermi energy E_F and in the low-lying excited state region.

3.2.2.1 $\frac{1}{2}$ ML W / O-terminated α -Fe₂O₃

Structures with varying degrees of oxygen coadsorption were investigated for $\frac{1}{2}$ ML W adsorbed to a clean O-terminated hematite surface. Here, a single W atom was placed in either the A or B cation surface site (structures denoted W_A or W_B) of a 1x1 supercell, and the opposite surface site was kept empty. These surfaces were then modeled with 0, $\frac{1}{3}$, and 1 ML of adsorbed O' (i.e. 0, 1, or 3 O atoms per 1x1 surface cell) to study the adsorption and oxidation states of surface-bound tungsten. Structural data derived from selected ground-state periodic cells, including interlayer and interatomic distances, are provided in **Tables 3.2(A)** and **3.3(A)**, and select structures are shown in **Figure 3.3**. The predicted cohesive energy and W net charge, as determined from both R_S volume integration and Bader schemes, are provided in **Table 3.4** for these structures and additional unstable isostoichiometric structures with lower predicted cohesive energy. Included for comparison are results from our predictions for W in bulk WO₂ and WO₃. Note that the nominal configuration for WO₃ is W⁶⁺ (s⁰p⁶d⁰).



(a)



(b)

Figure 3.2: Atom-projected partial densities of states (PDOS) for surface and near-surface atoms on clean (a) O-terminated and (b) Fe-terminated hematite. (a) and bottom panel of (b): solid line O_s , dashed Fe_C , dotted Fe_B ; upper panel of (b): terminal Fe_A . Here and in following figures, $n(E)$ is the density of states for each cation or the average density of states per atom for each oxygen layer.

Table 3.2: Calculated interlayer distances R_L (Å) for various W and O adsorption scenarios on hematite (0001). Surface identifiers indicate adsorbate sites with underlying (I) surface termination; O' represents overlayer oxygen. For Fe, subscripts t, B, and C refer to terminal sites and surface/near-surface B and C sites, respectively. Subscript notation is as described in Table 1. Numbers in parentheses indicate the standard deviation of the z-positions (last digit) in the oxygen plane of interest. If no such number is present, the standard deviation is less than 0.005 Å.

Surface Identifiers for columns in Table:

1: W_A	2: W_B	3: $O_A'W_A$	4: $O_3'W_B$	5: $O_B'Fe_BW_A^{(a)}$
6: $O_A'W_AFe_B$	7: $O_A'Fe_AW_B$	8: $O_B'W_BFe_A$	9: $O_{AB}'W_BFe_A$	10: $O_3'W_BFe_A$
11: W_AW_B	12: $O_{AB}'W_AW_B$	13: $O_3'W_AW_B$	14: W_AO_V	15: W_AO_{V2}
16: W_BO_{V3}	17: $W_AFe_BO_V$	18: $W_AFe_BO_{V2}$	19: $W_AFe_BO_{V3}$	20: $HO_A'W_A$
21: $(HO')_3W_B$	22: $HO_B'W_BFe_A$	23: $(HO')_{AB}W_AFe_B$	24: $(HO')_3W_AFe_B$	

(a) In this case, one surface O is displaced to the O' position (see text).

Surface	1	2	3	4	5	6	7	8	9	10
O'-W	--	--	1.73	0.7(4)	1.49	1.69	1.63	1.68	1.12(1)	0.71
O'-Fe _t	--	--	--	--	1.18	2.16	0.81	2.56	1.30(1)	1.26
W-Fe _t	--	--	--	--	-0.31	0.47	-0.82	0.88	0.18	0.55
W-O _s	0.43	-0.4(3)	0.66	1.95(8)	0.34(6)	0.8(4)	0.2(6)	0.8(5)	1.2(5)	1.55
Fe _t -O _s	--	--	--	--	0.65(6)	0.3(4)	1.0(6)	-0.0(5)	1.0(5)	1.00
O _s -Fe _C	1.26	1.3(3)	1.16	0.82(8)	1.30(6)	1.3(4)	1.6(6)	1.3(5)	1.2(5)	0.86
Fe _C -Fe _B	0.34	1.46	0.33	0.28	0.49	0.82	0.68	0.81	0.64	0.66
Fe _B -O _{s-1}	0.90	0.2(2)	0.93	0.99	0.80(5)	0.60(5)	0.65(3)	0.58(7)	0.73(3)	0.81

(A) Absorbed cations on oxygen-terminated hematite (0001) substrate. Coadsorbed oxygen is designated as O', with subscripts indicating site/occupancy.

Surface	11	12	13
O _t -W _A	--	1.7(5)	1.10(9)
O _t -W _B	--	1.1(5)	0.94(9)
W _A -O _s	1.21	1.0(3)	1.22(4)
W _B -O _s	0.29	1.6(3)	1.37(4)
O _s -Fe _C	1.39	1.1(3)	1.08(4)
Fe _C -Fe _B	0.90	0.62	0.56
Fe _B -O _{s-1}	0.47	0.74(3)	0.79(4)

(B) Monolayer W_AW_B overlayer with and without coadsorbed oxygen.

Surface	14	15	16	17	18	19
Fe _t -W	--	--	--	0.97	0.96	1.45
O _s -W	0.9(1)	0.93	--	1.0(1)	1.19	--
O _s -Fe _t	--	--	--	0.0(1)	0.23	--
O _s -Fe _C	0.9(1)	1.00	--	1.0(1)	1.41	--
W-Fe _C	0.05	0.06	1.13	0.04	0.22	-0.01
Fe _t -Fe _C	--	--	--	1.01	1.18	1.44
Fe _C -Fe _B	0.27	-0.07	0.90	1.39	1.08	0.39
Fe _B -O _{s-1}	1.1(1)	1.2(1)	0.49	0.3(3)	0.3(5)	0.87(5)

(C) W and bimetallic W, Fe adsorption on defected/reduced (oxygen vacancy O_v) surfaces. O_{v3} represents a fully depleted O₃ surface layer, i.e., metallic Fe termination.

Surface	20	21	22	23	24
H-O'	0.56	-0.3(7)	-0.12	0.4(2)	0.6(5)
O'-W	1.91	1.0(2)	1.58	1.9(2)	1.4(2)
O'-Fe _t	--	--	2.22	1.9(2)	1.0(2)
W-Fe _t	--	--	0.65	-0.03	-0.34
W-O _s	0.66(4)	1.3(2)	0.6(8)	0.9(5)	1.00(9)
Fe _t -O _s	--	--	-0.1(8)	0.9(5)	1.33(9)
O _s -Fe _C	1.27(4)	1.0(2)	1.7(8)	1.6(5)	1.13(9)
Fe _{Cs} -Fe _B	0.42	0.66	0.48	0.60	0.51
Fe _B -O _{s-1}	0.80(1)	0.78(5)	0.80(5)	0.65(7)	0.79(3)

(D) Protonated mono- and bi-metallic surface resulting in hydroxyl-bonded tungsten.

Table 3.3: Interatomic distances R_{ij} (Å) for half-monolayer W deposited on O_3 - and Fe-terminated hematite (0001) surfaces. Atom labels and surface identifiers are same as defined in **Table 3.2**. Upper and lower limits are given for varying bond lengths. Surface identifiers 1, 2, 3... are the same as in preceding tables. Interaction lengths greater than 3.25 Å are not reported.

Surface	1	2	3	4	5	6	7	8	9	10
O'-W	--	--	1.73	1.75-1.79	1.81	1.73	1.89	1.73	1.8	1.79
O'-Fe _t	--	--	--	--	1.93	>3.25	1.88	>3.25	1.95-1.99	2.00-2.01
W-Fe _t	--	--	--	--	2.54-2.79	2.46, 3.10	2.56	2.48	2.55-2.79	2.94
W-O _s	1.80	1.78-1.80	1.84	2.09-2.58	1.89	1.88-1.94	1.80-1.96	1.86-1.97	1.87-2.35	2.18-2.19
Fe _t -O _s	--	--	--	--	1.94-2.01	1.80-1.99	1.91-2.14	1.80-1.91	1.88-1.92	1.99-2.00
O _s -Fe _C	2.08	1.93-2.07	2.04	1.76-1.86	2.09	2.03-2.17	2.04-2.08	2.03-2.26	1.93-2.33	1.95-1.96
O _s -Fe _B	2.27	>3.25	2.19	1.81-1.90	2.11	2.27	2.02	2.15	2.05-2.16	2.16-2.17
W-Fe _(B/C)	>3.25	2.36, 2.75, 3.10	>3.25	3.10	2.57, 3.10	>3.25	2.59-2.94	2.9-3.10	3.10	3.08
Fe _t -Fe _(B/C)	--	--	--	--	2.65	2.48	>3.25	2.70	>3.25	>3.25

(A) Surface identifiers are as given in **Table 3.2**.

Surface	11	12	13
O _t -W _A	--	1.87	1.83- 2.05
O _t -W _B	--	1.72- 1.99	1.80- 2.00
W _A -W _B	3.03	2.73-2.92, 3.22	2.55, 3.08-3.09
W _A -O _s	1.98	1.87- 2.13	2.00- 2.19
W _B -O _s	1.91	2.02- 2.69	2.02- 2.23
O _s -Fe _C	2.1	2.06- 2.10	2.05- 2.13
O _s -Fe _B	>3.25	2.11, 2.29	2.20, 2.26
W-Fe _(B/C)	2.58	>3.25	3.04

(B) Surface identifiers are as given in **Table 3.2**.

Surface	14	15	16	17	18	19
W-Fe _t	--	--	--	2.63	2.55, 2.88	2.74
W-O _{s, s-1}	1.85- 2.17	1.93- 2.13	>3.25	1.92- 2.16	1.89- 2.01	2.03- 2.09
Fe _t -O _{s, s-1}	--	--	--	1.91, 2.03	1.92	>3.25
O _s -Fe _{Cs}	1.99, 2.13	2.03	--	2.01, 2.11	2.22	--
O _s -Fe _{Bs}	1.99	2.02	--	>3.25	>3.25	--
W-Fe _{(B/C)s,} (A/C)s-1	2.54- 2.78, 3.05- 3.12	2.53, 2.54, 2.97- 3.02	2.03, 3.10	2.56- 2.65, 3.00- 3.07	2.64- 2.80, 3.07	2.66- 2.99, 3.12
Fe _t -Fe _{(B/C)s,} (A/C)s-1	--	--	--	2.42, 2.63	2.32	2.19, 2.44

(C) Surface identifiers are as given in **Table 3.2**. The subscripts (B/C)s and (A/C)s-1 refer respectively to surface and sub-surface sites.

Surface	20	21	22	23	24
H-O'	0.97	0.98- 1.02	1.00	0.99, 1.00	0.97- 0.99
O'-W	1.92	1.77- 2.11	1.89	1.80	2.08- 2.13
O'-Fe _t	--	--	>3.25	1.99	2.05- 2.13
W-Fe _t	--	--	2.32	2.62, 2.70	2.56, 3.04
W-O _s	1.79- 1.80	1.88- 2.21	1.83- 2.09	1.82- 2.02	1.86- 1.97
Fe _t -O _s	--	--	1.82- 1.94	1.92- 2.02	2.04- 2.36
O _s -Fe _C	2.1	1.85- 1.96	1.96, 2.00	1.95, 2.12	2.02- 2.08
O _s -Fe _B	2.30, 2.38	1.97, 2.25	2.06	2.10	2.23, 2.31
W-Fe _(B/C)	>3.25	2.98	2.75	>3.25	>3.25
Fe _t -Fe _(B/C)	--	--	2.68	>3.25	>3.25

(D) Surface identifiers are as given in **Table 3.2**.

Surface	WO ₃	WO ₂	W _A	W _B	O' _A W _A	O' _B W _B	O' ₃ W _A	O' ₃ W _B
Relative energy (eV)	--	--	0.44	0	0	0.84	0.18	0
$\Delta E_{-\frac{1}{2}O_2}$	--	--	--	--	4.86	3.79	--	--
ΔE_{-O_2}	--	--	--	--	--	--	-0.66	0.36
Q _{ws} (W)	5.50	5.38	5.34	5.38	5.41	5.41	5.40	5.40
s	0.03	0.03	0.04	0.04	0.04	0.04	0.04	0.04
p	5.21	5.17	5.14	5.16	5.18	5.18	5.16	5.16
d	1.23	1.43	1.48	1.42	1.38	1.38	1.40	1.40
Q _B (W)	3.02	2.11- 2.12	2.06	2.30	2.73	2.79	2.75	2.77
BVS(W)	5.79	3.39	4.27	4.30	5.51	5.56	5.30	5.42

Table 3.4: Comparison of chemical characteristics of bulk WO₃ and WO₂ and different configurations of $\frac{1}{2}$ ML W atop the O-terminated α -Fe₂O₃ (0001) surface. The relative supercell energy is given for multiple configurations with the same stoichiometry; a value of 0 represents the most stable structure, with positive values indicating the energy relative to the lowest-energy structure. $\Delta E_{-\frac{1}{2}O_2}$ and ΔE_{-O_2} are the energies required to remove an O atom or O₂ molecule, respectively, from the structure; positive values indicate a stable structure, whereas negative values suggest the corresponding reduced configuration is more stable. Ionic charge Q (in elementary charge units, *e*) is reported as measured by the Wigner-Seitz method (Q_{WS}, broken down into *s*, *p*, *d* orbital populations) and Bader method (Q_B). Bond valence sums (BVS) are also provided.

With no coadsorbed O', the PDOS for W_A and W_B, **Figure 3.4(a)** and **(b)**, respectively, show some similarity in the form of extensive broad features extending to ~8 eV below E_F representative of covalent mixing with the oxygen valence band (as verified in the charge analysis, discussed below). W_A shows strong spin-polarization doublets just below and above E_F while such features are mostly absent from the W_B spectrum. Examination of **Figure 3.4(a)** shows a coherent spin superposition of W_A, Fe_B, Fe_C, and O_s, where the W response is dominated by superexchange coupling through its three ligands to neighboring Fe moments. In oxides this coupling normally results in antiferromagnetic coupling to the dominant Fe moments, but here this is apparently not the case. The unexpected behavior in the W_A surface is perhaps due to the unusually low coordination and rather large distance to neighboring Fe, in contrast to W_B (**Figure 3.4(b)**), which

sits below the surface O', with short W-Fe_{B/C} distances. The surface O_s and subsurface Fe_B and Fe_C PDOS are recognizable as those of hematite (**Figure 3.2(a)**) but are significantly distorted by the adsorbed cation. Coadsorption of O, as in O'_AW_A (**Figure 3.4(c)**), causes a compression of the W PDOS, effectively opening a gap ~3 eV around E_F due to its strong overlap/interaction with the rather localized O' band starting ~ 2 eV below E_F. This W_A gap is spectral evidence of oxidation relative to the initial metal-terminated state in vacuum.

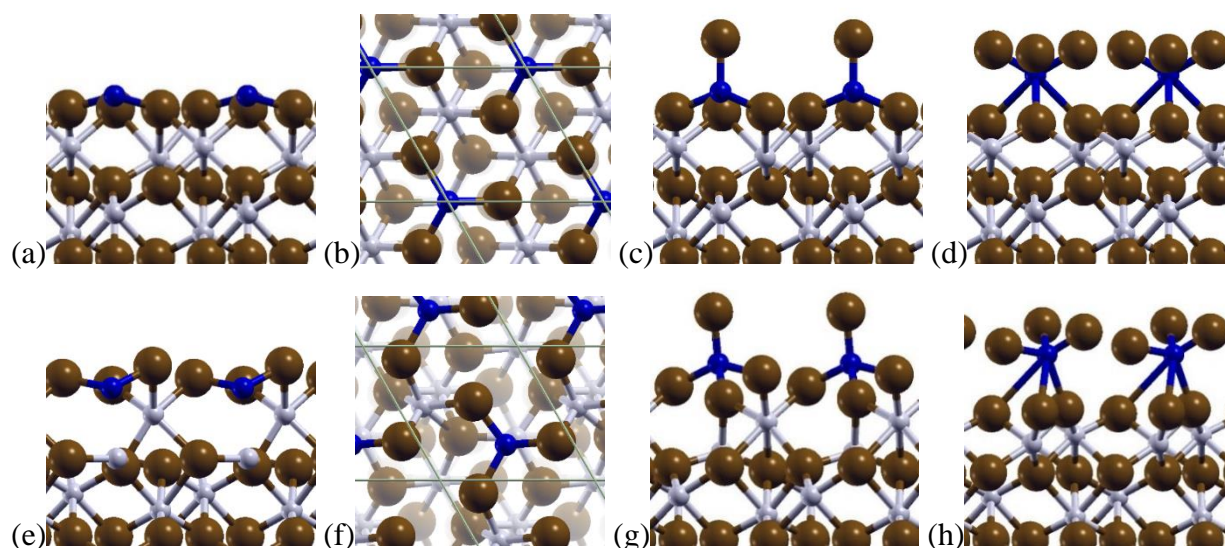


Figure 3.3: Three-, four-, and six-fold coordinated $\frac{1}{2}$ ML W O-terminated structures representing 0, $\frac{1}{3}$ and 1 ML coadsorbed oxygen. Top row shows (a) side view of W_A, (b) top view of W_A, (c) side view of $\frac{1}{3}$ ML O' on W_A, and (d) side view of 1 ML O' on W_A. Bottom row shows (e) side view of W_B, (f) top view of W_B, (g) side view of $\frac{1}{3}$ ML O' on W_B, and (h) side view of 1 ML O' on W_B. W atoms are shown in blue; Fe, gray; and O, brown, with lines showing the supercell boundaries in (b) and (f).

Due to increasing charge transfer from W to O, the volume-integrated cation charges would be expected to increase with rising W-O coordination number; however, no significant change is found in the W charge within a fixed-radius WS sphere, denoted as $Q_{WS}(W)$ in **Table 3.4**. This

might be attributed to over-counting of electrons, since the radius of integration R_S is fixed at 0.9 Å, compared to the empirical W^{6+} radius of 0.74 Å and the presumably larger radius for W^{5+} . Another traditional measure of transition metal valence state is the *d*-electron population: here, it is expected to change from 1 to 0 electron for the transition from W^{5+} to W^{6+} . The R_{WS} volume integration indicates a larger and less variable *d* occupancy (1.23 *e* in WO_3 vs. 1.43 *e* in WO_2), essentially due to the formation of strong covalent interactions with the ligands.

Bader charge analysis shows somewhat greater variation with environment. Bader charges on W, denoted as $Q_B(W)$, range from 3.02 *e* for WO_3 to 2.06 *e* for the W_A surface site. The W_B site and O'W coadsorbed states show intermediate $Q_B(W)$ values; in accordance with qualitative expectations, increased oxygen coordination leads to increased W net charge. We note that, in the various environments considered here, $Q_B(W)$ appears to be approximately one-half of the nominal oxidation state. However, the predicted oxidation state remains ambiguous for the $\frac{1}{3}$ ML and 1 ML O' structures; it is unclear whether the related cation formal charge would be 6+, as in bulk WO_3 , or a partially reduced 5+ surface state, as inferred from core-level XPS (discussed below). The value of $Q_B(W)$ does not change greatly as the W-O coordination number increases from 4 to 6 in these cases, calling into question the simple assumption that increased O coordination always yields a more oxidized cation.

Both the Wigner-Seitz and Bader methods of atomic charge assignment rely on the converged charge density. However, bond valence sums, as reported in **Table 3.4**, gives values closest to the expected formal oxidation state of both WO_3 and WO_2 . As expected, the BVS increases dramatically from the metal-terminated W_A and W_B cases to those with one adsorbed O, almost to

the expected value for W^{6+} . Considering the number of W-O coordinating bonds, these valences seem anomalously high, implying some reduction of the underlying Fe^{3+} cations in favor of oxidizing W.

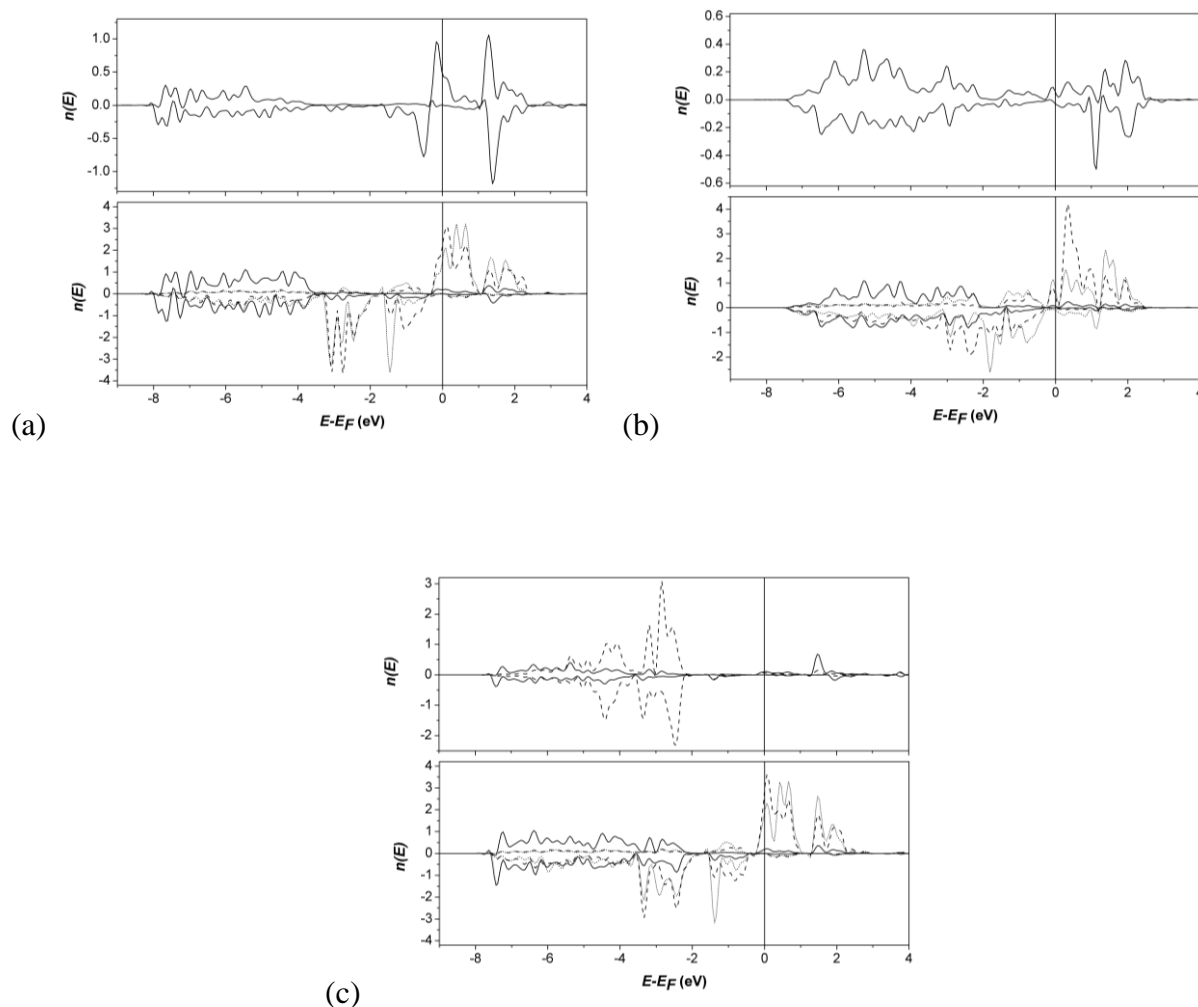


Figure 3.4: Atom-projected PDOS for structures (a) W_A , (b) W_B , and (c) $O'_A W_A$ on O-terminated hematite. Upper panel, solid W, dashed O'; lower panel, solid O_s, dashed Fe_C, dotted Fe_B.

If bulk-like hematite stacking were to continue up from the O-terminated surface, the next Fe^{3+} ion would occupy the Fe_A site, residing over the hollow in the cation layer below it. One might expect, therefore, that W_A would be energetically favored over W_B . However, the energetic preference for

surface W position depends on oxygen coverage: with either no adsorbed O' or a complete monolayer O'₃, B-site W_B is preferred by about 0.4 eV. For the case of a single adsorbed O', corresponding to 4-fold W-O coordination, the A-site is preferred by over 0.8 eV. The relative stability of these structures under different chemical environments can also be predicted by the energies of oxygen removal. In both singly oxygenated cases in **Table 3.4**, the energy for O removal is very high. However, for the O'₃W_A case, the removal of an oxygen molecule (resulting in the O_A'W_A structure) is exothermic by -0.66 eV, although the same reaction for the O'₃W_B case is endothermic. This is sensible by charge balance comparison: assuming the most oxidized states of the near-surface cations are Fe³⁺ and W⁶⁺, then there would not be sufficient charge to donate to three adsorbed O atoms per surface cell. W BVS for the structures with single O termination are close to those expected for W⁶⁺, so the relative chemical stability of these cases (especially the O_A'W_A structure) makes sense.

Bond lengths of the surface structures are presented in **Table 3.3(A)** in order to explore connections between structure, charge, and apparent oxidation state. Only the energetically favored structures for each stoichiometry are presented in this Table; a considerable number of additional structures were also analyzed. The W-O bond lengths are very similar between the 3-fold O_s-coordinated W_B-(I) and 4-fold O'W_A-(I) cases. The terminal O' in the 4-fold case has the shortest W-O bond length, indicating a stronger covalency, while the bond lengths between W and the surface O₃ layer increase by only 0.04-0.06 Å versus the 3-fold case. There is an insignificant difference in Bader charges (2.79 vs. 2.77 *e*) and a small drop in BVS (5.56 vs. 5.42 *e*) between 4-fold O'W_B and the nominally saturated O'₃W_B 6-fold case with a complete O' overlayer; similar values (2.73 vs. 2.75 *e*) are observed for W_A. This seemingly anomalous oxidation behavior,

indicating nearly identical chemical state of W in these four cases, may be explained by a closer look at the W-O bond length variations. For the relaxed $O_3W_B(I)$ case the underlying WO_3 tetrahedron (**Fig. 3.3(H)**) is heavily distorted, with only one W-O_s bond shorter than the longest W-O distance calculated for bulk WO_3 (2.13 Å). The W-O' distances, however, are comparable to the bond lengths observed for the 3- and 4-fold cases. W might then be considered to be 4-fold coordinated in this highly distorted case. **Table 3.2(A)** shows the distances between relaxed atomic layers at and near the surface. For the relaxed 3-fold $W_B(I)$ case, as seen in **Fig. 3.3(E,F)**, W sits *below* the surface O layer, screened from the vacuum. However, this puts strain on the underlying B-site cation, and so the distance between sub-surface Fe atoms is remarkably larger than that of the more oxidized cases.

A volume-rendered ground state electron density map for the surface region of the simplest $W_A(I)$ configuration is shown from two perspectives (a birds-eye view of multiple cells from within the interslab region toward the surface) in **Figure 3.5**. The displayed charge density levels were chosen to highlight the covalent character of metal-oxygen interactions as seen both in W_A-O_s bond regions and in Fe-O lobes. The adsorbed W is easily identified by its three-fold coordination to substrate oxygen atoms. With the exception of the W-O lobes, a notable feature, found by examining a variety of density maps for varying compositions and geometries, is the lack of clear differentiation between valence density around the W- as opposed to Fe-sites.

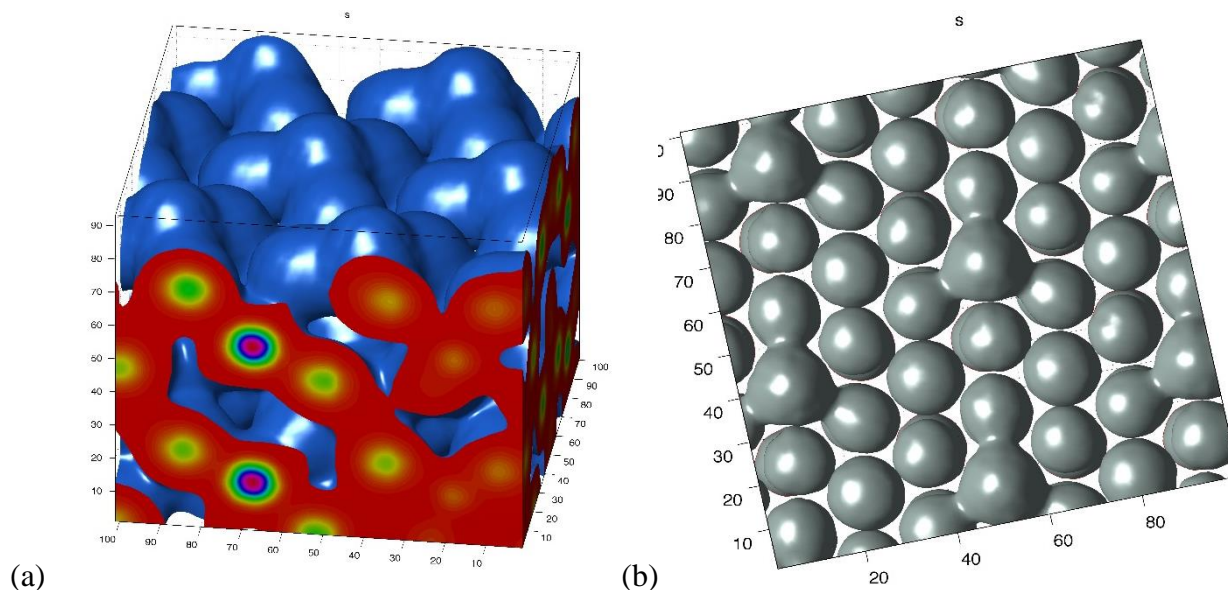


Figure 3.5: (a) Side view and (b) top view of a volume-rendered valence electron density map of $\frac{1}{2}$ ML W_A adsorbed on O-terminated hematite (0001) surface. Surface W_A can be identified by its three-fold covalent bonding lobes to O_s .

The predicted relative homogeneity of cation electron densities shows the considerable ability of valence electrons to screen the differently charged cations, suggesting that unoccupied states are perhaps most important for describing reactivity with incoming molecules and atoms. Such vacant states are not visible in conventional (i.e. ground-state) density maps such as **Figure 3.5**. However, differences in ground-state densities between different states, or orbitally-resolved charge densities, can be of considerable value, as discussed in **Chapter 4** and **Chapter 5**.

3.2.2.2 $\frac{1}{2}$ ML W / O-terminated α - Fe_2O_3 : Hydroxyl termination

For many catalytic reactions, hydrogen will be present in some form (*e.g.* H_2 , H_2O , NH_3 , or hydrocarbons). Furthermore, in the experimental redox studies on the present system, H_2 was used as the reducing agent. It is therefore important to investigate the effects of adsorbed hydrogen on the surface structure and chemistry. Hydrogen atoms were placed above the terminal oxygen atoms

to simulate hydroxyl groups, and the structures were relaxed. Structural and chemical results for $\frac{1}{3}$ and 1 ML hydroxylated W on the O-terminated hematite (0001) surface are given in **Tables 3.2(D), 3.3(D), and 3.5**. There is a 0.18 eV preference for $\text{HO}'_A\text{W}_A$ (pictured in **Fig. 3.6(a,d)**) vs. $\text{HO}'_B\text{W}_B$. While this site ordering agrees qualitatively with that found for the $\text{O}'_A\text{W}_A$ vs. $\text{O}'_B\text{W}_B$ case (0.84 eV), the energy preference is significantly weaker. Under vacuum conditions, the $\text{HO}'_B\text{W}_B$ structure would be stable, as the removal of H is endothermic; however, the dehydrogenation of the $\text{HO}'_A\text{W}_A$ structure is exothermic by -0.33 eV. Under flowing H_2 , as in the experimental conditions reported in [66], this structure might be stable. A complete *ab initio* thermodynamic treatment might assess the stability of this surface under different partial pressures of hydrogen, but such a study is beyond the scope of this work.

The key structural difference between the singly O- and OH-terminated structures is in the $\text{W}_A\text{-O}'$ bond length, which extends by 0.19 Å for the hydroxyl ligand, while the $\text{W}_A\text{-O}_s$ bonds contract by about 0.05 Å. These bond length dilations and contractions appear to chemically compensate for each other; the W_A Bader charge is hardly affected, while the BVS decreases from 5.51 to 5.22. This decrease is smaller than might be expected for a removal of one O acceptor state, but the reduction of W appears to be “cushioned” by the reducible substrate. Indeed, PDOS for the model $\text{HO}'_A\text{W}_A$, given in **Figure 3.7**, show a slight upward shift of E_F and an attenuation of the Fe_C acceptor states as compared to those of model $\text{O}'_A\text{W}_A$ in **Figure 3.4(c)**. The O' valence band is somewhat broadened and shifted to lower energy by interaction with H, shifting the W covalent components downward in turn. While the top of the W valence ends at ~4 eV below E_F , a small amount of W conduction band character now appears near E_F .

System	HO' _A W _A	HO' _B W _B	(HO') ₃ W _A	(HO') ₃ W _B
Relative energy (eV)	0	0.18	0.10	0
$\Delta E_{-\frac{n}{2}H_2}$	-0.33 $n = 1$	0.33 $n = 1$	5.53 $n = 3$	5.25 $n = 3$
Q _{ws} (W)	5.38	5.41	5.55	5.49
s	0.04	0.04	0.03	0.04
p	5.17	5.18	5.22	5.20
d	1.42	1.38	1.19	1.27
Q _B (W)	2.77	2.71	2.96	2.93
BVS(W)	5.22	5.28	5.13	5.42

Table 3.5: Chemical details for hydroxylated $\frac{1}{2}$ ML W on O-terminated hematite (0001). Values as defined before, with $\Delta E_{-\frac{n}{2}H_2}$ representing the energy to remove n hydrogen atoms per surface cell.

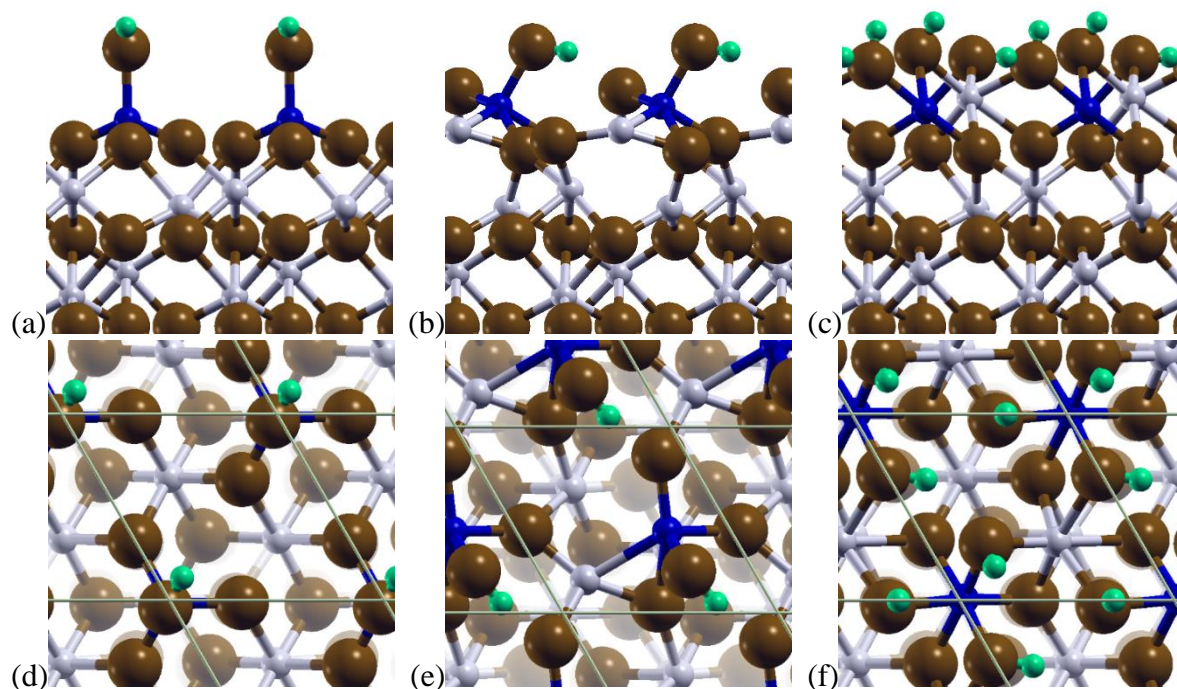


Figure 3.6: Four- and six-fold coordinated $\frac{1}{2}$ ML W hydroxylated surfaces. Top row shows side views of (a) $\frac{1}{3}$ ML HO' on W_A, (b) $\frac{1}{3}$ ML HO' on W_BFe_A, and (c) 1 ML HO' on W_AFe_B. Bottom row shows top views of (d) $\frac{1}{3}$ ML HO' on W_A, (e) $\frac{1}{3}$ ML HO' on W_BFe_A, and (f) 1 ML HO' on W_AFe_B. Colors as before, with H atoms shown in green.

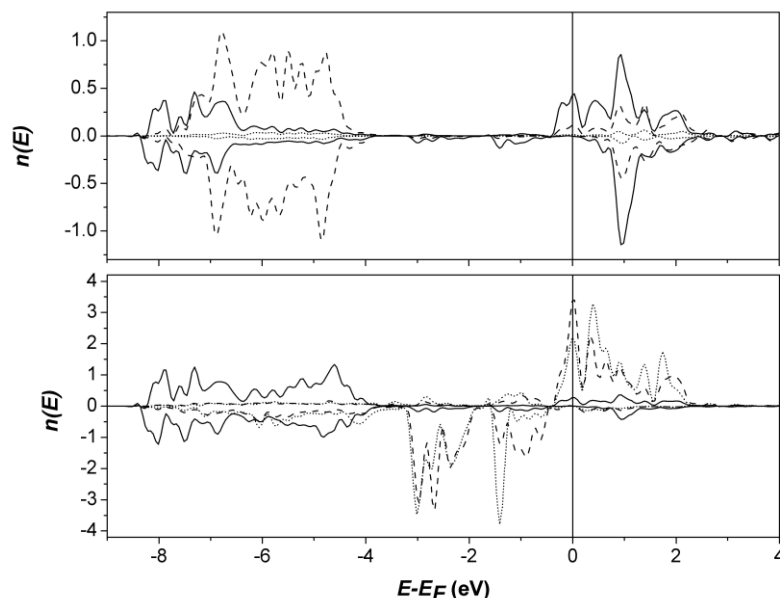


Figure 3.7: PDOS of surface and near-surface atoms of $\text{HO}'_A \text{W}_A$ ($\frac{1}{3}$ ML OH) on O-terminated hematite (0001). Upper panel, solid W_A , dashed O'_A , dotted H; lower panel, solid O_s , dashed Fe_C , dotted Fe_B .

After the surface has been in contact with a humid environment, higher hydroxyl coverages may be expected. As indicated in **Table 3.5**, the two triply hydroxylated cases are much more stable than their triply oxygen-terminated counterparts in vacuum; the energy cost to remove all the H from these surfaces is well over 5 eV per surface cell. As in the case of $\text{O}'_3 \text{W}$, there is little effect of the cation surface site on its chemical state. Bader charges for the triply hydroxylated W are $\sim 0.2 e$ more positive than the O terminations, although the BVS is lower for the W_A configuration and unchanged for the W_B structure. Wigner-Seitz and Bader charges show the six-fold coordinated $(\text{HO}')_3 \text{W}$ cations to be more positive, by $\sim 0.1 e$, compared to the four-fold hydroxylated complexes. However, the effect on the BVS of increased hydroxylation is mixed, with W_A undergoing a *decrease* in valence with the addition of hydroxyl groups, whereas the valence of W_B increases. This discrepancy can be attributed to strongly ionic interactions with hydroxyl groups (see **Chapter 5** for a more detailed analysis of this phenomenon), reducing the

W $5d$ covalency. These electronic structure changes accompany significant shifts in position relative to the underlying lattice and in W-O bond lengths; for example, $R(\text{W-O}')$ changes from 1.91 Å (4-fold $\text{HO}'\text{W}_\text{A}$) to 1.77-2.11 Å (6-fold $(\text{HO}')_3\text{W}_\text{B}$), and $R(\text{W-O}_\text{s})$ lengthens, on average, from 1.79-1.80 Å to 1.77-2.11 Å. With saturated 1 ML HO' ligation, W_B is favored over W_A (by 0.1 eV), although less strongly than in the $\text{O}'_3\text{W}$ case (0.18 eV). The W_B cation coordination for 1 ML OH ligation is closer to that of bulk WO_3 than its $\text{O}'_3\text{W}_\text{B}$ surface counterpart, as expected due to the saturation of the O valence.

3.2.2.3 $\frac{1}{2}$ ML W / O-terminated $\alpha\text{-Fe}_2\text{O}_3$: Effects of surface oxygen vacancies

Surface cations in metal oxides have been shown to be highly catalytically active in the presence of surface O defects[150, 151]. Thus, the consequences of an O-defective surface were studied for different cation configurations. Structures were calculated with 1, 2, or all 3 surface anions removed per surface cell, denoted as O_V , $\text{O}_\text{V}2$, and $\text{O}_\text{V}3$. Due to the 3-fold symmetry of the O plane in hematite, there was generally a small energetic and structural difference between the three different possible O-defective configurations; the lowest-energy structures (usually varying by only ~1 meV) for each different surface cation arrangement and stoichiometry are reported herein. Structural details of energetically preferred cases with depleted surface O layers of each stoichiometry are presented in **Tables 3.2(C)** and **3.3(C)**. Converged energies and calculated surface cation charges are shown in **Table 3.6**.

System	W _A O _V	W _B O _V	W _A O _{V2}	W _B O _{V2}	W _A O _{V3}	W _B O _{V3}
Relative energy (eV)	0	1.62	0	1.56	0.91	0
$\Delta E_{-\frac{1}{2}O_2}$ (eV)	1.97	3.80	4.06	4.00	7.38	4.92
Q _{ws} (W)	5.42	5.33	5.40	5.31	5.37	5.27
s	0.03	0.04	0.03	0.04	0.03	0.04
p	5.17	5.12	5.16	5.08	5.14	5.05
d	1.38	1.51	1.41	1.57	1.47	1.64
Q _B (W)	2.16	1.63	1.79	0.86	1.17	0.17
BVS(W)	3.55	2.82	2.91	1.39	1.89	0

Table 3.6: Chemical details for $\frac{1}{2}$ ML W on O-terminated hematite (0001) with one, two, or three surface O vacancies (O_V). Values as defined before, with $\Delta E_{-\frac{1}{2}O_2}$ representing the O vacancy formation energy per surface cell.

We find that the W_B site which is most favored on the O₃-terminated substrate is replaced by O_VW_A as the lowest energy O_V surface with a large advantage of 1.62 eV over O_VW_B. Structurally, this suggests that during a reduction reaction, W_B sitting 0.37 Å below the O₃ layer might be displaced to the A-site, ~0.9 Å above the oxygen plane. The bond lengths W-O_s, initially 1.79-1.80 Å for the most stable O₃-terminated hematite surface, increase to 1.85-2.17 Å. Other near-surface bonds involving Fe-O and W-Fe are affected, but less strongly; e.g., W-Fe, initially 2.32-3.06 Å, increases to 2.54-3.12 Å. These metal-metal distances are sufficiently short to permit significant bonding interaction. Concerning charge distribution, the W Bader charge decreases as 2.23 > 2.16 > 1.63 *e* for W_B, W_AO_V, W_BO_V respectively with decreasing coordination and increasing bond lengths; the same trend is observed in the BVS. As an extreme example of distortion, the more highly reduced W_BFe_AO_{V2} configuration shows a W dislocation of ~1.8 Å away from registry. As W-O_s coordination decreases, the corresponding reduction of W is apparent in the lengthening of bond lengths R(W-O_s): 1.79-1.80 (W_B(I)) < 1.85-1.91 (W_AO_V) < 1.93 Å (W_AO_{V2}). Systematic reductions in W Bader charges are also observed, with the [Q(W_A), Q(W_B)] charges being [2.16,

1.63] > [1.79, 0.86] > [1.17, 0.17] e for O₃, O_V, and O_{V2} cases, respectively. BVS follow the same pattern, but the method is no longer reliable as the number of W-O bonds becomes very small as direct W-Fe coordination increases. For the W_BO_{V3} case, W_B has no near oxygen coordination; this is in contrast to W_A, which is coordinated with at least one O atom, even in the mixed metal terminated W_AFe_BO_{V3} case (see **Section 3.2.2.7** below). This is reflected in the anomalously large z-spacing between W_B and the underlying Fe_C atom, which in all other cases is < 0.22 Å but here is greater than 1.1 Å. The vacancy formation energy of the first O per unit cell is comparable with results reported for the clean hematite (0001) surface[152], and the removal of further O is increasingly endothermic.

In summary, for the less-reduced O_S-terminated cases, W_A is preferred by about 1.6 eV; however, when the substrate O₃ layer is completely removed, the preference shifts to W_B. W_A is also generally more oxidized; indeed, the Bader charge (0.17 e) and lack of any direct W-O coordination on the fully O-depleted W_BO_{V3} case indicates that W is metallic, compared to W_AO_{V3} (1.17 e). In the W_BO_{V3} case, W_B sits well above the Fe layer instead of being part of a mixed metal surface layer, as in every other case. The surface O_S atoms are clearly a controlling factor in transverse positioning of W, as the more oxygen deficient surfaces show greater displacements away from bulk cation registry. In all cases, extreme reducing environments would be necessary to produce these structures. As removal of an O atom from these surfaces is increasingly endothermic with the number of vacancies, none of these structures are expected to be stable in the presence of oxygen.

3.2.2.4 1 ML W / O-terminated α -Fe₂O₃

Relaxed structures for a full W monolayer (W_AW_B) are provided in **Figure 3.8**, with structural information in **Tables 3.2(B)** and **3.3(B)**. For the case with no coadsorbed O', W_A relaxes to a position further above the O_s plane than W_B in the z -direction. This leaves a large sub-surface hollow space as the underlying Fe_B atom is repelled downward by W_B . The W- O_s bond lengths are relatively long, at 1.91 – 1.98 Å. The $\frac{2}{3}$ ML O' overlayer model $O'_{AB}W_AW_B$, initialized with 4-fold W-O coordination for both cations, shows the expected cation z -position ordering (W_A below W_B) after relaxation. While W_B appears to be 4-fold coordinated with O, a weak fifth W-O interaction is observed at a distance of 2.69 Å. If this bond is considered, then the BVS (given in **Table 3.7**) suggest a slight oxidation of W_B over W_A , although both values are close to that expected for W^{4+} (3.39 e). The 1 ML O' overlayer model $O'_3W_AW_B$ shows relatively high symmetry, exhibiting little difference in distribution of W-O distances around the 6-fold coordinated W atoms. Some distortion of the terminal O layer is observed.

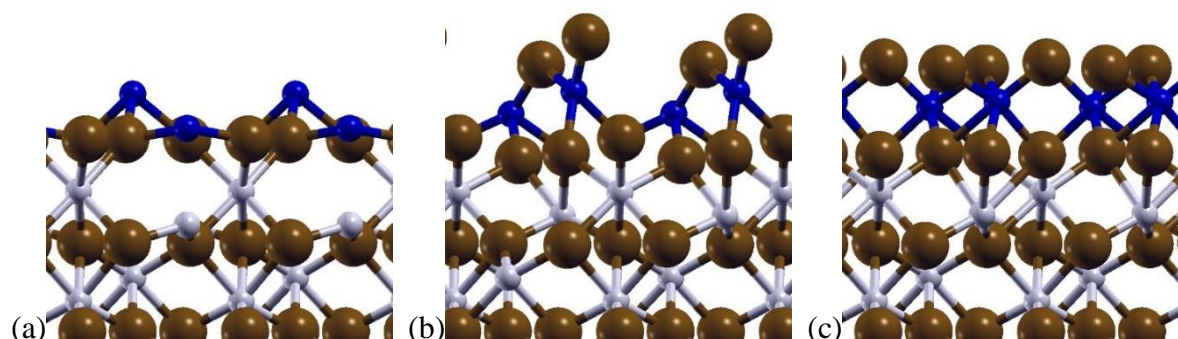


Figure 3.8: Side views of three-, four-, and six-fold coordinated 1 ML W representing $\frac{1}{3}$, $\frac{2}{3}$, and 1 ML coadsorbed oxygen. (a) W_{AB} , (b) $\frac{2}{3}$ ML O' on W_{AB} , and (c) 1 ML O' on W_{AB} .

System	$W_A W_B$	$O'_{AB} W_A W_B$	$O'_3 W_A W_B$
ΔE_{-O_2} (eV)	--	9.81	--
$\Delta E_{\frac{1}{2}O_2}$ (eV)	--	--	4.50
$Q_{WS}(W_A)$	5.29	5.40	5.42
s	0.03	0.03	0.03
p	5.11	5.16	5.18
d	1.57	1.41	1.36
$Q_B(W_A)$	1.23	2.08	2.51
BVS(W_A)	2.18	3.48	4.33
$Q_{WS}(W_B)$	5.35	5.37	5.42
s	0.03	0.03	0.03
p	5.14	5.15	5.19
d	1.48	1.46	1.37
$Q_B(W_B)$	1.44	1.93	2.53
BVS(W_B)	2.82	3.57	4.52

Table 3.7: Chemical details for 1 ML W on O-terminated hematite (0001). Values as defined before.

For the 3-fold O-coordination state with no coadsorbed O', the charges $Q_{WS}(W_{A,B})$ (5.29, 5.35 e) and $Q_B(W_{A,B})$ (1.23, 1.44 e) observed for the W cations (see Table 4D), are among the lowest predicted for non-defective surfaces. The predicted Bader charges for a metal-terminated W monolayer surface are lower than for a mixed W-Fe metal termination, indicating an increased competition for charge from the surface O layer. The low ionicities for the W monolayer case correspond to the long W-O_s bond lengths reported above. The $\frac{2}{3}$ ML O' case shows an additional increase in ionicity of 0.49 – 0.85 e from the metal-terminated case (as measured by the Bader method), with W_A becoming more oxidized than W_B . The corresponding $Q_{WS}(W)$ charges increase by 0.02 – 0.11 e , again showing W_A as more oxidized, correlating to the shorter average $R(W_A-O)$ (vs. W_B-O). With O'₃ co-adsorption, the W charges increase further: $Q_B(W_{A,B})$ are 2.51, 2.53 e and $Q_{WS}(W_{A,B})$ are 5.42, 5.42 e for W_A and W_B , respectively. Thus, in moving from 3- to 6-fold W-O coordination, the W Bader charges indicate a net charge transfer of 1.48 e in the oxidation process

while the fixed-radius Q_{WS} only detects a change of $0.13 e$. In the O_3 case, both 6-fold coordinated W atoms are in nearly geometrically identical configurations, exhibiting little difference in ionicity and the distribution of W-O distances. In the 6-fold coordinated state, both Bader charges and BVS suggest that W is not fully oxidized to W^{6+} ; indeed, three more electron acceptor states per unit cell would be needed to do so. As the W cations compete for limited acceptor states, the energy required to remove oxygen from these surfaces is very large.

PDOS for the reduced W_AW_B surface are given in **Figure 3.9**. The usual covalent mixing with oxygen in the valence band is observed, but a strong metallic conduction band structure spanning E_F , about 4 eV in width, is also present. Antiferromagnetic superexchange coupling between W (especially W_A) and the near-surface Fe is observed, with W_A and both Fe atoms having largely opposing spin character that switches above E_F . Along with the metallic W states, Fe and O substrate states are also pulled into the region around E_F , leading to the characterization of this state as highly metallic, at least in the surface region. This is explained by the additional valence electrons provided by the two W atoms; even the O band has some states available at E_F .

3.2.2.5 $\frac{1}{2}$ ML W / Fe-terminated α - Fe_2O_3

The complex interaction between different metal atoms in redox reactions can be exploited to generate high activity and selectivity towards specific products in mixed catalysts with neighboring species of different metals or oxides[29, 30]. The Fe-terminated hematite surface is therefore particularly interesting for bimetallic catalytic surface studies. Both W_AFe_B and W_BFe_A configurations were investigated, corresponding to $\frac{1}{2}$ ML of each cation (the so-called mixed-ML surface). Surface annealing leading to cation migration under reaction conditions could allow for

reconstructions with both configurations; recall that for $\frac{1}{2}$ ML W coverage, W_A and W_B are separately favored under different conditions. To begin, O' overlayer coverages of 0, $\frac{1}{3}$, $\frac{2}{3}$, and 1 ML were modeled in order to explore different levels of metal oxidation. Geometric details of selected stable mixed-ML surfaces are provided in **Tables 3.2(A)** and **3.3(A)**. Three comparable $\frac{1}{3}$ ML O' structures are presented here, but only the most stable isostoichiometric structures are given for the 0, $\frac{2}{3}$, and 1 ML O' cases (as enumerated in **Table 3.8** and **Table 3.9**, along with other chemical details).

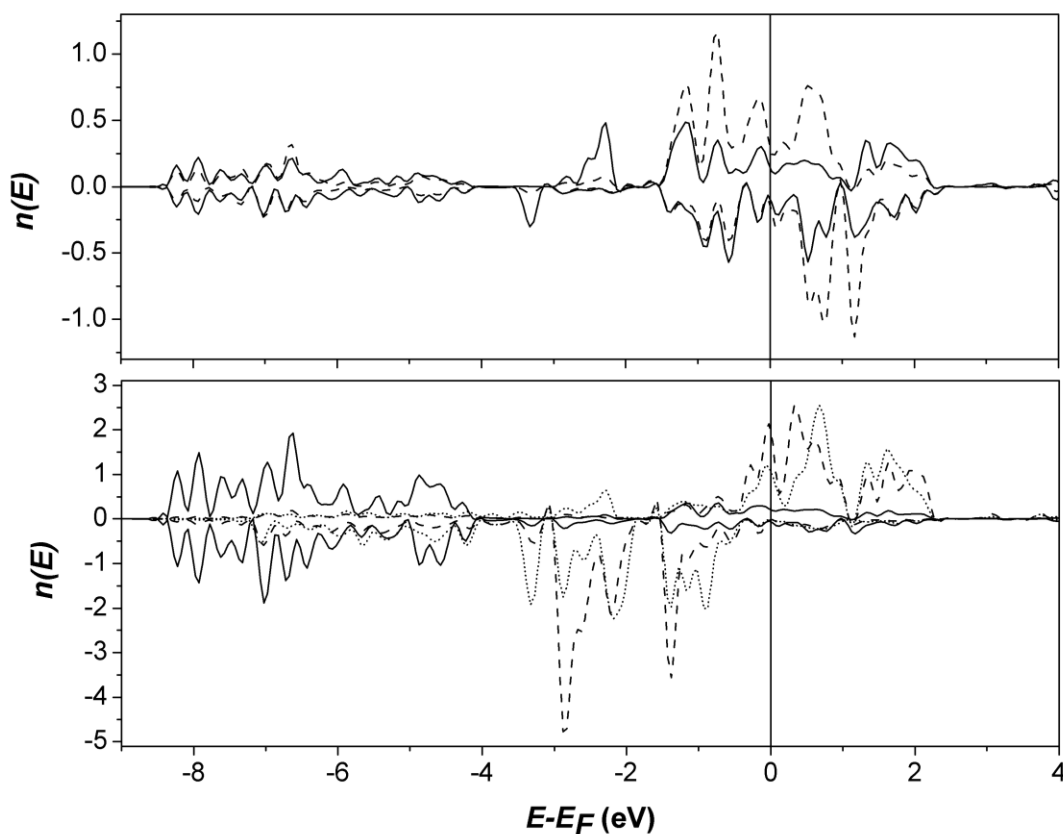


Figure 3.9: PDOS for surface and near-surface atoms of 1 ML $W_A W_B$ on O-terminated hematite. Upper panel, solid W_B , dashed W_A ; lower panel, solid O_s , dashed Fe_C , dotted Fe_B .

For the metal-terminated cases with no coadsorbed oxygen, the addition of surface Fe_B appears to stabilize W_A in the W_AFe_B -**(I)** case. However, this stabilization is at the expense of the surface O_3 layer symmetry: one O atom moves above both the surface Fe and W species, leaving a vacancy O_V in the surface layer (**Figure 3.10(a)**). As the terminal O coverage increases, the B-site W becomes more stable; for the cases with $\frac{1}{3}$ or $\frac{2}{3}$ ML coverage, the two cation configurations are nearly equally stable. The 1 ML $\text{O}'_3\text{W}_B\text{Fe}_A$ structure is clearly more stable over the $\text{O}'_3\text{W}_A\text{Fe}_B$ structure and shows relatively high symmetry, with nearly flat O planes and consistent interatomic distances (**Figure 3.10(j)**).

Coverage-dependent behavior is also observed for the relaxed surface cation positions. In bulk hematite, an Fe_A cation sits 0.63 \AA below an Fe_B . However, the surface cation order in this mixed-ML case depends on the O' adsorption site in the $\frac{1}{3}$ ML O' overlayer cases. In these examples, if the starting configuration before relaxation has O' placed above the A- or B-site cation, then that cation rises to a higher z -position after relaxation. For the stable cases with higher O' coverage, however, the regular cation configuration is restored, with Fe_AW_B preferred. For the $\frac{2}{3}$ ML O' cases, both W and Fe are vertically coordinated with one O' atom before relaxation. In both the W_AFe_B and W_BFe_A cases (**Figure 3.10(g)** and **(h)**, respectively), the structure relaxes to a 5-fold W-O coordination and distorted Fe-O tetrahedra.

Surface	Fe ₂ O ₃	W _A Fe _B	W _B Fe _A	O' _B W _A Fe _B	O' _A W _A Fe _B	O' _{br} W _A Fe _B	O' _A W _B Fe _A	O' _B W _B Fe _A	O' _{br} W _B Fe _A
Relative energy (eV)	--	0	0.81	0.35	0	0.62	0.06	0.02	0.15
$\Delta E_{-\frac{1}{2}O_2}$	--	--	--	2.91	3.26	2.64	4.01	4.05	3.92
Q _{ws} (W)	--	5.37	5.32	5.41	5.38	5.40	5.39	5.39	5.39
s		0.04	0.04	0.04	0.03	0.03	0.03,	0.03,	0.03
p		5.15	5.14	5.17	5.17	5.17	5.17	5.17	5.17
d		1.44	1.50	1.38	1.42	1.41	1.40	1.41	1.41
Q _B (W)	--	1.81	2.02	2.50	2.41	2.31	2.34	2.40	2.34
BVS(W)	--	3.40	3.54	4.61	4.60	4.28	4.30	4.55	4.23
Q _{ws} (Fe)	3.13	2.93	2.83	2.88	2.80	2.95	2.94	2.93	2.87
s	0.06	0.07	0.07	0.08	0.08	0.06	0.06,	0.08	0.06
p	5.85	5.83	5.83	5.82	5.85	5.82	5.83	5.85	5.83
d	4.96	5.17	5.27	5.22	5.27	5.17	5.17	5.15	5.24
Q _B (Fe)	1.64	0.83	1.07	0.83	0.81	1.03	1.26	0.98	1.14
BVS(Fe)	2.91	1.70	2.19	1.68	2.19	1.85	2.24	2.27	2.16

Table 3.8: Chemical details for $\frac{1}{2}$ ML W with 0 or 1 adsorbed O atoms per Fe-terminated hematite (0001) cell, including Wigner-Seitz and Bader charges and BVS for the surface Fe species. Values as defined before, with subscript *br* denoting O species initialized at a bridging position between W and Fe.

As in the case of 0.5 ML W on the O-terminated hematite surface (**Section 3.2.2.1**), there is very little variation in the spherically-integrated W net charge $Q_{ws}(W)$ with surface configuration and W-O coordination; *i.e.*, $5.37 (W_A Fe_B) < 5.41 (O'_A W_A Fe_B)$, $(O'_{AB} W_B Fe_A) < 5.45 e (O'_3 W_B Fe_A)$. While the trend of increasing net charge with oxygen ligation is as expected, the magnitude of changes is small. The surface Fe orbital occupancies vary significantly more than those of W; nevertheless the net charge differences remain small. The corresponding Fe WS charge is $2.93 > 2.88 < 3.04 < 3.13 e$, in the same site order as above, indicating a slight oxidizing tendency with increasing O' coordination about either metal.

System	O' _{AB} W _A Fe _B	O' _{AB} W _B Fe _A	O' ₃ W _A Fe _B	O' ₃ W _B Fe _A
Relative energy (eV)	0.05	0	0.35	0
ΔE_{-O_2} (eV)	7.24	6.38	-	-
$\Delta E_{-\frac{1}{2}O_2}$ (eV)	-	-	2.65	2.95
Q _{ws} (W)	5.41	5.41	5.47	5.45
s	0.04	0.04	0.04	0.04
p	5.18	5.18	5.20	5.19
d	1.38	1.37	1.30	1.33
Q _B (W)	2.61	2.64	2.88	2.86
BVS(W)	4.87	5.05	5.25	5.44
Q _{ws} (Fe)	3.03	3.04	3.12	3.13
s	0.07	0.07	0.07	0.06
p	5.86	5.85	5.86	5.86
d	5.05	5.05	4.95	4.95
Q _B (Fe)	1.31	1.32	1.67	1.69
BVS(Fe)	2.63	2.50	3.27	3.04

Table 3.9: Chemical details for $\frac{1}{2}$ ML W with 2 or 3 adsorbed O atoms per Fe-terminated hematite (0001) cell, including Wigner-Seitz and Bader charges and BVS for the surface Fe species. Values as defined before.

Bader charges and BVS again prove to be more sensitive to changes in the cation chemistry due to differences in the local structure. Taking again the 3-, 4-, 5-, and 6-fold W-O coordination subset of W_AFe_B, O'_AW_AFe_B, O'_{AB}W_AFe_B, and O'₃W_BFe_A, the W net Bader charges Q_B(W) are 1.81 < 2.41 < 2.62 < 2.86 *e*, respectively. The corresponding Fe net charges are 0.83 > 0.81 < 1.31 < 1.69 *e*, respectively. The BVS follow the same trends. Interestingly, for $\frac{1}{3}$ ML O' coverage over W_AFe_B, both O'_A and O'_B terminations give nearly identical Fe_B charges (0.81 vs. 0.83 *e*), indicating dominance of the A-site in the local charge transfer process. Lateral dislocations of W and Fe from the nominal A and B cation sites are observed, reaching a maximum of 1.1 Å with no adsorbed O' and diminishing to nearly perfect lateral registry with the expected A and B sites with O'₃ coverage.

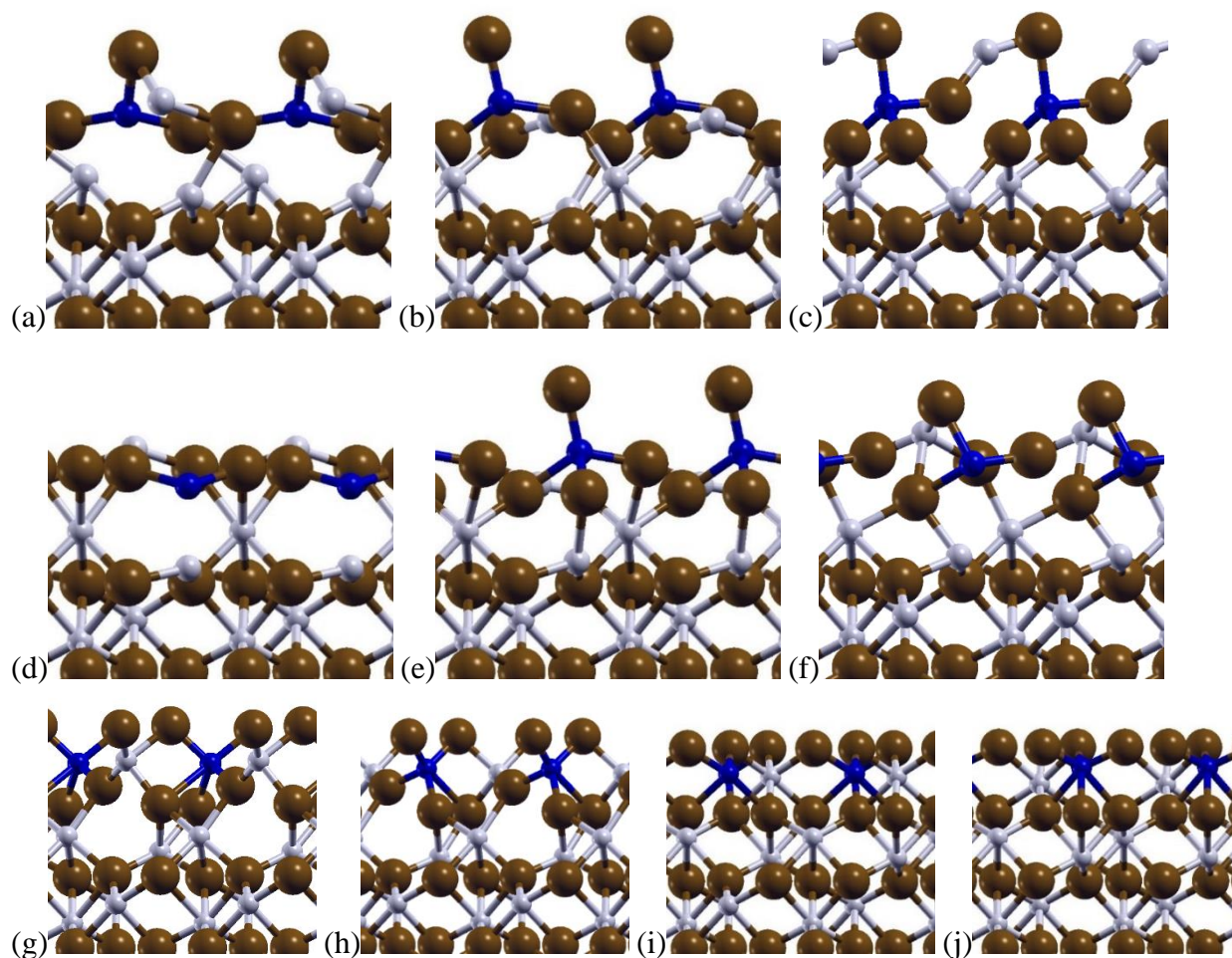


Figure 3.10: Side views of $\frac{1}{2}$ ML W representing 0, $\frac{1}{3}$, $\frac{2}{3}$, and 1 ML coadsorbed oxygen with additional surface Fe. (a) W_AFe_B ; (b) $O'_AW_AFe_B$; (c) $O'_BW_AFe_B$; (d) W_BFe_A ; (e) $O'_BW_BFe_A$; (f) $O'_AW_BFe_A$; (g) $O'_{AB}W_AFe_B$; (h) $O'_{AB}W_BFe_A$; (i) $O'_3W_AFe_B$; (j) $O'_3W_BFe_A$.

Site-specific trends appear for both Fe and W, depending on the coverage. At 0 or $\frac{1}{3}$ ML O' coverage, surface Fe_B atoms tend to have a lower Bader charge and valence than their isostoichiometric Fe_A counterparts. The charge on W changes little with cation position, or even by the initial position of the terminal O atoms; it simply rises with increasing O coverage. For the $\frac{2}{3}$ and 1 ML O cases, however, the calculated valence is significantly higher for B-site cations than their A-site counterparts.

By Bader analysis, W atoms on the mixed-ML cases of no or $\frac{1}{3}$ ML O' coverage are seen to be less oxidized compared with their W-only counterparts on O-terminated hematite (see **Section 3.2.2.1** above), likely due to competition between the surface Fe and W species for covalency with available O. When O is plentiful, as in the case of 1 ML O' coverage, the W cations on the mixed-ML surface are noticeably more oxidized than with no Fe present. However, little change in BVS is observed between the 1 ML O' cases on O- vs. Fe-terminated hematite. We recall that for 1 ML O' on $\frac{1}{2}$ ML W on O-terminated hematite, there were too many O' acceptor states available for the available W valence electrons; this might have led to more covalent interactions and therefore a lesser degree of W ionicity. On the W-Fe mixed-metal case, three O^{2-} ions would perfectly balance the surface W^{6+} (assuming a stoichiometric Fe^{3+} -terminated Fe_2O_3 surface).

The partial densities of states for $O'_{AB}W_BFe_A$ and $O'_3W_BFe_A$, shown in **Figure 3.11**, illustrate differences between bimetallic coverage and single W-terminations. In contrast with the O'_AW_A structure of **Figure 3.4(c)**, showing rather localized O' and W PDOS, the adsorbed O' $\frac{2}{3}$ ML PDOS (**Figure 3.11(a)**) is broadened into a band covering essentially the entire valence band region due to its delocalization over both metal centers and interaction with the underlying O_3 substrate. The terminal Fe_A shows a well-defined spin-up band starting ~ 1 eV below E_F with a strong spin-down structure just above E_F , characteristic of strongly polarized bulk Fe. The W_B structure is spread over the entire valence band, characteristic of its covalency with oxygen ligands, with defined excited state structures ranging over 1.5-2.5 eV above E_F . The 1 ML O'_3 spectra (**Figure 3.11(b)**) show further delocalization, with displacements of both substrate and surface Fe features leading to the opening of a distinct band gap around E_F characteristic of the highly oxidized surface. The Fe magnetic structure shows some interesting features, with considerable localization indicated by

narrow spin-down bands above E_F . Thus, the occupied Fe spin-up states are strongly interacting with the substrate and broadened, while non-occupied spin-down states are presumably dominant in interactions with incoming atoms and molecules.

Mixed-ML surfaces with varying degrees of hydroxyl coverage ($\frac{1}{3}$, $\frac{2}{3}$, 1 ML) were studied, and structural results are given in **Tables 3.2(D)** and **3.3(D)**. The vertical position shifts of the atomic layers for the most stable structure for each stoichiometry is significantly altered by protonation, compared to O' coverage. The interlayer spacing $R_L(W-O')$ increases by 0.1 – 0.7 Å, with the smallest change represented by $O'_B W_B Fe_A \rightarrow (HO'_B) W_B Fe_A$ and the largest by $O'_3 W_B Fe_A \rightarrow (HO')_3 W_A Fe_B$. For energetically favored states $O'_A W_A Fe_B$ vs. $(HO'_B) W_B Fe_A$, pictured in **Figure 3.6(b,e)**, the surface interlayer spacings shift by about 0.2 Å, while the bond lengths shift by 0.1 - 0.2 Å, with effects extending all the way down to the subsurface Fe layers. The key difference is found in $R(W-O')$, which extends by 0.16 Å for the hydroxylated version, while the $W-O_s$ tetrahedron becomes more asymmetric. These relatively small bond length dilations and contractions reinforce the charge analysis conclusion (see below) that small changes in electronic structure are involved in site-switching. For mono-hydroxyl coverage the $(HO'_B) W_B Fe_A$ case is most favored; however, there is only a 0.15 eV difference between HO' binding on W_B or Fe_A . For $\frac{2}{3}$ and 1 ML HO' co-adsorption, $(HO')_2 W_A Fe_B$ and $(HO')_3 W_A Fe_B$ (shown in **Figure 3.6(c,f)**) configurations are favored by 0.09 and 0.34 eV, respectively. Differing degrees of hydroxylation due to reaction with hydrogen or water can therefore modify the stable W cation site occupancy.

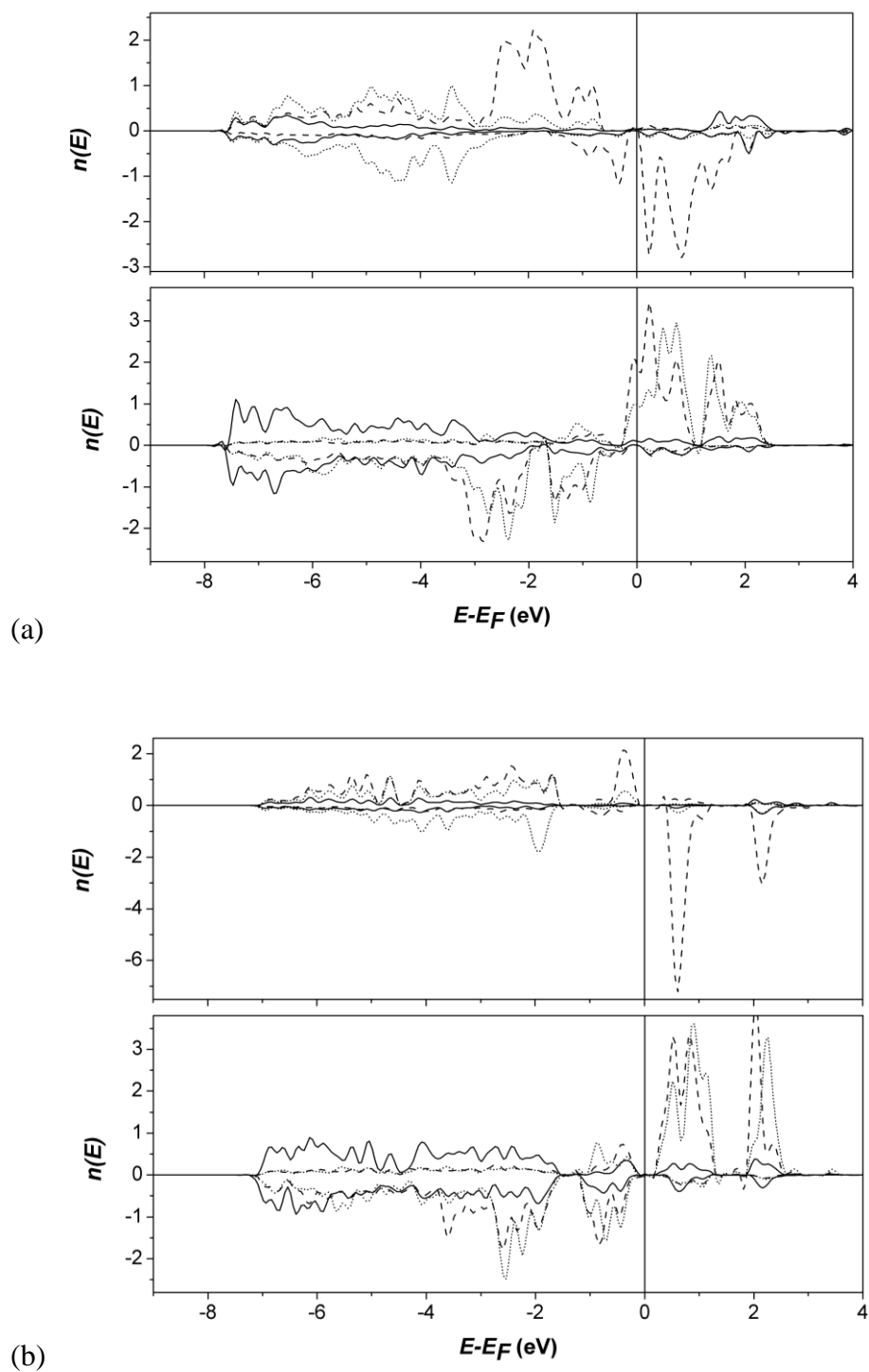


Figure 3.11: PDOS for surface and near-surface atoms of the (a) $O'_2W_BFe_A$ and (b) $O'_3W_BFe_A$ structures on Fe-terminated (0001) hematite. Upper panels, solid W_B , dashed Fe_A , dotted O' ; lower panels, solid O_s , dashed Fe_C , dotted Fe_B .

3.2.2.6 $\frac{1}{2}$ ML W / Fe-terminated α -Fe₂O₃: Hydroxyl termination

Charge distribution details of energetically favored hydroxylated 1 ML W-Fe structures are presented in **Table 3.10**. These can be compared directly to their O' coadsorbed counterparts in **Table 3.8** and **Table 3.9** to understand the effect of hydroxylation versus oxidation. For example, comparing the most stable O'_AW_AFe_B configuration with various (HO')W-Fe possibilities, one finds that the site preference is shifted from (HO'_A)W_AFe_B to (HO'_B)W_BFe_A with an energy advantage of 0.20 eV. Thus surface hydroxylation may provide a driving force to shift W from one site to another. Changes in cation charges upon hydroxylation, $\Delta Q_{ws}(W, Fe) = (+0.02, +0.09 e)$ and $\Delta Q_B(W, Fe) = (-0.26, -0.04 e)$ show that reconfiguration can take place with minimal perturbation of the electronic density. Bond valence sums tell a different story as the valence of W is reduced from 4.60 to 3.65 e between the O'_AW_AFe_B and (HO'_B)W_BFe_A configurations. The stable Bader charge paired with the reduction in valence suggests a more ionic interaction with a hydroxyl group *vs.* a terminal, ostensibly double-bonded O. This trend continues with higher ligand coverage, as the W BVS in the (HO')_{AB} structures are found to be significantly reduced from their values with O'_{AB} ligation.

$Q_{ws}(W)$ and $Q_B(W)$ are relatively unaffected by cation position but are heavily influenced by the OH binding site. Comparing the slightly favored (HO')_{AB}W_AFe_B cation ordering of the $\frac{2}{3}$ ML hydroxyl coverage with the opposite cation configuration, site reversal leads to $\Delta Q_{ws}(W, Fe) = (+0.0, -0.03 e)$ and $\Delta Q_B(W, Fe) = (+0.33, -0.01 e)$ with the Bader charge indicating that W is more oxidized at the B site; however, as BVS shows A-site W to be slightly more oxidized, this is probably an indication of more ionic W-OH *vs.* W-O_s interactions. The two hydroxyl ligands can be viewed as a single oxygen ligand plus a water molecule, and as indicated by the calculated

ΔE_{-H_2O} value, dissociative chemisorption of water on the “tungstyl” group appears to be irreversible. The removal of a H_2 molecule to form O ligands would also be endothermic, although not nearly as much (0.14 – 0.29 eV).

Finally, for the saturated $(HO')_3W$ -Fe surfaces, the W_AFe_B configuration is favored by 0.34 eV over its reverse, again swapping favored sites compared to $O'_3W_BFe_A$. Comparing the O'_3 vs. $(HO')_3$ charge transfers, $\Delta Q_{ws}(W, Fe) = (-0.01, -0.16 e)$ and $\Delta Q_B(W, Fe) = (-0.26, -0.35 e)$, it seems that the three OH groups capture somewhat less charge for either cation. However, the reduction implied by ΔQ_B is not as large as that caused by oxygen vacancies, as discussed below.

System	HO'_AW_A Fe _B	HO'_BW_A Fe _B	HO'_BW_B Fe _A	HO'_AW_B Fe _A	$(HO')_{AB}$ W _A Fe _B	$(HO')_{AB}$ W _B Fe _A	$(HO')_3$ W _A Fe _B	$(HO')_3$ W _B Fe _A
Relative energy (eV)	0.20	0.65	0	0.15	0	0.09	0.34	0
ΔE_{-H_2O} (eV)	--	--	--	--	0.83	0.76	--	--
$\Delta E_{-\frac{n}{2}H_2}$	-0.07 $n = 1$	-0.28 $n = 1$	0.21 $n = 1$	-0.08 $n = 1$	0.29 $n = 2$	0.14 $n = 2$	1.10 $n = 3$	0.42 $n = 3$
$Q_{ws}(W)$	5.38	5.39	5.40	5.38	5.39	5.39	5.44	5.43
s	0.03	0.04	0.03	0.04	0.03	0.03	0.03	0.03
p	5.16	5.15	5.16	5.15	5.17	5.17	5.19	5.19
d	1.42	1.42	1.40	1.43	1.40	1.41	1.34	1.35
$Q_B(W)$	2.31	1.94	2.15	1.98	2.34	2.67	2.60	2.59
BVS(W)	4.09	3.51	3.65	3.68	4.44	4.30	4.26	4.28
$Q_{ws}(Fe)$	2.86	3.09	2.89	3.06	2.91	2.88	2.97	2.90
s	0.08	0.06	0.08	0.07	0.06	0.06	0.05,	0.06
p	5.85	5.84	5.85	5.84	5.84	5.84	5.83	5.83
d	5.22	5.01	5.19	5.04	5.18	5.22	5.15	5.21
$Q_B(Fe)$	0.72	1.32	0.85	1.38	1.06	1.05	1.32	1.31
BVS(Fe)	2.09	2.28	2.13	2.35	2.21	2.16	2.33	2.39

Table 3.10: Chemical details for $\frac{1}{2}$ ML W with 1, 2, or 3 adsorbed hydroxyl groups per Fe-terminated hematite (0001) cell, including Wigner-Seitz and Bader charges and BVS for the surface Fe species. Values as defined before.

3.2.2.7 $\frac{1}{2}$ ML W / Fe-terminated α -Fe₂O₃: Effects of surface oxygen vacancies

Surface oxygen vacancies cause considerable structural rearrangement on the mixed-ML cases, as shown in **Tables 3.2(C)** and **3.3(C)**; partial cation reduction is reported in **Table 3.11**. With the rather small supercell used here, the defect density of $\frac{1}{3}$, $\frac{2}{3}$ and 1 ML (complete) oxygen deficiency may be used to track the transition from a saturated O₃-terminated surface to one terminated by 1.5 ML Fe and 0.5 ML W. In all states of extreme reduction, the W_AFe_B configuration is strongly favored, by 0.97, 0.87, and 1.70 eV over the W_BFe_A state for O_V, O_{V2}, O_{V3} oxygen vacancy models, respectively. The vertical Δz between W_A, Fe_B, O_s, and Fe_C varies considerably with vacancy concentration (**Table 3.2(C)**), ranging over 0.97- 1.45 Å for W-Fe, and increasing monotonically (1.01 < 1.18 < 1.44 Å) for Fe_{A,B,C}. Bond lengths vary in a somewhat irregular manner (**Table 3.3(C)**): W_A-Fe_B ranges over 2.63 \approx 2.55-2.88 \approx 2.74 Å and W_A-O_{s/s-1} as 1.92-2.16 \approx 1.89- 2.01 \approx 2.03-2.09Å. In every case the presence of surface oxygen vacancies drives a considerable structural rearrangement. The W and Fe Bader charges follow a reduction pattern with increasing vacancy concentration: Q_B(W): 1.77 > 1.41 > 1.14 *e* and Q_B(Fe_B): 0.79 > 0.30 > 0.00 *e*, with similar results for BVS. The WS volume integrated charges show a similar but weaker and less distinct trend. In all reported cases, the removal of O is strongly endothermic, albeit less so than for W on the reduced O-terminated hematite surface reported in **Table 3.6**.

System	$W_{\text{AFe}_B\text{O}_V}$	$W_{\text{BFe}_A\text{O}_V}$	$W_{\text{AFe}_B\text{O}_{V2}}$	$W_{\text{BFe}_A\text{O}_{V2}}$	$W_{\text{AFe}_B\text{O}_{V3}}$	$W_{\text{BFe}_A\text{O}_{V3}}$
Relative energy (eV)	0	0.97	0	0.87	0	1.70
$\Delta E_{-\frac{1}{2}\text{O}_2}$	2.71	2.86	3.53	3.43	4.29	5.12
$Q_{\text{WS}}(\text{W})$	5.40	5.33	5.36	5.34	5.37	5.27
s	0.03	0.04	0.03	0.04	0.03	0.04
p	5.16	5.12	5.14	5.11	5.14	5.07
d	1.41	1.52	1.46	1.52	1.46	1.62
$Q_{\text{B}}(\text{W})$	1.77	1.30	1.41	0.90	1.14	-0.03
BVS(W)	2.92	2.33	2.55	1.33	1.71	0
$Q_{\text{WS}}(\text{Fe})$	3.00	2.99	2.92	2.94	2.95	3.02
s	0.07	0.07	0.09	0.07	0.09	0.07
p	5.83	5.82	5.82	5.83	5.80	5.80
d	5.11	5.13	5.17	5.16	5.15	5.10
$Q_{\text{B}}(\text{Fe})$	0.79	0.77	0.30	0.46	0.00	0.34
BVS(Fe)	1.18	1.46	0.63	1.14	0	0.34

Table 3.11: Chemical details for $\frac{1}{2}$ ML W on Fe-terminated hematite (0001) with one, two, or three surface O vacancies (O_V). Values as defined before.

3.2.2.8 Convex hull analysis of W / $\alpha\text{-Fe}_2\text{O}_3$ structures

The stability arguments in the above section have been addressed case-by-case for different surface compositions. However, the stability of surface phases is better modeled by convex hull analysis, which has proven valuable in theoretical studies on bulk materials[153, 154] as well as surfaces[121, 122, 155]. By plotting the relative surface energy as a function of composition (e.g. the number of O_2 or H_2 molecules adsorbed), the relative stability of a particular surface phase – or its decomposition into different phases – can be predicted. Convex hull plots for W / $\alpha\text{-Fe}_2\text{O}_3$ structures calculated in this work are shown in **Figure 3.12**. Surface energies used for convex hull analysis are calculated relative to the energy of a particular structure named on the ordinate label of each plot. The relative surface energy is calculated by adding or subtracting the total energy of

an appropriate quantity of H_2 or O_2 molecules so as to correct for the stoichiometry. Absolute surface energies are likely inaccurate under this calculation scheme and are not considered.

For 0.5 ML W / O-terminated $\alpha\text{-Fe}_2\text{O}_3$ (0001), **Figure 3.12(a)** shows that the most stable ground-state structures have either W_AO_A or $W_B(\text{HO}')_3$ terminations under vacuum conditions. It is clear that the structures with no additional O, including structures with hydrogenated W, are very unstable. In a hydrogen-free environment, **Figure 3.12(b)** reveals that the W_AO_A structure has the lowest surface energy. Surprisingly, the case of W adsorption onto a clean O-terminated $\alpha\text{-Fe}_2\text{O}_3$ (0001) surface is predicted to be unstable; it would decompose into W_AO_A and phases with O vacancies. On the other hand, the case of 0.5 ML W atop Fe-terminated $\alpha\text{-Fe}_2\text{O}_3$ (0001) (**Figure 3.12(c-d)**) shows that complete O coverage is strongly preferred, with a slight reduction in surface energy upon hydroxylation for most cases. The surface energy drops nearly linearly with increasing O coverage in hydrogen-free conditions. 1.0 ML W / O-terminated $\alpha\text{-Fe}_2\text{O}_3$ (0001) similarly shows a preference for complete coordination of W.

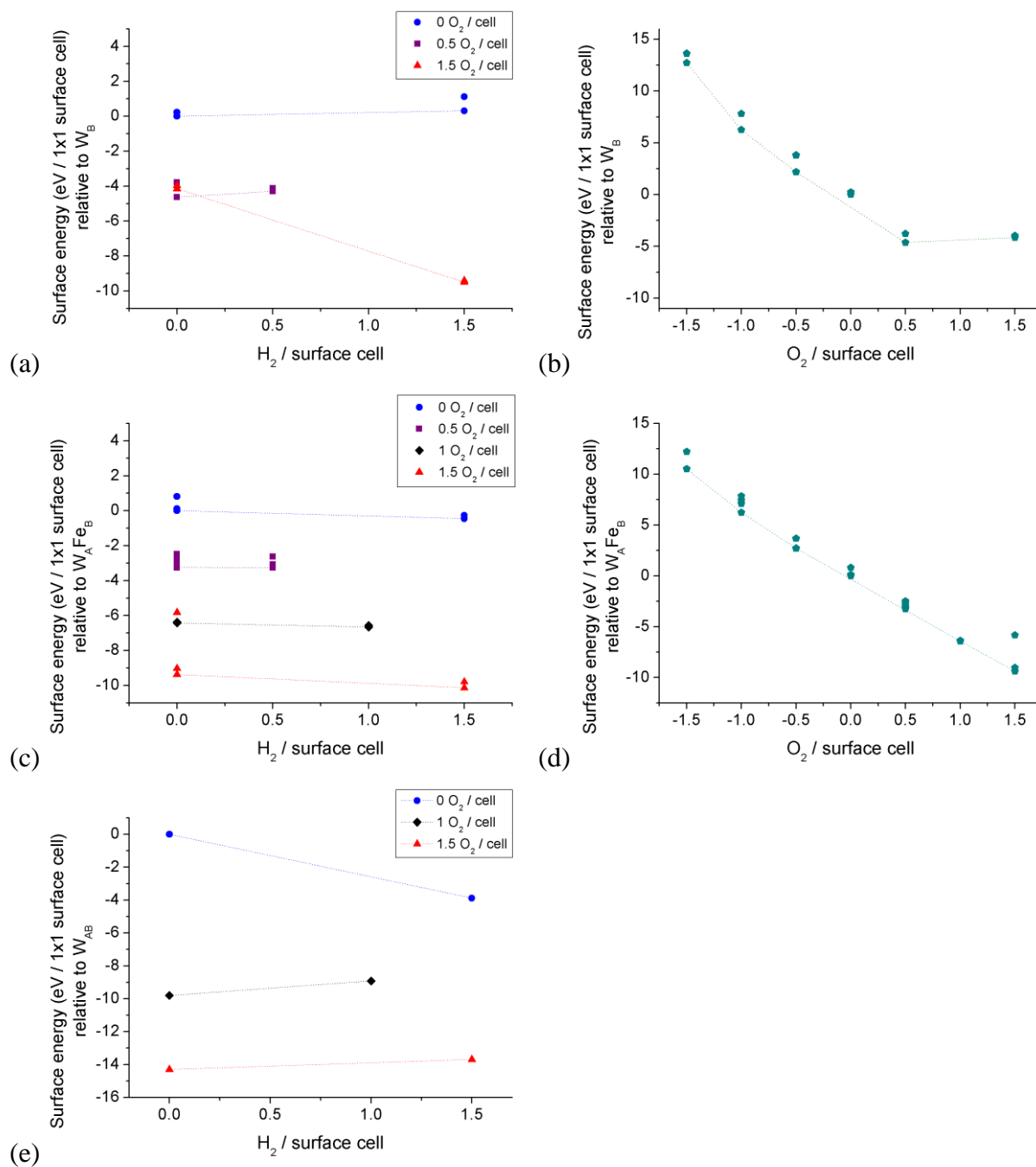


Figure 3.12: Convex hull analysis of relative surface energies for several W / α -Fe₂O₃ (0001) surface structures. (a,b) 0.5 ML W / O-terminated hematite; (c,d) 0.5 ML W / Fe-terminated hematite; (e) 1.0 ML W / O-terminated hematite. Results are shown for (a,c,e) fixed terminal O₂ coverage with varying H₂ content or (b,d) varying terminal O₂ coverage with no adsorbed hydrogen. Negative values of O₂ / surface cell indicate surface O vacancies. Surface energies are calculated relative to the structure named on the ordinate.

3.2.2.9 Fe d-electron correlation effects

Despite the success of L(S)DA and GGA exchange-correlation approximations used in DFT calculations for many materials systems, electron localization and correlation cannot be properly calculated due to errors intrinsic to these schemes[156, 157], leading to poor predictions of bandgaps and magnetic moments of hematite[158] and certain other 3d transition metal oxides[159-162]. A few approaches have been developed to confront this problem, typically by adding a correction term to the exchange-correlation energy E_{xc} such as a self-interaction correction (SIC)[159, 163] or Hubbard $+U$ [161, 164, 165]. In the simplified L(S)DA+ U approach[161] the $+U$ term is applied to the Hamiltonian of a particular orbital (e.g. the 3d orbital of a transition metal cation), simulating Coulomb repulsion between d electrons. This localizes 3d electron density on the cations and subsequently widens the energy gap between occupied and unoccupied d -states. This heuristic method has the merit that its functional derivative yields the desired one-electron Hamiltonian. Furthermore, examination of the contributions of the semi-empirical correlation term has proved helpful in understanding effects of correlation in narrow band systems. The use of a $+U$ correction modifies the phase stability of hematite; for example, the high-pressure ferromagnetic phase predicted by GGA calculations is destabilized when a $+U$ term is added[158]. Of greater relevance to this work are the surface phase diagrams of Rohrbach *et al.*[59] which show significant changes in the stability of clean α -Fe₂O₃ (0001) surface phases over a range of oxygen chemical potentials upon addition of the $+U$ term.

In a similar spirit, the GGA+ U method of Dudarev *et al.*[164] was employed here (in the PW91 implementation, see **Section 3.2.1**) to investigate the dependence of the electronic structure and phase stability of the WO_x/ α -Fe₂O₃ (0001) surface on the value of $U - J$, which combines both

Coulomb (U) and exchange (J) interactions. $U - J$ values are often selected empirically; however, an accurate $U - J$ value of 4.3 eV for bulk α -Fe₂O₃ has recently been derived from first principles[166]. Generally speaking, the additional interaction is applied only to the partially occupied localized cation Hamiltonian matrix elements for a particular angular momentum – here, Fe 3*d*. Values of $U - J$ (simply referred to as U in the following) of 0, 2, and 4 eV for Fe 3*d* states were selected to span a range of interesting values for the present investigation. No such terms were considered for the W atoms.

U (eV)	O' _A W _A	O' _B W _B	O' _A W _A Fe _B	O' _A W _B Fe _A	O' _B W _B Fe _A	O' _{AB} W _A Fe _B	O' _{AB} W _B Fe _A
0	0	-0.84	0	-0.06	-0.02	-0.05	0
2	0	-0.80	-0.16	0	-0.03	-0.25	0
4	--	--	-0.13	-0.05	0	-0.19	0

Table 3.12: Comparison of converged electronic energies (in eV) of selected relaxed configurations converged with the PW91+ U method. The energies shown are relative to the most stable isostoichiometric supercell, which therefore has a relative energy of 0 eV per 1x1 supercell.

The relative stabilities of different surface structures determined at different U values are shown in **Table 3.12**. Cases shown include $\frac{1}{3}$ ML O' atop $\frac{1}{2}$ ML W and mixed-metal surfaces as well as $\frac{2}{3}$ ML O' atop mixed-metal surfaces. The structures were relaxed at $U = 0$ eV, and their electronic states were re-converged at $U = 2$ and 4 eV. For the $\frac{2}{3}$ ML O' case, the addition of U changed the energy difference between the isostoichiometric structures, increasing the calculated stability of the O'_{AB}W_BFe_A configuration by 0.14 – 0.20 eV versus the O'_{AB}W_AFe_B case. The relative stability of the O'_AW_A case compared to the O'_BW_B dropped insubstantially at $U = 2$ eV. For the $\frac{1}{3}$ ML O' on $\frac{1}{2}$ ML W cases, no acceptable electronic convergence could be achieved for $U = 4$ eV.

The addition of a U term yielded more interesting results for $\frac{1}{3}$ ML O' on mixed-metal terminated surfaces. Without U , the $O'_A W_A Fe_B$ configuration is slightly more stable than the two $W_B Fe_A$ structures, with O' sitting over either the W or Fe. However, the addition of $U = 2$ eV significantly destabilizes the $W_A Fe_B$ configuration, instead favoring the opposite arrangement by 0.12 – 0.15 eV, with the O' bound to the Fe_A atom (which actually relaxes to a more bridging configuration between W and Fe, see **Figure 3.10(f)**) in the most stable condition. Increasing the U value to 4 eV shifts the stable coordination of the O' atom from a bridging position between cations to the W_B atom exclusively. Since the $+U$ procedure amounts to opening a gap between occupied and vacant Fe d states, we can infer that resulting shifts in s - d , p - d hybridization and accompanying Fe-O covalency is sufficient to modify relative stability of surface structures. The variability of W $5d$ occupancy upon hydroxylation, discussed above, suggests that future GGA+ U studies should employ corrections for both Fe and W correlation effects; this could have consequences for both the relative stability and chemical properties of surface W due to charge localization and corresponding increases in W ionicity. However, exploring such two-parameter models is nontrivial and not considered in this work.

3.2.3 Comparison with experimental results

Previously, plausible surface structures were proposed for the nominally “reduced” (via exposure to H_2) and “oxidized” surfaces (referred to as *Re* and *Ox*, respectively) for $\frac{1}{3}$ ML W grown by atomic layer deposition (ALD)[102, 167] on hematite (0001)[66]. XSW results provided the proposed W ion positions, while X-ray absorption fine structure (XAFS) suggested a saturated oxygen coordination of 6 for the *Ox* case. Models resulting from fits to XSW amplitude and phase data suggest that the position of the coherent fraction of W (or V) on hematite (0001) remains well-

centered above Fe surface sites, moving in the (0001) surface normal direction upon undergoing chemical change[66, 131]. Thus, in order to correlate theoretical predictions with XSW data, the W z -position is compared to bulk-like Fe lateral positions and O planes. The fact that roughly 35-55% of surface-adsorbed W is not “visible” by XSW and thus not in registry with the underlying cation lattice suggests that there exist further energetically attractive surface sites, perhaps associated with native defects or combinations of several of the structures explored herein. Transverse cation displacements, observed for some structures above, may also contribute to lower XSW-measured coherent fractions. With the small supercells used in the present work, we are unable to offer concrete structural models for this missing fraction. Instead, we search for the closest match to experiment between calculated Δz values and energetically favored sites in a given chemical environment.

As to comparisons with XPS data, Bader charge analysis fulfills general expectations of oxidation state *vs.* oxygen coordination, although the local cation charges Q_B are less, by almost 50%, than those expected from nominal high-valence configurations. This is certainly not a surprise in light of a wealth of theoretical studies on ionic-covalent compounds, and it motivates more subtle analyses based upon energetics and bond valence sums.

Given the considerable number of surface configurations and non-stoichiometric compositions studied, certain 'reduced' and 'oxidized' models adequately reproduce the XSW results for lattice site and position. These models, summarized in **Table 3.13**, are found to be relatively stable, lending some credence to their identification as candidates to represent the experimentally derived coherent fraction. The W valence calculated by BVS for each case is given, along with the valence

determined experimentally by XPS. BVS values are corrected by reducing the size of the unit cell by a factor of 0.994 along each direction before calculating the W-O bond lengths fed into the BVS equation. This correction yields the appropriate bulk Fe valence of 3.00 (recall from **Section 2.4.3** that Fe in the relaxed bulk hematite unit cell has a BVS of 2.91). The most likely candidates for the surface configuration of the oxidized and reduced cases, based on the position and valence of W, are shown in **Figure 3.13**.

	Experiment "Reduced"	O' _A W _A	HO' _A W _A	O' _{AB} W _B Fe _A	(HO') _{AB} W _B Fe _A	Experiment "Oxidized"	O' ₃ W _B Fe _A
z_A (Å)	0.88	0.79	0.89	--	--	--	--
z_B (Å)	1.46	--	--	1.51	1.25	1.56	1.58
W valence	5	5.73	5.43	5.26	4.47	6	5.61

Table 3.13: Comparison of W A- and B-site z displacements above the bulk-like O₃ plane derived from XSW experiments[66] with selected energetically favored DFT-calculated configurations. Valence values are from XPS (experiment) or BVS corrected for the hematite lattice parameter, as discussed in the text.

It is particularly interesting to consider the predicted ground state configuration of W_BFe_A in the oxidized state as well as the likely protonation at a fraction of reduced W sites. The HO'_AW_A structure has 0.33 eV higher surface energy per 1x1 surface cell than the O'_AW_A structure in vacuum (**Figure 3.12**), but it may still be present when subjected to a higher chemical potential of H₂, such as constant H₂ flow as in the *in situ* XSW experimental conditions. Conversely, the (HO')_{AB}W_BFe_A structure, which has a W z_B height of 1.25 Å, has a lower surface energy (by 0.14 eV) than its oxygen-terminated counterpart (W z_B = 1.51 Å), but the hydroxylated structure does not resemble the experimental data in terms of W valence or position. Kinetic barriers might prevent this reduction from fully occurring under experimental conditions; some fraction of the (HO')_{AB}W_BFe_A structure on the surface might lower the average W z_B to a value closer to the

experimentally derived value of 1.46 Å, with a consequential decrease in the measured coherent fraction. As shown in **Section 3.2.2.9**, relative stabilities are dependent on strong electron correlation effects, whereas structural details are much less affected. We may therefore ascribe the apparent stability of the $(\text{HO})'_{\text{AB}}\text{W}_\text{B}\text{Fe}_\text{A}$ structure to the omission of a $+U$ correction, as the $\text{O}'_{\text{AB}}\text{W}_\text{B}\text{Fe}_\text{A}$ structure more closely matches experimental results in both position and valence.

The poor match of all 1 ML $\text{W}_\text{A}\text{W}_\text{B}$ calculations with XSW results suggests that the $\frac{1}{3}$ ML WO_x species do not grow as atomically thin, W-dense rafts or islands. The better match with the $\frac{1}{2}$ ML cases implies that the WO_x was more evenly dispersed over the sample surface, as suggested by atomic force microscopy[66]. However, the small unit cell size precludes any stronger conclusions regarding such long-range effects.

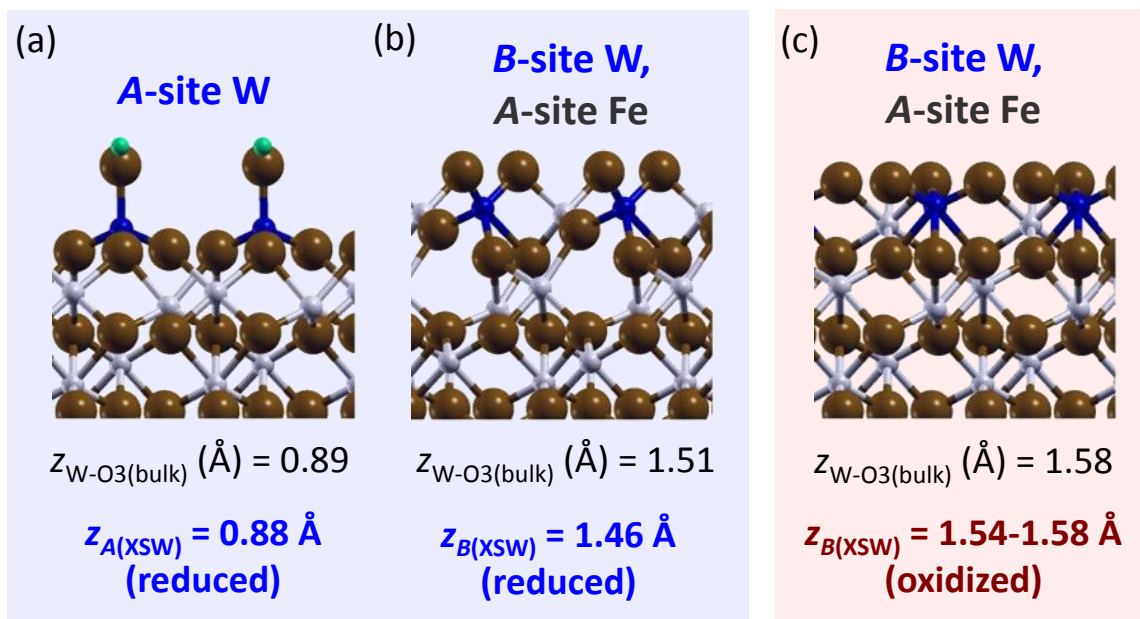


Figure 3.13: Proposed structures for oxidized and reduced sub-ML W / $\alpha\text{-Fe}_2\text{O}_3$ (0001) by comparison of theoretical models to experimental results. (a,b) Reduced case: (a) $\text{HO}'_{\text{A}}\text{W}_\text{A}$, (b) $\text{O}'_{\text{AB}}\text{W}_\text{B}\text{Fe}_\text{A}$. (c) Oxidized case: $\text{O}'_3\text{W}_\text{B}\text{Fe}_\text{A}$. Color scheme is as before.

In addition to the c-axis displacements discussed throughout, nontrivial x- and y- displacements from the symmetric A- and B-site positions are also predicted. Nevertheless, it remains generally possible to clearly identify A- and B-site cation origins, and due to the 3-fold symmetry of the experimental surface, XSW measurements would give an average of these displacements in all three symmetry-identical lattice directions.

In the three “reduced” models reported in **Table 3.13**, the BVS of W is between 5.05 – 5.51 e . While these values are between those expected for W^{4+} (3.39) and W^{6+} (5.79), there is no bulk model for the W^{5+} state reported in the XPS experiment[66]. Considering the best oxidized-case model ($O_3W_BFe_A$) has a W BVS of 5.44, it seems that this should correspond to a W^{6+} assignment. The oxidation state as measured by XPS is probably more dependent on the degree of ionicity due to charge screening effects, so the higher Bader charge of the $O_3W_BFe_A$ case (2.86 e) vs. the reduced cases (2.64 – 2.77 e) may account for the observed XPS shift. These methods of charge division are somewhat arbitrary, but the “reduced” cases presented here are evidently less oxidized than $O_3W_BFe_A$.

W $4f_{5/2,7/2}$ XPS core-level measurements on surfaces and non-stoichiometric films and particles have typical values for W^{6+} (35.6, 37.7 eV) and W^{5+} (34.5, 36.6 eV)[168, 169], revealing a spin-orbit splitting of 2.1 eV and a oxidation-state shift of 1.1 eV. A number of molecular cluster calculations were carried out in the Transition State scheme described previously, in an effort to identify theoretical core-level shifts with changes in W chemical environment. Since the core-hole effects are essentially Coulombic in nature, with energy differences due mostly to charge screening from the environment, we examine the difference of two environments using non-relativistic

models. Calculated core-level energies taken relative to the local Fermi energy show a variation of 1.19 eV over various W coordination environments, in quantitative agreement with experiment. However, we cannot cleanly identify distinct valence states that can be confidently assigned as W^{5+} or W^{6+} ; rather, we find a range of values between the extremes of W-ligand coordination.

3.3 Structure and Chemistry of $WO_x / \alpha\text{-Fe}_2\text{O}_3$ Nanopowders

As is shown through most of this dissertation, studies of single crystal surfaces as model heterogeneous catalysts using surface science methods contribute to the understanding of the reaction dynamics and processes in industrial and environmental catalysis[11, 128]. While the details of reaction mechanisms can be very precisely determined through the study of single crystal surfaces and ultrathin films, these are removed from the properties of the real catalyst, which is much more structurally complex. Bridging this “materials gap” requires the use of *in situ* measurements which are sensitive to the surfaces of reactive particles. To understand the catalytic active site, the atomic scale structure of small-volume surface regions must be characterized.

Real catalysts consist of nanostructured materials with a high surface area and density of under-coordinated, chemically active surface sites. However, because of this complexity, they are difficult to characterize. In an attempt to bridge single crystal surface results with real catalyst nanopowders, we use *in situ* synchrotron X-ray absorption fine structure (XAFS) and other laboratory techniques to probe the chemical state and coordination environment of W deposited on the surface of hematite nanopowders (HNPs).

3.3.1 Methods

HNPs (20 – 40 nm, American Elements) were coated with WO_x using atomic layer deposition (ALD) by J. Libera, A. Mane, and J.W. Elam at Argonne National Laboratory (ANL). ALD parameters for some of the prepared samples and the resulting coverages are shown in **Table 3.14**. The WO_x loading of the HNPs was measured by monitoring the mass increase of particles in the reactor, which is measured as a percentage increase in weight (% w/w). This weight gain can be approximated as a coverage (1 ML = 9.1 W nm⁻²) for comparison with single crystal results. Assuming that the nanoparticles are spheres of 30 nm diameter and that W is fully oxidized to WO₃ by the end of deposition (when the weight is measured), and knowing the density of hematite and WO₃ (5.27 and 7.16 g cm⁻³, respectively), the coverage can be approximated as 1% w/w WO₃ = 1.37 W nm⁻² = 0.15 ML, or 6.6% w/w WO₃ = 1 ML.

WO _x loading (% w/w)	Approximate coverage (MLE)	D1	D2	D3
0.29	0.04	5 torr WF ₆ , 100 s	5 torr H ₂ O, 200 s	--
2.43	0.36	0.2 torr CH ₃ OH in 300 sccm N ₂ , 10 s	0.2 torr Si ₂ H ₆ in 300 sccm N ₂ , 3 s	5 torr WF ₆ , 100 s
2.69	0.40	1.5 torr CH ₃ OH in 300 sccm N ₂ , 100 s	0.2 torr Si ₂ H ₆ in 300 sccm N ₂ , 3 s	5 torr WF ₆ , 100 s
3.40	0.51	0.3 torr Si ₂ H ₆ in 300 sccm N ₂ , 3 s	5 torr WF ₆ , 100 s	--

Table 3.14: ALD parameters used for WO_x deposition on hematite nanopowders (HNPs). D1, D2, and D3 correspond to the different steps used in the deposition; the pressure of the reagent and exposure time are also given. Between each step, the reactor was purged with an inert gas. For the samples listed, only one ALD cycle was performed.

After ALD, the powders were imaged using transmission electron microscopy (TEM) by Y. Lei at ANL. X-ray diffraction (XRD) patterns were collected on a Scintag XDS2000 instrument with Cu

$K\alpha$ radiation ($\lambda = 1.5418 \text{ \AA}$). The composition and chemical states of the powders were characterized by X-ray photoelectron spectroscopy (XPS) on an Omicron instrument equipped with a hemispherical analyzer using Al $K\alpha$ (1486.6 eV) radiation at a 45° incident beam angle. An electron flood gun was used to compensate for sample charging. XPS and XRD data were collected by N. Ray, an undergraduate student from the University of Texas at San Antonio who participated in our research group through the summers of 2010 and 2011. Due to limited sample volumes and sample contamination or loss between experiments, most WO_x -coated HNP samples could only be characterized by a limited regimen of techniques.

XAFS studies were conducted at the 5-BM-D and 9-BM-C beamlines of the Advanced Photon Source (APS) synchrotron at Argonne National Laboratory with the assistance of S. Stoltz and I.-C. Tung and beamline scientists Q. Ma and T. Bolin. Nanopowder samples were pressed into 15 mm diameter, ~ 1 mm thick pellets of mass ~ 0.4 g. Pellets were protected from contamination by covering the pressing die surface with clean weighing paper. The pellets were loaded into a steel gas-sealed sample chamber (provided by Prof. H. Kung) with a polyimide film window. The cylindrical chamber was heated by resistive heating tape wrapped around it, and sample temperature was monitored via a thermocouple in contact with the back side of the pressed pellet. Samples were mounted at a 45° angle relative to the incident X-ray beam. X-ray fluorescence (XRF) was collected using either a Canberra N_2 -cooled 13-element Ge drift detector or a SII Vortex 4-element Si drift detector, with the detector axis oriented along the direction of X-ray polarization. The XRF mode was chosen to optimize the signal from low loadings of W on strongly absorbing Fe_2O_3 . Al foil was used to attenuate the incoming fluorescence in order to reduce dead-time effects. The setup at APS beamline 5-BM-D is shown in **Figure 3.14**. For XAFS experiments,

the incident X-ray energy was scanned through the W L_3 absorption edge (10206.8 eV). Spectra were collected from 200 eV below the absorption edge to $k = (14 - 16) \text{ \AA}^{-1}$ (750 - 960 eV) above the edge. The W $L\alpha$ (8.38 keV) fluorescence signal was monitored as an indicator of W L_3 X-ray absorption. The beam spot size on the sample ranged from $500 \mu\text{m} \times 500 \mu\text{m}$ to $1 \text{ mm} \times 3 \text{ mm}$.

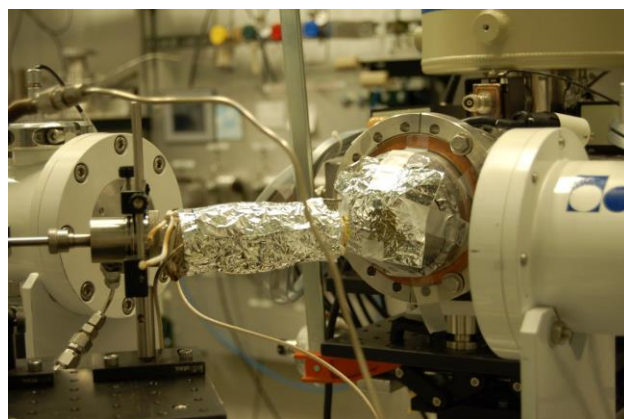
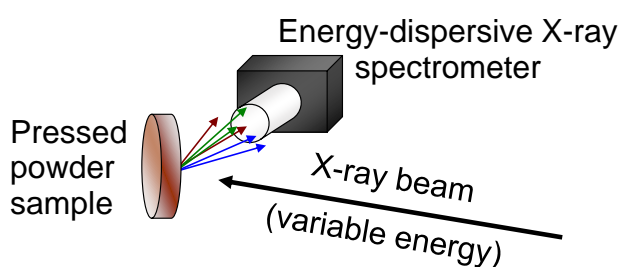


Figure 3.14: Schematic and corresponding photograph of the XAFS setup at APS beamline 5-BM-D. The sample is held at the end of a cylinder (left of center on the photograph) wrapped in heating tape and Al foil. The 13-element Canberra Ge detector (right of center on the photograph) is covered with Al foil to attenuate the incoming fluorescence intensity.

3.3.2 Results

3.3.2.1 Particle characterization: XRD, TEM

Prior to redox reactions, the WO_x -coated HNPs were characterized by powder X-ray diffraction (XRD) to confirm that the powders were of the $\alpha\text{-Fe}_2\text{O}_3$ (hematite) structure and to check for the presence of crystalline WO_x . X-ray diffraction patterns for the sample with the highest weight gain during deposition (18.8% w/w) are shown in **Figure 3.15**. XRD patterns are shown for powders in both the as-deposited state (AD) as well as after oxidation in O_2 at $400 \text{ }^\circ\text{C}$ for 30 min. (OX). In both cases, the XRD peaks all match well to hematite, whereas no other peaks are observed. TEM

micrographs at a lower WO_x loading of 4.3% w/w (0.65 MLE) (**Figure 3.16**) show a conformal film of <1 nm thickness coating the HNPs. No such coating is visible for the 0.29% w/w (0.04 MLE) case (**Figure 3.17**), suggesting a sparse distribution of W species on the HNP surface. Taken together, XRD and TEM data suggest that WO_x does not form crystallites at these coverages.

The average minimum HNP crystallite size τ increased from $30.3 \pm 1.5 \text{ nm}$ (AD) to $34.5 \pm 1.9 \text{ nm}$ (OX) as calculated by the Scherrer equation

$$\tau = \frac{K \lambda}{\beta_{1/2} \cos(\theta)} \quad (3.1)$$

where $K = 0.94$ is a constant that assumes a spherical particle geometry, λ is the X-ray wavelength, $\beta_{1/2}$ is the full width at half maximum (FWHM) of the diffraction peak, and θ is the Bragg angle of the peak. This increase may be attributed to the sintering of smaller particles or an improvement in HNP crystallinity during annealing[170]. A broad feature in the background at $2\theta \approx 30^\circ$ ($q \approx 4 \text{ \AA}^{-1}$) also appears in the pattern for the annealed sample. Although high-coverage WO_x catalysts tend to form nanocrystals on oxide supports[171], the range of this feature does not correspond to any strong WO_3 diffraction features.

3.3.2.2 Chemical characterization: XPS

XP spectra were recorded for a HNP sample with 3.4% w/w deposited WO_x . Fits to the W 4f spectra are shown in **Figure 3.18**. In the W 4f spectra of the as-deposited (AD) state, there exists a mix of broad states assigned as 70% W^{6+} and 30% W^{5+} . Despite calibration to the C 1s peak at 284.8 eV, the peak assigned to W^{6+} sits at a somewhat higher binding energy than expected. Upon oxidation (OX, 400 °C in 200 sccm flowing O_2 for 30 min.), W becomes completely oxidized to W^{6+} . An attempt at reduction was made (RD, 400 °C in 200 sccm flowing 5% H_2 bal. N_2 for 30

min.), but no change in the W 4f XPS spectrum was observed. The substantial broadening of the W 5p peak at ~41 eV is an artifact of fitting and is not considered here.

3.3.2.3 In situ structural and chemical characterization: XAFS

In situ XAFS spectra were collected for several W loadings on HNPs. XAFS spectra were measured in the “as-deposited” (AD) condition and were then measured after redox steps in O₂ and dilute H₂ as tabulated in **Table 3.15**. After each annealing step, the sample was allowed to cool to room temperature, and gas flow was continued through the experiment.

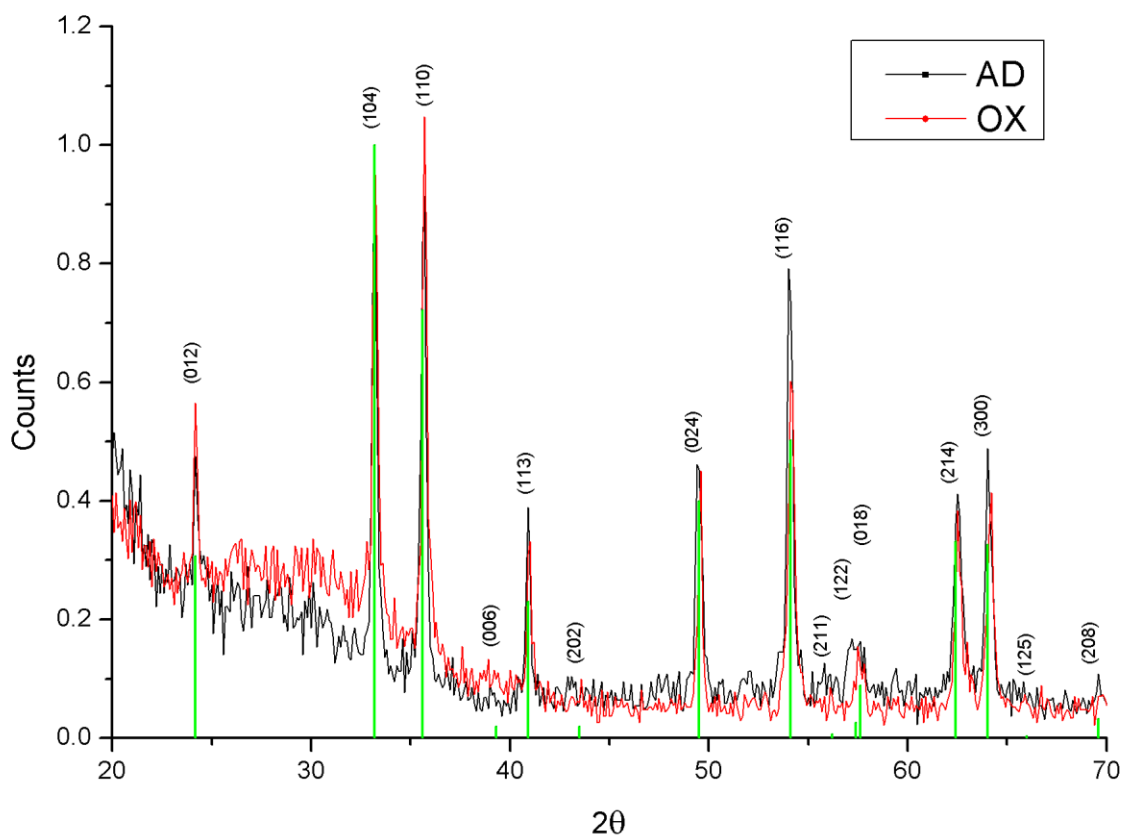


Figure 3.15: XRD patterns of HNPs deposited with 18.8 % w/w WO_x coverage with α-Fe₂O₃ peak positions and bulk relative intensities overlaid in green.

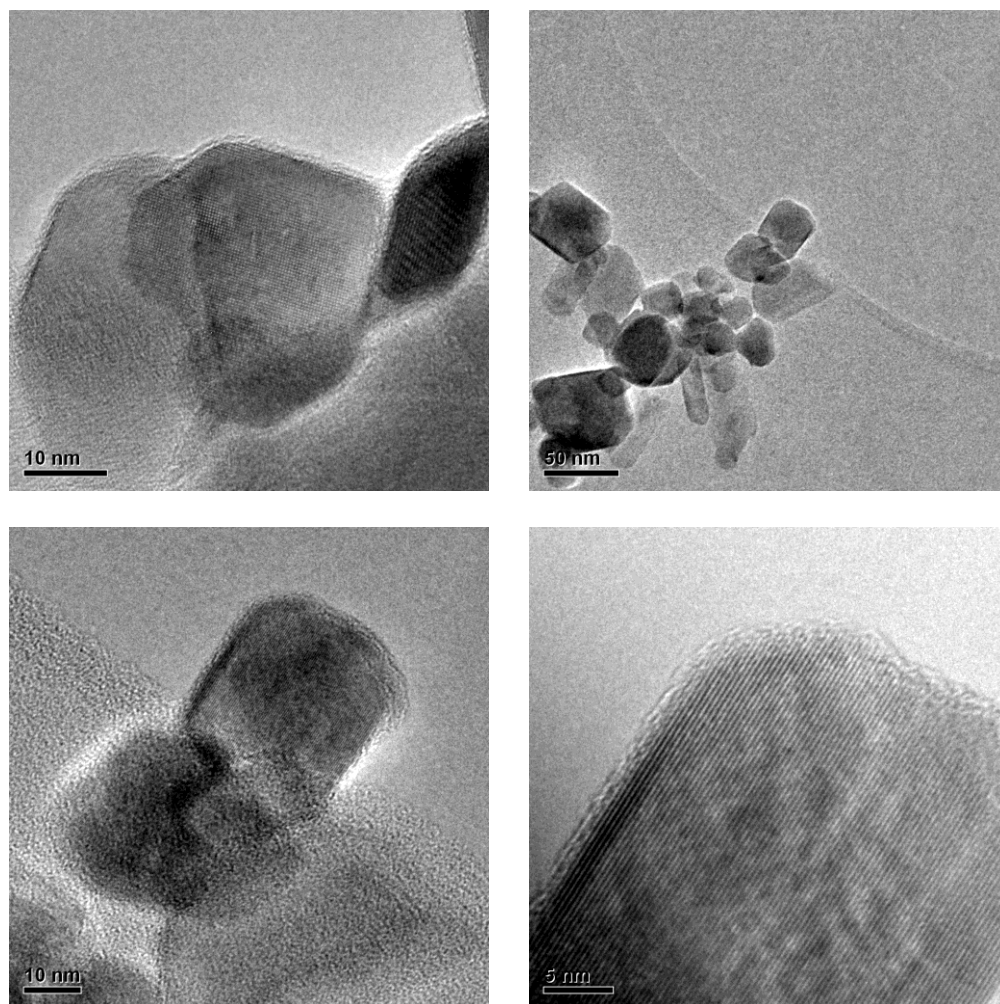


Figure 3.16: TEM micrographs of W-coated HNPs with a coverage of 4.3% w/w WO_x .

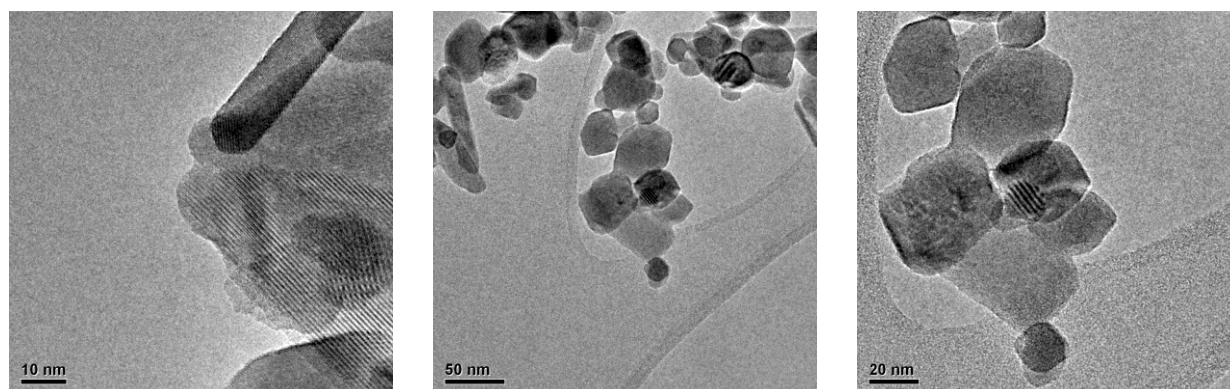


Figure 3.17: TEM micrographs of W-coated HNPs with a coverage of 0.29% w/w WO_x .

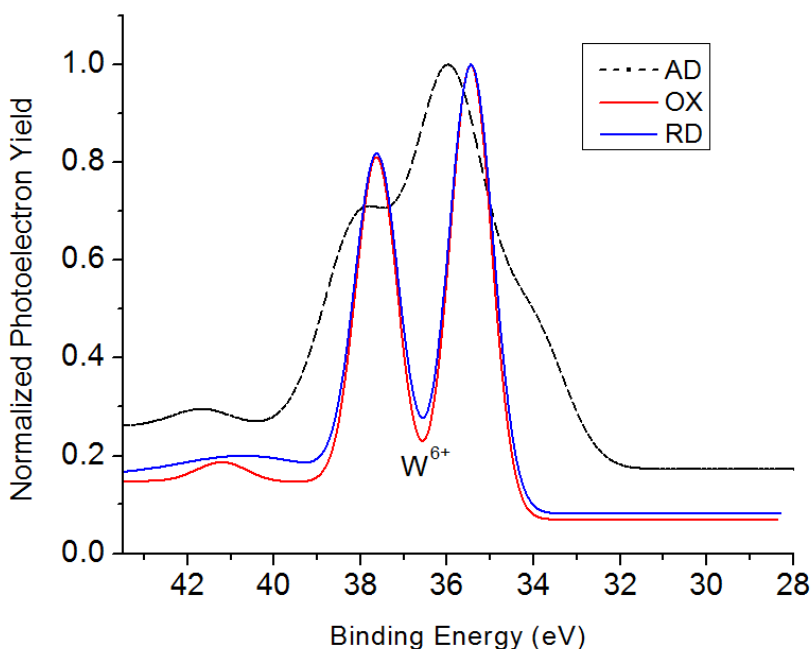


Figure 3.18: W 4*f* XP spectra fits (calibrated to the adventitious C 1*s* peak) for 3.4% w/w WO_x deposited on HNPs in the as-deposited (AD) state as well as after oxidation (OX) and reduction (RD) as described in the text. Data is normalized to the peak intensity.

WO _x loading (% w/w)	Approximate coverage (MLE)	OX1	RD	OX2
0.29	0.04	350 °C in ~100 sccm O ₂ , 60 min.	--	--
2.43	0.36	350 °C in ~100 sccm O ₂ , 30 min.	350 °C in ~100 sccm 3% H ₂ bal. He, 30 min.	350 °C in ~100 sccm O ₂ , 30 min.
2.69	0.40	350 °C in ~100 sccm O ₂ , 30 min.	--	--
3.40	0.51	350 °C in ~100 sccm O ₂ , 30 min.	390 °C, 60 min., then 400 °C, 30 min. in ~100 sccm 3% H ₂ bal. He	350 °C in ~100 sccm O ₂ , 30 min.
6.19	0.93	350 °C in ~100 sccm O ₂ , 30 min.	390 °C in ~100 sccm 3% H ₂ bal. He, 60 min.	350 °C in ~100 sccm O ₂ , 30 min.

Table 3.15: Annealing conditions for HNP samples coated by ALD with different coverages of WO_x. XAFS measurements were taken at room temperature after annealing, with gas continuing to flow. After each measurement, the reactor was purged with He. All samples start in the “as deposited” (AD) condition.

Single-shell EXAFS fits were performed using FEFF software[92-94] as implemented in the ARTEMIS package[95]. First, an amplitude reduction factor for all fits was derived by fitting a WO_3 powder spectrum to a single-shell model with an effective W-O distance of 1.8265 Å and a nominal coordination number (N) of 6.00. This is a gross approximation, considering that the first W-O coordination shell of triclinic WO_3 (the stable room-temperature structure) has bond lengths ranging from 1.75 to 2.21 Å[172] whose contributions would add in amplitude and phase to generate the final spectrum. Because of this structural complexity, similar few-shell approximations have been used before to derive meaning from complex WO_x EXAFS spectra[173-177]. The fit amplitude parameter, fit for the WO_3 standard powder, acts as a universal scaling factor for the EXAFS modulation amplitude and was determined to be 0.325 with an uncertainty of 0.054. For the WO_3 fit, N was arbitrarily fixed at 6.00 (the fit amplitude parameter scales inversely with N) and σ^2 was set to 0.001 in light of previous results[174]. Other fit parameters include a fitted spectral energy offset E_0 , which is not explicitly part of the EXAFS equation (see **Chapter 2**) but acts as an offset correction factor, and the ΔR change in path length vs. the nominal path length. While $(1.8265 \text{ Å} + \Delta R)$ would ostensibly give the W-O bond length, due to the single-shell approximation this is better used as a relative parameter (along with N). The R-factor is a goodness-of-fit parameter that describes the fractional error of the fit, with $R < 0.05$ indicating a reasonably good fit[178]. All fits were performed in both k -space (from $k = 2.5 - 10.2 \text{ Å}^{-1}$) and real space (from $R = 1 - 2 \text{ Å}$, k^2 -weighted). These ranges cover a reliable segment of k -space while covering the major first coordination shell feature in the inverse Fourier-transformed real-space distribution function.

Best-fit parameters for samples with WO_x loadings ranging from 0.29 to 6.19% w/w (corresponding to 0.04 – 0.93 ML coverage, given the assumptions above) are shown in **Table 3.16** for fits with unconstrained σ^2 values and **Table 3.17** for fits with σ^2 set to 0.001. This constraint was employed to counter a broad variation in σ^2 as shown in **Table 3.16** as well as unrealistic negative values of σ^2 . While this value is somewhat small, it provides generally good fits to all data considered below. It also reduces uncertainties in N caused by correlations with σ^2 [179]. While the R-factor values increase slightly upon fixing σ^2 , the constrained fit is expected to be more physically accurate. We note that the uncertainty on ΔR is within a few hundredths of an Ångström, but the uncertainty for N is on the order of 0.5 for the constrained cases and well over 1 for the unconstrained fits. While the uncertainties on N are rather large, many published EXAFS studies on WO_x do not mention an uncertainty value at all.

W radial distribution functions (RDFs) for all measured samples as well as WO_3 powder are given in **Figure 3.19**. The single-shell fit to WO_3 is also shown to provide context for the scope of the fitting. These RDFs are not corrected for the photoelectron phase shift upon scattering; the real interatomic distances are approximately 0.45 Å longer than those shown in the RDFs. All RDFs are dominated by a strong peak at about 1.3 Å, corresponding to the first W-O ligand peak. Significant features are also present between 2.5 – 3.5 Å, corresponding to longer photoelectron scattering paths. These features become narrower and more intense with chemical treatment. However, there is no clear redox-reversible transition in any tested cases; each chemical treatment step appears to act only as an annealing step. The reducing (RD) treatment seems to be critical, as the following oxidation step (OX2) yields a structure that is almost exactly the same as that after reduction. While the reduction temperature (390 – 400 °C) is higher than the oxidation temperature

(350 °C) in the 3.40% and 6.19% w/w samples, the temperature for all treatments is the same (350 °C) for the 2.43% w/w sample. We note that for the 3.40% w/w WO_x case, a reduction step was performed, but EXAFS data was not collected as XANES performed during reduction did not indicate a change in oxidation state.

An anomalous case is that of 2.69% w/w coverage WO_x, in which the first coordination shell shows a feature about 0.5 Å below the first W-O coordination peak. Unlike the other samples, this sample as well as the 2.43% w/w WO_x sample were prepared using methanol in intermediate doses between WF₆ and Si₂H₆ during ALD. The methanol exposure was 10 times longer (100 sec vs. 10 sec) for the 2.69% w/w WO_x sample. While one might hypothesize that this feature is due to some W-C interaction, previous studies of tungsten carbonyl and organic ligands show a much longer W-C bond length than could be attributed to this feature[180]. The feature might also be caused by an artifact in $\chi(k)$ due to a poor spline fit to the $\mu_0(E)$ background (see **Chapter 2**).

WO _x loading, % w/w [MLE]	Chemical state	E_0	ΔR	σ^2	N	R-factor
WO ₃ powder	--	0.52 (6.11)	-0.073 (0.030)	0.001 (constrained)	6.00 (constrained)	0.044
0.29	AD	7.88 (3.21)	-0.038 (0.019)	0.0025 (0.0026)	6.19 (1.38)	0.008
[0.04]	OX1	7.61 (3.76)	-0.032 (0.021)	0.0017 (0.0030)	6.01 (1.56)	0.011
2.43	AD	1.44 (4.40)	-0.074 (0.021)	0.0005 (0.0028)	5.23 (1.45)	0.010
	OX1	2.42 (5.36)	-0.056 (0.030)	0.0038 (0.0040)	6.23 (2.14)	0.016
	RD	2.82 (5.66)	-0.050 (0.033)	0.0048 (0.0044)	6.44 (2.33)	0.017
	OX2	2.12 (4.78)	-0.055 (0.027)	0.0043 (0.0036)	6.50 (1.97)	0.012
2.69	AD	-1.94 (3.86)	-0.087 (0.018)	0.0016 (0.0024)	5.86 (1.39)	0.007
	[0.40] OX1	0.31 (2.15)	-0.071 (0.011)	0.0037 (0.0015)	6.72 (0.90)	0.002
3.40	AD	-0.90 (7.93)	-0.089 (0.033)	-0.0023 (0.0044)	3.84 (1.87)	0.028
	OX1	4.38 (3.20)	-0.062 (0.016)	0.0005 (0.0022)	5.57 (1.17)	0.006
	OX2	2.81 (5.80)	-0.047 (0.034)	0.0050 (0.0046)	6.95 (2.58)	0.018
6.19	AD	-1.35 (9.40)	-0.093 (0.038)	-0.0024 (0.0051)	3.90 (2.24)	0.038
	OX1	4.05 (3.51)	-0.070 (0.017)	-0.0001 (0.0023)	5.39 (1.23)	0.008
	RD	4.91 (4.25)	-0.051 (0.024)	0.0026 (0.0032)	6.19 (1.74)	0.012
	[0.93] OX2	3.38 (3.81)	-0.056 (0.020)	0.0022 (0.0027)	5.99 (1.47)	0.009

Table 3.16: Best-fit parameters for unconstrained fits of EXAFS spectra for several loadings of WO_x on hematite nanopowders (HNPs). WO_x coverage is given in units of percent weight loading and monolayer equivalents (MLE) as defined in the text. Parameters as defined in **Chapter 2** and in the text. Error values for each parameter are given in parentheses.

WO _x loading, % w/w [MLE]	Chemical state	E_0	ΔR	N	R-factor
0.29 [0.04]	AD	8.00 (2.54)	-0.040 (0.014)	5.49 (0.45)	0.012
	Ox1	7.72 (2.53)	-0.033 (0.014)	5.70 (0.47)	0.012
2.43 [0.36]	AD	1.32 (2.93)	-0.073 (0.014)	5.46 (0.44)	0.011
	OX1	2.69 (4.48)	-0.059 (0.023)	4.93 (0.64)	0.027
	RD	3.10 (5.23)	-0.050 (0.027)	4.73 (0.72)	0.037
	OX2	2.53 (4.56)	-0.058 (0.023)	4.95 (0.65)	0.028
2.69 [0.40]	AD	-1.71 (2.61)	-0.086 (0.012)	5.53 (0.38)	0.007
	OX1	1.03 (3.20)	-0.071 (0.016)	5.36 (0.47)	0.013
3.40 [0.51]	AD	-2.12 (6.64)	-0.090 (0.031)	5.21 (0.89)	0.045
	OX1	4.29 (2.17)	-0.062 (0.011)	5.81 (0.37)	0.007
	OX2	3.11 (5.35)	-0.052 (0.028)	5.04 (0.78)	0.039
6.19 [0.93]	AD	-2.58 (7.49)	-0.093 (0.035)	5.37 (1.03)	0.055
	OX1	3.81 (2.59)	-0.069 (0.013)	5.91 (0.45)	0.009
	RD	5.11 (3.14)	-0.053 (0.017)	5.46 (0.52)	0.015
	OX2	3.60 (2.75)	-0.057 (0.014)	5.43 (0.44)	0.011

Table 3.17: Best-fit parameters for constrained fits ($\sigma^2 = 0.001$) of EXAFS spectra for several loadings of WO_x on hematite nanopowders (HNPs). WO_x coverage is given in units of percent weight loading and monolayer equivalents (MLE) as defined in the text. Parameters as defined in **Chapter 2** and in the text. Error values for each parameter are given in parentheses.

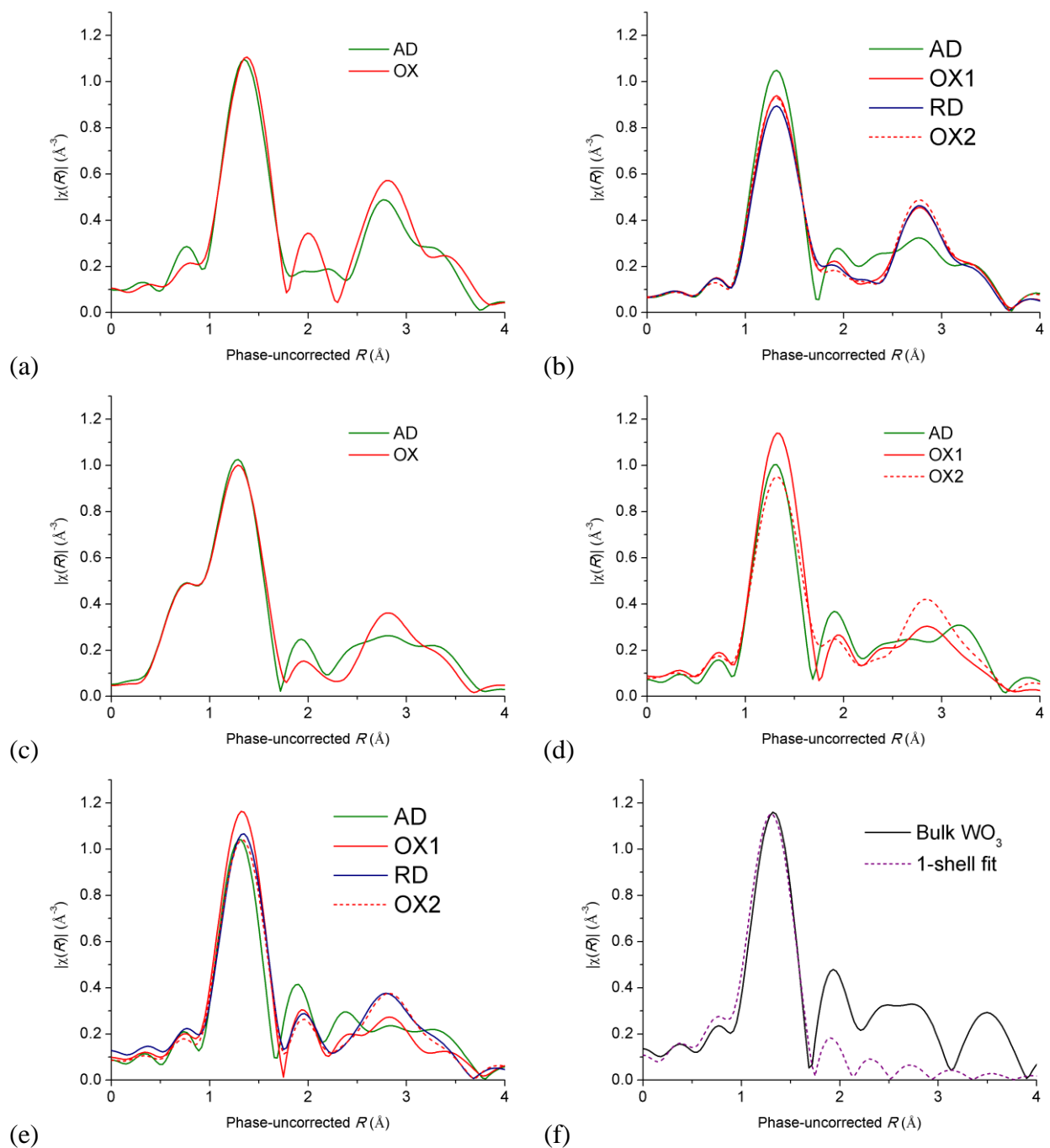


Figure 3.19: Phase-uncorrected W radial distribution functions (RDFs) derived from EXAFS scans for samples with different WO_x loadings (% w/w): (a) 0.29, (b) 2.43, (c) 2.69, (d) 3.40, (e) 6.19, and (f) bulk WO_3 powder (including a 1-shell fit). RDFs are calculated from an inverse Fourier transform of $k^2\chi(k)$ over the range $2.5 \text{ \AA}^{-1} \leq k \leq 10.2 \text{ \AA}^{-1}$ within a Hanning window.

We provide further analysis for the sample with 2.43% w/w WO_x coverage, which has approximately the same WO_x coverage as the hematite single crystal investigated by XSW[66]. XANES scans for this sample are shown along with data for bulk WO_2 and WO_3 in **Figure 3.20(a)**. The white lines of the dispersed WO_x phase are sharper than those measured for bulk WO_2 and WO_3 , suggesting a stronger localization of the $5d$ states in the dispersed material relative to bulk WO_3 . The position of the absorption edge can be determined by the maximum of the derivative of the X-ray absorption coefficient $\mu(E)$, which is shown in **Figure 3.20(b)**. The absorption edge of the dispersed WO_x is at the same energy as WO_3 , confirming an assignment of the W^{6+} oxidation state in accordance with XPS. There is no discernible absorption edge shift through the redox cycle, indicating that the “reduction” step does not actually change the oxidation state of W for this sample.

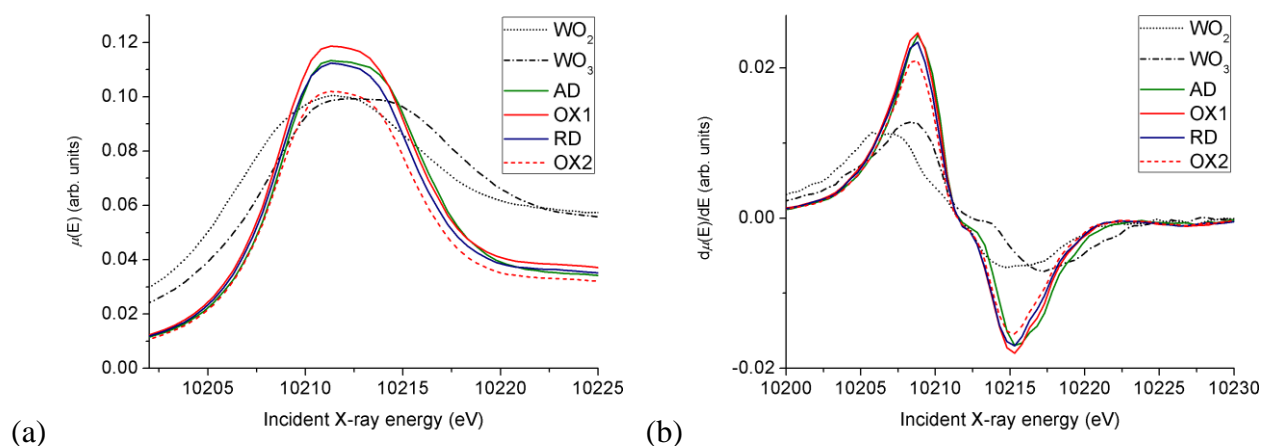


Figure 3.20: (a) XANES spectra for the four reported states of the sample with 2.43% w/w WO_x coverage. XANES for WO_3 and WO_2 powders are also shown. The derivatives of all spectra with respect to the incident beam energy are shown in (b).

3.3.3 Discussion

XAFS results for 0.3 ML W / α -Fe₂O₃[66] suggest that oxidized W takes on a local coordination structure very similar to that of bulk WO₃. We see similar results for W / α -Fe₂O₃ nanopowders (HNPs), since (1) the RDFs of the dispersed WO_x phase are similar to that of WO₃, and (2) the oxidation state of W is clearly W⁶⁺. As the W/HNP samples are annealed in nominally oxidizing and reducing conditions, an irreversible structural change occurs, as peaks corresponding to longer-range interactions appear in the RDFs. These longer-range features are qualitatively similar for samples with W coverages from 0.29 – 6.29% w/w (0.04 – 0.93 MLE) WO_x loading, although they are more pronounced at lower coverages. It is possible that these features correspond to W-Fe interactions, as the interaction distances (~3 Å) roughly correspond to W-Fe distances on the most oxidized W/ α -Fe₂O₃ surfaces (see **Table 3.3**) but are shorter than the first W-W interaction in bulk WO₃ (3.8 Å).

Analysis of the best-fit results in **Table 3.17** shows that in the as-deposited cases, the average first-shell W-O bond lengths are slightly shorter than their annealed counterparts. This is a somewhat surprising result: XPS shows that W is not completely oxidized to the 6+ state in the as-deposited condition, and oxidation would be expected to convert surface hydroxyl groups to shorter W=O bonds. Residual fluorine from the ALD precursor might contribute to the AD signal. The W-F bond length in WF₆ is almost exactly the same as that of the W-O path length used in the fits herein[181], but the phase shift for F may be different than for O, resulting in a contribution to the RDF at a slightly different distance.

Changes in the W-O coordination number occur with the reaction steps, but the nature of these changes depends strongly on the WO_x coverage. For the 0.29 and 2.69% w/w WO_x samples, there is barely any change in the first-shell coordination number upon oxidation, and the average bond length increases slightly. The 2.43% w/w WO_x sample, on the other hand, undergoes a drop in the average coordination number by about 0.5 bonds per W upon oxidation from the as-deposited state, resulting in the lowest coordination numbers measured in this study. The W-O coordination numbers of the two samples with the highest loading increase upon the first oxidation, but they drop back to close to their AD values upon reduction and re-oxidation. Overall, it is difficult to judge the annealing behavior of dispersed, sub-ML WO_x on hematite nanopowders based on this EXAFS analysis, as the changes in W-O coordination are complex and subtle. Combined with sintering of the HNPs (as shown by powder XRD), a complete description of the physical changes in this model catalyst system cannot be made by analysis of W-O interactions alone.

This study of HNP-supported WO_x is an attempt to bridge atomic-scale phenomena observed on single crystal surfaces[66, 126] to the properties of more realistic catalysts with complex structures. The most striking difference between these two approaches on the same material system is the reducibility of W^{6+} : on the single crystal, W^{6+} reduces to W^{5+} , whereas under similar conditions and with a similar coverage, W^{6+} on a nanopowder support does not reduce. Some possible reasons for these discrepancies are as follows:

1. The behavior of WO_x may depend on the termination of the substrate. While (0001) is a low-energy termination of hematite, the nanopowder surfaces are comprised of many other

terminations on which the reduction of W^{6+} might be less favored. Reduced states might be less stable on defect-rich nanopowder surfaces.

2. Due to the much higher surface area and tortuosity of the pressed nanopowder pellet, the reductant may not have reached the surfaces of the nanopowders as effectively as it would over a single crystal surface. Longer reaction times, different reactor designs, or a more concentrated reducing gas might have better facilitated the percolation of the reductant through the pellet.

3. Different reactors were used for single crystal and nanopowder experiments. In the beryllium dome mini-chamber used for single crystal studies, the thermocouple was attached to the side or surface of the sample using a metal sample retention clip. The temperature of the pressed nanopowder pellet was measured at the bottom of the ~1 mm thick pellet. Both reactors used K-type thermocouples which had been used in previous experiments. Since no unifying standard was used to calibrate each individual thermocouple, it is possible that temperature measurement was inaccurate.

4. It is possible that instead of remaining as a surface phase, WO_x could be incorporated into the hematite lattice. If this were the case, then W might be agnostic to oxidizing or reducing conditions at the HNP surface. In the bulk, $\alpha\text{-Fe}_2\text{O}_3$ and WO_3 combine to form Fe_2WO_6 [182], but W^{6+} does not appear to be miscible in the hematite lattice. However, it is conceivable that the geometric flexibility of the HNP surface could accommodate W cations in the near-surface lattice. This possibility could be addressed by further TEM studies.

3.4 Conclusions

Using DFT, various reduced and oxidized configurations of tungsten on the hematite (0001) surface have been explored, using both ground state band structure and localized-orbital W core-hole models. Adsorption of W on surfaces with compositions ranging from oxygen saturated to Fe terminated was considered, as were coadsorption with iron, oxygen, or hydroxyl groups. By comparing calculated relaxed structural and electronic data to experimental results, models are found to describe XSW data for nominally oxidized and reduced configurations. Experimental W $4f$ binding energy shifts which show reversible oxidation and reduction of W on the surface are quantitatively reproduced by Transition State cluster calculations. However, it was not possible to identify distinct "W⁵⁺" and "W⁶⁺" oxidation states in cluster models containing 3-, 4-, 5-, and 6-fold O-coordinated tungsten; rather, a continuous variation of net charge and core-level energies was observed. As found in many other theoretical studies, cation charges are calculated to be notably less than nominal oxidation-state values (Fe³⁺, W⁵⁺, W⁶⁺), whether defined by spherically-integrated Rws charges or by the zero-flux surface Bader approach. Bond valence sums provide an alternative view that takes into account the covalent interactions between metal cations and their ligands. The possible effects of Fe $3d$ correlation corrections on surface structures were considered using the GGA+ U approach. It was found that in some cases, re-ordering of site energies could occur; however, the small differences in stability in these cases, as well as a lack of established values of the parameter U for surface species, preclude any strong predictions from this approach.

The small crystal unit cells and molecular clusters used in this work prevent any study of larger scale phenomena such as surface reconstruction, metal agglomeration, coexistence of different W oxidation states, and raft/cluster formation. The use of such small surface cells may also result in

a "periodic image" effect caused by the lateral interaction between an atom and itself in a neighboring identical cell. To this end, larger supercells are used to study molecular adsorption on hematite-supported V, among other chemistries, in **Chapter 5**.

For comparison with experimental and theoretical results on single crystals, the structure and chemical behavior of $\text{WO}_x / \alpha\text{-Fe}_2\text{O}_3$ nanopowders was studied by *in situ* XAFS and other methods. TEM confirmed that as deposited by ALD, WO_x was conformal with the surface of the nanopowders. Subtle changes occurred in the local structure of WO_x through a series of treatments in O_2 and dilute H_2 , but redox-reversible chemical changes were not observed. Instead, each treatment step appeared to anneal the WO_x phase toward a final state which was similar for all WO_x coverages studied. Comparison of radial distribution functions for annealed states with different WO_x coverages suggests that the annealed structure might feature W-O-Fe interactions. As opposed to the single crystal results, XPS and XANES measurements showed no reduction of nanopowder-supported W^{6+} . These differences may be symptomatic of the design of the experiment and may serve to inform future experiments with the goal of bridging the "materials gap" between single crystal surfaces and real catalysts.

4. V-W Interactions on the α -Al₂O₃ (0001) Surface

In this chapter, I discuss the interaction of tungsten and vanadium with a non-reducible, ionic support: the non-polar α -Al₂O₃ (sapphire) (0001) surface. Through structural (XSW, AFM) and chemical (XPS) studies combined with theoretical calculations (DFT), we develop models of near-monolayer V and W as well as V-W mixed cases. While W was shown in the previous chapter (as well as previously published work[66]) to be reducible on the α -Fe₂O₃ (0001) surface, it does not appear to reduce on less reducible oxide substrates such as α -TiO₂ (110)[32, 36]. We show that, as expected, W is not easily reducible on α -Al₂O₃, but it does reduce in the presence of V. We also observe a redox-reversible structural shift in V, from an incoherent V⁵⁺-containing phase to a V⁴⁺ phase which is coherent with the substrate lattice. DFT calculations reveal V-W interactions that could contribute to the improved catalytic activity. Overall, I aim to inform the study of oxide-supported catalysts by contributing precise models, informed by experimental evidence, of their interface structures and chemical relationships.

4.1 Introduction: V and W in heterogeneous catalysis

Oxide-supported vanadium species are among the most versatile catalysts[16]. They are widely used for selective oxidation reactions and for the selective catalytic reduction of environmentally harmful nitric oxides with ammonia (NO-SCR)[14, 17]. The choice of substrate can affect the local structure and distribution of V species, which has important implications for the catalytic properties[16, 24, 183-187].

Our understanding of vanadium catalysis comes from our knowledge of the active site of the catalyst, which can be characterized to some degree by spectroscopic methods[20, 184]. While

spectroscopy can provide an idea of the interaction of V and its ligands, it is not always easy to unequivocally link a spectroscopic feature with a particular structure. One example of this is a Raman band near $900 - 940 \text{ cm}^{-1}$, which has been reported to correspond to V-O-V[188], V-O-substrate[22, 184, 189], or peroxo[190, 191] structures. While novel deposition methods can be used to isolate V species in known coordination environments for study[186, 192], this debate suggests the need for experimental methods that can accurately identify the position of catalyst surface species (and their ligands) relative to the support.

Oxide-supported tungsten is also a very useful catalyst, providing Brønsted acid sites for a variety of industrially relevant reactions[132, 193-196]. The mechanism of Brønsted acidity is thought to involve a transient reduction from W^{6+} to a state that can be thought of as $W^{(6-\delta)+}$ upon exposure to a reductant[194, 195]. This transient state is attributed to the appearance of a *d-d* transition state near the Fermi energy. However, there is little evidence of low-coverage W (supported on relatively non-reducible substrates, namely Al_2O_3 and TiO_2) reducing from a nominal 6+ oxidation state except at >1 ML coverages or under severe reducing conditions[32, 171, 197, 198].

When V and W are combined, there is a synergistic effect that improves catalyst performance for NO-SCR[28-31] and other reactions[199, 200]. As a lone catalyst, V has been proposed to play two roles in this reaction: it provides Brønsted acid sites for NH_3 adsorption, which subsequently activate nearby redox sites for NO adsorption and N-N interaction[17]. The promotional effect of W could therefore relate to its Brønsted acidity, and indeed the addition of a small amount of W to a V-loaded catalyst drastically increases the number of available Brønsted acid sites[29, 30, 199]. W serves a structural role as well, forming mixed oxide layers with V and preventing the aggregation of VO_x species into less reactive nanoparticles[31, 36, 200].

In previous work by our group on VO_x and WO_x on oxide single crystal supports, it was observed that the structural and chemical behavior of the catalysts clearly depends on their coverage (measured in monolayer equivalents, ML) and the support material. For example, 2 ML VO_x on $\alpha\text{-TiO}_2$ (110) was observed to undergo a redox-reversible structural transition from V_2O_5 , which is incoherent with the rutile substrate lattice, to rutile VO_2 [33]. Sub-ML $\text{VO}_x / \alpha\text{-TiO}_2$ (110), however, only partially reduced to V^{3+} under similar chemical conditions as the 2 ML study, forming a more complex surface structure which was validated by density functional theory (DFT)[34]. Sub-ML[32] and ML[36] $\text{WO}_x / \alpha\text{-TiO}_2$ (110) did not reduce at all from W^{6+} . Redox-reversible structural shifts were observed for 0.5 ML $\text{VO}_x / \alpha\text{-Fe}_2\text{O}_3$ (0001), although the reduction of V^{5+} to V^{3+} occurred concurrently with a slight reduction of the surface Fe species from Fe^{3+} to Fe^{2+} [131]. Sub-ML $\text{WO}_x / \alpha\text{-Fe}_2\text{O}_3$ (0001) could be reduced from W^{6+} to W^{5+} with accompanying structural shifts under relatively mild conditions[66, 126]. In recent work on mixed V-W ultrathin films supported on TiO_2 , we have observed that V enables the reduction of W^{6+} to W^{5+} and W^{4+} under similar conditions (400 °C in flowing dilute H_2)[36]. These observations of W^{6+} reduction in the presence of more reducible cationic species (V^{5+} , Fe^{3+}) suggest that W could also play a redox role in some reactions, in addition to its role as a dispersant and Brønsted acid site. In light of this, we approach the chemical physics of W, V, and the promotional effect of W on V using the tools of surface and interface science.

4.2 Methods

Single-side epi-polished $\alpha\text{-Al}_2\text{O}_3$ (0001) wafers from Rubicon Technologies (miscut angle $\sim 0.2^\circ$), provided by J. Ciraldo, were cleaved into 10 mm x 10 mm x 1 mm substrates. The substrates were sonicated in acetone, then methanol, and finally rinsed in ultrapure (18 M Ω cm) DI water before

drying under a compressed air jet. They were then annealed in a tube furnace for 4 hours at 1200 °C in flowing dry air[201]. Atomic force microscopy (AFM) measurements taken after annealing showed smooth surfaces ($<2 \text{ \AA}$ RMS roughness) with ~50-100 nm wide terraces separated by single- or few-step edges.

V ALD was carried out by T. Drake in Prof. P. Stair's group. Thin films of vanadia were deposited onto the $\alpha\text{-Al}_2\text{O}_3$ crystals using a viscous flow ALD reactor[202] maintained at 1 torr under vacuum by flowing 200 sccm of N_2 . The surface of the crystals was cleaned *in situ* at 100°C by flowing ozone at a rate of 200 sccm for 10 minutes. Vanadium oxytriisopropoxide (VOTP, Sigma Aldrich) and Millipore water were then alternately dosed into the reactor[203]. Each dose was separated by purges of N_2 to prevent gas phase reactions between the precursors. The dose and purge length was 30 seconds per step (2 minutes per ALD cycle). To ensure sufficient VOTP pressure in the vapor phase, the vessel containing the VOTP was heated to 45°C. To prevent condensation, the line leading from the VOTP vessel to the reactor was heated to 100°C.

W deposition was performed by Dr. J. Elam at Argonne National Laboratory. Substrates were loaded into an ALD reactor at 200 °C, which was pumped to 1 Torr and then purged with ultra high purity (UHP) N_2 for 20 minutes at 400 sccm. The sample surface was subsequently exposed to Si_2H_6 and WF_6 [102] with N_2 purges after each exposure for 30 – 100 sec. Details for W ALD are given in **Table 5.2**. For the mixed V-W samples, W was deposited first at Argonne National Laboratory, then oxidized and transferred to Northwestern University for V deposition.

Catalyst coverage after ALD was measured by X-ray fluorescence (XRF) on two different instruments in the J.B. Cohen X-ray Diffraction Facility at Northwestern University. XRF spectra were collected using a Vortex Si-drift diode detector. The coverage C of an element of interest

(typically measured in atoms nm⁻²) is calculated by measuring the integrated intensity I_F of its associated XRF peak and by comparison to a measurement of a calibrated standard of known coverage C_{std} , as follows:

$$C = C_{std} \frac{I_F}{I_{Fstd}} \frac{XC_{std}}{XC} \frac{DE_{std}}{DE} \frac{LTF_{std}}{LTF} \quad (4.1)$$

Here, DE is the detector efficiency, i.e. the fractional absorption of the fluorescence photons by the 350 μm thick Si element in the detector. XC is the XRF emission cross-section, which is calculated using XRF-XSECT software[204]. LTF is the live-time fraction, or the fraction of time for which the detector is actively analyzing incoming photons. While the calculation of LTF depends on the detector and its signal processing hardware and software, it is usually dominated by the ratio of the output count rate to the input count rate ($\frac{OCR}{ICR}$). In the XRF calibration equation, geometrical effects are neglected; the geometry should be kept exactly the same for the measured sample and the calibrated standard.

For V coverage, a monochromated Cu $K\alpha$ source ($h\nu = 8.04$ keV) was used to excite V K fluorescence (V K edge: 5.47 keV). For W coverage, a monochromated Mo $K\alpha$ source ($h\nu = 17.44$ keV) was used to excite W L fluorescence (W L₁ edge: 12.10 keV; W L₂: 11.54 keV; W L₃: 10.21 keV). V $K\alpha$ ($h\nu = 4.95$ keV) and W L β_1 ($h\nu = 9.67$ keV) peaks were used for the coverage measurement. For calibration, Ba and As ion-implanted standard samples (8.6 Ba nm⁻² and 32 As nm⁻², as measured by Rutherford backscattering) were used, owing to their similar fluorescence energies to those of V and W (Ba L β_1 $h\nu = 4.83$ keV; As $K\alpha$ $h\nu = 10.53$ keV). Fluorescence peaks were fitted with a Gaussian profile, and XRF emission cross-sections were calculated using XRF-XSECT software[204].

X-ray photoelectron (XP) spectra were taken on a Thermo Scientific ESCALAB 250Xi instrument with a monochromated AlK α beam ($h\nu = 1.49$ keV). A pass energy of 20 eV was used for fine scans of the peaks of interest. Charge compensation via an electron beam and low-energy Ar⁺ beam (the “Charge Compensation Standard” setting in the instrument software user interface) was employed. Peaks were fit using Thermo Scientific Avantage software using a Gaussian-Lorentzian mixed peak shape.

The nanoscale surface morphology of the samples was recorded using a Bruker ICON atomic force microscope (AFM) operated in tapping mode using Si cantilever tips. Images were processed using flattening and/or plane-fit algorithms as implemented in NanoScope software. Some images were Fourier filtered to remove periodic oscillations due to noise; however, this also reduced the sharpness of the images.

The X-ray standing wave (XSW) technique[32, 66, 73, 74, 205] was used to probe the statistically averaged interfacial structure of V and W on α -Al₂O₃ (0001). This method was described in **Chapter 2**, but we reiterate that by simultaneously monitoring the X-ray Bragg reflectivity $R_H(\theta)$ from a single crystal and normalized XRF yield $Y_H(\theta)$ of a selected surface species (i.e. V or W) as the angle θ between the crystal and the incident is changed, the coherent fraction (f_H) and position (P_H) of that selected surface species with respect to the $H = hkl$ substrate diffraction planes may be determined from the following equation:

$$Y_H = 1 + R_H + 2\sqrt{R_H}f_H\cos(\varphi_H - 2\pi P_H) \quad (4.2)$$

XSW data can be measured at several different hkl crystal reflections to obtain a more precise measurement of the atomic position or to identify multiple occupation sites.

XSW measurements at the α -Al₂O₃ (006) Bragg reflection were carried out at the 5-ID-C and 33-ID-D undulator beamlines at the Advanced Photon Source at Argonne National Laboratory. The experimental setup at 5-ID-C is described in Ref. [206] and depicted in **Figure 4.1**. Samples were kept in a beryllium dome mini-chamber which enabled treatment at high temperatures in a controlled gas environment. A 7.00 or 13.00 keV beam was selected with a liquid nitrogen-cooled Si(111) double-crystal monochromator and further conditioned using two Si(220) channel-cut monochromator crystals. The second crystal was detuned to 30% of its maximum output intensity, causing a ~70% reduction in the angular width of the emitted beam[81]. The technical goal of this optical setup is to provide a very high fringe visibility for the XSW field in the sample crystal by making the angular width of the incident beam small compared to the angular width of the sample reflection. The Si(220) monochromator reflection ($d_{\text{Si}(220)} = 1.92 \text{ \AA}$) was chosen because of the close match in d -spacing with the α -Al₂O₃ (006) reflection ($d_{\text{Al}_2\text{O}_3(006)} = 2.17 \text{ \AA}$), reducing wavelength dispersive effects. A beam size of ~1 mm x ~1 mm was used. Crystal reflectivity was measured using an Oxford CyberStar NaI scintillation detector. X-ray fluorescence was measured using a Vortex-EX or Vortex-EM Si drift detector. The peak shaping window of the XIA signal processing electronics was set to 4.00 μs to optimize the energy resolution; for reference, the full width at half maximum (FWHM) of the Fe K α peak was 125 eV. At the geometry used for XSW studies of the α -Al₂O₃ (006) reflection, the Vortex detector dead time was less than 5% and was not a significant factor in XSW analysis. Further details about XSW measurements on sapphire single crystals are provided in **Appendix B**. The collection of XSW data was aided by G.P. Campbell, L. Zeng, S. Kewalramani, and Z. Feng, with beamline support from D.T. Keane and Z. Zhang.

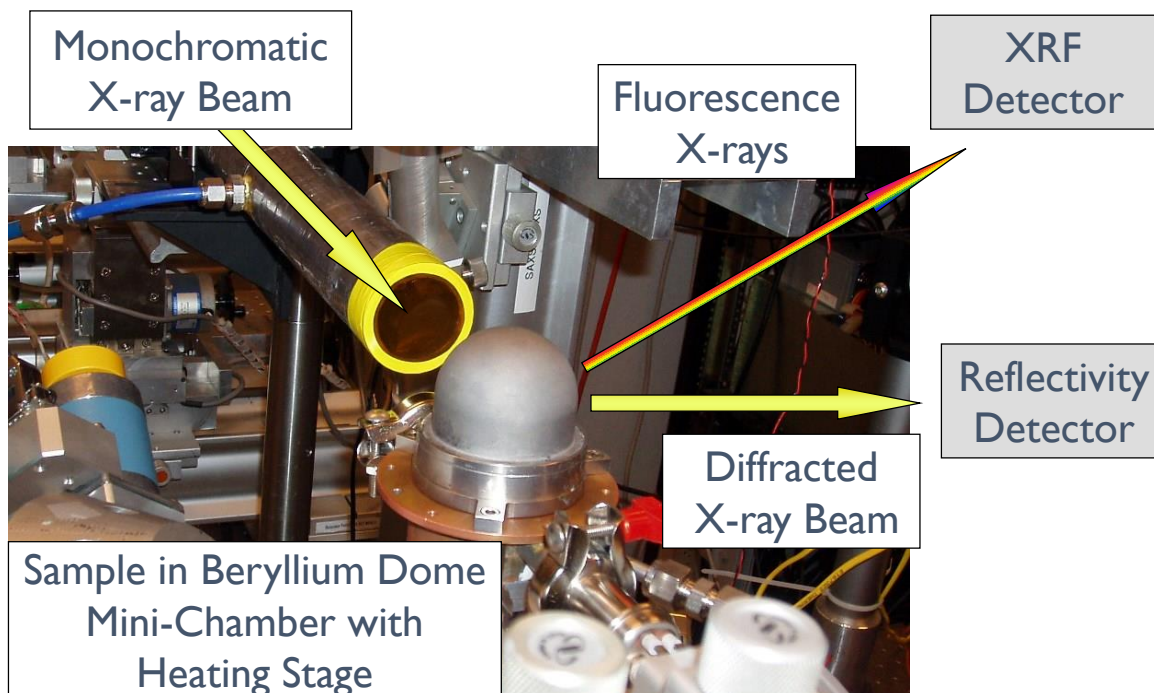


Figure 4.1: Perspective view of the Be dome mini-chamber mounted on the kappa-geometry diffractometer at APS beamline 5-ID-C. The X-ray detection scheme is shown schematically.

Slab-model DFT calculations were carried out using VASP code[108-111] with generalized gradient approximation (GGA) exchange-correlation corrections implemented in PW91 functionals[113] using a projector augmented wave (PAW) pseudopotential method[112]. The plane-wave cutoff energy was typically 400 eV. k -point meshes were generated by the method of Monkhorst and Pack[115]. The monoclinic ($\gamma = 120^\circ$) α -Al₂O₃ 1x1 supercell lattice parameters were fixed at $a = b = 4.784 \text{ \AA}$, $c = 25 \text{ \AA}$. a and b were derived from a relaxed bulk α -Al₂O₃ unit cell with an elevated cutoff energy of 500 eV (see **Appendix A**), which has an Al BVS of 3.01 (see **Table 2.2**). The the c parameter provides over 10 \AA of vacuum separation between slab atoms.

The clean 20-atom α -Al₂O₃ (0001) supercell, shown in **Figure 4.2**, consists of 4 Al₂O₃ layers with the bottom layer fixed to enforce bulk-like boundary conditions. This supercell was validated by

comparison to previously published experimental[52] and theoretical[65] results, summarized in **Table 4.1**. The surface interlayer relaxation is quantified as the percent change in the spacing between surface layers; the bulk interlayer spacings are given in the right-most column of **Table 4.1**. As shown in **Figure 4.2(b)**, the O layers are labeled O_s and O_{s-1} for the surface and first sub-surface O layers, respectively. Similarly, the terminal Al is labeled Al_t , and below the O_s layer are two Al atoms, Al_{Cs} and Al_{Bs} , named for the surface site under which they sit. Al_{As-1} is directly below the O_{s-1} layer and laterally sits under the surface A site. While the degree of relaxation differs between our work and previous reports, we note that the interlayer relaxations are qualitatively similar: Al_t relaxes significantly into the O_s layer, and Al_{Cs} and Al_{Bs} move closer together. X-ray scattering data[52] suggests that this singly Al-terminated surface is the most stable α - Al_2O_3 (0001) surface termination in vacuum. (It is not generally true that Al will always occupy the A site; under humid conditions, for example, α - Al_2O_3 (0001) has been shown to be O-terminated, with water molecules compensating the surface polarity[53].)

Three symmetry-inequivalent surface cation sites, labeled A, B, and C, are of interest in our work on α - Al_2O_3 (0001) and in comparable studies on α - Fe_2O_3 [33, 66, 126, 129-131, 207]. These sites are shown in **Figure 4.2**. The A and B sites represent the two occupied cation sites if the O-terminated corundum-type lattice were to continue into the vacuum. The C site sits where the hollow site would be in a bulk-like cation layer. These symmetry-inequivalent surface sites have been shown to have different adsorption energies and chemical behavior for metal atoms[45, 126].

	This work	Theory[65]	Experiment[52]	Bulk spacing (\AA)
$\text{Al}_t - \text{O}_s$	-84.8	-77	-51	0.79
$\text{O}_s - \text{Al}_{Cs}$	6.7	10.6	16	0.79
$\text{Al}_{Cs} - \text{Al}_{Bs}$	-47.7	-34.3	-29	0.57
$\text{Al}_{Bs} - \text{O}_{s-1}$	20.3	18.5	20	0.79
$\text{O}_{s-1} - \text{Al}_{As-1}$	3.3	1	--	0.79

Table 4.1: Comparison of percent interlayer relaxations between the $\alpha\text{-Al}_2\text{O}_3$ (0001) supercell used in this work and previously published experimental and theoretical data. The values are defined as the percent differences between the calculated and bulk interlayer values.

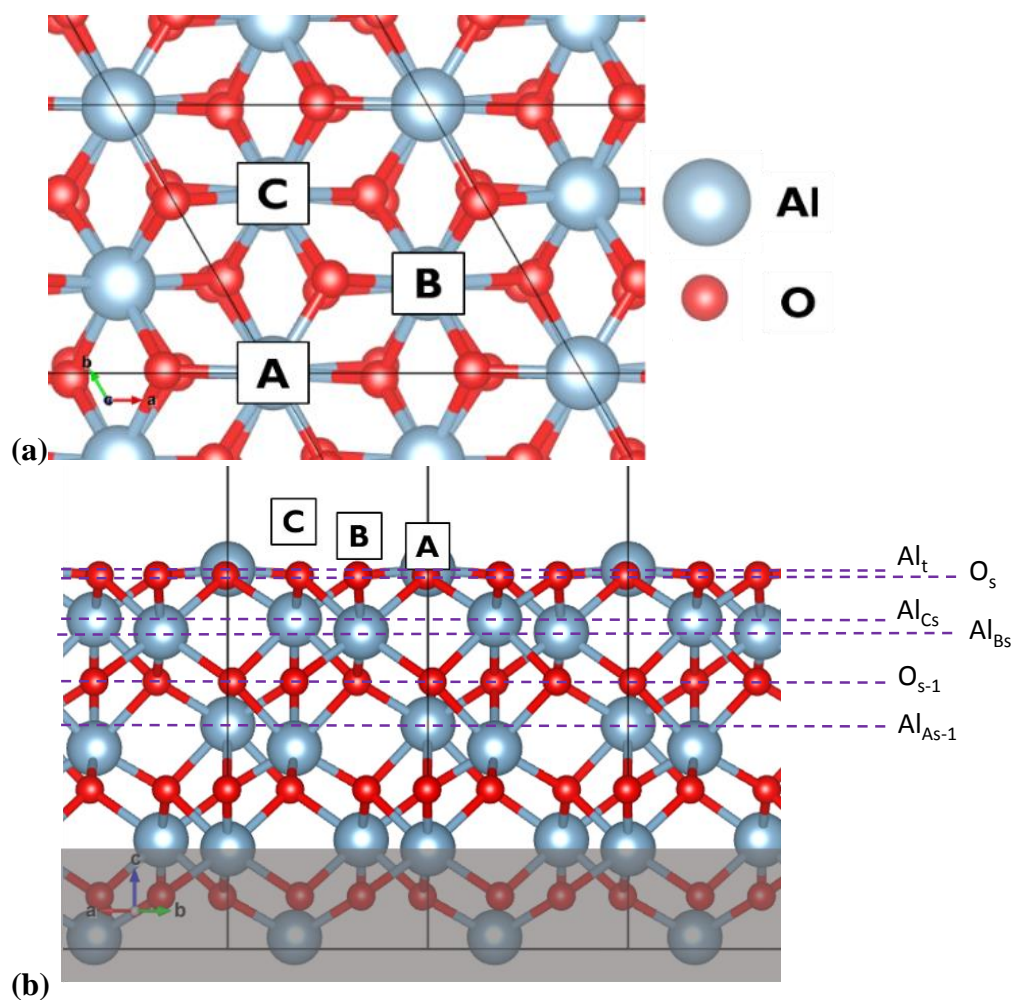


Figure 4.2: (a) Top (0 0 0 1) and (b) side (1 1 -2 0) views of the relaxed Al-terminated $\alpha\text{-Al}_2\text{O}_3$ surface supercell. Black lines indicate the divisions between periodic cells. The positions of the surface cation sites A, B, and C are shown. The bottom Al_2O_3 layer of the slab (shown darkened in the side view) is fixed to impose bulk-like boundary conditions.

(V,W) / α -Al₂O₃ (0001) surface structures are simulated by decorating the surface of the above slab with V, W, and coordination environments including O and OH ligands. Atomic charges are reported by two methods, which were discussed in **Chapter 2**: Bader charge partitioning[116] and bond valence sums (BVS)[119]. These views of atomic charge are complementary: bond valences provide a more accurate estimate of the formal charge, while the Bader value suggests the degree of covalency in the metal-ligand bond.

4.3 Results

4.3.1 Experiment

4.3.1.1 Sample preparation and morphology: ALD, AFM

Four samples were produced by ALD and studied, with coverages calibrated by XRF. For the α -Al₂O₃ (0001) surface, 1 ML is the coverage with both surface cation positions filled, or 10.1 atoms nm⁻². The coverage of all samples, as well as the number of ALD cycles used, is outlined in **Table 4.2**. The number of ALD cycles required for V and W deposition is relatively high, especially for V deposition; this is likely due to the difficulty of nucleating growth on the clean and relatively inert sapphire surface. Interestingly, the W coverage is not monotonic with the number of deposition cycles. For VW2, the time of W deposition was extended to allow for a more complete nucleation. The resulting V:W ratios for VW1 and VW2 are 1.17 and 1.91, respectively.

Sample	MV	MW	VW1	VW2
Number of V cycles	16	--	16	16
V nm ⁻²	9.18 [0.91 ML]	--	9.06 [0.90 ML]	10.5 [1.04 ML]
Number of W cycles and details	--	4 (5 sec. 1.2 Torr Si ₂ H ₆ , 5 sec. 0.7 Torr WF ₆)	5 (5 sec. 1.25 Torr Si ₂ H ₆ , 5 sec. 0.5 Torr WF ₆)	3 (8 sec. 1.5 Torr Si ₂ H ₆ , 8 sec. 0.8 Torr WF ₆)
W nm ⁻²	--	9.18 [0.92 ML]	7.77 [0.77 ML]	5.50 [0.55 ML]

Table 4.2: Coverage of atomic layer deposited V and W on the four α -Al₂O₃ (0001) samples referred to in this work. ALD parameters varied for W deposition and are shown here. Coverages are reported in atoms×nm⁻² as well as monolayers (ML) in brackets.

AFM images for each sample are shown in **Figures 4.3, 4.4, 4.5, and 4.6**. In each of these images, the initial morphology of the clean α -Al₂O₃ (0001) crystal is shown. **Figure 4.4** shows the evolution of ALD W on the crystal surface. In the “as deposited” case for sample MW, W exists as particles only a few nanometers in size. After undergoing redox cycling (annealing in O₂ at 350 °C and dilute H₂ at 400 °C, described in more detail later in this work), W forms a very conformal film. Some larger nanoparticles – possibly left over from polishing or crystal cutting – remain on the sample surface and do not change substantially after processing. The V-only sample (Sample MV) has nanoparticles on the surface after the redox cycles, as shown in **Figure 4.3**. These particles do not appear to change in size or distribution after exposure to oxidizing or reducing environments. The mixed V-W films show a different morphology than either the V- or W-only samples. After several reaction cycles, ending with an oxidation in O₂ at 350 °C for 30 minutes, both VW1 (**Figure 4.5**) and VW2 (**Figure 4.6**) show two types of surface features: wide islands, about 1-2 nm high, and larger particles on the order of 20 nm high. After a final reduction in 5% H₂ (bal. N₂) at 400 °C, the larger and smaller particles both appear to increase in size. This is

especially visible for Sample VW2. AFM does not provide element sensitivity, so the composition of these different regions cannot be explicitly assigned from these images.

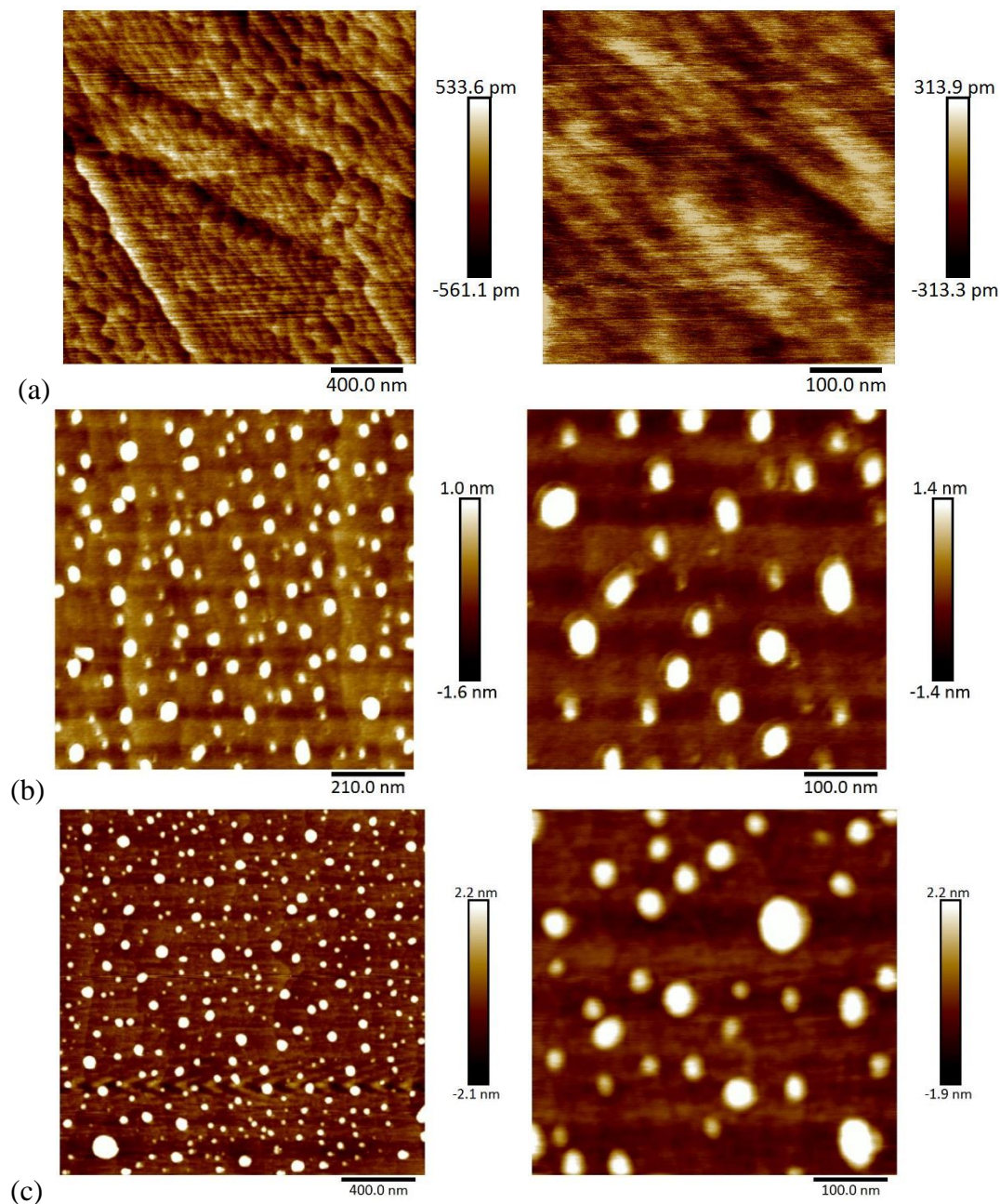


Figure 4.3: AFM images of sample MV (a) before V deposition ($2 \mu\text{m} \times 2 \mu\text{m}$, $500 \text{ nm} \times 500 \text{ nm}$); (b) after several redox cycles, ending with reduction ($1.05 \mu\text{m} \times 1.05 \mu\text{m}$, $500 \text{ nm} \times 500 \text{ nm}$); (c) after several redox cycles, rinsing in ultrapure DI water, and oxidation ($2 \mu\text{m} \times 2 \mu\text{m}$, $500 \text{ nm} \times 500 \text{ nm}$).

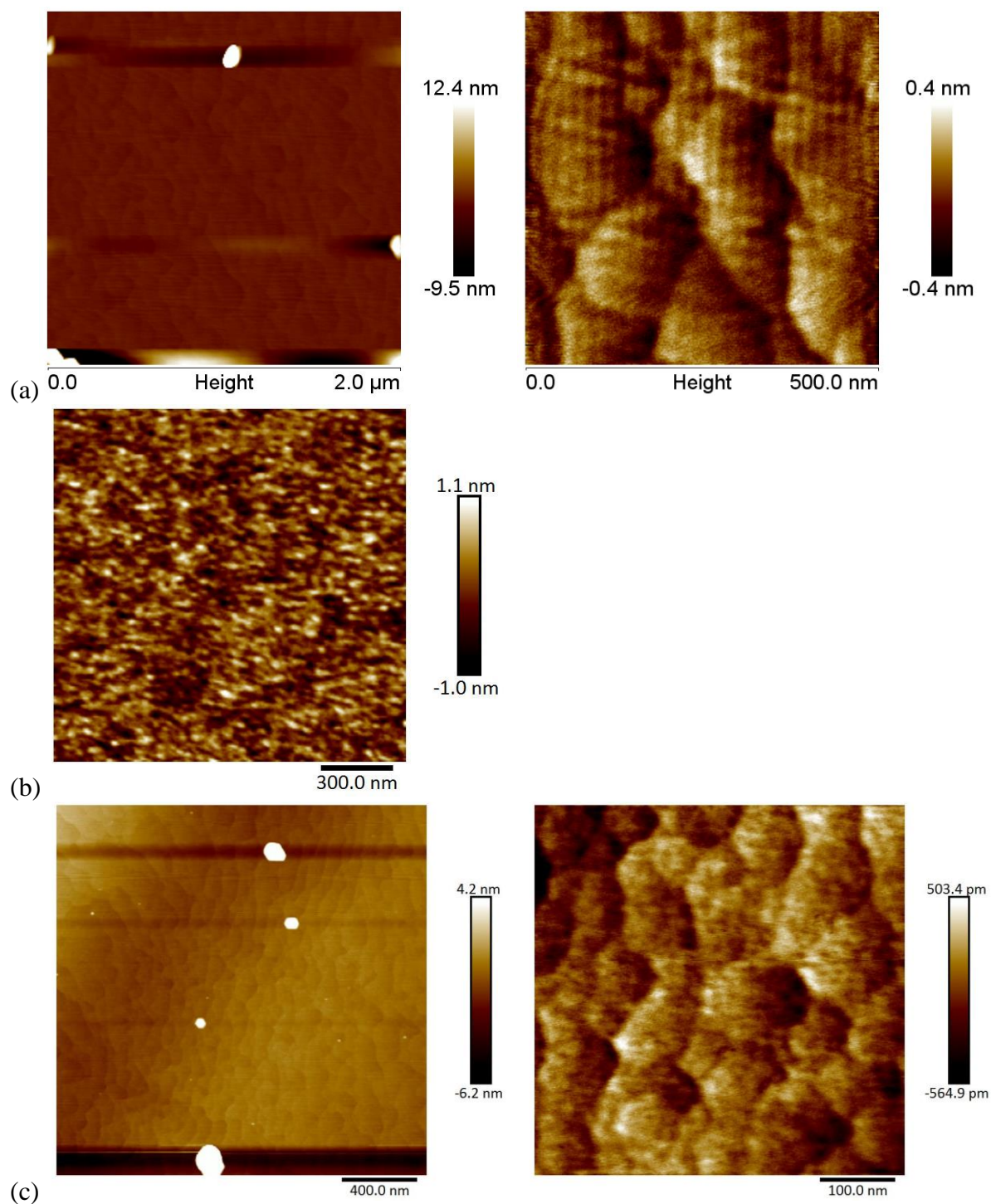


Figure 4.4: AFM images of sample MW (a) before W deposition ($2 \mu\text{m} \times 2 \mu\text{m}$, $500 \text{ nm} \times 500 \text{ nm}$); (b) after W deposition ($1.5 \mu\text{m} \times 1.5 \mu\text{m}$); (c) after several redox cycles, rinsing in ultrapure DI water, and oxidation ($2 \mu\text{m} \times 2 \mu\text{m}$, $500 \text{ nm} \times 500 \text{ nm}$).

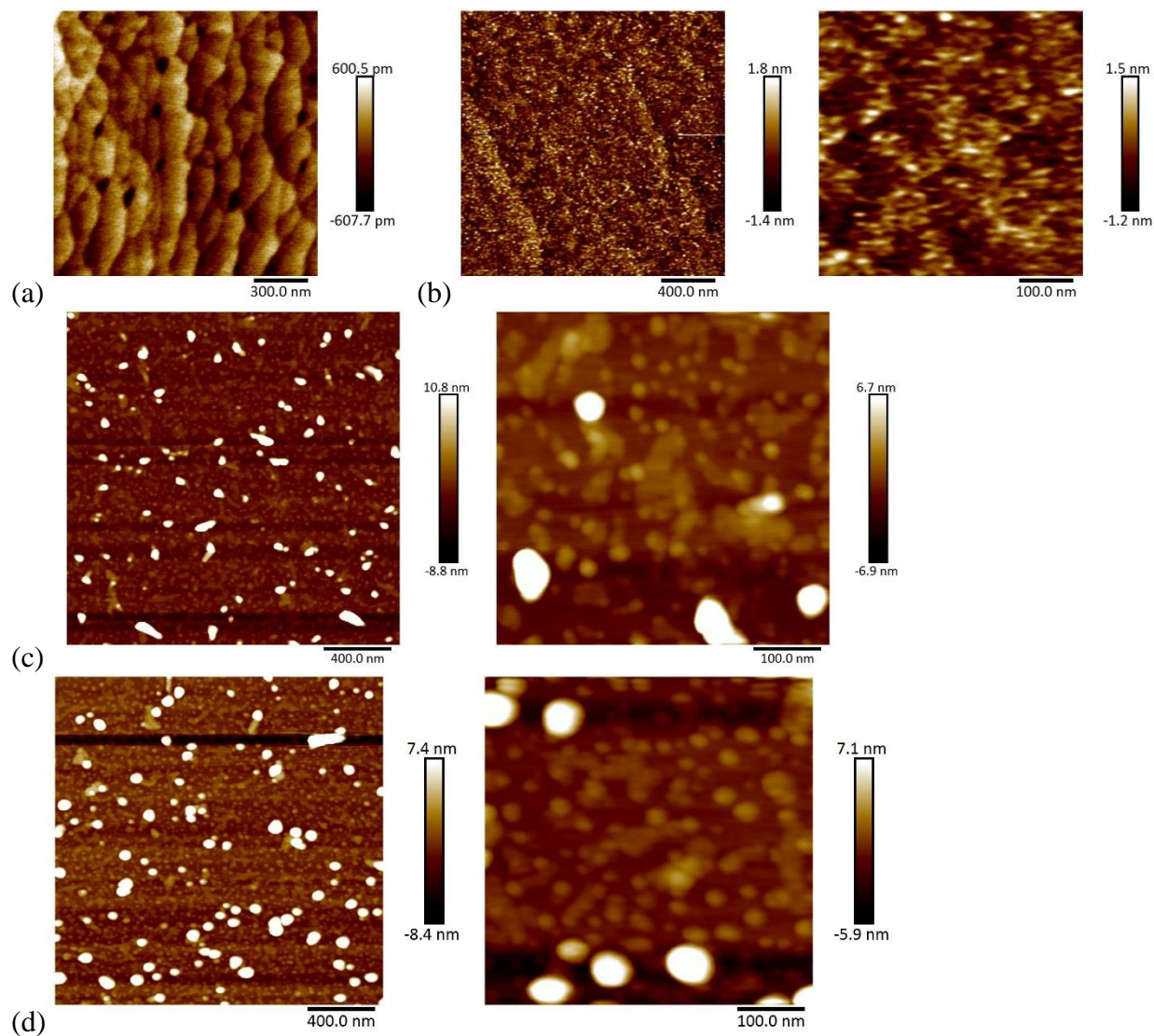


Figure 4.5: AFM images of sample VW1 (a) before W deposition ($1.5 \mu\text{m} \times 1.5 \mu\text{m}$); (b) after W deposition ($2 \mu\text{m} \times 2 \mu\text{m}$, $500 \text{ nm} \times 500 \text{ nm}$); (c) after several redox cycles, rinsing in ultrapure DI water, and oxidation ($2 \mu\text{m} \times 2 \mu\text{m}$, $500 \text{ nm} \times 500 \text{ nm}$) and (d) reduction ($2 \mu\text{m} \times 2 \mu\text{m}$, $500 \text{ nm} \times 500 \text{ nm}$).

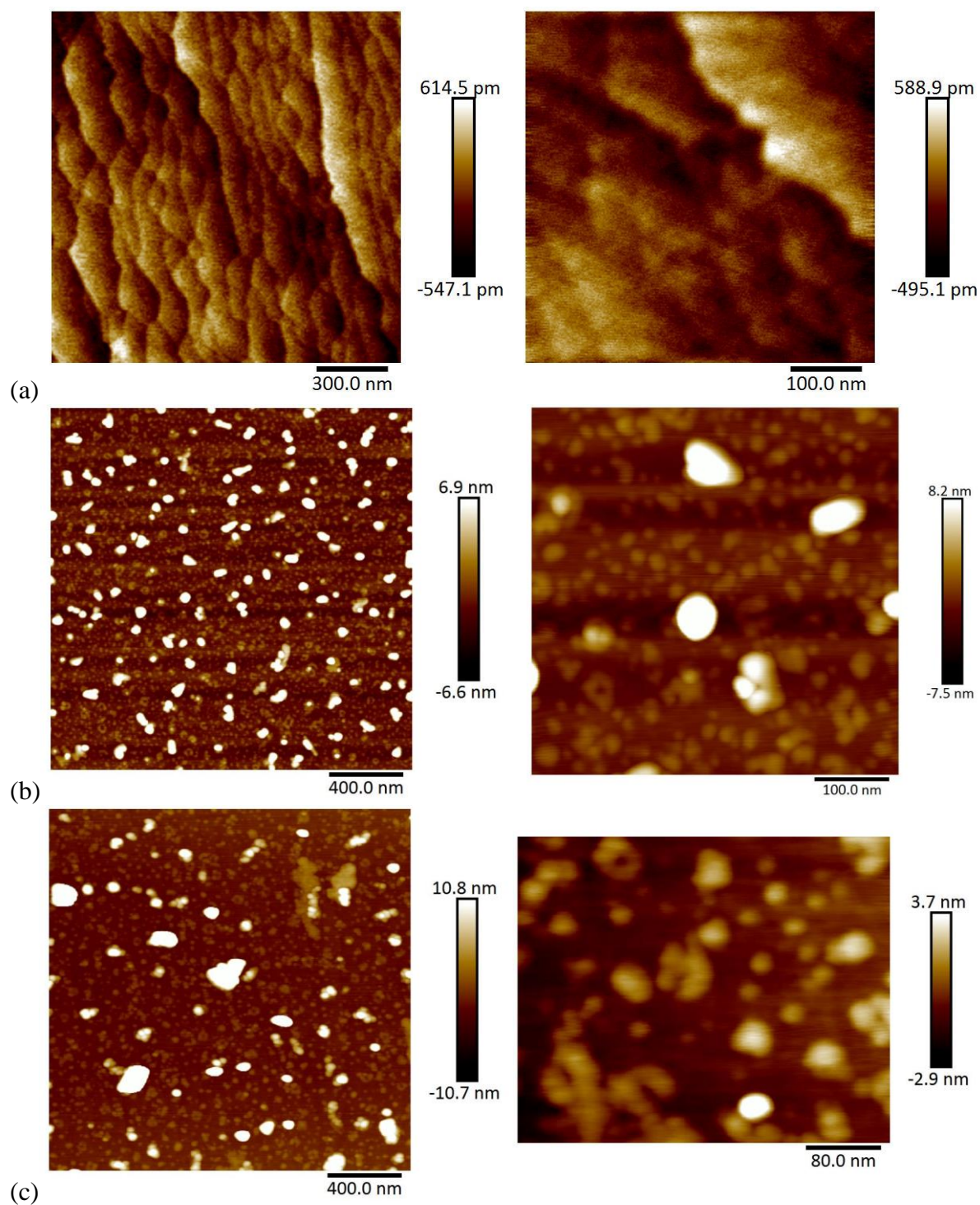


Figure 4.6: AFM images of sample VW2 (a) before W deposition ($1.5 \mu\text{m} \times 1.5 \mu\text{m}$); (b) after subsequent V deposition and several redox cycles, rinsing in ultrapure DI water, and oxidation ($2 \mu\text{m} \times 2 \mu\text{m}$, $500 \text{ nm} \times 500 \text{ nm}$) and (c) reduction ($2 \mu\text{m} \times 2 \mu\text{m}$, $400 \text{ nm} \times 350 \text{ nm}$).

4.3.1.2 Surface chemical characterization: XPS

In XPS survey spectra, shown in **Figure 4.7**, peaks were assigned to W, V, O, Al, and adventitious C as well as other impurities. Sample VW2 is notable for being contaminated with In, Zn, and Fe; this may be due to sample mishandling on equipment which was used for concurrent experiments. Some other contaminants, such as Na and K, were observed in small concentrations, even after repeated rinsing in ultrapure (18 MΩ cm) DI water. The O 1s peak dominates the spectrum and was truncated to make the other peaks more visible.

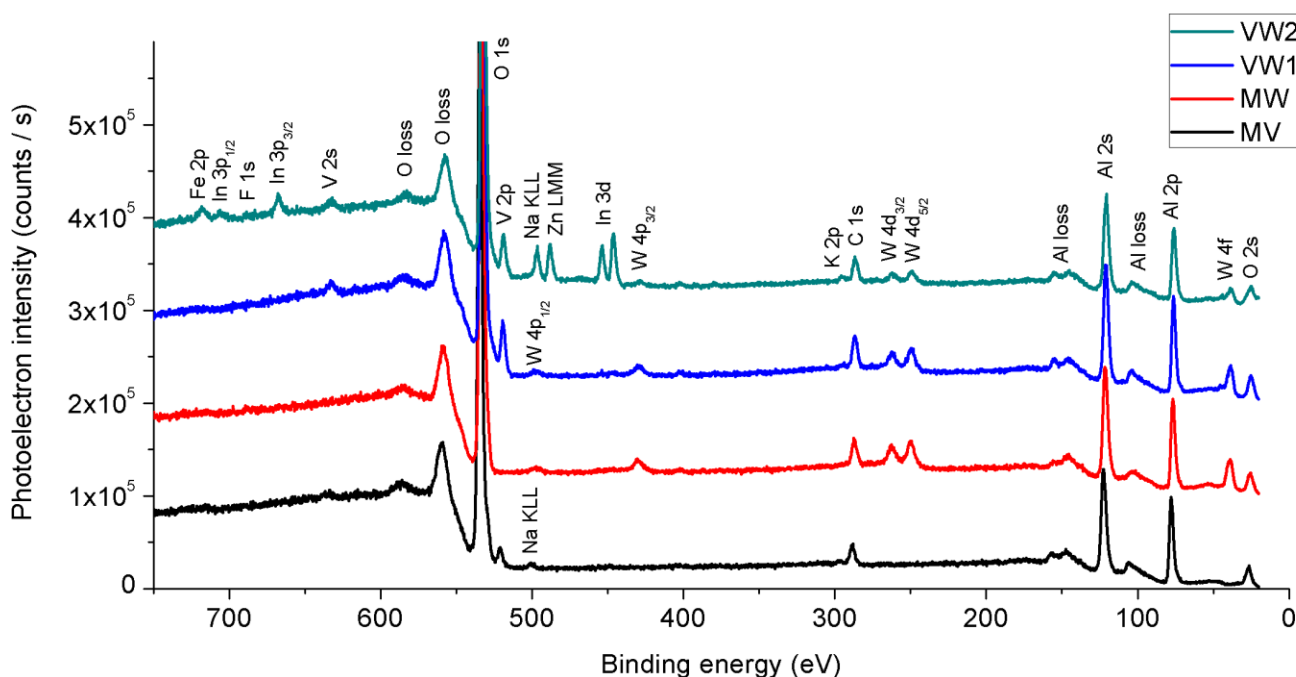


Figure 4.7: XPS survey scans for the four samples referred to in this chapter. The O 1s line is truncated to clarify the smaller peaks. Spectra are displaced along the y-axis for clarity.

Detailed scans of the V and W signals (as well as Al, O, C, and F) were conducted for the samples after exposures to oxidizing (**OX**, 350 °C in O₂) and reducing (**RD**, 400°C in 5% H₂ bal. N₂) conditions. These reactions took place in a quartz tube furnace with a gas flow rate of about 200

sccm. After the reactions, the samples were transported in air to the XPS system. The samples were exposed to air for no more than a few minutes.

For all four samples supported on α -Al₂O₃ (0001), significant surface charging effects were observed despite using simultaneous low energy Ar⁺ ion and electron flooding for charge compensation. These effects resulted in tails in the low-BE region of each peak in the XP spectrum. This may be due to lateral differential charging[208] caused by inadequate or inhomogeneous charge compensation, although reduction of the X-ray spot size from 500 μ m to the instrumental minimum of 200 μ m did not improve the spectra. All XPS peaks were therefore modeled using two Gaussian-Lorentzian peaks, one for the primary peak and a second to model the tail. These models were fit for a peak showing one chemical state, such as in a fully oxidized condition, and the same ratio of peak maximum intensities, widths, and energy offsets was used to fit for multiple chemical states in the reduced condition.

The formal oxidation state of W can be determined by analyzing the W 4f doublet: the W 4f_{7/2} BE for W⁶⁺, W⁵⁺, and W⁴⁺ are 35.5 – 35.6, 34.5 – 34.7, and 33.1 – 33.3 eV, respectively[32, 168, 198, 209]. Adventitious carbon, with a C 1s XP peak at 284.8 eV, is frequently used as a calibration standard to ensure an accurate absolute binding energy. However, the Al 2p peak of sapphire may be a more appropriate internal standard for calibration, with a binding energy of 74.7 eV[210], much closer to the range of W binding energies.

Similarly, the oxidation state of V can be determined by measuring the BE of the V 2p doublet. However, on an insulating substrate such as sapphire, it is helpful to use an internal standard to calibrate XP binding energies in order to overcome sample charging effects. O 1s is a convenient

internal standard, and so herein we consider the binding energy difference (BED) between the V $2p_{3/2}$ and O $1s$ peaks. The O $1s$ - V $2p_{3/2}$ BEDs for V^{5+} , V^{4+} , and V^{3+} are 12.8 – 12.9 eV, 13.8 – 14.35 eV, and 14.6 – 14.84 eV, respectively, from the O $1s$ peak at 530.1 eV in bulk vanadium oxides[211, 212] and on other oxide substrates[33-35, 131, 213]. For these films, which are only a few Å thick, the bulk sapphire O $1s$ signal, with a BE of 531.6 eV, may dominate the O $1s$ spectrum instead[210]. The O $1s$ – V $2p_{3/2}$ BEDs may therefore be somewhat larger than the values for bulk vanadium oxide. For V XPS, the V $2p_{3/2}$ and V $2p_{1/2}$ peaks do not necessarily have the same width and symmetry; additionally, overlap between the O $1s$ and V $2p_{1/2}$ states further complicates fitting[189, 214]. Thus, for V binding energy determination, only the V $2p_{3/2}$ peak was fit. The V $2p_{1/2}$ contribution was modeled in the full O $1s$ – V $2p$ spectrum by a broad Gaussian-Lorentzian peak. Due to sample charging effects, a detailed analysis of the O $1s$ peak is elusive.

O $1s$ – V $2p$ XPS results and fits for the V-containing samples are shown in **Figure 4.8**. In **Table 4.3**, the fitted binding energies of the peaks are given, as well as the fractional composition if two different binding energies were fit. After oxidation, the O $1s$ – V $2p_{3/2}$ BEDs are 13.1 – 13.3 eV, which is slightly larger than the expected value of 12.8 – 12.9 eV for V^{5+} in bulk vanadium oxide. Considering that the Al_2O_3 O $1s$ peak is at a somewhat higher binding energy than that of vanadium oxides, these signals are assigned to V^{5+} . In the reduced state, two-state fits reveal a significant fraction of V with a lower binding energy, centered at a BED value of 14.5 – 14.6 eV. Assuming the same BED shift from the expected bulk VO_x values for V^{5+} (about 0.3 – 0.4 eV), we assign the reduced fraction to V^{4+} .

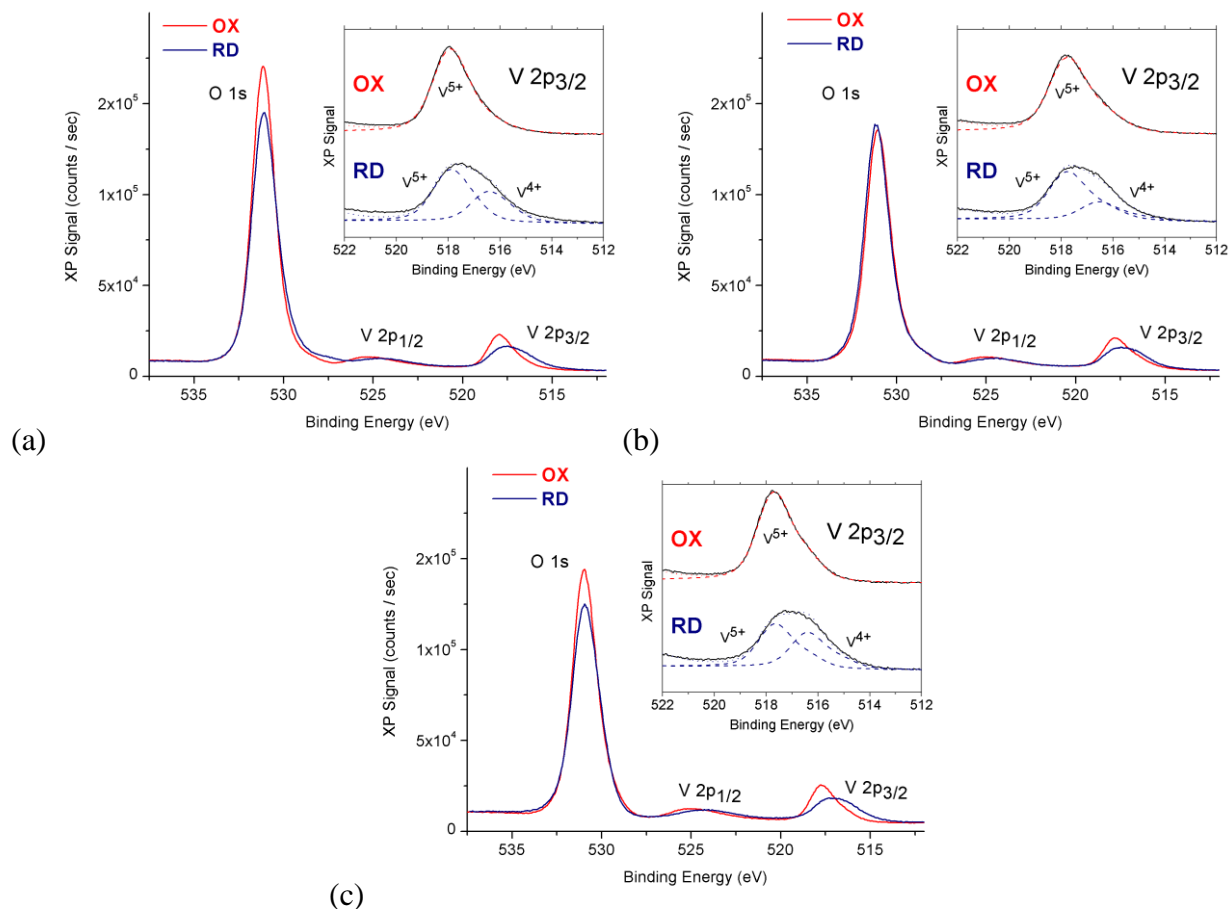


Figure 4.8: O 1s – V 2p XP spectra for samples (a) MV, (b) VW1, and (c) VW2. Fits for the V 2p_{3/2} peaks are shown as dashed lines in the insets for the oxidized (OX) and reduced (RD) surfaces.

	MV	VW1	VW2
OX	13.13 (100%)	13.27 (100%)	13.26 (100%)
RD	13.13 (63%)	13.32 (72%)	13.33 (55%)
	14.6 (37%)	14.54 (28%)	14.58 (45%)

Table 4.3: Fitted O 1s – V 2p_{3/2} binding energy differences (BEDs) (and fractions thereof) for V-deposited samples after oxidation and reduction as described in the text.

The effect of reduction on W is more subtle. W 4f XPS signals (calibrated to the adventitious C 1s peak at 284.8 eV) are compared in **Figure 4.9(a)**, and the fits are broken down in **Figure 4.9(b-d)**

and **Table 4.4**. Calibration to the Al 2*p* substrate peak was also attempted, with results given in **Table 4.5**. Before any fitting, it is clear that the spectrum does not change substantially for sample MW, but there are shifts towards lower binding energies upon reduction for the mixed V-W samples. Indeed, the MW OX and RD spectra, as well as the OX spectra for samples VW1 and VW2, are fit well with a one-state model (including a small shoulder to account for the anomalous low-BE tails and a broad peak to accommodate the V 3*p* + W 5*p* peak centered at about 42 eV). However, two-state models best fit the data for the VW1 and VW2 reduced-case samples. For VW1, the two doublets are offset by only 0.45 eV from each other, and for VW2 the difference is somewhat larger, at 0.64 eV. However, neither of these separations between the higher-BE doublet (assumed to be W⁶⁺ and the lower-BE doublet reaches the expected 0.8 – 1.1 eV shift from W⁶⁺ to W⁵⁺. The W⁶⁺ BEs in the reduced cases are also slightly larger than for their oxidized counterparts. Overall, the fit results for VW1 suggest a broadening of the W⁶⁺ peak more so than a two-state condition, possibly indicating a variety of W⁶⁺ coordination environments with different degrees of covalency or charge screening, or alternatively a collective partial reduction (W^{(6-δ)+}, as will be discussed below). On the other hand, the results for VW2 suggest a more substantial reduction, and the interpretation of a partial reduction to W⁵⁺ will be carried forward.

	MW	VW1	VW2
OX	35.72 (100%)	35.77 (100%)	35.59 (100%)
RD	35.82 (100%)	35.93 (39%) 35.48 (61%)	36.01 (36%) 35.37 (64%)

Table 4.4: Fitted W 4*f*_{7/2} binding energies (and fractions thereof) for W-deposited samples after oxidation and reduction as described in the text. Binding energies are calibrated to the C 1*s* peak.

	MW	VW1	VW2
OX	36.13 (100%)	35.93 (100%)	36.40 (100%)
RD	36.10 (100%)	36.22 (39%) 35.77 (61%)	36.17 (36%) 35.53 (64%)

Table 4.5: Fitted W $4f_{7/2}$ binding energies (and fractions thereof) for W-deposited samples after oxidation and reduction as described in the text. Binding energies are calibrated to the Al $2p$ peak.

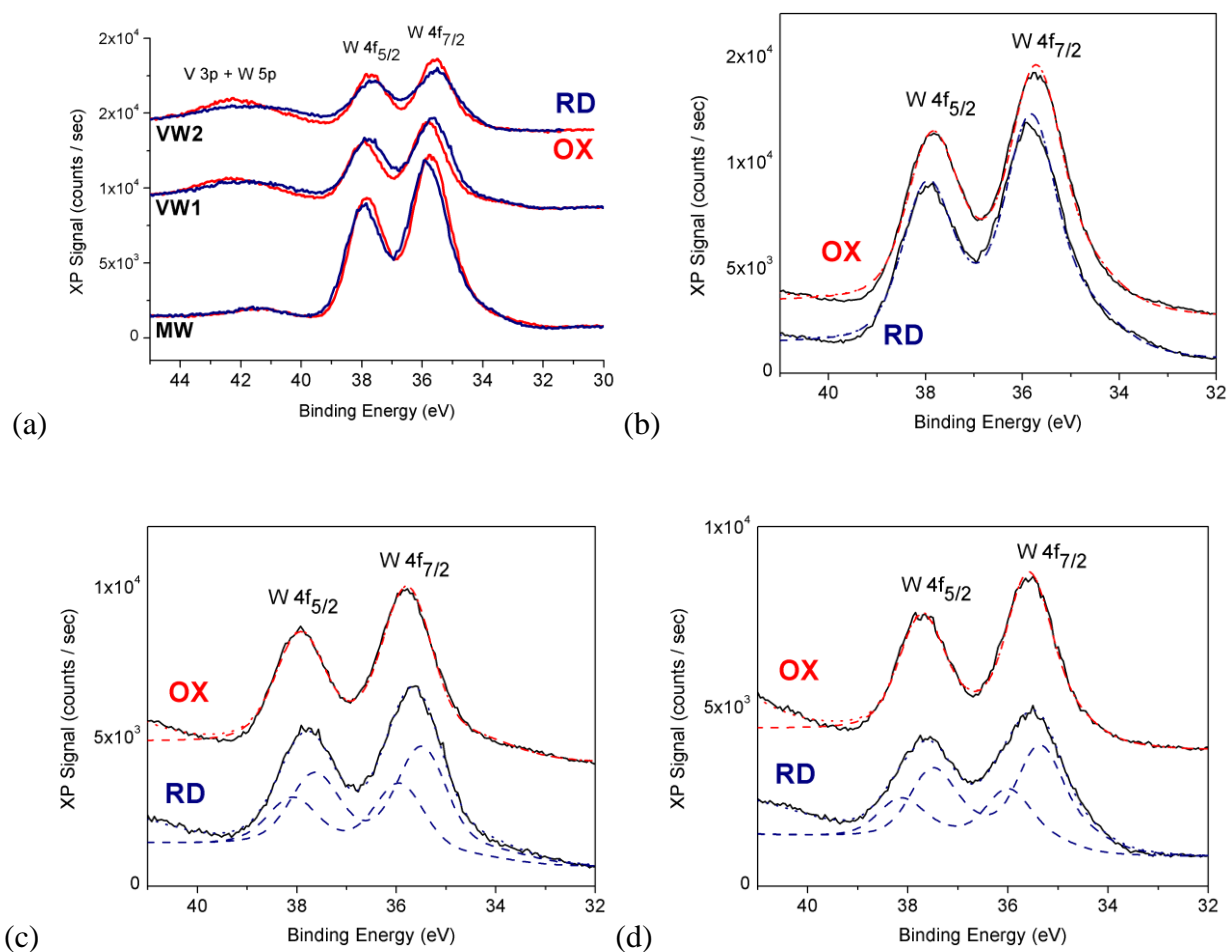


Figure 4.9: (a) Comparison of W $4f$ XP spectra. Binding energies are calibrated to the adventitious C $1s$ peak. (b,c,d) Fitted spectra for samples (b) MW, (c) VW1, and (d) VW2.

4.3.1.3 Surface structural characterization: XSW

The structure of the catalyst species were measured using XSW. In order to monitor the XSW effect, XRF spectra were monitored concurrently with the crystal reflectivity. XRF spectra for sample VW2 are shown in **Figure 4.10**. Each peak in the spectrum corresponds to a characteristic X-ray fluorescence line. Spectra for the as-deposited condition (sample in open air) and oxidized condition (Be dome applied with a pure O₂ environment inside) are shown, revealing the effect of the Be dome cell on the spectrum. In particular, the Ar K peaks are substantially suppressed with the Be dome attached; this can be attributed to the reduction in the air space viewed by the XRF detector. The V K peaks are only slightly attenuated, however, and there is nearly no difference in the intensity of the W L peaks when the Be dome is used. Ti, Cr, Fe, Ni, Cu, and Zn peaks are due to fluorescence of components of the Be dome mini-chamber base or contaminants on the dome. Zn, Fe, Ca, and In signals could also be attributed to sample contamination, as observed in XPS.

XSW measurements were performed on most samples in the untreated as deposited (AD) condition and after treating at 350°C for 30 min. in 200 sccm flowing O₂ (OX), 400°C for 30 min. in 200 sccm flowing 3% H₂ bal. He (RD), and re-oxidizing at the same conditions as Ox (OX2). In all cases, the “as deposited” measurements were made after the final ALD cycle; for the mixed VW samples, the W was pre-oxidized before V deposition. XSW data, shown in **Figure 4.11**, was collected at the “surface normal” (006) reflection under these conditions for all samples. (XSW measurements were also conducted for the (104), (113), and (012) reflections, but the data was not interpretable. See **Appendix B** for details.) The beam energy was 13 keV for samples MW, VW1, and VW2, and 7 keV for sample MV. In each of the plots in **Figure 4.11**, one representative reflectivity curve is shown, so the angular range of the fluorescence measurements might be

slightly different than that shown on the abscissa. The XSW-derived coherent fractions and positions (f_{006} , P_{006}) for the fits are shown in **Table 4.6**. The interpretation of these results is simplified to the most salient data in **Table 4.7**, which includes average values for each sample from different OX conditions. Coherent positions are reported relative to the bulk-like cation plane as a fraction of the (006) d -spacing of 2.166 Å.

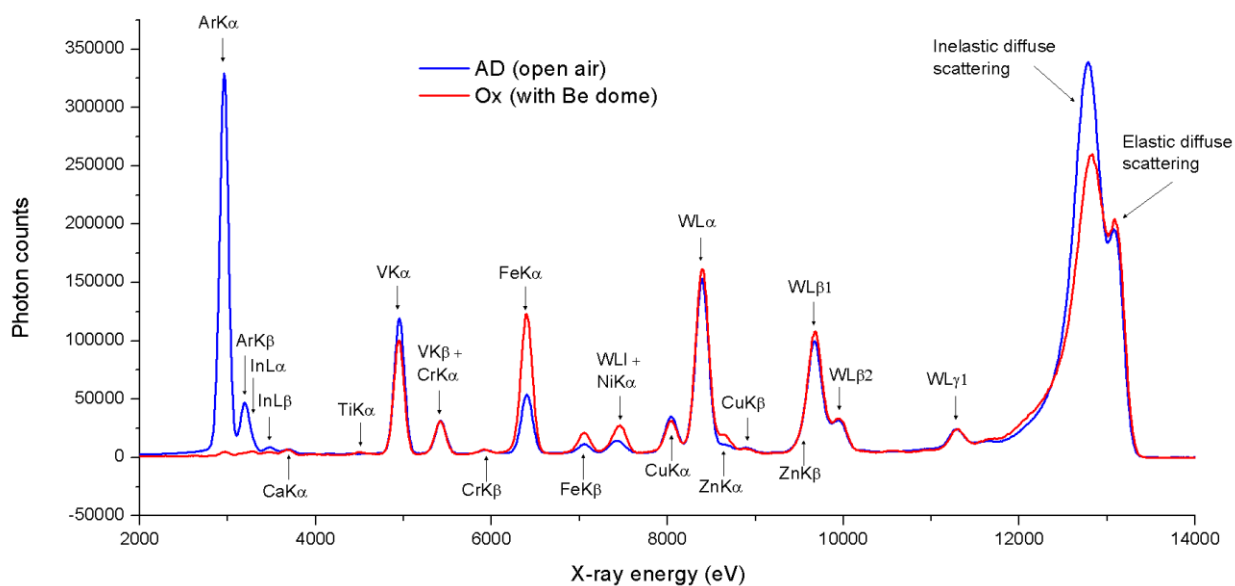
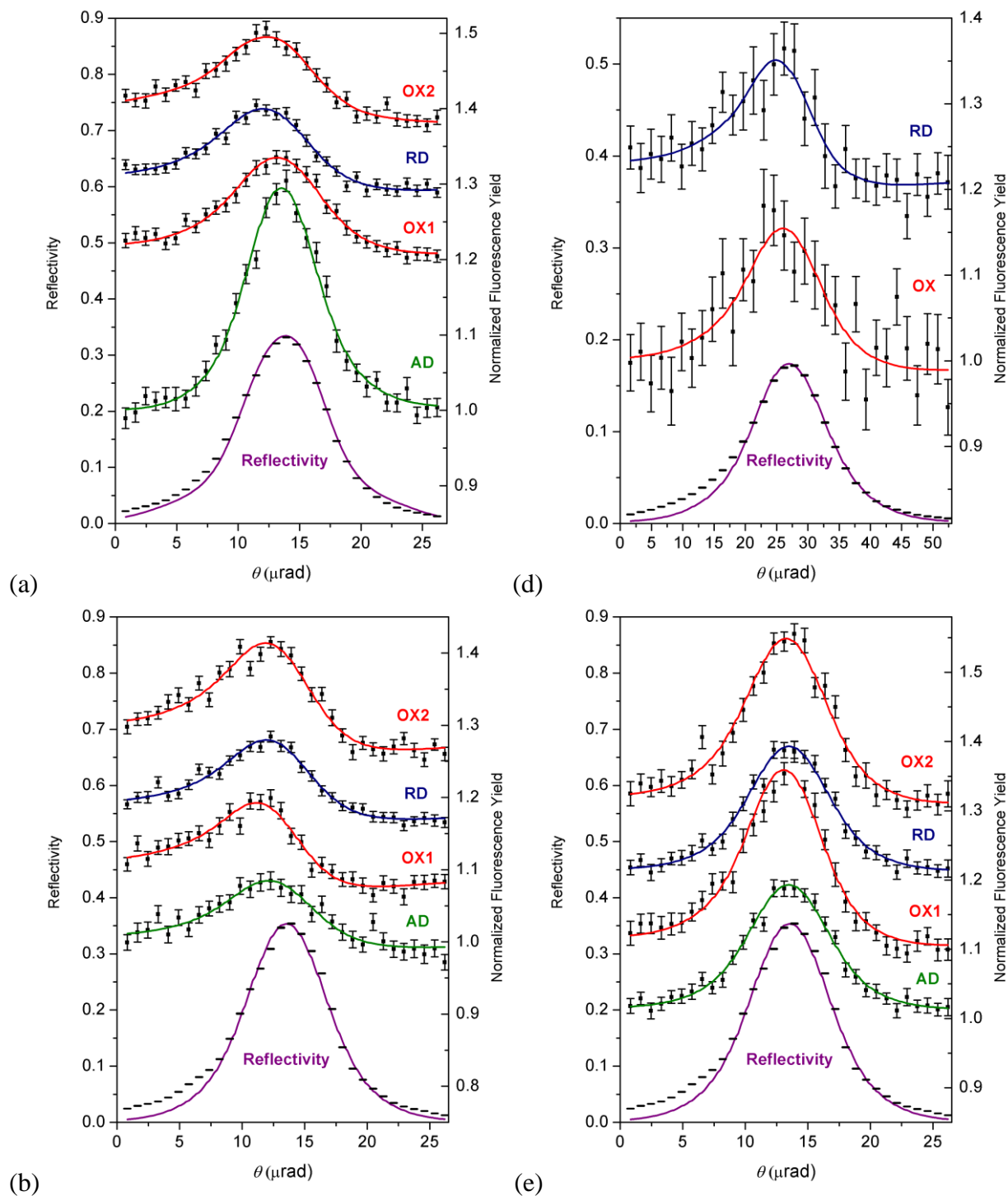
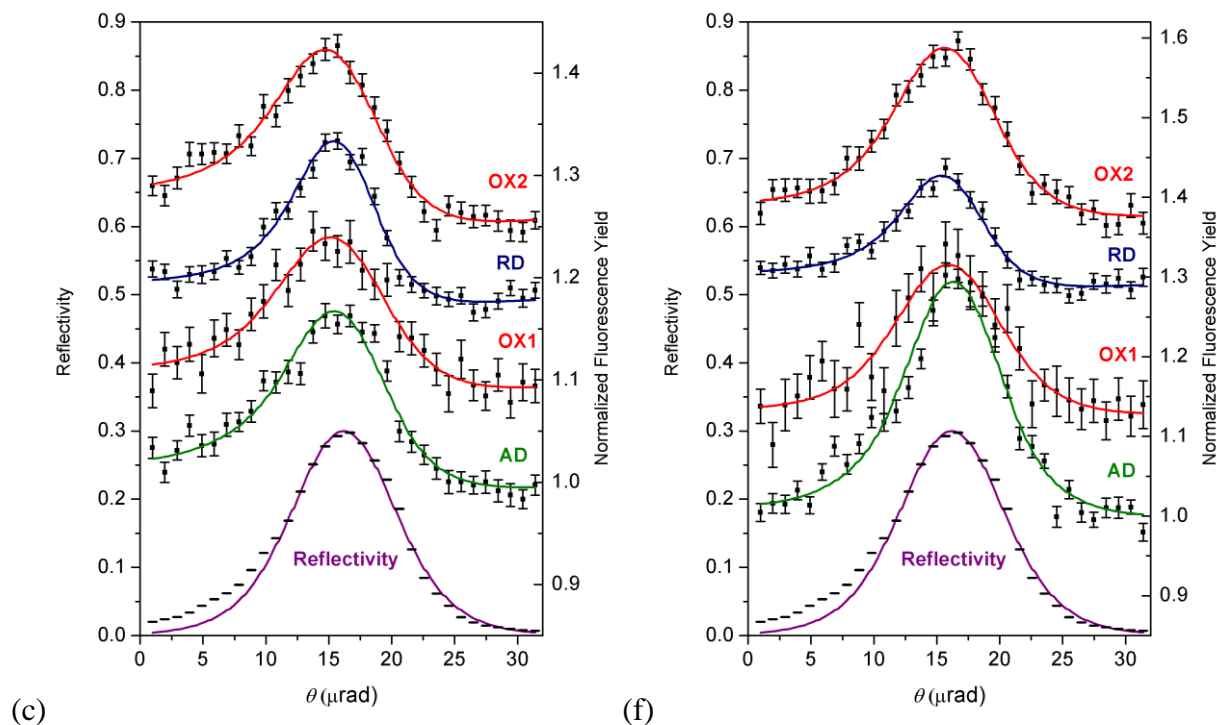


Figure 4.10: XRF spectra of 0.6 ML W / 1.0 ML V / α -Al₂O₃ (0001) sample in the as-deposited (AD) condition in open air and in the oxidized (OX) condition under a Be dome. Differences in intensity and impurity concentrations can be observed due to the dome's attenuation and impurities.

Figure 4.11: α - Al_2O_3 (006) XSW yield fits and a typical fitted reflectivity curve for (a-c) W and (d-f) V on samples (a) MW, (d) MV, (b,e) VW1, and (c,f) VW2. The chemical condition corresponding to each data set is indicated.





The (006) XSW results suggest a clear difference between the behavior of W and V on the α - Al_2O_3 (0001) surface. For the three samples with deposited W, there is virtually no change in the coherent position of W between the OX and RD states. The coherent fractions for W are between 0.3 – 0.5 (with the exception of the AD state of the MW sample, for which the un-annealed ALD W is likely disordered). Sample MW and VW1, with similar W coverages (0.8 – 0.9 ML), show almost identical coherent positions, and if the coherent fraction is multiplied by the W coverage, then the total amount of coherent W is similar between the two samples as well. The most notable difference is that for sample VW2, the W coherent fractions are suppressed, especially when the lower coverage of W is considered; the amount of coherent W is roughly half that of samples MW and VW1.

		MV	MW	VW1	VW2
AD	$f_{006}(V)$	<i>Not recorded</i>	--	0.09(6)	0.09(3)
	$P_{006}(V)$	<i>Not recorded</i>	--	--	--
	$f_{006}(W)$	--	0.06(3)	0.46(2)	0.32(2)
	$P_{006}(W)$	--	--	0.21(1)	0.17(1)
OX1	$f_{006}(V)$	<i>Not recorded</i>	--	0.09(2)	0.07(5)
	$P_{006}(V)$	<i>Not recorded</i>	--	--	--
	$f_{006}(W)$	--	0.33(1)	0.52(2)	0.27(3)
	$P_{006}(W)$	--	0.21(1)	0.18(1)	0.15(2)
RD	$f_{006}(V)$	0.23(3)	--	0.21(3)	0.33(2)
	$P_{006}(V)$	0.11(2)	--	0.23(1)	0.17(1)
	$f_{006}(W)$	--	0.42(2)	0.46(2)	0.30(2)
	$P_{006}(W)$	--	0.19(1)	0.19(1)	0.16(1)
OX2	$f_{006}(V)$	0.10(5)	--	0.09(3)	0.14(2)
	$P_{006}(V)$	0.1(1)	--	--	0.09(2)
	$f_{006}(W)$	--	0.43(3)	0.42(2)	0.33(2)
	$P_{006}(W)$	--	0.19(1)	0.16(1)	0.13(1)

Table 4.6: XSW-derived coherent fractions (f) and coherent positions (P) for the (006) crystal reflections in oxidized (OX1), reduced (RD), and re-oxidized (OX2) conditions. Error values on the last reported digit are given in parentheses. For values of f below 0.1, systematic errors make the value of P less reliable; some results for P have been omitted accordingly.

		MV	MW	VW1	VW2
RD	$f_{006}(V)$	0.23(3)	--	0.21(3)	0.33(2)
	$P_{006}(V)$	0.11(2)	--	0.23(1)	0.17(1)
	$f_{006}(W)$	--	0.42(2)	0.46(2)	0.30(2)
	$P_{006}(W)$	---	0.19(1)	0.19(1)	0.16(1)
OX	$f_{006}(V)$	0.10(5)	--	0.09(3)	0.11(5)
	$P_{006}(V)$	0.1(1)	--	--	0.1(1)
	$f_{006}(W)$	--	0.39(6)	0.47(7)	0.30(5)
	$P_{006}(W)$	--	0.20(2)	0.17(2)	0.14(3)

Table 4.7: XSW-derived coherent fractions (f) and coherent positions (P) for the (006) crystal reflections, with average values for separate oxidized (OX) cases. Error values on the last reported digit are given in parentheses. For values of f below 0.1, systematic errors make the value of P less reliable; some results for P have been omitted accordingly.

XSW results for V tell a much different story. In most of the AD and OX cases, V has a very low coherent fraction ($f_{006} < 0.1$). This precludes an accurate measurement of the coherent position of V, as the subtle shifts in the symmetry of the fluorescence yield curve cannot be accurately fit and quantified. However, upon reduction, the coherent fraction of V increases dramatically. The coherent position of reduced V is close to that of W in the VW1 and VW2 cases, but it is significantly lower on the V-only MV sample.

XSW coherent fractions and positions for an element at one substrate crystal reflection can be interpreted as the amount and position of an ensemble of atoms of the element occupying the same position relative to the reflecting crystal planes. Alternatively, the results can be construed as an average of different coherent fractions and positions added together in a complex plane. The “virtual” $f_{H(v)}$ and $P_{H(v)}$ from atoms occupying more than one position relative to a particular $\mathbf{H} =$

hkl can be calculated by adding complex vectors with arguments $e^{2\pi i(\mathbf{r}_N \cdot \mathbf{H})}$ and magnitudes C_N corresponding to the coherent positions and fractions of the atoms occupying each position, as follows:

$$f_{\mathbf{H}(\mathbf{v})} = \left| \sum_N C_N e^{2\pi i(\mathbf{r}_N \cdot \mathbf{H})} \right| \quad (4.3)$$

$$P_{\mathbf{H}(\mathbf{v})} = \frac{1}{2\pi} \arg \left(\sum_N C_N e^{2\pi i(\mathbf{r}_N \cdot \mathbf{H})} \right) \quad (4.4)$$

While the virtual coherent position would resemble a weighted average between the atomic site positions considered in this model, the virtual coherent fraction could be significantly smaller than the actual fractions corresponding to each site. This could be an explanation for the low measured coherent fraction of V, but the actual coherent positions cannot be explicitly derived from this data. A detailed interpretation of these results is aided by density functional theory calculations of ground-state surface structures.

4.3.2 Theory

4.3.2.1 0.5 ML W / Al-terminated α -Al₂O₃ (0001)

The Al-terminated α -Al₂O₃ (0001) surface supercell, discussed above, was decorated with one W atom per 1x1 cell, resulting in a nominal coverage of ½ ML. In each case, W was placed in either the A or B surface site, with Al occupying the other site of the two. The configurations are labeled W_AAl_B, with W in the A-site and Al in the B-site, and W_BAl_A, the reverse occupation. The C-site is ignored in this case, as it is expected to be unfavorable for W adsorption. Oxygen and hydroxyl ligands were adsorbed to oxidize W to nominally 3+, 4+, 5+, and 6+ oxidation states.

Table 4.8 details the ground-state energy differences (in eV) between the two different cation configurations, and these energies are shown in a convex hull analysis in **Figure 4.12**. For reference, the thermal energy available to real systems at room temperature is about 0.025 eV. The energy differences between different coordination structures of W / α -Al₂O₃ (0001) are relatively small, particularly for the hydroxylated cases. Still, for the oxygen-only and W-O,(OH)₂ coordinations, the energy differences are substantial enough to clearly identify one stable structure.

	W-O ₂	W-(OH) ₃	W-O,(OH) ₂	W-O ₂ ,OH	W-O ₃
W _A (Al _B)	0.39	0	0	0.03	0.19
W _B (Al _A)	0	0.03	0.16	0	0

Table 4.8: Relative differences in converged supercell energy (in eV) for $\frac{1}{2}$ ML W / Al-terminated α -Al₂O₃ (0001). A value of 0 denotes the most stable ground-state configuration. The top row refers to the terminal ligands added atop the W atom.

Structural and electronic details of the most stable structures are given in **Table 4.9**. The table includes the expected formal charge on W (q_W) with the adsorbed ligand environment, assuming that the other atoms present are also formally fully ionized (Al³⁺, O²⁻, and H⁺). In the next line, we quantify the stability of each structure in a “reduction series” by considering the energy of adding a H atom (more accurately considered as $\frac{1}{2}$ of a H₂ molecule) to a structure s is given as:

$$\Delta E_{+\frac{1}{2}H_2} = E_{s+H} - \left(E_s + \frac{1}{2} E_{H_2} \right) \quad (4.5)$$

E_s is the total supercell binding energy of relaxed structure s , E_{s+H} is the energy of a relaxed structure with one additional adsorbed H atom, and E_{H_2} is the calculated total energy of a H₂ molecule (-6.788 eV). If $\Delta E_{+\frac{1}{2}H_2}$ is negative, the surface with one additional H atom can be considered stable in vacuum; if positive, then the structure represents the upper limit of adsorbed

H. While this does not constitute a true thermodynamic treatment of the surface, it gives a starting guess as to the relative stability of a particular structure under H_2 treatment. An alternative reduction mechanism, the removal of an O atom, can be calculated similarly.

The following two rows of **Table 4.9** give structural information. z_W is the offset of the relaxed W atom from a bulk-like oxygen plane in the surface-normal direction. This value is converted to a virtual XSW coherent position P_{006} by calculating the z -position of W relative to a relaxed Al_2O_3 bulk cell. The next line gives the W-O bond distances in the first coordination shell. Finally, the calculated Bader charge (Q_B) and bond valence sum values are given. While DFT does not provide the formal oxidation state of a cation (which, regardless, is not a very physical quantity for atoms in a semi-covalent lattice), a formal oxidation state for W in these cases is proposed based on the BVS.

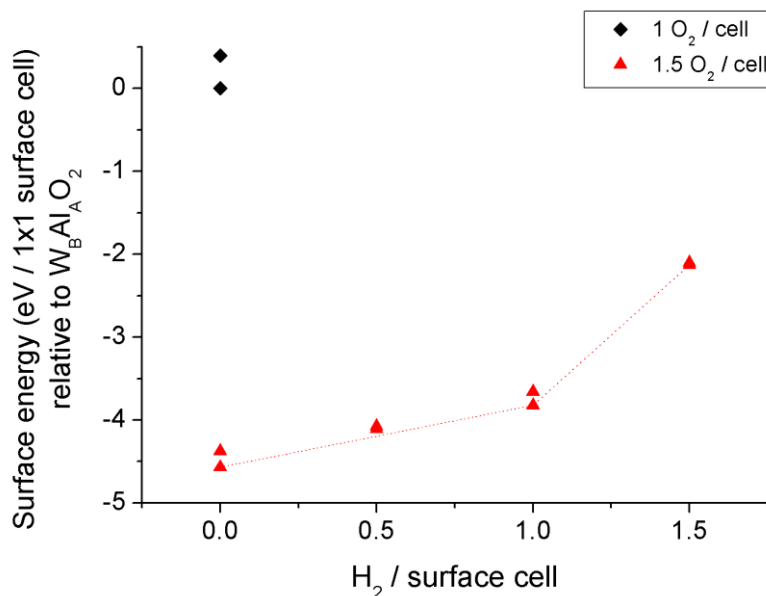


Figure 4.12: Convex hull analysis of the calculated 0.5 ML W / α - Al_2O_3 (0001) structures.

	W _B -O ₂	W _A -(OH) ₃	W _B -(OH) ₃	W _A -O, (OH) ₂	W _A -O ₂ ,OH	W _B -O ₂ ,OH	W _B -O ₃
Nominal q_W assuming Al _A ³⁺	4+	3+	3+	4+	5+	5+	6+
$\Delta E_{+\frac{1}{2}H_2}$	--	--	--	1.56	0.25	0.45	0.46
$\Delta E_{-\frac{1}{2}O_2}$	--	--	--	--	--	--	4.57
z_W (Å)	1.64 $P_{006} =$ 0.256	1.05 $P_{006} =$ -0.015	1.39 $P_{006} =$ 0.140	1.18 $P_{006} =$ 0.047	1.22 $P_{006} =$ 0.062	1.48 $P_{006} =$ 0.184	1.52 $P_{006} =$ 0.202
W-O coordination (Å)	1.72, 1.82, 2.15, 2.20, 2.27	2.02, 2.02, 2.02, 2.09, 2.09, 2.09	1.96, 2.01, 2.02, 2.05, 2.05, 2.08	1.81, 2.02, 2.03, 2.04, 2.08, 2.09	1.81, 1.81, 1.99, 2.01, 2.08, 2.13	1.78, 1.79, 1.95, 2.05, 2.12, 2.13	1.78, 1.78, 1.78, 2.17, 2.17, 2.17
Q _B (W) (e)	2.08	2.15	2.17	2.43	2.79	2.78	2.89
BVS(W) (e)	4.20	3.44	3.77	4.24	5.07	5.27	5.71

Table 4.9: Structural and chemical information for low-energy $\frac{1}{2}$ ML W structures and coordination environments atop the Al-terminated α -Al₂O₃ (0001) surface supercell. The meaning of each row is described in the text.

The energy of H addition $\Delta E_{+\frac{1}{2}H_2}$ is positive in all cases for the $\frac{1}{2}$ ML W / Al-terminated α -Al₂O₃ (0001) slab, indicating a resistance to reduction of the surface by H₂. The threshold from the most oxidized case (W_B-O₃) to the singly hydroxylated case (W_B-O₂,OH) would require an energy input of 0.46 eV, not accounting for any kinetic barriers. The surface energy of the W_B-O₂,OH structure sits slightly above the convex hull, suggesting that it may not be stable; reduction by H₂ may instead result in separate regions of W_B-O₃ and W_A-O,(OH)₂. However, the high energetic barrier to reduction by H makes this transition seem unlikely, and the z_W position of W_A-O,(OH)₂ is far below the experimental value. Additionally, no chemical state shift is observed in XPS for the MW sample, further suggesting that no transition occurs upon reduction. Finally, the energy cost of removing one of the three terminal O atoms from the W_BAl_A-O₃ structure, $\Delta E_{-\frac{1}{2}O_2}$, is over 4.5 eV, so reduction by oxygen removal is very unlikely. The W_BAl_A-O₃ model is therefore a good

candidate for describing the experimental case after oxidation or reduction. Its structure and W density of states are shown later in this chapter, in **Fig. 4.15**.

4.3.2.2 0.5 ML V / O- and Al-terminated α -Al₂O₃ (0001)

The structural and chemical characterization of V on sapphire yielded a more complex story for V than W, and so a more detailed theoretical treatment of this system is necessary. Herein we describe a few different examples of V decorating the O- and Al-terminated α -Al₂O₃ (0001) surface, beginning with the ½ ML case (one adsorbed V atom per unit cell). The simplest geometry has ½ ML V adsorbed atop the O-terminated α -Al₂O₃ (0001) surface. Assuming a simple ionic model, this surface has a charge of -3 per surface unit cell in vacuum. The coordination environments of V were therefore chosen for a nominal V cationic charge of 3+ to 5+: V is terminated by a single O (vanadyl), one or two hydroxyl groups, or no extra ligands. For the latter case, V was tested in the A, B, and C surface sites. Relaxed supercell energies for these configurations are reported in **Table 4.10**. The relaxed energy difference between the most stable (A-site, referred to as V_A) and least stable (C-site, V_C) is very large (>2.4 eV); this is similar to the case for 0.5 ML V / O-terminated α -Fe₂O₃ (0001)[130]. The unstable V_C configuration was not considered in further calculations. In the three remaining coordination environments, A-site V adsorption was substantially more stable than in the B-site. As a trend, the stability of V_A over V_B becomes less prominent with the addition of hydroxyl groups. However, the vanadyl V_A-O is preferred over its B-site counterpart more than any other coordination tested. We note that the V Bader charge (2.19) for an analogous V_A-O case on O-terminated α -Fe₂O₃ (0001)[130] was nearly the same as that shown here for sapphire (2.20 *e*), whereas the BVS is somewhat lower for the

hematite case (approximately 4.54 e vs. 4.69 e), providing further evidence that the valence is a more sensitive measure of catalyst cation chemistry than the Bader charge.

	V	V-OH	V-(OH) ₂	V-O
V _A	0	0	0	0
V _B	1.10	0.95	0.31	1.24
V _C	2.42	--	--	--

Table 4.10: Relative differences in converged supercell energy (in eV) for $\frac{1}{2}$ ML V / O-terminated α -Al₂O₃ (0001). A value of 0 denotes the most stable ground-state configuration. The top row refers to the terminal ligands added atop the W atom.

	V _A	V _A -OH	V _A -(OH) ₂	V _A -O
Nominal q_V	+3	+4	+5	+5
$\Delta E_{+\frac{1}{2}H_2}$	--	--	--	-0.22
ΔE_{+H_2O}	--	--	--	0.08
z_V (Å)	0.52 $P_{006} = -0.261$	0.66 $P_{006} = -0.193$	0.80 $P_{006} = -0.131$	0.62 $P_{006} = -0.213$
V-O coordination (Å)	1.75, 1.75, 1.76	1.77, 1.77, 1.78, 1.80	1.77, 1.78, 1.80, 1.88, 1.92	1.61, 1.80, 1.80, 1.80
Q _B (V) (e)	1.74	2.15	2.31	2.20
BVS(V) (e)	3.33	4.13	4.44	4.69

Table 4.11: Structural and chemical information for low-energy $\frac{1}{2}$ ML V structures and coordination environments atop the O-terminated α -Al₂O₃ (0001) surface supercell.

Table 4.11 shows details for the most stable cases of $\frac{1}{2}$ ML V atop O-terminated α -Al₂O₃ (0001) as indicated in **Table 4.10**, which in all cases has V in the A site. Analysis of the V adsorption heights shows values significantly displaced from the experimental values, so we conclude that these configurations are not observed under experimental conditions reported above. Bond valence sums for the V_A, V_A-OH, and V_A-O cases are close to the values for bulk-like V³⁺, V⁴⁺, and V⁵⁺, validating the BVS approach to V oxidation state determination. The doubly hydroxylated V_A-

(OH)₂ case is more ambiguous, with a BVS value almost exactly between those expected for V⁴⁺ and V⁵⁺.

In the presence of H₂, the reduction of V_A-O to V_A-OH is favorable by 0.22 eV. The stoichiometric difference between the V_A-O and V_A-(OH)₂ surfaces suggests that water adsorption or desorption may play a role in the surface chemistry. The energy of water adsorption is calculated as ΔE_{+H_2O} in a similar manner as $\Delta E_{+\frac{1}{2}H_2}$. Dissociative adsorption of water over the V_A-O surface to V_A-(OH)₂ is calculated to be endothermic by only 0.08 eV. This reaction results in two hydroxyl groups, as expected; however, they remain closely hydrogen-bonded, with the oxygen atom at the end of the longest V-O bond (at 1.92 Å) relaxing to O-H distances of 0.97 Å (typical of a hydroxyl O-H bond) and 1.39 Å.

Table 4.12 shows the relative stabilities (in eV) of different coordination environments around $\frac{1}{2}$ ML V atop the Al-terminated α -Al₂O₃ (0001) surface. The coordination environments were selected to oxidize V to its 3+, 4+, or 5+ state, assuming that the Al-terminated α -Al₂O₃ (0001) surface is charge neutral, as discussed earlier. In all cases the V_BAl_A configuration is significantly more stable than the opposite configuration, similar to the case for V adsorption on Fe-terminated α -Fe₂O₃ (0001)[130]. This is in contrast to the case for W, where the stability of A-site vs. B-site W depends upon the coordination environment of W.

	V-O,OH	V-(OH) ₃	V-O ₂	V-O,(OH) ₂	V-O ₂ ,OH
V _A Al _B	0.52	0.17	0.44	0.21	0.47
V _B Al _A	0	0	0	0	0

Table 4.12: Calculated total supercell binding energy differences (eV) for different coordination environments of V atop an Al-terminated cell. A value of 0 denotes the most stable ground-state configuration.

	V _B -O,OH	V _B -O ₂	V _B -(OH) ₃	V _B -O,(OH) ₂	V _B -O ₂ ,OH
Nominal q_V assuming Al _A ³⁺	+3	+4	+3	+4	+5
$\Delta E_{+\frac{1}{2}H_2}$	0.53	-0.19	--	0.65	-0.21
ΔE_{+H_2O}	-1.15	-1.99	--	--	-
z_V (Å)	1.55 $P_{006} = 0.214$	1.51 $P_{006} = 0.199$	1.28 $P_{006} = 0.092$	1.35 $P_{006} = 0.125$	1.43 $P_{006} = 0.163$
V-O coordination (Å)	1.75, 1.75, 2.07, 2.09, 2.22	1.61, 1.74, 1.94, 2.19, 2.22	1.91, 1.92, 1.95, 1.95, 1.98, 1.98	1.67, 1.87, 1.93, 1.97, 1.99, 2.16	1.68, 1.69, 1.85, 2.04, 2.13, 2.16
$Q_B(V)$ (e)	1.83	2.02	1.99	2.12	2.23
BVS(V) (e)	3.33	4.04	3.64	4.24	4.74

Table 4.13: Structural and chemical information for low-energy $\frac{1}{2}$ ML V structures and coordination environments atop the Al-terminated α -Al₂O₃ (0001) surface supercell.

Table 4.13 shows more detailed results regarding the V position, coordination, and chemical state. In particular, it is interesting to note the difference in V oxidation by ligands which might be expected to provide the same number of available states to accept electrons from V. In general, more ligands lead to a higher valence, although this behavior might be attributed to the BVS technique, which was originally developed for bulk materials. In the presence of water, however, the two-ligand cases (V_B-O,OH and V_B-O₂) both show a very strong tendency for the dissociative adsorption of H₂O, leading to three-ligand configurations. Thus, under real conditions, the three-ligand configurations are probably more stable.

Analysis of structural and chemical results from **Table 4.13** reveals that the closest structural matches with the experimental “reduced” value for coherent position ($P_{006} = 0.11(2)$) are the V_B-O(OH)₂ and V_B-(OH)₃ cases. However, analysis of the $\Delta E_{+\frac{1}{2}H_2}$ values indicates that there is a significant barrier to reduce V_B-O(OH)₂ to V_B-(OH)₃ in near-vacuum conditions. This does not

preclude the existence of the $V_B-(OH)_3$ structure under higher chemical potentials of H_2 , and indeed the experimental conditions included flowing H_2 . If both structures were to coexist on the surface during the experiment, then the measured P_{006} would be closer to the value for Sample MV, and the measured f_{006} would be slightly reduced. Coexistence of these two structurally similar phases across the surface could also lead to larger-scale surface phases which are beyond the scope of our experiments.

In a catalytic reaction, the chemical state of the ligands can be as important as the state of the metal. For example, the ionicity of a hydroxyl group's O atom could reveal the potential of that group as a Brønsted acid site. We therefore tabulate the Bader charges on O atoms coordinating V and W for the cases in **Table 4.9** and **Table 4.13**, which are compiled in **Table 4.14**. For anions, the Bader charge approaches the expected value as the charge becomes more localized on the anion; indeed, in the extreme case of highly ionic sapphire, the average O charge is -2.00. We therefore use the Bader charges as indicators of the degree of covalency of each type of O. (The Bader charge on H atoms in the structures studied is invariably close to +1.)

Three different types of O coordination exist on the surfaces of the examples in **Table 4.9**: terminal $W=O$ (only found on the $W_BAl_A-O_2$ case) and “bridging” $W-O-Al$ and $W-OH-Al$ oxygen atoms. The $W=O$ anion shows a very covalent character, with a Bader charge magnitude of less than half the expected ionic value. The bridging $W-O-Al$ oxygen is somewhat more ionic, with an average Bader charge of about -1.2 e. The magnitude of the anionic $W-O-Al$ Bader charge decreases slightly with increasing W Bader charge. The “bridging hydroxyl” $W-OH-Al$ anion is the most ionic, with an average Bader charge of -1.76. By comparison, the same structures for V are slightly more covalent; this is especially apparent for the $V=O$ group in the V_B-O_2 case. However, the

bridging M-O-Al and M-OH-Al oxygen atoms do not show significantly different Bader charges whether $M = V$ or W .

	M = W	M = V
M=O	-0.84	-0.78
M-O-Al	-1.20(6)	-1.2(1)
M-OH	<i>not observed</i>	-1.46
M-OH-Al	-1.76(4)	-1.72(5)
Bulk Al ₂ O ₃	-2.00(2)	

Table 4.14: Average Bader charges for O (in units of electron charge, e) in different coordinating environments for $\frac{1}{2}$ ML V and W on stable Al-terminated α -Al₂O₃ (0001) surfaces. Numbers in parentheses represent the standard deviation of the last digit.

Atom-projected partial densities of states are shown for V and terminal O and H ligands in **Figures 4.13** and **4.14** for the low-energy cases described in **Table 4.13**. For each case, regardless of the coordination environment, there are two sets of features near the Fermi energy E_F separated by a gap of about 2 eV: a broad feature below E_F which corresponds to V $3d - O 2p$ hybridization, and a sharp V $3d$ feature (or set of features) near or above E_F . Both sets of features include contributions from the ligands, with the broad feature dominated by O and the sharp features dominated by V. States corresponding to the hydroxyl group appear as spikes at the low-energy end of the broad feature. The sharp features are partially occupied for all ligand terminations except for the $V_{BA}Al_A-O_2OH$ case, where only the broad V $3d - O 2p$ feature is filled. The sharp feature is split into two main lines in the $V_{BA}Al_A-O(OH)$ and $V_{BA}Al_A-O(OH)_2$ cases, with splittings of about 0.5 and 0.7 eV, respectively. The features are largest for the $V_{BA}Al_A-(OH)_3$ and $V_{BA}Al_A-O_2OH$ cases, indicating multiple-state degeneracy.

The features near or above E_F are visualized in real space as band-projected charge density maps, which are shown for each sharp feature in **Figures 4.13** and **4.14**. The color gradients on the charge density images are selected to emphasize the contributions from the cations; charge densities (or available states) show up as red “hot spots” or lobes. Some localized states associated with the substrate Al atoms appear as well. The charge density lobes observed in these maps represent donor orbitals that may transfer charge to adsorbates, or acceptor orbitals that may mix with the donor states of molecules approaching the surface. Characterization of the spatial and energetic properties of the frontier orbitals may inform predictions about molecular adsorption and surface reactivity, although these ground-state charge densities would be distorted by incoming molecules.

4.3.2.3 1 ML V / O-terminated α -Al₂O₃ (0001)

A series of cases with V occupying both the A and B surface sites of α -Al₂O₃ (0001) was investigated. Both V atoms were prepared with sixfold O coordination in all cases, but they differ by the number of H atoms adsorbed on the surface. Results from this series are reported in **Table 4.15**. This configuration does not allow a complete oxidation of both V atoms on the 1x1 surface cell; the maximum achievable sum of the two V cationic charges is 9+. In addition to the positions (and calculated coherent positions) of both V atoms, the virtual $P_{006(v)}$ and $f_{006(v)}$, calculated as discussed above, are included. These virtual values assume equal occupation of the A and B sites and complete coherency across the surface; $f_{006(v)}$ can be considered a scaling factor by which the observed coherent fraction would be divided to calculate the actual fraction of coherent V in the two-site phase.

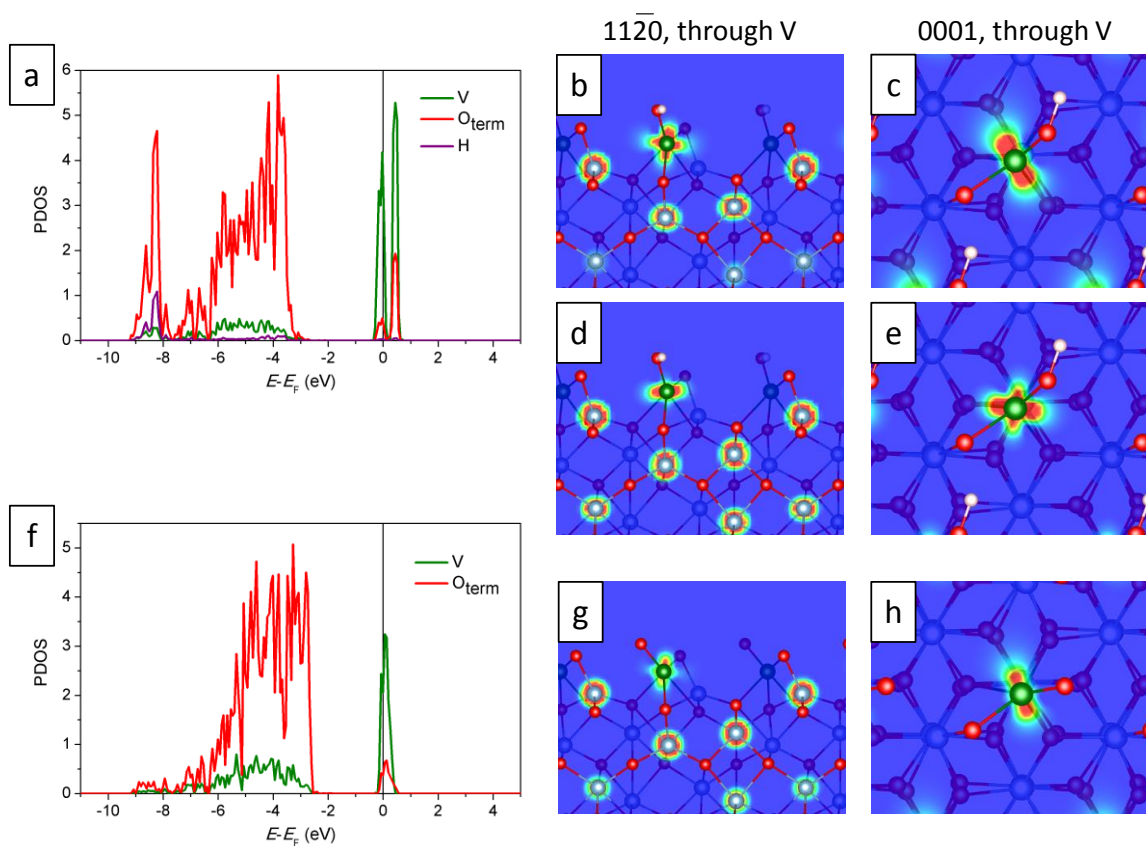


Figure 4.13: (a,f) PDOS and (b-e, g-h) band-projected charge densities for V, terminal O species, and H in the (a-e) $V_B-O(OH)$ and (f-h) V_B-O_2 structures on Al-terminated $\alpha-Al_2O_3$ (0001). The charge density is projected onto a plane in the $(1\ 1\ -2\ 0)$ or $(0\ 0\ 0\ 1)$ direction which slices through the V atom, as specified at the top of the columns. The lobes of the charge density show the shape of the electronic states at energies (in eV) relative to the Fermi level E_F : $V_B-O(OH)$, (b-c) $-0.4 - 0.2$ and (d-e) $0.2 - 0.6$; (g-h) V_B-O_2 , $-0.2 - 0.45$. V atoms are shown in green; Al, gray; O, red; and H, off-white.

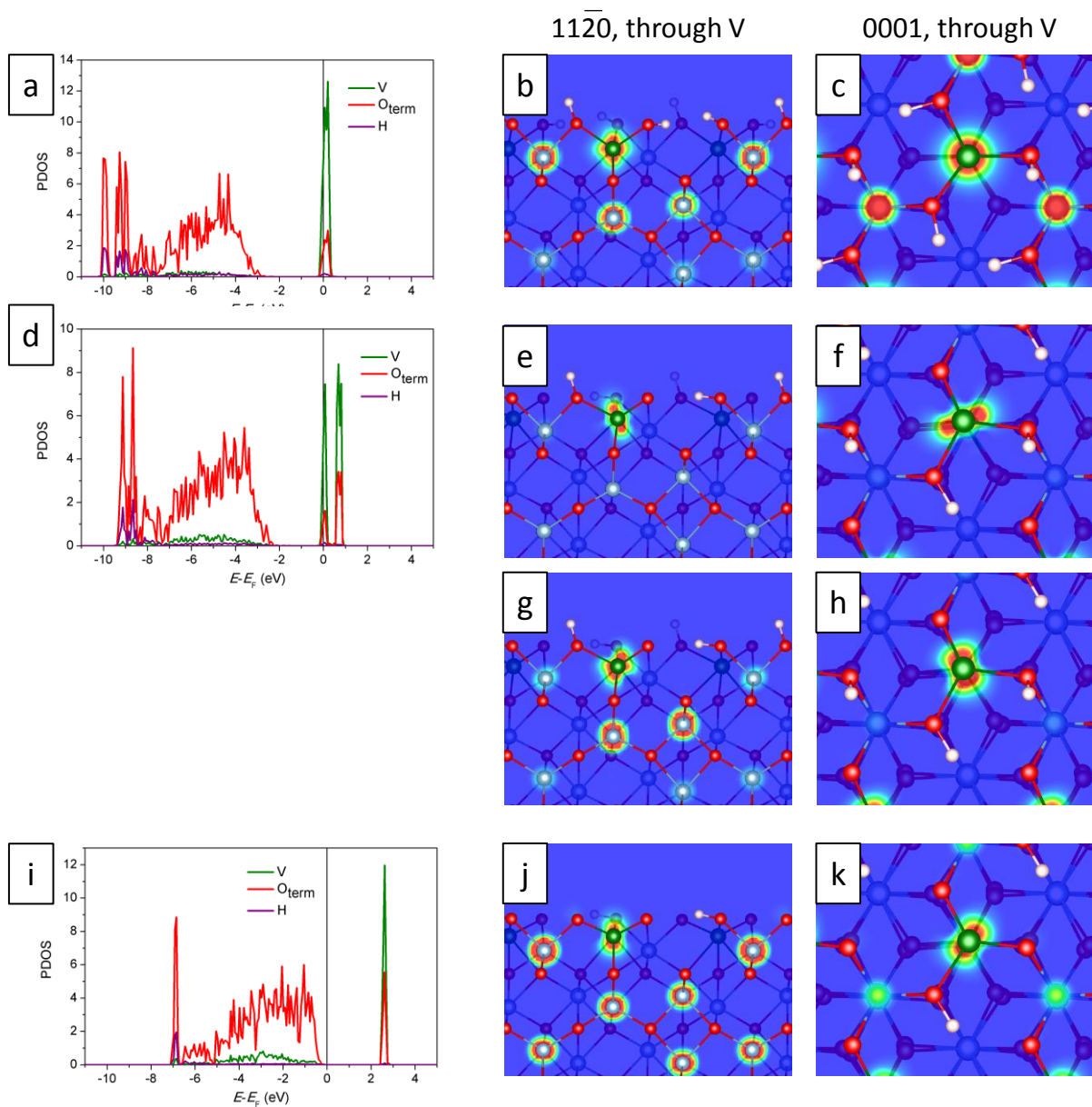


Figure 4.14: (a,d,i) PDOS and (b,c,e-h,j,k) band-projected charge densities for V, terminal O species, and H in the (a-c) $V_B-(OH)_3$, (d-h) $V_B-O(OH)_2$, and (i-k) V_B-O_2OH structures on Al-terminated $\alpha-Al_2O_3$ (0001). The charge density is projected onto a plane in the $(1\ 1\ -2\ 0)$ or $(0\ 0\ 0\ 1)$ direction which slices through the V atom, as specified at the top of the columns. The lobes of the charge density show the shape of the electronic states at energies (in eV) relative to the Fermi level E_F : (b-c) $V_B-(OH)_3$, $-0.2 - 0.4$; $V_B-O(OH)_2$, (e-f) $-0.2 - 0.15$ and (g-h) $0.5 - 0.9$; (j-k) V_B-O_2OH , $2.4 - 2.75$. V atoms are shown in green; Al, gray; O, red; and H, off-white.

Analysis of the $\Delta E_{+\frac{1}{2}H_2}$ values in **Table 4.15** suggest that the O,(OH)₂-terminated case is the most stable under reducing conditions. The complete reaction sequence from V_{AB}-O₃ to V_{AB}-(OH)₃ is exothermic, so a complete reduction to V_{AB}-(OH)₃ may be possible. However, with each reduction step, the average coherent position moves further from the experimentally measured value for sample MV reduced experimental case, and we see that while the most oxidized cases come close, none of these structures provide a very good match for the reduced case. As for the experimental OX case, it is possible that several coherent V positions could in effect “cancel out” each other if their positions were a half-phase apart. However, none of the above cases with 1 ML V show a difference in coherent positions any larger than 0.16, which results in a reduction in the apparent coherent fraction of only about 11%. We can therefore assume that none of these models individually matches the OX case.

4.3.2.4 0.25 ML V / Al-terminated α -Al₂O₃ (0001): isolated dimers

While only near-ML coverages of V and W were experimentally studied, it is possible that well-dispersed V species could exist on the surface. A few cases with 0.25 ML V were therefore studied using 2x2 surface supercells. The ligands surrounding V were selected for nominal oxidation state sums of 8+, 9+, and 10+. In most of the cases, the sapphire surface was completely Al-terminated; these are labeled with Al₄ in **Table 4.16**. In addition, one case was studied with a missing Al, corresponding to an Al-terminated surface for only $\frac{3}{4}$ of the total slab. To construct V dimers, neighboring open occupation sites had to be considered; as only A- and B-site V were used, one Al atom was displaced to a nearby B site to accommodate A-site V.

	$V_{AB}-(OH)_3$	$V_{AB}-O_3(OH)_2$	$V_{AB}-O_2,OH$	$V_{AB}-O_3$
Nominal $q_{VA} + q_{VB}$	6+	7+	8+	9+
$\Delta E_{+\frac{1}{2}H_2}$	--	0.69	-0.17	-0.82
z_{VA} (Å)	1.10 $P_{006} = 0.010$	1.04 $P_{006} = -0.021$	1.13 $P_{006} = 0.020$	1.09 $P_{006} = 0.001$
V_A-O coordination (Å)	1.94, 1.94, 2.02, 2.02, 2.13, 2.13	1.88, 1.94, 1.97, 2.01, 2.02, 2.09	1.71, 1.95, 1.95, 2.00, 2.05, 2.07	1.76, 1.87, 1.89, 1.96, 2.00, 2.03
$Q_B(V_A)$ (e)	1.83	1.96	2.07	2.18
BVS(V_A) (e)	2.89	3.32	3.84	4.16
z_{VB} (Å)	1.27 $P_{006} = 0.087$	1.37 $P_{006} = 0.131$	1.35 $P_{006} = 0.124$	1.41 $P_{006} = 0.151$
V_B-O coordination (Å)	1.91, 1.92, 1.95, 1.96, 2.03, 2.14	1.71, 1.90, 1.96, 2.01, 2.05, 2.16	1.68, 1.89, 1.92, 1.96, 2.07, 2.09	1.70, 1.74, 1.80, 2.01, 2.11, 2.13
$Q_B(V_B)$ (e)	1.82	1.98	2.07	2.18
BVS(V_B) (e)	3.32	3.82	4.19	4.63
$P_{006(v)}$	0.048	0.055	0.072	0.076
$f_{006(v)}$	0.971	0.889	0.947	0.892

Table 4.15: Structural and chemical information for low-energy 1 ML V structures and coordination environments atop the O-terminated α - Al_2O_3 (0001) surface supercell.

The $V_2Al_4-O_4OH$ dimer configuration, in separate calculations, relaxed into two significantly different structures with similar total energies. These are both reported in **Table 4.16**. In a reduction cycle, these structures are only intermediate, however; the $V_2Al_4-O_3(OH)_2$ configuration is more stable in the presence of H_2 . The same structure is also preferred over $V_2Al_4-O_4$ in the presence of water. Thus, the $V_2Al_4-O_3(OH)_2$ is a good candidate for the reduced case of sample MV, with a virtual coherent position $P_{006(v)}$ within experimental error, but it could only exist on the surface at relatively low density.

	V ₂ Al ₄ -O ₄	V ₂ Al ₄ -O ₃ (OH) ₂	V ₂ Al ₄ -O ₄ OH (1)	V ₂ Al ₄ -O ₄ OH (2)	V ₂ Al ₄ -O ₅	V ₂ Al ₃ - O ₃ (OH)
Nominal $q_{VA} + q_{VB}$	+8	+8	+9	+9	+10	+10
$\Delta E_{+\frac{1}{2}H_2}$ (eV)	--	--	-0.27	-0.22	-2.03, -2.08	--
$\Delta E_{-\frac{1}{2}O_2}$ (eV)	--	--	--	--	1.25	--
ΔE_{+H_2O} (eV)	-0.98	--	--	--	--	--
z_{VA} (Å)	1.02 $P_{006} =$ -0.030	1.34 $P_{006} =$ 0.118	1.21 $P_{006} =$ 0.057	1.08 $P_{006} =$ -0.001	1.65 $P_{006} =$ 0.261	0.84 $P_{006} =$ -0.113
V _A -O coordination (Å)	1.78, 1.80, 1.82, 1.86, 2.20	1.61, 1.77, 1.81, 1.91	1.60, 1.75, 1.82, 1.95	1.62, 1.74, 1.83, 2.04, 2.19	1.60, 1.80, 1.82, 1.87	1.73, 1.75, 1.82, 1.93, 1.96
Q _B (V _A) (e)	2.16	2.19	2.21	2.18	2.22	2.28
BVS(V _A) (e)	3.94	4.44	4.54	4.49	4.40	4.45
z_{VB} (Å)	1.56 $P_{006} =$ 0.219	1.38 $P_{006} =$ 0.139	1.47 $P_{006} =$ 0.177	1.48 $P_{006} =$ 0.185	1.48 $P_{006} =$ 0.182	1.46 $P_{006} =$ 0.176
V _B -O coordination (Å)	1.74, 1.74, 1.78, 2.07, 2.15, 2.26	1.76, 1.81, 1.97, 2.02, 2.07, 2.08	1.73, 1.77, 1.78, 2.06, 2.10, 2.17	1.73, 1.75, 1.77, 2.07, 2.13, 2.17	1.74, 1.77, 1.77, 1.99, 2.16, 2.20	1.74, 1.75, 1.75, 2.09, 2.16, 2.19
Q _B (V _B) (e)	2.21	2.17	2.24	2.24	2.25	2.24
BVS(V _B) (e)	4.30	3.91	4.38	4.41	4.39	4.41
$P_{006(V)}$	0.095	0.129	0.117	0.092	0.222	0.032
$f_{006(V)}$	0.709	0.998	0.930	0.834	0.969	0.615

Table 4.16: Structural and chemical information for low-energy 0.25 ML V structures and coordination environments atop the Al-terminated α -Al₂O₃ (0001) 2x2 surface supercell.

4.3.2.5 0.5 ML V / W+Al-terminated α -Al₂O₃ (0001)

The nature of V-W interactions on the sapphire surface is investigated by considering V and W together atop the sapphire surface. Recalling that the relaxed, fully O-terminated W_BAl_A model was a very good match with experimental data for sample MW (0.9 ML W), this 1x1 surface supercell is used as the “substrate” for V adsorption. Several different combinations of O and OH

coordinating with V are considered, corresponding to V oxidation states between 3+ and 5+ (assuming that W remains in its 6+ state). V is adsorbed atop the C and A sites, as these are the first and second cation positions, respectively, in the next layer of surface cations. For these structures, C-site V therefore sits above a hollow cation site, whereas A-site V sits above the underlying Al cation. The relative energies of each of these configurations are detailed in **Table 4.17**. In most cases, C-site V occupation is preferred, as expected. However, with O,(OH)₂ and O₂,OH termination, the energy gap between the two V cation sites is only about 0.1 eV. Either could therefore be stable under real conditions.

Structural and chemical details of the stable cases, including both configurations for the O,(OH)₂ and O₂,OH configurations, are given in **Table 4.18**. The first row in **Table 4.18** gives the total nominal oxidation state of V and W together, assuming that all the other ions in the system are Al³⁺, O²⁻, and H⁺. In all cases in **Table 4.18**, the oxidation state of V appears to be near 4+ or 5+, while W appears to be somewhat reduced from the W_BAl_A-O₃ case, in which the W BVS is 5.71. In considering the valence and ionicity of the V and W cations, it is therefore apparent that the sub-surface W, although fully coordinated with O, is reduced somewhat by the presence of V nearby. To check for an effect of Al³⁺ reduction, the Bader charge and BVS of the near-surface Al_A atom is provided in **Table 4.18**. While there are some subtle changes in these values, they are all close to those expected for bulk-like Al³⁺.

Considering the $\Delta E_{+\frac{1}{2}H_2}$ series of the mixed V-W cases described in **Table 4.18**, a few differences between the nearly co-stable C- and A-site V cases emerge. For C-site V, 2-3 H atoms per surface cell are stable, whereas there is a very sharp energy penalty for the addition of a third H atom to A-site V. The V_A-O,(OH)₂ structure therefore appears to be very stable in vacuum after hydrogen

treatment, whereas the $V_C\text{-(OH)}_3$ structure is only slightly more favored than the $V_C\text{-O, (OH)}_2$ structure. However, only the V_C structures match well with experimental data. A mixed termination of $V_C\text{-O, (OH)}_2$ and $V_C\text{-(OH)}_3$ would lead to a V coherent position between 0.18 – 0.28, with a minimum virtual coherent fraction of 0.95 with an equal distribution of the two (leading to a virtual coherent position of 0.23). This would match the experimental value of 0.23(1) which is observed for the VW1 sample. This slight depression in the coherent fraction does not, however, account for the significant difference in W and V coherent fractions on the reduced-case VW1 sample ($f_{006}(W) = 0.46(2)$, $f_{006}(V) = 0.21(3)$). The coherent position and fraction of W in the VW1 case is not much different than its position without V in the MW case. It is possible that there are large regions of incoherent V on the surface, possibly forming V_2O_5 species which are incoherent with the substrate lattice[33].

	V-(OH) ₂	V-O,OH	V-(OH) ₃	V-O ₂	V-O,(OH) ₂	V-O ₂ ,OH
V _C	--	0	0	0	0.11	0
V _A	--	0.23	1.49	0.53	0	0.10

Table 4.17: Calculated total supercell binding energy differences (eV) for different coordination environments of V atop a fully O-terminated $W_B A_L A$ cell.

	V _C -O,OH	V _C -O ₂	V _C -(OH) ₃	V _C -O,(OH) ₂	V _C -O ₂ ,OH	V _A -O, O,(OH) ₂	V _A -O ₂ ,OH
Nominal $q_w + q_v$	+9	+10	+9	+10	+11	+10	+11
Nominal terminal ligand charge	-3	-4	-3	-4	-5	-4	-5
$\Delta E_{+\frac{1}{2}H_2}$ (eV)	-0.42	-0.32	--	-0.12	-0.55	1.48	-0.76
ΔE_{+H_2O} (eV)	-1.09	-1.29	--	--	--	--	--
z_V (Å)	1.38 $P_{006} = 0.138$	1.18 $P_{006} = 0.047$	1.47 $P_{006} = 0.181$	1.68 $P_{006} = 0.278$	1.84 $P_{006} = 0.349$	1.85 $P_{006} = 0.356$	1.83 $P_{006} = 0.344$
V-O coordination (Å)	1.61, 1.80, 1.91, 2.06, 2.34	1.60, 1.74, 1.90, 2.00, 2.29	1.61, 1.93, 1.99, 2.05, 2.10, 2.40	1.60, 1.79, 1.80, 2.25, 2.30, 2.39	1.63, 1.72, 1.75, 1.94	1.60, 1.79, 1.79, 2.21, 2.24, 2.38	1.64, 1.73, 1.73, 1.93
$Q_B(V)$ (e)	2.03	2.12	2.04	2.16	2.18	2.18	2.18
BVS(V) (e)	4.03	4.37	3.91	4.34	4.64	4.42	4.65
Z_{WB} (Å)	1.48 $P_{006} = 0.185$	1.64 $P_{006} = 0.256$	1.47 $P_{006} = 0.179$	1.49 $P_{006} = 0.186$	1.64 $P_{006} = 0.258$	1.52 $P_{006} = 0.201$	1.65 $P_{006} = 0.261$
W _B -O coordination (Å)	1.82, 1.86, 1.88, 2.09, 2.09, 2.11	1.83, 1.86, 1.87, 2.12, 2.18, 2.22, 2.24	1.81, 1.85, 1.87, 2.08, 2.09, 2.11	1.81, 1.82, 1.83, 2.10, 2.10, 2.10	1.78, 1.78, 1.90, 2.11, 2.23, 2.26, 2.27	1.80, 1.81, 1.82, 2.11, 2.12, 2.12	1.78, 1.78, 1.90, 2.10, 2.23, 2.25, 2.28
$Q_B(W)$ (e)	2.67	2.79	2.77	2.85	2.87	2.85	2.87
BVS(W) (e)	4.94	4.92	5.09	5.38	5.32	5.43	5.31
$Q_B(Al)$ (e)	2.91	2.99	2.90	2.88	3.00	2.89	3.00
BVS(Al) (e)	2.90	3.15	2.86	2.87	3.21	2.93	3.21

Table 4.18: Structural and electronic parameters for V atop a fully O-terminated Al_AW_B cell.

A few other configurations relax to interesting structures worth noting. In the fully oxidized V_A- and V_C-O₂OH structures, V shifts significantly from the bulk-like cation position, occupying a bridging site between two surface O atoms. This leads to a significantly higher coherent position for V, but also distorts the W coordination environment such that there are three extremely long (>2.2 Å) W-O bonds. Although W is coordinated with *seven* O atoms, the BVS is calculated to be

slightly lower than for a nominally more reduced surface. Another structurally interesting case is the $V_C-(OH)_3$ model, for which one hydroxyl H atom migrates to another adsorbed O. This results in the terminal coordination structure $V=O,-OH,-OH_2$, analogous to V_C-O,OH with an adsorbed H_2O molecule. Comparison of the relaxed supercell binding energies with the total energy of an H_2O molecule gives the H_2O adsorption energy as 1.09 eV. A similar result for V_C-O_2 suggests that the three-ligand coordinations, as in previous examples, are the most stable.

We can also compare the O Bader charges of the terminal ligands. Across the cases listed in **Table 4.18**, the Bader charge of H is invariably +1.00. The O charges depend on the coordination environment; these are listed in **Table 4.19**. The O Bader charge for the adsorbed H_2O in the $V_C-(OH)_3$ case is the closest to the expected value of -2, but the value drops significantly for the hydroxyl O. For O that is only coordinated with metals, the values are even lower, with V-O-W bridging oxygen having an average value of -0.89, and vanadyl groups smaller still. Comparison with the values in **Table 4.14** above shows that the Bader charge of $V=O$ and $V-OH$ species is not changed by the presence of underlying W. However, the V-O-W bridging oxygen ($Q_B = -0.89(1) e$) is much more covalent than the V-O-Al oxygen ($Q_B = -1.2(1) e$). This is chemically significant, as V-O-(support) oxygen atoms play a crucial role in catalysis[24].

The effect of V on the chemistry of W can be assessed by comparing the W partial density of states (PDOS) from the $W_BAl_A-O_3$ cell, which describes the experimental W-deposited sample, with the W PDOS from structures with V adsorbed. A clear starting point is the fully oxidized V_C-O_2,OH case; the relaxed structure, as well as its V and W PDOS, are shown alongside analogous data for $W_BAl_A-O_3$ in **Figure 4.15**. As discussed above, this structure relaxes such that the V occupies a bridging site at the surface, and W moves upward slightly. However, the W PDOS is relatively

unaffected by the presence of oxidized V. The V $3d - O 2p$ feature occupies similar energies as that of W, although its states are concentrated closer to E_F ; in fact, the O $2p$ band extends slightly above E_F . No sharp unoccupied states above the Fermi level are observed, unlike for the most oxidized V-only case.

Surface atom PDOS analysis of the two most relevant mixed V-W cases ($V_C-(OH)_3$ and $V_C-O,(OH)_2$), presented in **Figure 4.16**, show significant changes for W relative to the clean W_BAlA-O_3 surface. In the $V_C-(OH)_3$ case, a narrow band in the projected PDOS appears near the Fermi energy. This band consists of three primary peaks. The largest, at about $E-E_F = 0.55$ eV, is mostly from the W d_{z^2} orbital, with contributions from the V d_{z^2} and $d_{x^2-y^2}$ orbitals. These orbitals also comprise the feature at the Fermi level, albeit in the opposite ratio. The feature at $E-E_F = 0.25$ eV comes from the W d_{xy} and d_{yz} orbitals, with contributions from V $d_{x^2-y^2}$ as well. W and V in this structure are separated by 3.31 Å, and since the Wigner-Seitz radii upon which the W and V states are projected are only 0.9 and 0.8 Å, respectively, then the presence of these states for both V and W cannot be accounted for by *direct* orbital overlap between cations. Analysis of the band-projected charge density maps in **Figure 4.16** shows no direct overlap between these states. However, as before, an O $2p$ component is mixed with the contributions from the cations. Additionally, we note that the PDOS of the O layer between V and W (not shown here) almost perfectly overlaps the W states at and above E_F . A similar story emerges for the $V_C-O,(OH)_2$ case. Here, the W d_{z^2} orbital dominates the features centered at about 0.35 eV above E_F . The V d_{z^2} orbital, on the other hand, composes the features around 0.1 eV above E_F , with all other d orbitals contributing at slightly higher energies.

	Average O Bader charge (e)
V=O	-0.76(4)
V-O-W	-0.89(1)
V-OH	-1.45(6)
V-OH ₂	-1.95
Bulk Al ₂ O ₃	-2.00(2)

Table 4.19: Average Bader charges for O (in units of electron charge, e) of surface structures described in **Table 4.18**, including the value from bulk α -Al₂O₃ for comparison. Numbers in parentheses represent the standard deviation of the last digit.

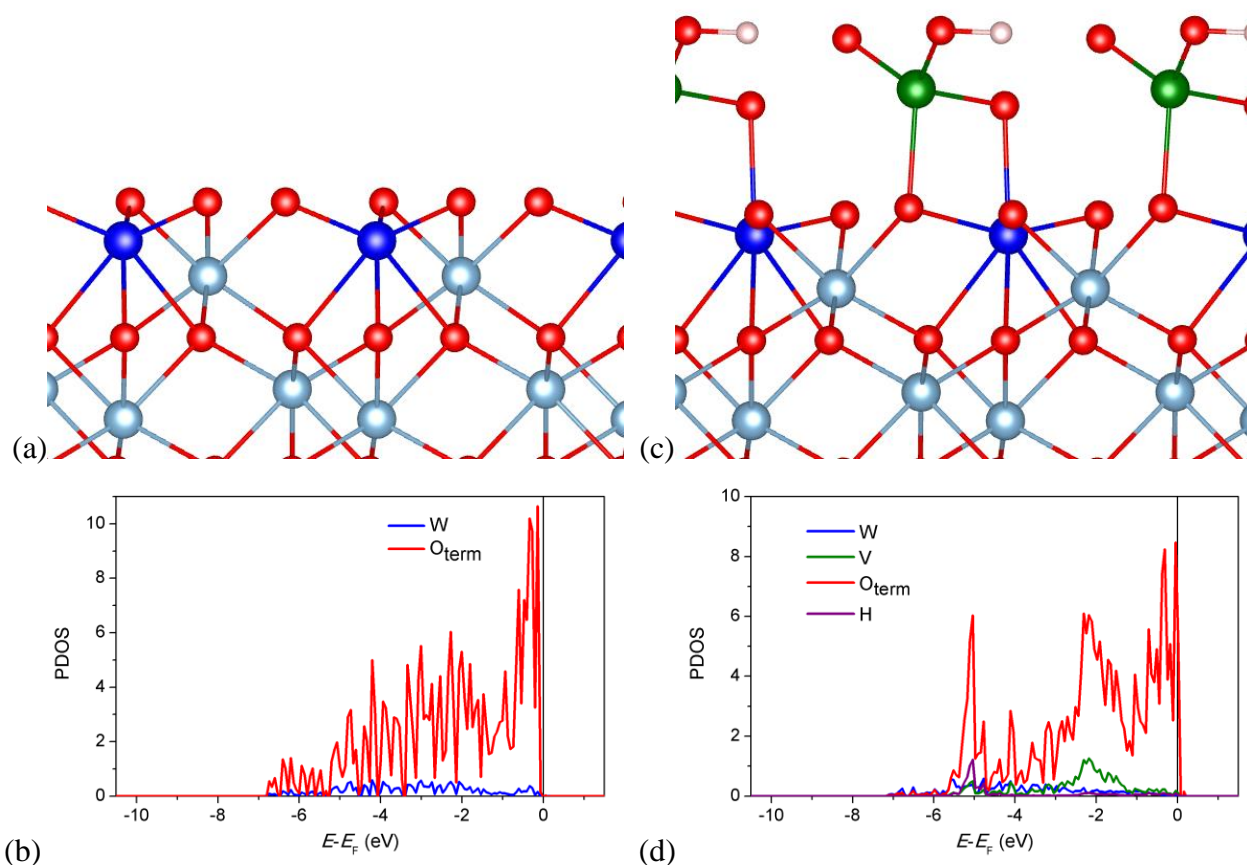


Figure 4.15: (a,c) Structures and (b,d) W, V, terminal O, and H partial densities of states (PDOS) for the fully oxidized (a,b) W_BAl_A-O₃ and (b,d) W/Al₂O₃-supported V_C-O₂OH structures. Energies (in eV) are given relative to the Fermi energy E_F , denoted by a vertical line. W atoms are shown in blue; V, green; Al, gray; O, red; and H, off-white.

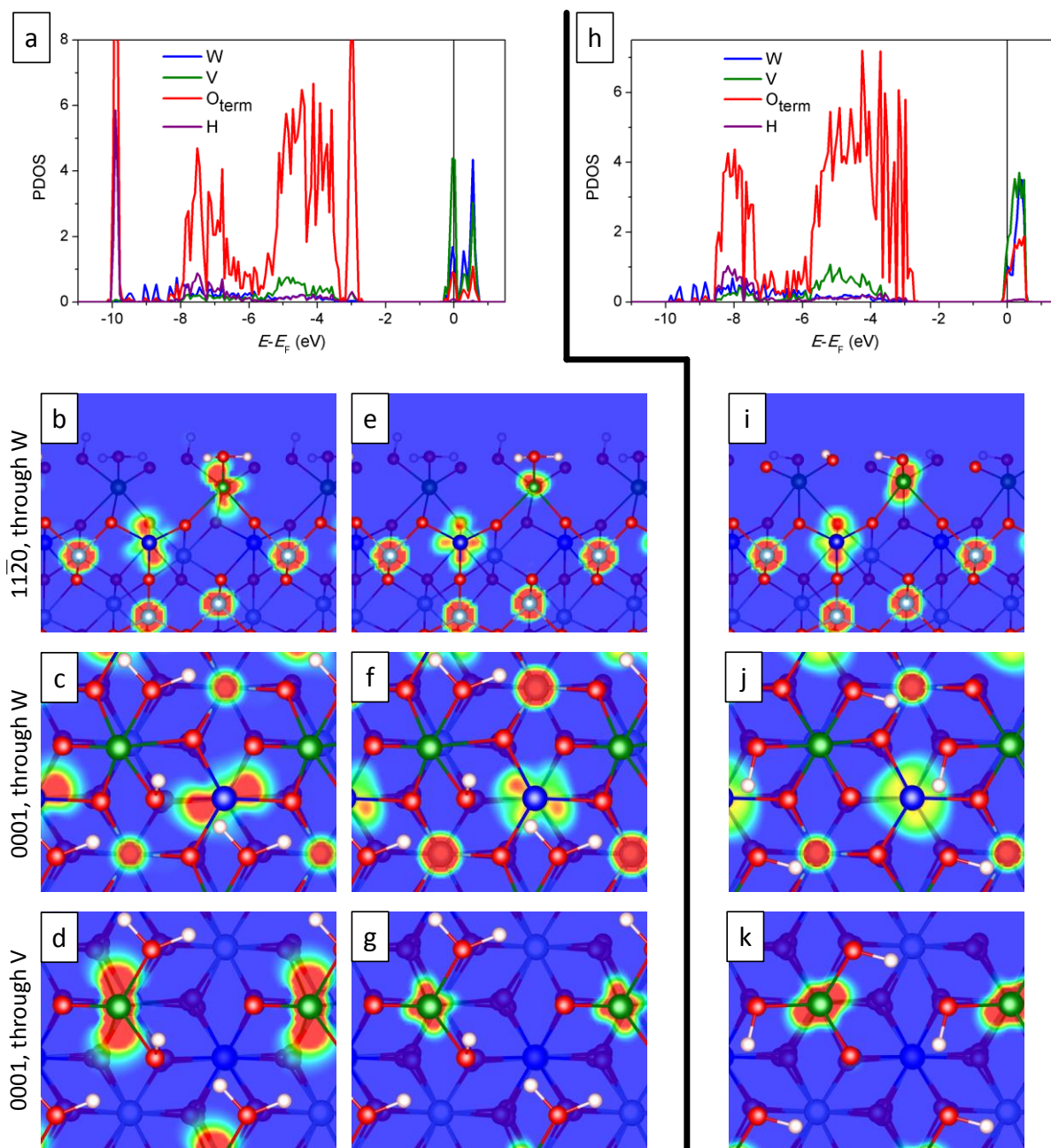


Figure 4.16: (a,h) W, V, terminal O, and H PDOS for the W/Al_2O_3 -supported (a) $V_C-(OH)_3$ and (h) $V_C-O(OH)_2$ structures. O PDOS features are truncated in (a) for clarity. (b-g, i-k) Band-projected charge densities for the W/Al_2O_3 -supported (b-g) $V_C-(OH)_3$ and (i-k) $V_C-O(OH)_2$ structures in the following energy ranges (in eV, relative to E_F): (b-d) $-0.30 - 0.15$; (e-g) $0.15 - 0.75$; (i-j) $-0.15 - 0.6$. The charge densities are shown as slices along particular planes as specified on the left side of the image. Regions of relatively high charge density are in red, and low are in blue. Atom colors are as defined previously.

4.4 Discussion

Taking together experimental and theoretical evidence, the structure of sample MW is the most straightforward to solve. AFM images show a flat, conformal film on the substrate terraces, and DFT calculations for completely oxidized B-site W (with a coverage of 0.5 ML) atop the Al-terminated α -Al₂O₃ (0001) surface match well with the XSW-derived position of W. While the coherent fraction is only about 0.4, this corresponds to a total coherent W coverage of about 0.35-0.40 ML, which approaches the coverage used in the calculation. Bond valence sums suggest a W⁶⁺ state, in agreement with XPS. Theoretical comparisons with reduced structures show that this structure is very stable. We observe that W is much more stable with 6-fold octahedral coordination than with lower coordination, in agreement with X-ray absorption spectroscopy on industrially relevant catalysts[173, 215]. From structural and chemical perspectives, we conclude that the W_B-O₃ / Al-terminated sapphire model, shown in **Fig. 4.14**, is the best model for near-monolayer W on α -Al₂O₃ (0001). This structure strongly resembles that calculated for oxidized W on α -Fe₂O₃ (0001)[126].

The interpretation of the V-containing samples is much more difficult. AFM images taken after several reduction-oxidation cycles on all three V-containing samples (MV, VW1, and VW2) show an ensemble of well-defined nanoparticles on the substrate surface after treatments in reducing or oxidizing conditions. For VO_x with the coverage studied here (9.2 V nm⁻²) supported on commercial Al₂O₃ powder material, polyvanadate species are prevalent, and V₂O₅ particles may be observed[183]. It is therefore possible that the VO_x phase consists of V₂O₅ aggregates which partially reduce upon treatment in dilute H₂, yielding V⁴⁺ species. This hypothesis is supported by

flood analysis of AFM images for the oxidized MV sample, which reveals that the total volume of the particles is roughly equivalent to that expected for about a monolayer of V_2O_5 .

Bulk V_2O_5 has an orthorhombic unit cell with lattice parameters $a = 11.512 \text{ \AA}$, $b = 3.564 \text{ \AA}$, $c = 4.368 \text{ \AA}$, and it consists of weakly interacting corrugated sheets of 5-fold O-coordinated V layered along the [001] direction. There is therefore no XSW-measurable lateral epitaxy expected between (001)-oriented V_2O_5 sheets and the sapphire (0001) surface. In the surface normal direction, however, one might expect to see a V coherent fraction for well-ordered, bulk-like V_2O_5 : there is almost no mismatch between d_{001} of V_2O_5 and $2*d_{006}$ of sapphire (4.332 \AA). The lack of correlation of V^{5+} with the sapphire substrate as shown by XSW suggests that V_2O_5 is either not crystalline or not epitaxial in the expected (001) direction. It is also possible that VO_x is interacting strongly to form a mixed V-Al oxide at the interface which may contribute to the particle volume [184, 189].

In any case, the XSW results correspond to the $VO_x / \alpha\text{-Al}_2\text{O}_3$ (0001) interface whether V is conformal to the surface or is part of the particles. With coherent fractions of 0.2 or higher in the reduced state, a significant fraction of the V must be forming a coherent interface with the crystal surface, or forming an epitaxial bulk phase with a very similar d -spacing to the $\alpha\text{-Al}_2\text{O}_3$ lattice. We note that the XSW-measured coherent coverage of V in the reduced MV case is somewhat greater than the area of the interface between the particles and the $\alpha\text{-Al}_2\text{O}_3$ (0001) surface ($\sim 15\%$) as determined by analysis of AFM images. In the oxidized state, however, the coherent fractions are almost too small to be analyzable, suggesting a structure incoherent with the substrate.

In earlier work by Kim *et al.*, metallic V deposited in ultra-high vacuum (UHV) conditions onto a clean $\alpha\text{-Fe}_2\text{O}_3$ (0001) substrate was shown to donate electrons to the substrate to yield V^{3+} cations,

reducing surface Fe^{3+} species to Fe^{2+} [213]. In further work on 0.5 ML V / $\alpha\text{-Fe}_2\text{O}_3$ (0001), it was found that V undergoes a reversible transition between V^{3+} under exposure to atomic H and V^{5+} under oxidizing conditions[131]. In both cases, 1/3 of the V occupies the surface A site. However, there is a shift in position of the remaining fraction of V, from 27% in the C site under reducing conditions to 8% in the B site under oxidizing conditions. Related theoretical investigations explained the low energy state of A-site V occupation but did not adequately explain the C site occupation in the reduced state[129, 130]. However, a more recent study suggested the importance of reduction conditions, as annealing in 2% H_2 bal. He resulted in V occupying the A and B sites, with no evidence of C site occupation[207].

Our results for 0.9 ML V / $\alpha\text{-Al}_2\text{O}_3$ (0001), in contrast, show a partial reduction to V^{4+} from V^{5+} . Considering the enhancement in the coherent fraction in the reduced phase, we consider the possibility of a transition between incoherent V^{5+} and coherently ordered V^{4+} similar to that observed for 2 ML VO_x / $\alpha\text{-TiO}_2$ (110)[33]. In that study, a redox-reversible shift from V^{5+} to V^{4+} corresponded with a dramatic increase in XSW-measured coherency with the substrate lattice. This involved a phase transition between V_2O_5 and rutile VO_2 which could form an epitaxy with the TiO_2 substrate. While these films are too thin to think of as bulk-like phases, some interface structures can be proposed.

From several V / $\alpha\text{-Al}_2\text{O}_3$ (0001) calculations at coverages from 0.25 to 1 ML, a few good matches with experimental data may be picked out, all on Al-terminated sapphire: 0.5 ML $\text{V}_B\text{-O(OH)}_2$ and $\text{V}_B\text{-(OH)}_3$, and 0.25 ML $\text{V}_2\text{Al}_4\text{-O}_3\text{(OH)}_2$ dimers. Each of these cases shows good agreement with XSW coherent positions and some reduction of V from a V^{5+} state. However, the measured coherent fraction suggests that, for a single-site model, only 0.2 ML V occupies a position near

the measured coherent position. There are two interpretations: (1) the remaining 0.7 ML V is part of some incoherent phase that is “invisible” to XSW, or (2) a multiple-site model should be used instead to account for higher coherent occupation of multiple sites, which add “in phase”, resulting in a lower measured coherent fraction for some average coherent position. With limited experimental evidence, these interpretations are open. Regardless, valuable chemical information may still be gleaned from the most stable structural models.

Two mixed V-W samples were studied, with compositions of 0.90 ML V / 0.77 ML W and 1.04 ML V / 0.55 ML W. Both of these samples show two features in AFM: broad islands, about 1-2 nm in height, and larger nanoparticles. In each sample, some fraction of V reduces to the 4+ oxidation state upon exposure to mild reducing conditions, and W shows shifts in binding energy as well. This is evidence of a co-reduction of W with another cation, as has been observed for W / α -Fe₂O₃[66, 126] and V / W / α -TiO₂[36]. The chemical nature of this co-reduction is investigated using DFT calculations. Upon adding fully oxidized V to a fully oxidized W / α -Al₂O₃ surface, there is little change in the W PDOS: only the broad W 5d – O 2p feature exists below the Fermi level, with no available unoccupied states above it (see **Figure 4.15**). When surface V is reduced, however, it is immediately clear that W is affected as well (see **Figure 4.16**): partially occupied W *d*-states appear at the Fermi level, indicating the possibility of electron exchange. These W *d*-states correspond to those involved in the W^{(6- δ)+} model of Brønsted acidity[194, 195], suggesting that the formation of Brønsted acid sites might be facilitated via co-reduction of W with V. While these ground-state DFT models cannot suggest a dynamic mechanism for reduction and charge transfer, the degeneracy of V and W states indicates that no perturbation is needed to facilitate

charge transfer between the two cations – a “zero-cost transfer” of charge from easily reducible V to less-reducible W would occur upon reduction.

As for an interpretation of the experimental structures, the models shown in **Figure 4.16** provide adequate matches to the XSW-derived coherent positions for V and W for sample VW1. This assumes that both structures co-exist in roughly equal fractions on the sample surface, which would imply a total coherent coverage of about 0.35 ML W and 0.20 ML V. One interpretation is to consider the coherent V as “floating” on W, as the coherent position of W is essentially no different with or without V. The remaining fraction of W and V could exist in an incoherent phase, such as in the larger nanoparticles on the surface.

A good model for the experimental results for sample VW2 is elusive, as none of the mixed V-W theoretical models adequately match the XSW results. The coherent W coverage (assuming a single-site model) is only about 0.17 ML, $\frac{1}{2}$ that of the MW and VW1 models, although the W position again does not change significantly between oxidizing and reducing environments. On the other hand, the coherent coverage of reduced V is 0.34 ML, higher than for the reduced MV or VW1 samples. Results for sample VW2 may be affected by contaminants on its surface as revealed by XPS. For both samples VW1 and VW2, the total coherent fraction of W and V is about 0.5 ML, with coherent V:W ratios of about 1:2 for VW1 and 2:1 for VW2. It is possible that a larger-scale periodic phase exists on the surface; however, characterizing such a phase is beyond the scope of this work.

4.5 Conclusions

V and W were deposited on the α -Al₂O₃ (0001) surface by ALD and studied using AFM, XSW, and XPS. AFM imaging reveals that W forms conformal films with the surface, whereas V-containing films have large nanoparticles on the surface. XPS measurements show redox-reversible chemical state changes for V (V⁵⁺ after oxidation in O₂, mixed V⁵⁺/V⁴⁺ after reduction in dilute H₂), whereas W only shows subtle reductions in binding energy on samples containing V. XSW measurements indicate that while the position of W along the surface normal direction does not change significantly through a redox cycle, V becomes partially coherent with the substrate lattice only after reduction. Low coherent fractions of V indicate that much of it may compose the nanoparticles observed by AFM.

Surface structures were calculated for Al- and O-terminated α -Al₂O₃ (0001) decorated with W, V, Al, and coordinating ligands. A model structure for 0.5 ML W on the Al-terminated surface was found to be an excellent match with experimental data. The assignment of V was more ambiguous, but models with B-site V and A-site Al best matched the measured XSW positions. Analysis of relative reducibilities, partial densities of states for V and W, and band-decomposed charge densities revealed that V enables the partial reduction of W. This partial reduction introduces electronic states which are crucial to Brønsted acidity, providing insight into V-W synergy observed in industrial catalysts.

5. VO_x for NO_x-SCR: Effect of WO_x addition and substrate chemistry

In **Chapter 3** and **Chapter 4**, I discussed the structure and chemical behavior of catalytically active species on α -Fe₂O₃ (0001) and α -Al₂O₃ (0001) surfaces which have a similar structure but drastically different chemical behavior. While this offers fundamental insight into the behavior of these model surfaces, it does not approach the actual technical application – the selective catalytic reduction of nitric oxides with ammonia (NO-SCR). The aim of this chapter is to explore (via DFT) and compare the structure and chemistry of VO_x surface species as they relate to the adsorption of NH₃ and subsequent protonation to NH₄⁺, proposed to be the first step in the NO-SCR reaction in the Topsøe model[17]. First, the behavior of surface V species in different monomer and oligomer geometries supported on a α -Al₂O₃ (0001) is explored. Then, the influence of W on V is investigated to seek clues about the catalytic synergy between V and W. Finally, the support is replaced with α -Fe₂O₃ (0001) to test the effect of substrate chemistry.

5.1 Introduction

TiO₂ is the substrate of choice for industrial NO-SCR over mixed VO_x-WO_x catalysts. This substrate is technologically relevant for its intermediate reducibility and bandgap (both between those of hematite and sapphire). TiO₂-supported catalysts have been the subject of previous studies in our group undertaken by Dr. Chang-Yong Kim[32, 33] and Dr. Zhenxing Feng[34-36]. While Dr. Feng successfully measured the effect of cyclohexene oxidation on the structure of 1.5 ML VO_x/ α -TiO₂[35], the exploration of NO-SCR has been hampered by the difficulty of handling the gases involved (NO, NH₃). With our combined experiment-theory approach validating the

theoretical models used thus far, exploring the chemistry of NO-SCR *in silico* was a viable option for studying the surface chemistry under these technologically relevant conditions.

Using theoretical methods, we investigate the structure and chemistry of VO_x and WO_x species on α -Al₂O₃ (0001) and α -Fe₂O₃ (0001) surfaces which have similar corundum-type structures but drastically different chemical properties. We focus on the coordination environment and electronic structure of isolated VO_x monomers as well as dimers and long-chain oligomers. The effect of WO_x on the stability and chemistry of these structures is also investigated. We model NH₃ adsorption onto Brønsted acid sites, proposed as the first step of the NO-SCR reaction, and observe different adsorption behavior over different surface structures and stoichiometries.

In the selective catalytic reduction of NO, the most prevalent oxide of nitrogen, V has been proposed to play two synergistic roles[17]. Some V species provide Brønsted acid sites for NH₃ adsorption, and the resulting ammonium cation transfers a proton to a nearby redox V site. This reduces the redox site, activating it to bind NO and interact with the NH₃ to form N₂. While other interpretations of the NO-SCR reaction exist, nearly all involve the adsorption of NH₃ over an acid site as the initial step. Whether this adsorption is favored over a Brønsted or Lewis acid site is debated[28], although a kinetic model with adsorption over a V⁵⁺-OH Brønsted site has been validated for several sets of experimental data[216]. DFT calculations of VO_x clusters with hydroxyl or adsorbed water ligands show that NH₃ adsorbs over an oligomeric V⁵⁺-OH Brønsted site with subsequent abstraction of a proton and conversion to NH₄⁺, with a total NH₃ adsorption energy of -110 to -135 kJ/mol (-1.14 to -1.40 eV), depending on the oligomer structure[217-219]. However, NH₃ adsorbed on V⁵⁺=O species or certain oligomer structures relaxes to a hydrogen-

bonding configuration, with an NH_3 adsorption energy of -50 to -72 kJ/mol (-0.52 to -0.75 eV)[217].

The nature of the catalytically active V species depends on several factors, including the total VO_x coverage and the choice of oxide support. VO_x can take different oligomeric forms on the surface, ranging from isolated monomers to crystalline species such as V_2O_5 , and in many cases the morphology has consequences for the reactivity. The characterization of these VO_x species typically relies on techniques such as Raman spectroscopy from which the bonding characteristics between V and its ligands can be inferred. A variety of possible coordination configurations of monomeric VO_x have been proposed under different chemical environments and coordination structures with the oxide support[190, 191, 220-224]. At higher coverages of VO_x , V-O-V bridging bonds form, with subsequent changes in the chemical behavior of V, such as improved reducibility[22, 23]. For zeolite-supported V for high-temperature NO_x SCR, monomeric VO_x tetrahedra are hypothesized to be more catalytically active than octahedrally coordinated VO_x , which is more typical of denser oligomeric VO_x phases[18]. However, oligomeric VO_x in octahedral sites at about half-monolayer loading is the most active surface species on anatase TiO_2 , supporting the Topsøe model[19].

For many reactions, such as the oxidation of methanol to formaldehyde, only one V site is required[20]. However, due to the requirement that both NO and NH_3 bind on nearby active sites for successful SCR, isolated V monomers are not expected to be reactive. Indeed, the SCR turnover frequency per V atom of TiO_2 -supported VO_x peaks at about $\frac{1}{2}$ monolayer of VO_x before dropping due to the loss of acid sites and the crystallization of lower-density VO_x species to V_2O_5 [21].

The catalytic properties of catalytically active species (including V) are heavily influenced by the substrate chemistry[24], such as its ionic or covalent nature[25, 26]. For example, the activity of methanol oxidation over vanadia on several different supports was found to be independent of the structure of VO_x or terminal $\text{V}=\text{O}$ bond but heavily dependent on the substrate[24]. In particular, differences in reactivity were attributed to the interaction between V, O, and the support material. Similar results were observed for the oxidative dehydrogenation of propane to propylene, wherein the ratio of V monomers to polymers did not affect the turn-over frequency of the reaction; only the choice of substrate had a significant effect[27]. V has also been shown to be more reducible in the presence of other reducible metal cationic species, such as Ti^{4+} , although its reducibility decreases as its density increases, since crystalline V_2O_5 does not interact as strongly with the support material[19]. This reducibility from V^{5+} is particularly important to NO_x SCR according to the Topsøe model. We are therefore interested in the dependence of catalytic behavior on substrate chemistry. Considering their structural similarity but difference in chemical properties, $\alpha\text{-Al}_2\text{O}_3$ (0001) and $\alpha\text{-Fe}_2\text{O}_3$ (0001) single crystal surfaces were chosen for comparison.

The addition of W to VO_x catalysts for NO_x SCR is known to significantly improve the catalytic activity[28-31, 133]. However, the mechanism of this promotional effect is still not clear. Some studies suggest that W plays a chemical role, providing Brønsted acid sites to promote NH_3 adsorption[29, 30]. Others suggest that W serves to disperse VO_x , preventing it from crystallizing into inert forms[31]. For comparison, sulfur species may have a similar effect: the addition of surface sulfates, which provide strong Brønsted acid sites in the presence of water, was shown to improve SCR at sub-ML VO_x coverage[21]. This promotion could also be attributed to structural effects, with sulfate species rounding up V monomers into more reactive oligomeric species.

The structure of VO_x on the rutile TiO_2 (110) surface has recently been studied in detail using experimental and theoretical methods[34]. VO_x forms complex chains on this surface which undergo structural shifts through a reduction-oxidation (redox) cycle. Different components of the chains are more stable than others, suggesting that surface VO_x chemistry is nuanced and requires more detailed study. The goal of this work is to reveal the effects of VO_x structure and ordering on the behavior of catalyst surfaces under different chemical conditions. We also investigate the effect of W to assess the structural and chemical changes it induces in nearby V species. In particular, we assess the role of catalyst structure and composition on the first step of the NO-SCR reaction: the adsorption of NH_3 at a Brønsted acid site and associated proton transfer from the catalyst, yielding NH_4^+ . By assessing the adsorption energy of NH_3 and the associated changes in the atomic and electronic structure of the catalyst upon NH_3 adsorption, we clarify the roles of adsorption site geometry, the V-W interaction, and the effect of the substrate in the initial reaction step. The steps of the NO-SCR reaction beyond NH_3 adsorption are rather complex[216], and considering the difficulty of accurately predicting NO adsorption on oxides[225], modeling of further steps is beyond the scope of this work.

5.2 Methods

For this work, plane-wave DFT as implemented in VASP was used; see previous chapters for a description of this method. A projector augmented wave (PAW) pseudopotential scheme was employed with a 400 eV cutoff energy, and PW91 exchange-correlation functionals were used for all calculations. The PW91 functional has been shown to give reasonable results for NH_3 adsorption on surfaces[226]. $\alpha\text{-Al}_2\text{O}_3$ (0001) and $\alpha\text{-Fe}_2\text{O}_3$ (0001) surface supercells similar to those described before were used, including (1x1) and (2x1) supercells. (4x4x1) k -point meshes

were used for all (1x1) supercell calculations. For (2x1) supercells, (2x4x1) meshes were sufficient for structural relaxation, and densities of states were calculated using (4x8x1) meshes. Bonding and charge transfer characteristics were measured by Bader integrated charge and bond valence sums (BVS). In all cases, the structures are set up by placing V, W, O and OH ligands, and NH₃ adsorbates onto the clean O-terminated (0001) surface of these substrates.

5.3 Results

5.3.1 0.5 ML V / O-terminated α -Al₂O₃ (0001)

To investigate the interaction between catalytically active surface species, vanadium atoms were placed on (2x1) O-terminated sapphire (0001) surface supercells at 0.5 monolayer equivalent coverage and allowed to relax. Adsorption structures included monomers, where the surface cations occupied the bulk-like A site, as well as dimers and polymers, where selected A and B sites were occupied. Because of the periodic boundary conditions, either isolated dimers or infinite-length polymers could be simulated by selecting particular metal adsorption sites in the supercell. From this point forward, the configurations are denoted V_{A12} for monomers, with two A-site V; V_{A1B1} for dimers, with the A and B sites occupied by V in one unit cell, and the other unit cell empty; and V_{A2B1} for polymers, with neighboring A and B sites in neighboring unit cells. The ligands will be similarly referred to by these subscripts. In tables, I and II will refer to the two different cation sites. In monomer cases, I and II refer to the A1 and A2 sites, respectively; for dimer and polymer structures, I and II refer to the A and B site, respectively.

Results for V atoms adsorbed on clean sapphire (0001) surfaces are shown in **Table 5.1**. The case of dispersed V monomers corresponds to a replacement of the surface A-site Al atoms in the model Al-terminated sapphire supercell with V atoms with a nominal charge of 3+. This configuration is

the most stable, with polymers relatively less stable by 1.33 eV and dimers by 1.89 eV. **Figure 5.1** gives a top-down view of the three configurations, with the V coordination environment shown in green. In the monomer case, the surface remains relatively undistorted; however, for the dimer and polymer cases, the symmetry of the surface oxygen lattice is broken, and the V-O coordination increases.

	V _{A12} (monomers)	V _{A1,B1} (dimers)	V _{A2,B1} (polymers)
Relative energy (eV)	0.00	1.89	1.33
V _{A1} -O coordination (Å)	1.75, 1.75, 1.75	1.75, 1.76, 1.88, 2.00	1.76, 1.78, 1.83, 2.04
Q _B (V _{A1})	1.72	1.84	1.93
BVS(V _{A1})	3.34	3.50	3.45
V _{A2} -O coordination (Å)	1.75, 1.75, 1.75	1.70, 1.70, 1.81	1.72, 1.85, 1.87, 2.15
Q _B (V _{A2})	1.73	1.25	1.53
BVS(V _{A2})	3.34	3.55	3.17

Table 5.1: Structural and chemical information for reduced $\frac{1}{2}$ ML V structures and coordination environments atop the O-terminated (2x1) α -Al₂O₃ (0001) surface supercell. The supercell total energy is given relative to the lowest-energy structure; positive values therefore indicate a thermodynamically unfavored structure. Bader charges (Q_B) and bond valence sums (BVS) are given in units of electron charge (*e*).

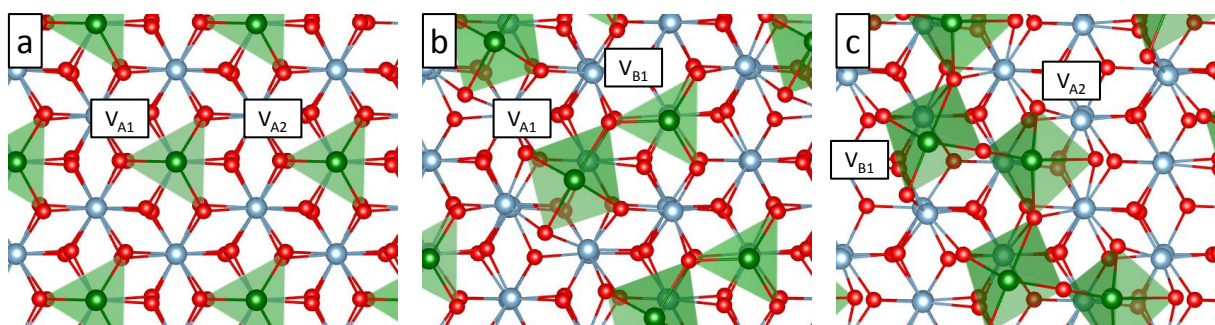


Figure 5.1: Top (0001) views of (a) V_{A12} (monomers); (b) V_{A1B1} (dimers); and (c) V_{A2B1} (polymers). V atoms and coordination polyhedra are shown in green; O, red; and Al, light blue. V positions are labeled near their respective polyhedra.

Under realistic non-vacuum conditions, it is unlikely that the V atoms would remain exposed without interacting with a molecule from the gas phase such as O₂, H₂O, or H₂. We therefore investigate a series of coordination environments for the three geometries shown above, starting with the most stable case, that of dispersed V monomers. On the O-terminated sapphire surface, with a nominal surface charge of 3-, V should have a 3+ formal charge; thus, a single terminal hydroxyl group (V-OH) should oxidize this cation to V⁴⁺, and a vanadyl group (V=O) would yield V⁵⁺. Data for three different coordination environments for the monomer case is given in **Table 5.2**, and structures are shown in **Figure 5.2**. In all cases, the surface symmetry is mostly preserved, and V forms distorted tetrahedra with the 4 coordinating O atoms. Bader charges do not show large differences between vanadyl species and hydroxylated V. However, bond valence sums of the O-terminated vanadia are close to those of bulk V₂O₅ (4.80), corresponding to a nominal V⁵⁺ formal charge, whereas the OH-terminated vanadia have bond valence sums closer to those for VO₂ (4.00), corresponding to V⁴⁺. Analysis of the underlying Al atoms show that the topmost Al_C atom is slightly more oxidized than the bulk-like Al³⁺ cation (BVS = 3.01), while the Al_B atom, which sits slightly lower, is partially reduced.

Analysis of the $\Delta E_{+\frac{1}{2}H_2}$ value (defined in **Chapter 4**) gives a similar result as for the 1x1 V_A-O → V_A-OH reaction for these larger (2x1) supercells. However, an intermediate step with only ½ hydroxylation is shown here. This intermediate is shown to be the exothermic step, with the second hydroxylation endothermic. In a reduction of V_A-O with H₂, the energy gained from the first step of the reaction would likely be more than enough to enable the complete reduction to V_A-OH. This stepwise addition of H to two adjacent and nearly identical V sites enables a simple way to study the interaction between coordinated metal groups at the catalyst surface. As the shifts in Bader

charge and BVS indicate, there is some interaction between the two V species here, despite their separation of over 4.7 Å. In particular, the nature of the hydroxylated V changes significantly in the “mixed termination” state in which it neighbors a vanadyl group instead of another hydroxyl group. The Bader charge increases significantly, and the BVS suggests a V charge state between 4+ and 5+. This V-V interaction is investigated herein by a detailed study of the electronic structure of the surface.

	$V_{A12}-(OH)_{A12}$	$V_{A12}-O_{A1}(OH)_{A2}$	$V_{A12}-O_{A12}$
$\Delta E_{+\frac{1}{2}H_2}$	--	0.20	-0.45
V_I -O coordination (Å)	1.77, 1.78, 1.78, 1.80	1.61 , 1.79, 1.79, 1.79	1.61 , 1.79, 1.79, 1.79
$Q_B(V_I)$	2.11	2.14	2.16
BVS(V_I)	4.11	4.69	4.72
V_{II} -O coordination (Å)	1.77, 1.77, 1.78, 1.80	1.75, 1.76, 1.76, 1.78	1.61 , 1.79, 1.79, 1.79
$Q_B(V_{II})$	2.11	2.24	2.16
BVS(V_{II})	4.10	4.33	4.72
Al_C -O coordination	1.87, 1.87, 1.88, 1.89, 1.89, 1.89	I: 1.86, 1.86, 1.89, 1.90, 1.90, 1.90 II: 1.85, 1.88, 1.88, 1.88, 1.89, 1.89	1.84, 1.84, 1.84, 1.92, 1.92, 1.92
BVS $_{AlC}$	3.20	I: 3.20 II: 3.23	3.22
Al_B -O coordination	1.85, 1.86, 1.86, 2.00, 2.01, 2.02	I: 1.85, 1.86, 1.87, 1.97, 2.00, 2.02 II: 1.85, 1.86, 1.87, 1.97, 1.98, 2.04	1.89, 1.89, 1.90, 1.94, 1.95, 1.95
BVS $_{AlB}$	2.87	I: 2.89 II: 2.88	2.91

Table 5.2: Structural and chemical information for $\frac{1}{2}$ ML monomer V structures on the (0001) sapphire surface with values as defined before, including for near-surface Al species. Energies of H addition are as described in **Chapter 4**. Coordination lengths in **bold** correspond to the bond length between vanadium and the terminal oxygen atom specified at the top of the column.

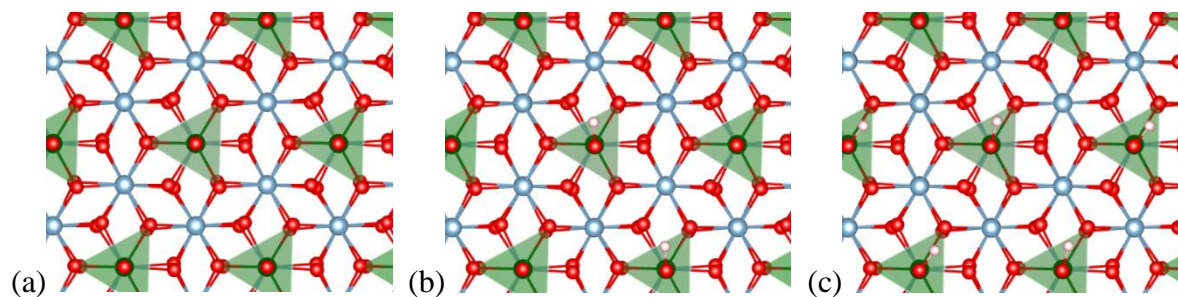


Figure 5.2: Top (0001) views of (a) $V_{A12}-O_{A12}$; (b) $V_{A12}-O_{A1}(OH)_{A2}$; and (c) $V_{A12}-(OH)_{A12}$. Colors as defined before, with H atoms as small white circles.

Atom-projected partial densities of states (PDOS) for the V atoms in these cases are plotted in **Figure 5.3**. The PDOS of each atom is plotted in a different line type and filled with diagonal lines to distinguish the two. In all cases, there are two primary sets of features: a broad V $3d - O 2p$ hybridization feature below the Fermi level E_F , and one or more localized d -states at or above E_F . For the structures with the same terminal ligands on each V atom ($V_{A12}-O_{A12}$ and $V_{A12}-(OH)_{A12}$), the PDOS of each are indistinguishable (as indicated by the cross-hatched lines under the PDOS curve). However, for the mixed-termination case ($V_{A12}-O_{A1}(OH)_{A2}$), the features in the PDOS can be clearly distinguished as belonging to one site or the other. The presence of a nearby vanadyl group narrows the distribution of electronic states on the hydroxylated V, a possible cause of the increases in Bader charge and BVS. Likewise, some of the vanadyl d -states above E_F disappear.

The sharp d -states can also be shown in real space using a band-projected charge density calculation as described in **Chapter 4**. The V-OH and V=O d -states in the mixed-termination structure are resolved in **Figure 5.4(a-d)**. Both structures show a fairly isotropic charge density in the surface plane due to mixing of several d -orbitals, although a slight triangular shape in the charge distribution around the hydroxylated V atoms can be discerned. The presence of a nearby vanadyl group does not change the shape of the near- E_F states of hydroxylated V.

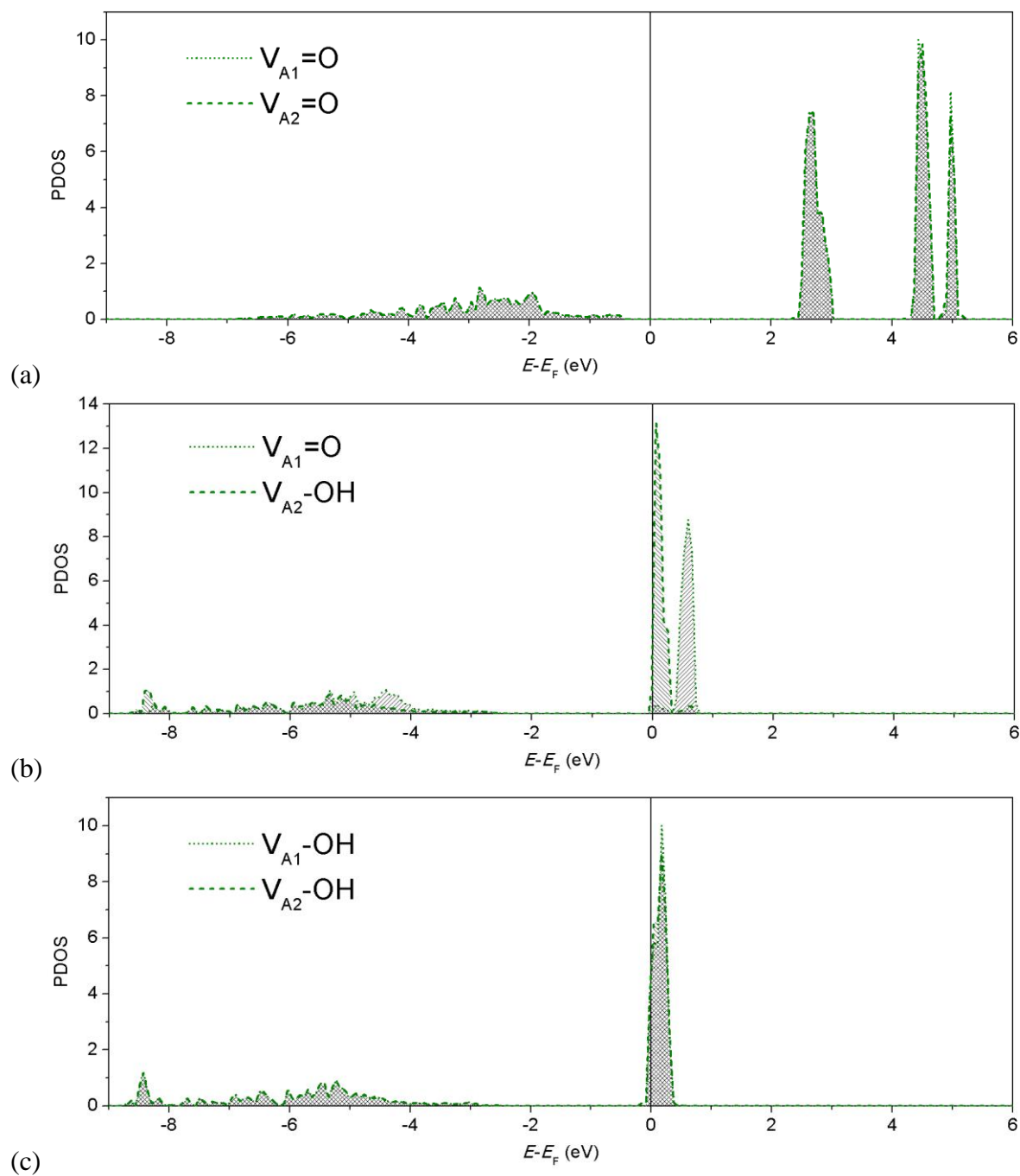


Figure 5.3: V atom-projected partial densities of states (PDOS) for relaxed structures of V monomers on sapphire: (a) $V_{A12}-O_{A12}$; (b) $V_{A12}-O_{A1}(\text{OH})_{A2}$; and (c) $V_{A12}-(\text{OH})_{A12}$. Diagonal cross-hatching is used to distinguish each atomic PDOS.

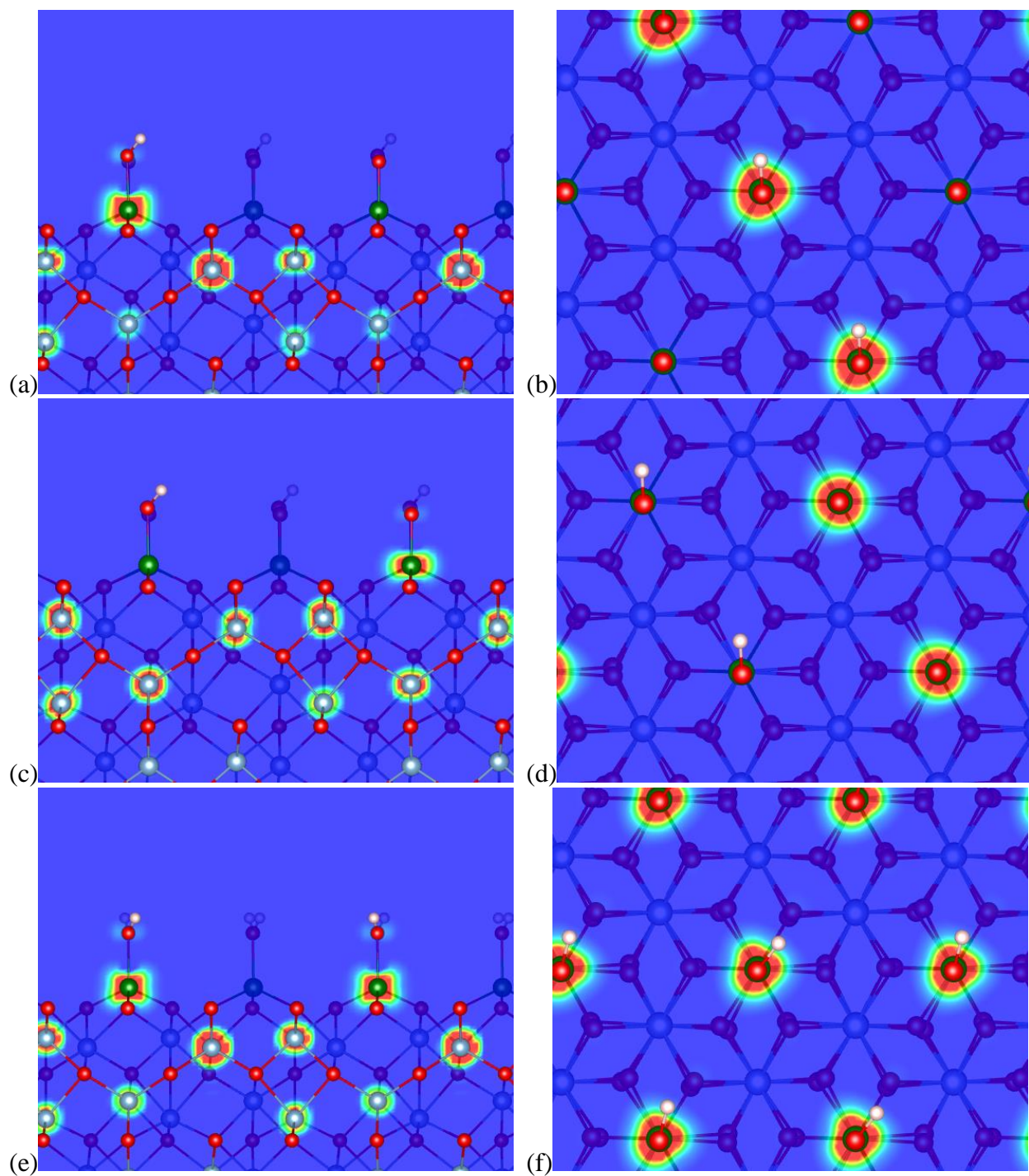


Figure 5.4: Band-projected partial charge densities for $V_{A12}-O_{A1}(OH)_{A2}$ from (a,b) $-0.1 - 0.3$ eV and (c,d) $0.3 - 0.8$ eV relative to E_F , and for $V_{A12}-(OH)_{A12}$ for (e,f) $-0.1 - 0.4$ eV. Images show slices of the partial charge density that pass through the V atoms in the (a,c,e) $(1\ 1\ -2\ 0)$ and (b,d,f) $(0\ 0\ 0\ 1)$ directions.

The effect of partial reduction to a mixed-termination state can also be visualized by subtracting the total charge density of one structure from another. The change in charge density through a reduction series from a fully oxidized (vanadyl-only) structure to the mixed-termination structure and finally to a fully hydroxylated structure is shown in **Figure 5.5**. Analysis of these maps show that when a hydrogen atom is added to the double vanadyl case, there is very little perturbation around the remaining vanadyl group. The hydroxylated V, however, shows significant shifts in the charge density associated with the coordinating oxygen at the surface and around the vanadium atom as compared to the vanadyl case. The addition of a single hydrogen atom induces significant charge density shifts throughout the near-surface atoms in the lattice: the O atoms are shifted slightly upward. (We note that there may be no visible charge density shift around Al since in our model the highly ionic Al atoms have nearly zero valence charge associated with them.)

The differences are smaller and fewer before and after a second hydrogen atom is added, completely hydroxylating the surface. There are no further perturbations in the electron distribution in the near-surface lattice, although perturbations are observed near the surface oxygen atoms. A significant shift is observed for the oxygen atom most proximal to the hydroxyl group on which the second H has been added. The electron density around the first hydroxylated V atom shifts slightly in response to the additional H about 5 Å away. The charge density difference map for the full reaction shows the aggregate shift after both reaction steps.

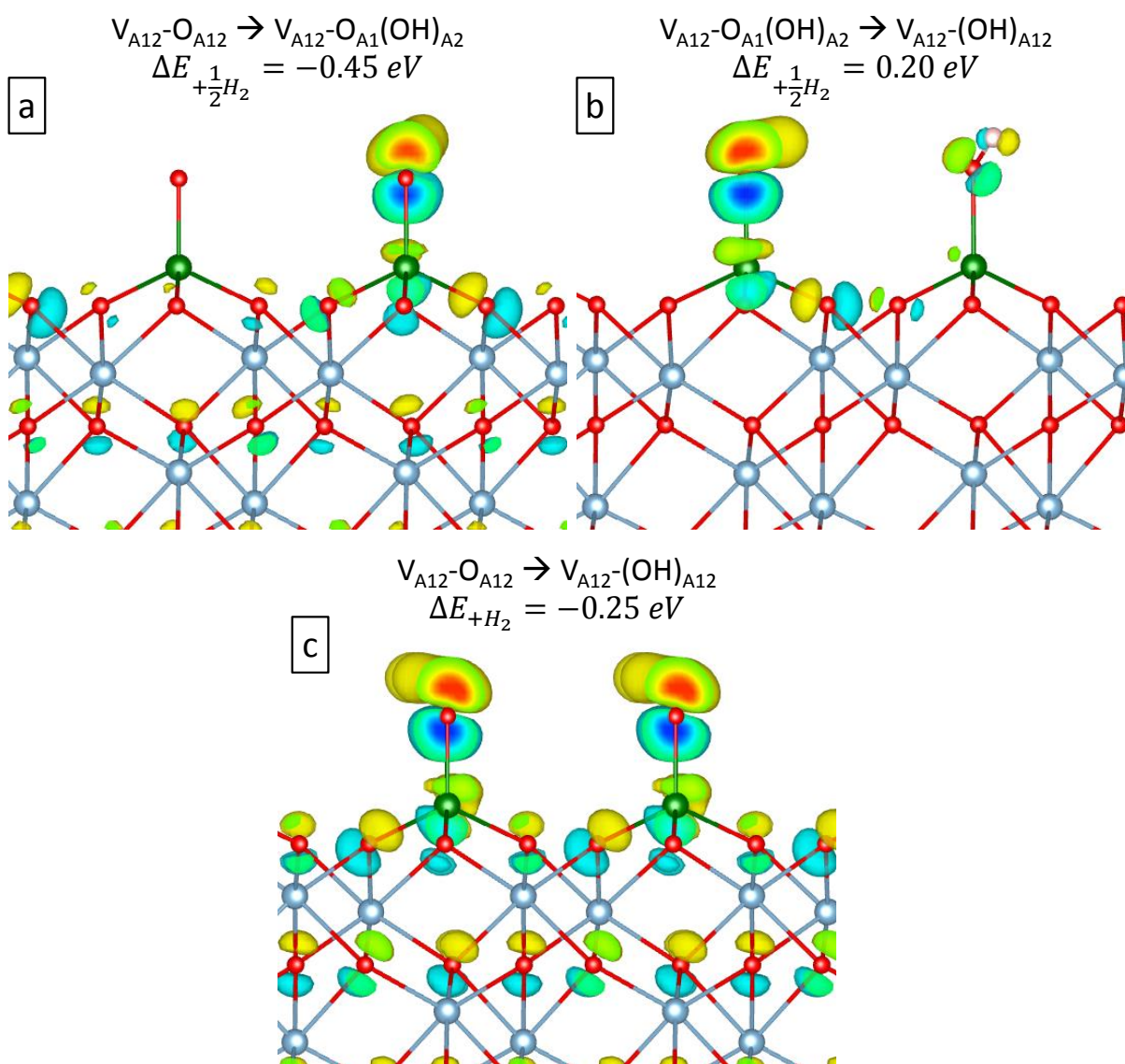


Figure 5.5: Charge difference maps for the reactions (a) $V_{A12}^-O_{A12} \rightarrow V_{A12}^-O_{A1}(OH)_{A2}$; (b) $V_{A12}^-O_{A1}(OH)_{A2} \rightarrow V_{A12}^-(OH)_{A12}$; (c) $V_{A12}^-O_{A12} \rightarrow V_{A12}^-(OH)_{A12}$. Energies of each reaction are included. Isosurfaces and charge densities in yellow and red indicate increases in charge density, while blue indicates decreases.

Table 5.3 compares the stabilities, geometrical parameters, and chemical / electronic states for monomer, polymer, and dimer configurations of 0.5 ML V with either one or two additional O atoms added per 2x1 supercell for an expected total formal charge of 8+ or 10+, respectively, among the two surface V species. The first two columns show results for dimer and polymer cases with a single bridging oxygen added between the V-O polyhedra, a configuration that is not possible in the monomer case. The dimer is much more stable than the polymer, although the charge states and valence are similar in both cases. For both the dimer and polymer case, the A-site cation (I) has a significantly higher valence than the B-site cation (II). These structures are shown in **Figure 5.6**.

For the structures with two additional oxygen atoms per (2x1) unit cell, the terminal O atoms were initially placed so as to make vanadyl groups on the surface in most cases. For the polymer configuration, an additional double-bridging configuration was relaxed. Overall, the monomer case (which is identical to the $V_{A12}-O_{A12}$ case described above) is the most stable by over 2 eV from the dimer case and by over 3 eV from the polymer structures. In all vanadyl cases, the V is close to its expected valence of 5+ as given by the BVS. The A-site V-O tetrahedra in the vanadyl dimer and polymer cases migrate away from the high-symmetry site, breaking apart the dimers and polymers into monomers and dimers, respectively. However, the vanadyl configuration is slightly less stable (by 0.11 eV) for the polymer case than the double-bridging configuration. While the shared bridging oxygen atoms help this structure retain its polymer configuration, the BVS is slightly lowered for both cations as longer bonds are required to bridge the polyhedra.

	$V_{A1B1}-O_{br}$	$V_{A2B1}-O_{br}$	$V_{A12}-O_{A12}$	$V_{A1B1}-O_{A1B1}$	$V_{A2B1}-O_2$	$V_{A2B1}-O_{2br}$
Relative energy (eV)	0.00	1.44	0.00	2.19	3.50	3.39
$V_{I}-O$ coordination (Å)	1.75, 1.81, 1.85 , 1.98, 2.04	1.74, 1.86, 1.87, 1.90 , 2.02	1.61 , 1.79, 1.79, 1.79	1.61 , 1.77, 1.79, 1.83	1.61 , 1.75, 1.77, 1.87	1.71 , 1.80, 1.84, 1.87, 1.92
$Q_B(V_I)$	2.10	2.10	2.16	2.20	2.20	2.26
$BVS(V_I)$	3.90	3.92	4.72	4.69	4.69	4.52
$V_{II}-O$ coordination (Å)	1.69, 1.81, 1.86 , 1.98	1.72, 1.77 , 1.89, 1.92	1.61 , 1.79, 1.79, 1.79	1.61 , 1.78, 1.79, 1.79	1.61 , 1.76, 1.77, 1.83	1.60 , 1.75, 1.88, 1.96, 2.19
$Q_B(V_{II})$	1.97	1.99	2.16	2.13	2.20	2.20
$BVS(V_{II})$	3.63	3.68	4.72	4.75	4.79	4.53

Table 5.3: Structural and chemical information for $\frac{1}{2}$ ML V structures on the (0001) sapphire surface with one or two additional O ligands, with values as defined previously.

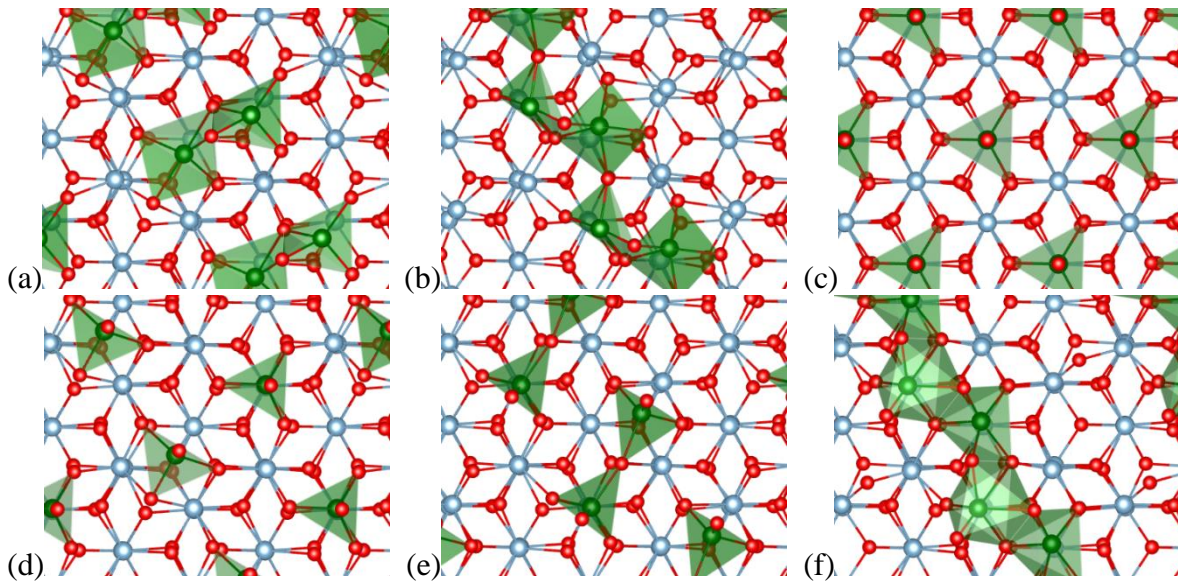


Figure 5.6: Top (0001) views of: (a) $V_{A1B1}-O_{br}$; (b) $V_{A2B1}-O_{br}$; (c) $V_{A12}-O_{A12}$; (d) $V_{A1B1}-O_{A1B1}$; (e) $V_{A2B1}-O_{A2B1}$; (f) $V_{A2B1}-O_{2br}$.

Table 5.4 and **Figure 5.7** show results for configurations wherein half of the V atoms are hydroxylated, whereas the other half are terminated with O atoms to simulate vanadyl groups. This corresponds to a moderately reduced surface with neighboring cations of different coordinations

and oxidation states. From the various starting conditions, these isostoichiometric configurations sometimes relax into the same structure; hence, some combinations of starting ligand positions are not reported here. The monomer case, which is the most stable of the series, has already been discussed above. The most stable dimer and polymer configurations are higher in energy by 1.92 and 1.78 eV, respectively. The V-O polyhedra in the most stable dimer case are separated; in fact, the A-site cation sits in a very similar position as for the fully oxidized case. The valence of the hydroxylated B-site cation is only reduced from the fully oxidized case by 0.14 e, whereas the A-site cation is barely changed. Similar behavior is observed for the most stable polymer configuration, which is not much different than its fully oxidized counterpart, with only slight reduction of both cations. Interestingly, the additional H atom is most stable at a surface oxygen site, forming a hydroxyl group on the alumina surface. This leaves two vanadyl groups with nominal 5+ charge as in the fully oxidized case.

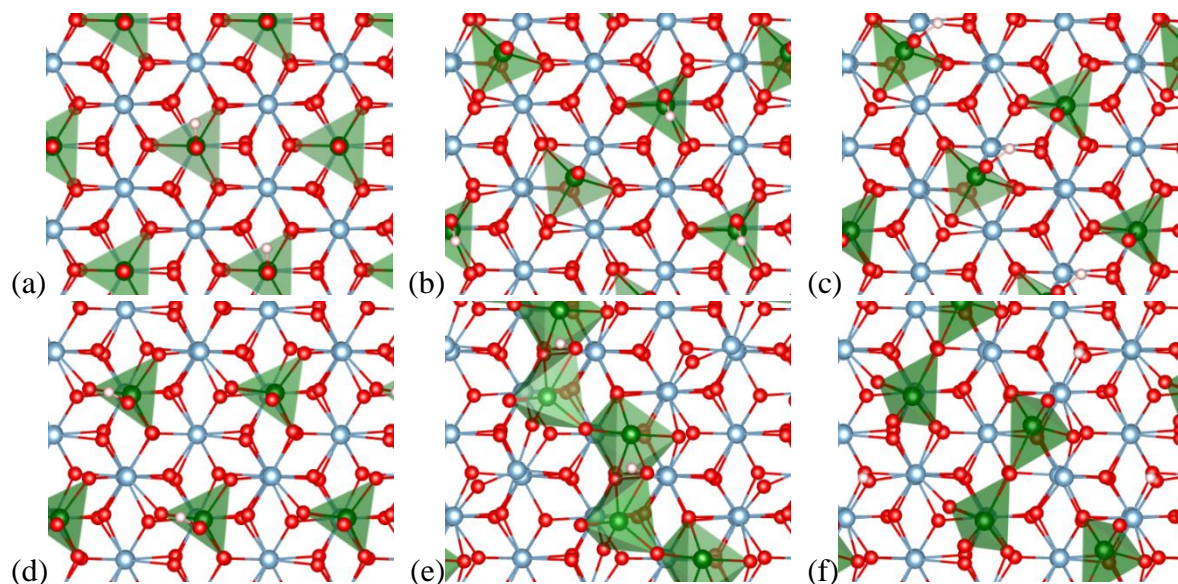


Figure 5.7: Top (0001) views of: (a) $V_{A12}-O_{A1}(OH)_{A2}$; (b) $V_{A1B1}-O_{A1}(OH)_{B1}$; (c) $V_{A1B1}-O_{br}(OH)_{A1}$; (d) $V_{A2B1}-O_{B1}(OH)_{A2}$; (e) $V_{A2B1}-O_{br}(OH)_{A2}$; (f) $V_{A2B1}-O_{br}(OH)_{B1}$.

	V_{A12^-} $O_{A1}(OH)_{A2}$	V_{A1B1^-} $O_{A1}(OH)_{B1}$	V_{A1B1^-} $O_{br}(OH)_{A1}$	V_{A2B1^-} $O_{B1}(OH)_{A2}$	V_{A2B1^-} $O_{br}(OH)_{A2}$	V_{A2B1^-} $O_{br}(OH)_{B1}$
Relative energy (eV)	0.00	1.92	1.97	2.18	3.44	1.78
V_I -O coordination (Å)	1.61 , 1.79, 1.79, 1.79	1.62 , 1.77, 1.79, 1.81	1.73, 1.75, 1.76 , 1.79	1.70, 1.72, 1.75, 1.78	1.77, 1.78, 1.83, 1.89 , 1.98	1.61 , 1.80, 1.80, 1.81
$Q_B(V_I)$	2.14	2.17	2.20	2.19	2.20	2.19
BVS(V_I)	4.69	4.70	4.40	4.68	4.23	4.60
V_{II} -O coordination (Å)	1.75, 1.76, 1.76, 1.78	1.70, 1.74, 1.75, 1.78	1.64 , 1.74, 1.77, 1.78	1.62 , 1.74, 1.78, 1.80	1.60, 1.75 , 1.90, 2.05 , 2.07	1.61 , 1.78, 1.80, 1.82
$Q_B(V_{II})$	2.24	2.17	2.18	2.17	2.18	2.17
BVS(V_{II})	4.33	4.61	4.80	4.82	4.48	4.64

Table 5.4: Structural and chemical information for $\frac{1}{2}$ ML V structures on the (0001) sapphire surface with one additional O and one OH ligands, with values as defined previously.

Table 5.5 and **Figure 5.8** show results for 2x1 supercells in which both V atoms are singly hydroxylated. For the dimer and polymer cases, an additional bridging O was added as well in order to fully coordinate the surface V. As expected, the valence in each case suggests that V is in the 4+ oxidation state in all cases. As for the oxidized and partially hydroxylated cases shown before, the monomer is the most stable structure, followed by the dimer and polymer. However, here the V-O polyhedra remain connected in the dimer and polymer cases. The H atoms remain near the terminal oxygen atoms, indicating that the hydroxyl groups are preserved and do not dissociate as in the previous partially hydroxylated polymer case. Upon the addition of an additional bridging O atom, the polymer case becomes more stable than the dimer. However, the V-O polyhedra separate, with the V atoms occupying A sites as in the monomer case. The additional O ends up as a vanadyl group on the V_{II} cation.

	$V_{A12}-(OH)_{A12}$	$V_{A1B1}-(OH)_{A1B1}$	$V_{A2B1}-(OH)_{A2B1}$		$V_{A1B1}-O_{br}(OH)_{A1B1}$	$V_{A2B1}-O_{br}(OH)_{A2B1}$
Relative energy (eV)	0.00	1.88	3.56		0.61	0.00
$V_{I}-O$ coordination (Å)	1.77, 1.78, 1.78, 1.80	1.75, 1.79 , 1.79, 1.89, 2.27	1.72, 1.81, 1.82 , 1.92, 2.18		1.76, 1.79 , 1.82 , 1.82, 1.96	1.75, 1.76 , 1.77, 1.82, 2.18
$Q_B(V_I)$	2.11	2.15	2.14		2.28	2.27
BVS(V_I)	4.11	3.82 (4.04)	4.05		4.46	4.49
$V_{II}-O$ coordination (Å)	1.77, 1.77, 1.78, 1.80	1.70, 1.78, 1.79, 1.81	1.71, 1.79, 1.82 , 1.92		1.69, 1.78 , 1.81, 1.90 , 1.94	1.63 , 1.78 , 1.79, 1.79
$Q_B(V_{II})$	2.11	2.13	2.05		2.29	2.24
BVS(V_{II})	4.10	4.27	3.84		4.62	4.62

Table 5.5: Structural and chemical information for $\frac{1}{2}$ ML V structures on the (0001) sapphire surface with two additional OH ligands, as well as one additional O and two OH ligands, with values as defined previously.

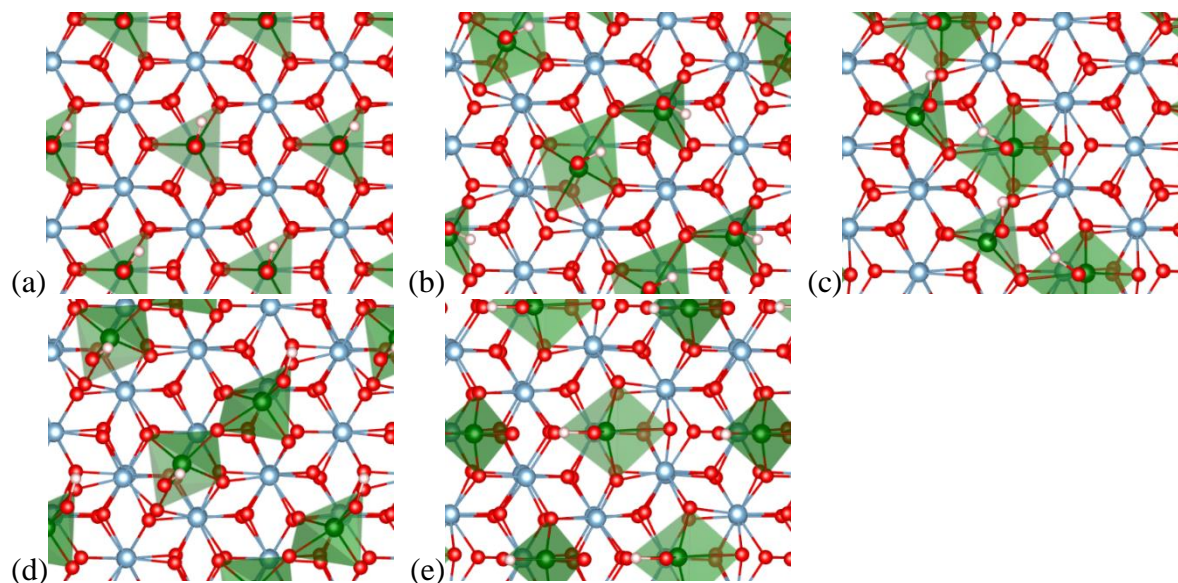


Figure 5.8: Top (0001) views of: (a) $V_{A12}-(OH)_{A12}$; (b) $V_{A1B1}-(OH)_{A1B1}$; (c) $V_{A2B1}-(OH)_{A2B1}$; (d) $V_{A1B1}-O_{br}(OH)_{A1B1}$; (e) $V_{A2B1}-O_{br}(OH)_{A2B1}$.

5.3.2 0.5 ML V / O-terminated α -Al₂O₃ (0001): NH₃ adsorption

Topsøe suggests that NH₃ adsorption onto a Brønsted acid site is the first step in a SCR reaction cycle[17]. This adsorption event may weaken nearby V=O bonds, reducing the vanadyl species on titania supports[227] and thereby activating these sites for NO adsorption[17]. We investigate this behavior for the singly hydroxylated VO_x / α -Al₂O₃ surfaces described above by adding an NH₃ molecule and relaxing the atomic configuration. In the monomer and dimer cases, this configuration simulates –OH - - - NH₃ hydrogen bonding, as has been observed for several hydroxylated oxide surfaces[228]. For the stable polymer case in which the hydroxyl group dissociated, there is no obvious Brønsted-like site, and so the molecule is adsorbed to the terminal O atom of each V, simulating a O - - - NH₃ interaction. Results are shown in **Table 5.6**, where $E_{\text{NH}_3\text{-ads}}$ is the adsorption energy of the NH₃ molecule, and structures are shown in **Figure 5.9**.

The monomer case is again the most stable, with a >2 eV advantage over the dimer and polymer cases. In fact, the adsorption of NH₃ destabilizes the dimer by 0.2 eV and the polymer by 0.52 eV relative to the NH₃-free cases. The monomer case has the largest NH₃ adsorption energy as well. In both the monomer and dimer cases, the NH₃ molecule interacts strongly with the hydroxyl, becoming an NH₄⁺ ion which weakly interacts with the terminal O of the surrounding V-O tetrahedra. Bader analysis shows the NH₄ structure has a total charge of +0.81, confirming the assignment as an ammonium cation. The bond length between each V and the terminal O atom (1.66 Å, 1.69 Å) is intermediate between that of the vanadyl (1.61 Å) and hydroxylated (1.78 Å) V-O bonds for the monomer case prior to NH₃ adsorption. While the original vanadyl site remains at V⁵⁺ (4.62 with NH₃ vs. 4.69 without), the originally hydroxylated site is substantially oxidized

(4.53 with NH_3 vs. 4.33 without), appearing more like V^{5+} than V^{4+} . Similar behavior is observed for the dimer case.

The polymer cases are the least favorable (by the same energy), but their behavior is significantly different from the monomer and dimer cases. With no nearby H, the NH_3 remains as a molecule (roughly neutral, with a Bader charge of $-0.10 e$) which interacts directly with the V atoms at the center of the V-O tetrahedra in a Lewis acid-like manner. While the adsorption is exothermic, the magnitude of the NH_3 adsorption energy is about 0.5 eV less than the $(-\text{O})_n - \text{NH}_4^+$ interaction demonstrated for the monomer case. The BVS contribution to V from N can be calculated using parameters given in Ref. [229] and is included in **Table 5.6**. If only the V-O coordination is considered in the BVS, V appears to be in a clear 4+ state in both Lewis acid-like cases; however, if the contribution from N is included, the BVS takes on a value about halfway between that of bulk-like V^{4+} (4.00) and V^{5+} (4.80). The local structures and NH_3 adsorption energies at Brønsted acid sites (monomer and dimer cases) and Lewis acid sites (polymer cases) are similar to those recently reported for the V_2O_5 (001) surface using similar theoretical methods[230].

Because the most stable ammonia-free polymer structures featured dissociated terminal hydroxyl groups, these cases were re-evaluated by moving the H onto either the terminal or bridging O sites on the relaxed polymer example and placing the NH_3 above, as in the monomer and dimer cases. However, these structures were all substantially less stable than those mentioned above and were not considered for further analysis.

Figure 5.10 shows the effect of NH_3 adsorption on the V PDOS of the monomer $\text{V}_{\text{A}12}\text{-O}_{\text{A}1}(\text{OH})_{\text{A}2}$ and nominally polymer $\text{V}_{\text{A}2\text{B}1}\text{-O}_{\text{br}}(\text{OH})_{\text{B}1}\text{-(NH}_3\text{)}_{\text{B}1}$ surfaces. In both cases, the structures relax such that the hydroxyl group ends up as a vanadyl group. Interestingly, the PDOS of the V associated

with the hydroxyl group is less affected than the vanadyl V in both cases, possibly due to the change in local symmetry and lengthening of the vanadyl bond. In fact, after NH_3 adsorption on the monomer configuration, the narrow V bands just above E_F become nearly degenerate, corresponding to their similar local structure. For the monomer configuration, the adsorbed ammonium cation is clearly very stable, as the main components of its PDOS sit in narrow bands more than 9 eV below E_F . On the other hand, in the polymer case, the sharp feature above E_F for the V atom acting as the Lewis acid site shifts towards E_F . There is also stronger mixing between NH_3 states and the V $3d - \text{O } 2p$ band as compared to the monomer case, likely due to hybridization with the lone pair from NH_3 (shown as a feature at E_F in **Figure 5.10(c)**). The strongest NH_3 features, however, remain relatively deep below E_F .

	$\text{V}_{\text{A12}}-\text{O}_{\text{A1}}(\text{OH})_{\text{A2}}-(\text{NH}_3)_{\text{A2}}$	$\text{V}_{\text{A1B1}}-\text{O}_{\text{A1}}(\text{OH})_{\text{B1}}-(\text{NH}_3)_{\text{B1}}$	$\text{V}_{\text{A2B1}}-\text{O}_{\text{br}}(\text{OH})_{\text{B1}}-(\text{NH}_3)_{\text{A2}}$	$\text{V}_{\text{A2B1}}-\text{O}_{\text{br}}(\text{OH})_{\text{B1}}-(\text{NH}_3)_{\text{B1}}$
Relative energy (eV)	0.00	2.09	2.30	2.30
$E_{\text{NH}_3\text{-ads}}$ (eV)	-1.34	-1.17	-0.81	-0.81
$\text{V}_I\text{-O}$ coordination (Å)	1.66 , 1.77, 1.78, 1.78	1.66 , 1.75, 1.78, 1.79	1.63 , 1.75, 1.83, 2.06, (2.21) _N	1.63 , 1.77, 1.78, 1.80
$Q_B(\text{V}_I)$	2.19	2.15	2.16	2.21
BVS(V_I)	4.62	4.62	4.03 (+0.39) _N	4.72
$\text{V}_{II}\text{-O}$ coordination (Å)	1.69 , 1.77, 1.77, 1.78	1.70 , 1.72, 1.74, 1.76	1.65 , 1.71, 1.77, 1.78	1.62 , 1.83, 1.85, 1.87, (2.25) _N
$Q_B(\text{V}_{II})$	2.18	2.14	2.20	2.19
BVS(V_{II})	4.53	4.81	4.89	4.15 (+0.35) _N
H_{OH} coord. (Å)	(1.06) _N	(1.06) _N	0.98	0.97
$Q_{\text{H-B}}$	1.00	1.00	1.00	1.00

Table 5.6: Structural and chemical information for $\frac{1}{2}$ ML V structures on the (0001) sapphire surface with one additional O and one OH ligands as well as one adsorbed NH_3 molecule, with values as defined previously or in the text. Coordination bond lengths are given for O except when specified in parentheses with a subscript N, signifying coordination with a N atom. Similarly, the contribution to the V BVS from N is given in parentheses for the affected cases.

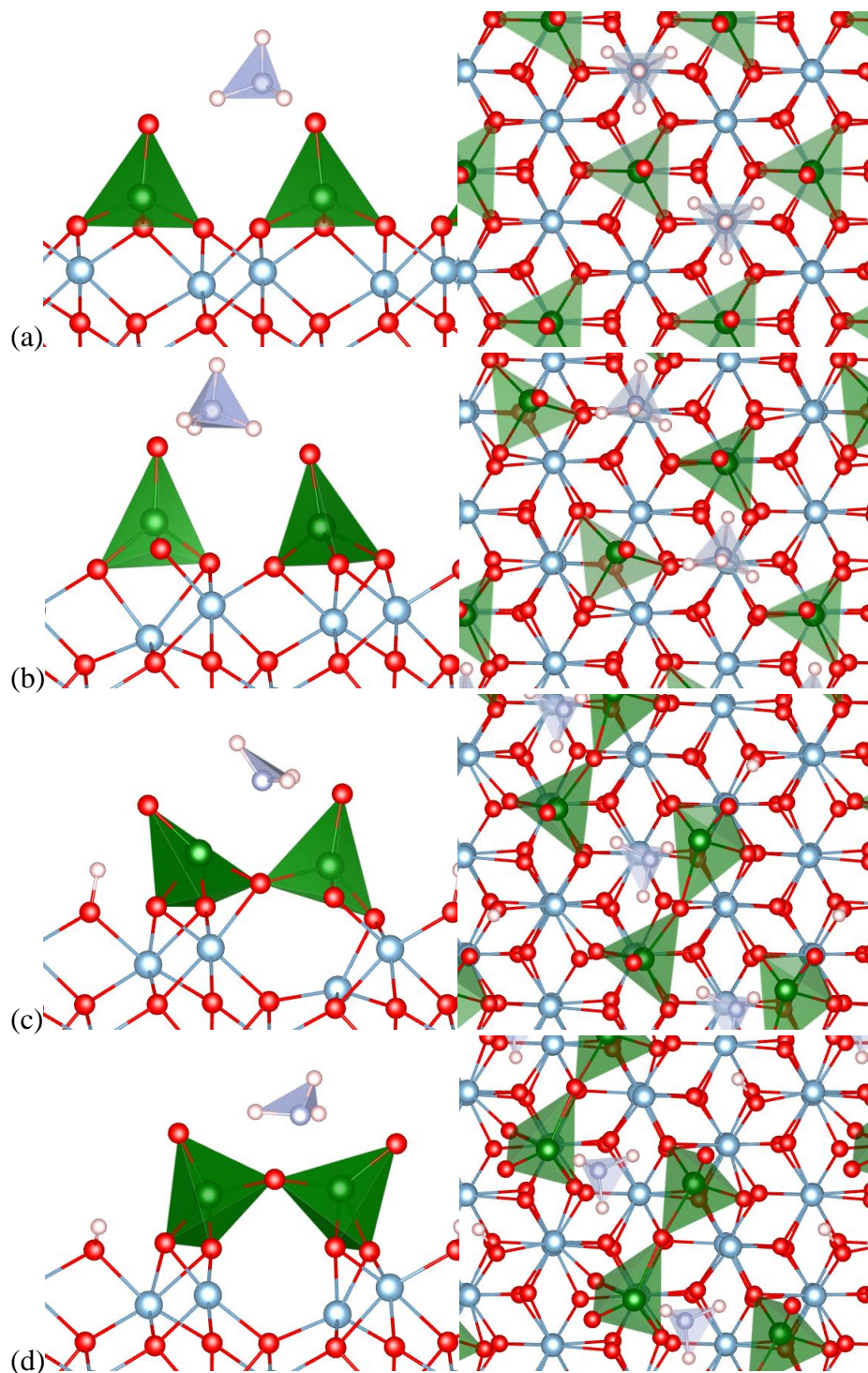


Figure 5.9: Side (1 1 -2 0) (left) and top (0001) (right) views of relaxed structures of NH_3 adsorbed on: (a) $\text{V}_{\text{A12}}\text{-O}_{\text{A1}}(\text{OH})_{\text{A2}}$; (b) $\text{V}_{\text{A1B1}}\text{-O}_{\text{A1}}(\text{OH})_{\text{B1}}$; (c) the A2 site of $\text{V}_{\text{A2B1}}\text{-O}_{\text{br}}(\text{OH})_{\text{B1}}$; (d) the B1 site of $\text{V}_{\text{A2B1}}\text{-O}_{\text{br}}(\text{OH})_{\text{B1}}$. The light gray-blue spheres represent N, and the light blue polyhedra represent the N-H coordination for NH_3 and NH_4^+ species.

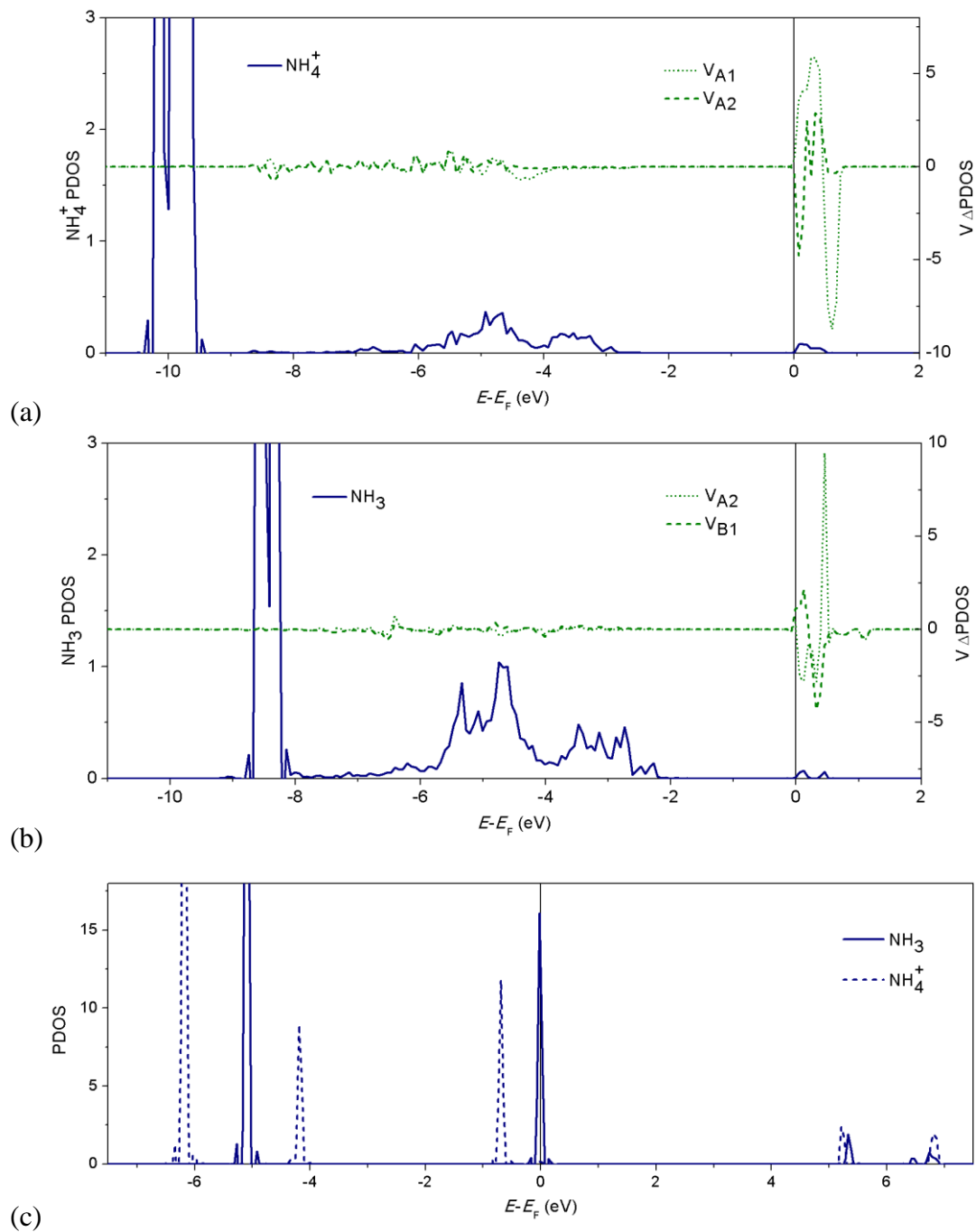


Figure 5.10: NH_n PDOS and V difference PDOS for the relaxed structure of NH_3 adsorbed on the (a) $\text{V}_{A12}\text{-O}_{A1}(\text{OH})_{A2}$ and (b) $\text{V}_{A2B1}\text{-O}_{br}(\text{OH})_{B1}\text{-(NH}_3\text{)}_{B1}$ surfaces, wherein the hydroxyl groups relax into vanadyl groups ($\text{V}_{A2}=\text{O}$). V difference PDOS indicate the change in V PDOS after NH_3 adsorption and subsequent relaxation. NH_n PDOS are truncated for clarity. (c) NH_3 and NH_4^+ (from NH_4Cl) PDOS are shown for comparison.

5.3.3 0.25 ML V + 0.25 ML W / O-terminated α -Al₂O₃ (0001)

In order to test the structural stability and chemical properties of mixed-metal monomers, dimers, and polymers similar to those above, one of the V atoms in each 2x1 supercell was substituted with W. The catalyst coverage of each (V,W) case is therefore 0.25 ML W and 0.25 ML V. First, we look at the cases of (W,V) deposition on a clean O-terminated sapphire (0001) surface with no additional coordinating ligands. Structures are shown in **Figure 5.11**, and structural and chemical details are given in **Table 5.7**.

As in the case with only V on the surface, the expected dimerization and polymerization of the metal-oxygen coordination polyhedra is observed. The surface symmetry is well preserved for the monomer case, whereas it is somewhat broken for the dimer and polymer cases. While the monomer case is the most stable, as in the V-only case, the dimers and polymers are not as unstable, with energy differences of only 0.20 and 0.29 eV, respectively. As in the V-only case, there are significant distortions of the surface O lattice in order to more fully coordinate V and W.

There are some differences in the valence of V when its nearest cation neighbor is W instead of V. In the most stable monomer case, this can be understood by considering the competition for charge donation. V is reduced further by about 0.2 e in the presence of W vs. V. Even though the monomers are separated, a neighboring W atom, with a valence of 4.10, donates roughly one more electron to the system than V, with a valence of 3.34 in the V-only case. This reduces the available states for V to donate to the system, leaving it in a more reduced state. In the dimer case where V sits in the B site, there is little difference in the charge state between the V-only and (V,W) cases, although the local coordination is more distorted due to the neighboring W. In the other dimer case, where V sits in the A site, V is reduced by about 0.4 e . The local structure tells why. In the

$W_I V_{II}$ case, the W and V polyhedra share only a corner, and a $V=O$ bond is present; however, in the $W_{II} V_I$ case, the polyhedra share an edge, and all the $V-O$ bonds are single bonds. V in the (V,W) polymer configuration shows site-dependent behavior similar to the V -only and case: in the A site, V is more oxidized by about $0.45 e$ than in the B site.

	$W_{A1}V_{A2}$ (monomers)	$W_{A1}V_{B1}$ (dimers)	$W_{B1}V_{A1}$ (dimers)	$W_{A2}V_{B1}$ (polymers)	$W_{B1}V_{A2}$ (polymers)
Relative energy (eV)	0.00	0.20	0.27	2.23	0.29
W-O coordination (Å)	1.81, 1.81, 1.81	1.90, 1.94, 1.98, 2.02	1.72, 1.92, 2.03, 2.19	1.72, 1.88, 1.98, 2.20	1.82, 1.87, 1.91, 1.98
$Q_B(W)$	1.99	1.72	1.60	1.81	1.77
BVS(W)	4.10	3.21	3.74	4.01	4.09
V-O coordination (Å)	1.77, 1.77, 1.78	1.60, 1.92, 1.95, 1.96	1.80, 1.86, 1.91, 1.92	1.71, 1.79, 1.91	1.76, 1.82, 1.85, 1.96
$Q_B(V)$	1.67	1.86	1.78	1.63	1.74
BVS(V)	3.15	3.61	3.11	2.95	3.40

Table 5.7: Structural and chemical information for $\frac{1}{4}$ ML V and $\frac{1}{4}$ ML W structures on the (0001) sapphire surface with no additional ligands. Values as defined previously.

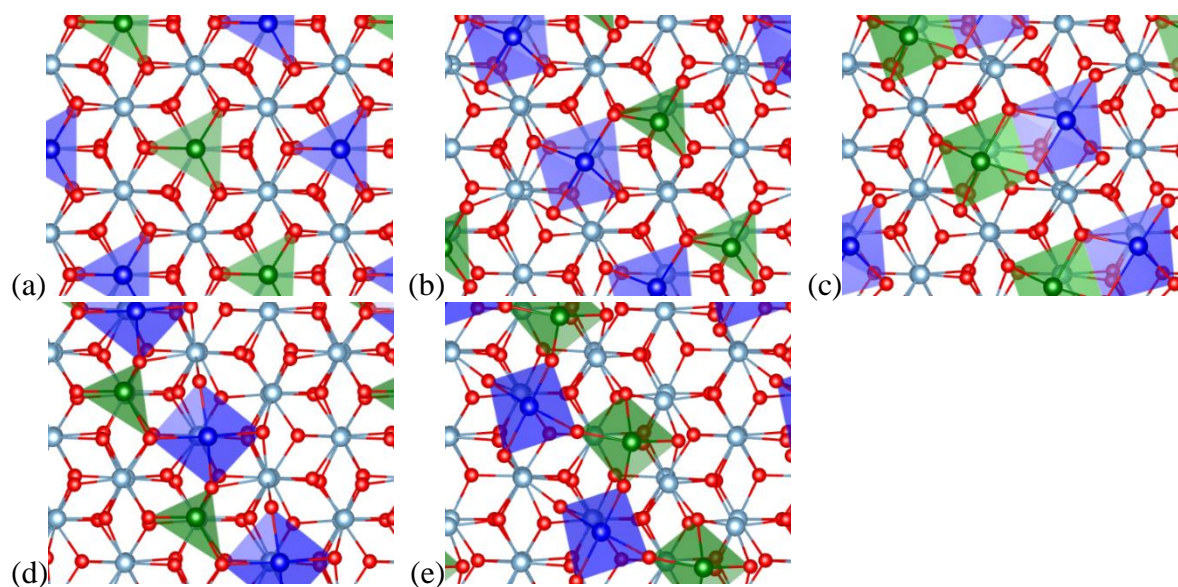


Figure 5.11: Top (0001) views of: (a) $W_{A1}V_{A2}$; (b) $W_{A1}V_{B1}$; (c) $W_{B1}V_{A1}$; (d) $W_{A2}V_{B1}$; (e) $W_{B1}V_{A2}$. W atoms and their coordination polyhedra are shown in royal blue.

Table 5.8 shows data for the (V,W)-adsorbed 2x1 supercells with one or two terminal oxygen atoms, and the structures are shown in **Figure 5.12**.. The first four data columns in **Table 5.8** show results for cases with an added “bridging” oxygen between two cations in the dimer and polymer cases. As in the V-only case, one dimer configuration, with W in the A-site and V in the B-site, is more stable than the polymer configurations as well as the opposite dimer configuration. However, as was observed above for the metal-terminated cases, the difference in energy between the most stable structure and least unstable structure is much smaller, with only 0.27 eV separating the stable dimer from the most stable polymer configuration. When an additional bridging oxygen is added, the A-site V is more oxidized than the B-site V in both the V-only and (V,W) data sets, although the influence of W causes V in either position to be more reduced.

When two O atoms are added to the surface in different configurations, the monomer case again is the most stable, followed by the $W_{B1}V_{A1}$ dimer case, which is of 0.77 eV higher energy. The dimers do not break apart, and the polymer chain remains intact for the $W_{B1}V_{A2}$ polymer case (although the lower-energy $W_{A2}V_{B1}$ polymer case breaks up into dimers). In the V-only case, the valence of vanadyl-terminated A- and B-site V atoms was the same within 0.1 e , and this is roughly true in the (V,W) case as well. In fact, not much reduction is observed as compared to the V-only case. With more O nearby, W is fully oxidized to W^{6+} .

Table 5.9 shows data for the (V,W) cases with W cations terminated by O and V by hydroxyl, yielding a mixed vanadium-hydroxyl / tungstyl surface as a starting configuration. Structures are shown in **Figure 5.13**. Structures with the opposite ligand termination were found to be higher in energy by at least 0.50 eV than their counterparts, which are reported here; this follows the expected trend of better reducibility for V than W. The monomer configuration is again the most

stable, followed by the dimer and polymer configurations with A-site W and B-site V. As opposed to the V-only case, the dimers are preserved in the presence of W, although the polymers are not. BVS of V shows a nominally 4+ oxidation state across the entire series, which is consistent with expectations for a hydroxylated distorted tetrahedron. However, the valence of W in the dimer and polymer configurations depends on the site occupancy, as it is much closer to the expected valence of W^{6+} in the B site (with the exception of the monomer case).

	$W_{A1}V_{B1}-O_{br}$	$W_{B1}V_{A1}-O_{br}$	$W_{A2}V_{B1}-O_{br}$	$W_{B1}V_{A2}-O_{br}$	$W_{A1}V_{A2}-O_{A1A2}$	$W_{A1}V_{B1}-O_{A1B1}$	$W_{B1}V_{A1}-O_{A1B1}$	$W_{A2}V_{B1}-O_{A2B1}$	$W_{B1}V_{A2}-O_{A2B1}$
Relative energy (eV)	0.00	0.86	0.27	0.42	0.00	1.33	0.77	1.46	1.84
W-O coordination (Å)	1.84, 1.89, 1.89 , 1.94, 2.04	1.79, 1.88, 1.88 , 2.06	1.71, 1.89 , 1.90, 1.99	1.72, 1.84 , 2.00, 2.00	1.72 , 1.83, 1.83, 1.84	1.72 , 1.88, 1.91, 1.91, 2.04	1.73 , 1.80, 1.81, 1.86	1.72 , 1.84, 1.88, 2.03, 2.07	1.72 , 1.79, 1.88, 1.97, 2.13
$Q_B(W)$	2.61	2.29	2.45	2.37	3.03	2.91	2.92	2.92	2.84
BVS(W)	4.70	4.10	4.62	4.50	5.62	5.46	5.73	5.32	5.59
V-O coordination (Å)	1.70, 1.84, 1.97 , 2.01	1.77, 1.81, 1.95 , 1.98, 2.04	1.69, 1.87 , 1.89, 1.92	1.60, 1.89 , 1.92, 1.93	1.61 , 1.80, 1.81, 1.81	1.60 , 1.73, 1.83, 1.85	1.61 , 1.78, 1.78, 1.88, 2.39	1.60 , 1.77, 1.79, 1.92	1.60 , 1.84, 1.86, 1.95, 1.98
$Q_B(V)$	1.84	2.04	1.91	1.95	2.12	2.20	2.17	2.16	2.22
BVS(V)	3.24	3.60	3.53	3.85	4.60	4.68	4.72	4.49	4.61

Table 5.8: Structural and chemical information for $\frac{1}{4}$ ML V and $\frac{1}{4}$ ML W structures on the (0001) sapphire surface with one or two additional O ligands. Values as defined previously.

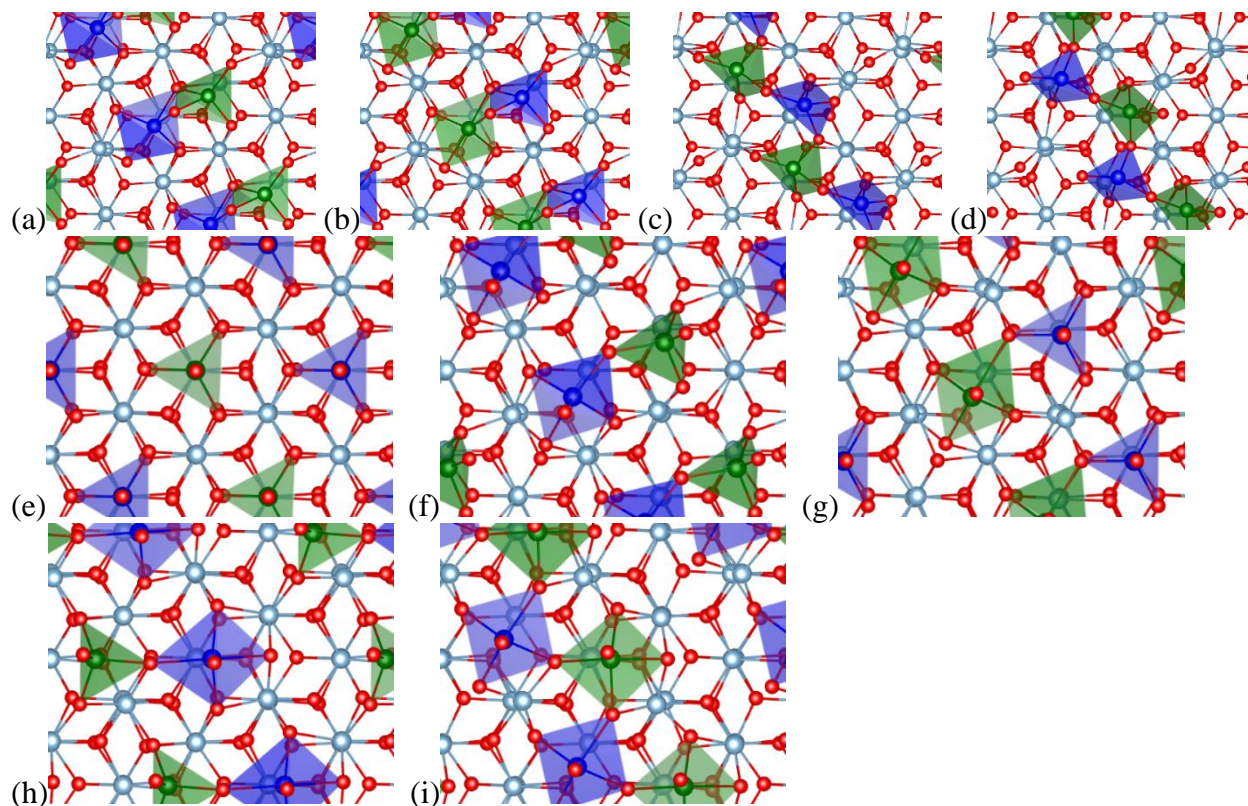


Figure 5.12: Top (0001) views of: (a) $W_{A1}V_{B1}-O_{br}$; (b) $W_{B1}V_{A1}-O_{br}$; (c) $W_{A2}V_{B1}-O_{br}$; (d) $W_{B1}V_{A2}-O_{br}$; (e) $W_{A1}V_{A2}-O_{A12}$; (f) $W_{A1}V_{B1}-O_{A1B1}$; (g) $W_{B1}V_{A1}-O_{A1B1}$; (h) $W_{A2}V_{B1}-O_{A2B1}$; (i) $W_{B1}V_{A2}-O_{A2B1}$.

	$W_{A1}V_{A2}-O_{A1}(OH)_{A2}$	$W_{A1}V_{B1}-O_{A1}(OH)_{B1}$	$W_{B1}V_{A1}-O_{B1}(OH)_{A1}$	$W_{A2}V_{B1}-O_{A2}(OH)_{B1}$	$W_{B1}V_{A2}-O_{B1}(OH)_{A2}$
Relative energy (eV)	0.00	1.27	1.54	1.38	1.85
W-O coordination (Å)	1.73 , 1.83, 1.84, 1.84	1.73 , 1.86, 1.90, 2.02, 2.05	1.73 , 1.80, 1.82, 1.90	1.73 , 1.86, 1.88, 2.04, 2.06	1.74 , 1.81, 1.83, 1.84
$Q_B(W)$	2.99	2.81	2.82	2.87	2.82
BVS(W)	5.54	5.15	5.50	5.15	5.61
V-O coordination (Å)	1.79 , 1.80, 1.80, 1.82	1.68, 1.78 , 1.83, 1.90	1.78 , 1.80, 1.81, 1.92, 2.11	1.76, 1.78 , 1.79, 1.90	1.75, 1.79 , 1.81, 1.87
$Q_B(V)$	2.04	2.07	2.13	2.07	2.07
BVS(V)	3.83	3.97	3.93	3.84	3.83

Table 5.9: Structural and chemical information for $\frac{1}{4}$ ML V and $\frac{1}{4}$ ML W structures on the (0001) sapphire surface with one additional O and one OH ligands. Values as defined previously.

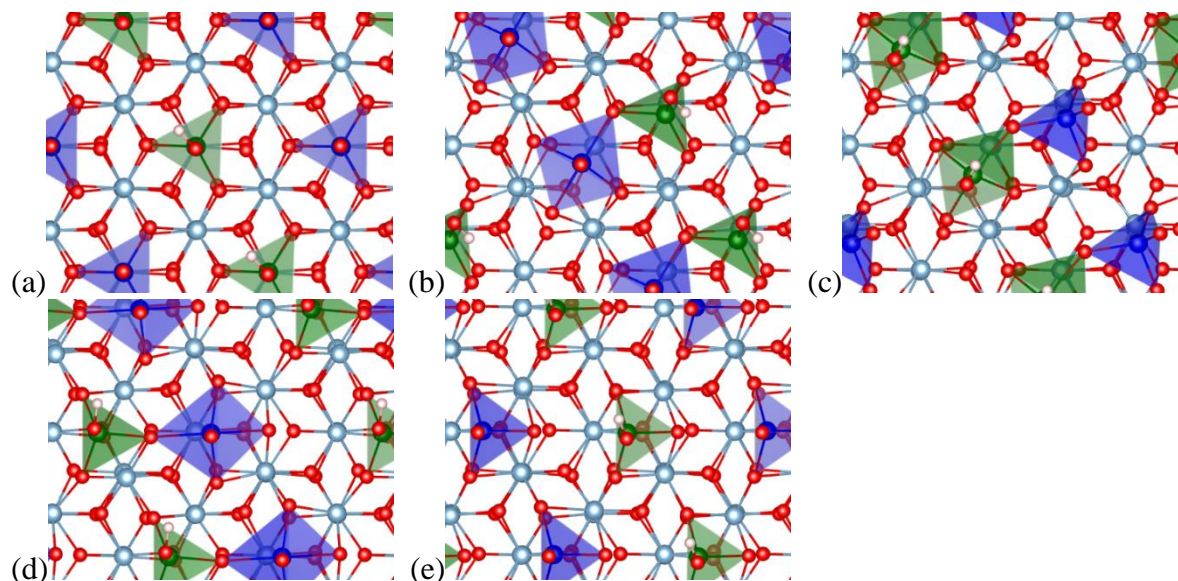


Figure 5.13: Top (0001) views of: (a) $W_{A1}V_{A2}-O_{A1}(OH)_{A2}$; (b) $W_{A1}V_{B1}-O_{A1}(OH)_{B1}$; (c) $W_{B1}V_{A1}-O_{B1}(OH)_{A1}$; (d) $W_{A2}V_{B1}-O_{A2}(OH)_{B1}$; (e) $W_{B1}V_{A2}-O_{B1}(OH)_{A2}$.

Several higher-coordination (V,W) structures were investigated to model more complex coordination environments such as those that might be encountered during hydration or reduction.

Table 5.10 and **Figure 5.14** show results for surfaces with a single oxygen atom and two hydroxyl groups adsorbed onto the monomer, dimer, and polymer configurations. The O atom is adsorbed onto V to simulate a vanadyl group, whereas both OH groups are adsorbed to the W to simulate the effect of H_2O dissociative adsorption onto a tungstyl site, leading to a possible Brønsted acid site. ΔE_{+H_2O} values give the energy of H_2O dissociative adsorption onto the corresponding tungstyl structure in **Table 5.8**.

The monomer is again the most stable structure, followed by dimer and polymer configurations. In nearly all cases except for the $W_{B1}V_{A1}-O_{A1}(OH)_{2B1}$ structure, H_2O adsorption is strongly favorable. The more stable cation configurations of the dimer and polymer structures (A-site W, B-site V) retain connected coordination environments, although the polymer structures relax into

dimers. In all cases, the valence of V suggests a 5+ oxidation state, in line with its full coordination polyhedron and one short V=O bond. W, however, does not appear to be fully oxidized in the monomer as well as most stable dimer and polymer configurations, despite coordinating with 6 oxygen atoms in the latter cases. Also in these structures, the V and W polyhedra are bridged by a hydroxyl group, which could act as a Brønsted acid site that, when activated by the abstraction of a proton, could reduce a neighboring cation, an integral step to the NO_x SCR reaction[17]. Nearly all the configurations in **Table 5.10** would be more stable forms of their counterparts in **Table 5.8** upon exposure to water, with the exception being the W_{B1}V_{A1} dimer case.

	W _{A1} V _{A2} ⁻ O _{A2} (OH) _{2A1}	W _{A1} V _{B1} ⁻ O _{B1} (OH) _{2A1}	W _{B1} V _{A1} ⁻ O _{A1} (OH) _{2B1}	W _{A2} V _{B1} ⁻ O _{B1} (OH) _{2A2}	W _{B1} V _{A2} ⁻ O _{A2} (OH) _{2B1}
Relative energy (eV)	0.00	1.38	1.50	1.61	1.64
ΔE_{+H_2O}	-0.60	-0.55	0.14	-0.45	-0.80
W-O coordination (Å)	1.82, 1.87, 1.87 , 1.91, 1.99	1.82, 1.84, 1.91 , 2.05, 2.09 , 2.11	1.79, 1.80, 1.88 , 1.93 , 1.98	1.79, 1.87, 1.90 , 2.00, 2.07, 2.18	1.79, 1.81, 1.87 , 1.92 , 1.99
Q _B (W)	2.91	2.91	2.95	2.93	2.97
BVS(W)	5.18	5.01	5.56	5.15	5.55
V-O coordination (Å)	1.61 , 1.79, 1.79, 1.80	1.63 , 1.74, 1.81, 2.04 , 2.19	1.65 , 1.78, 1.79, 1.80	1.62 , 1.73, 1.79, 2.03 , 2.26	1.66 , 1.73, 1.76, 1.78
Q _B (V)	2.14	2.18	2.19	2.19	2.22
BVS(V)	4.68	4.50	4.50	4.59	4.81

Table 5.10: Structural and chemical information for ¼ ML V and ¼ ML W structures on the (0001) sapphire surface with one additional O and two OH ligands. Values as defined previously, with ΔE_{+H_2O} giving the dissociative adsorption energy of a water molecule onto the corresponding structure with two additional O ligands.

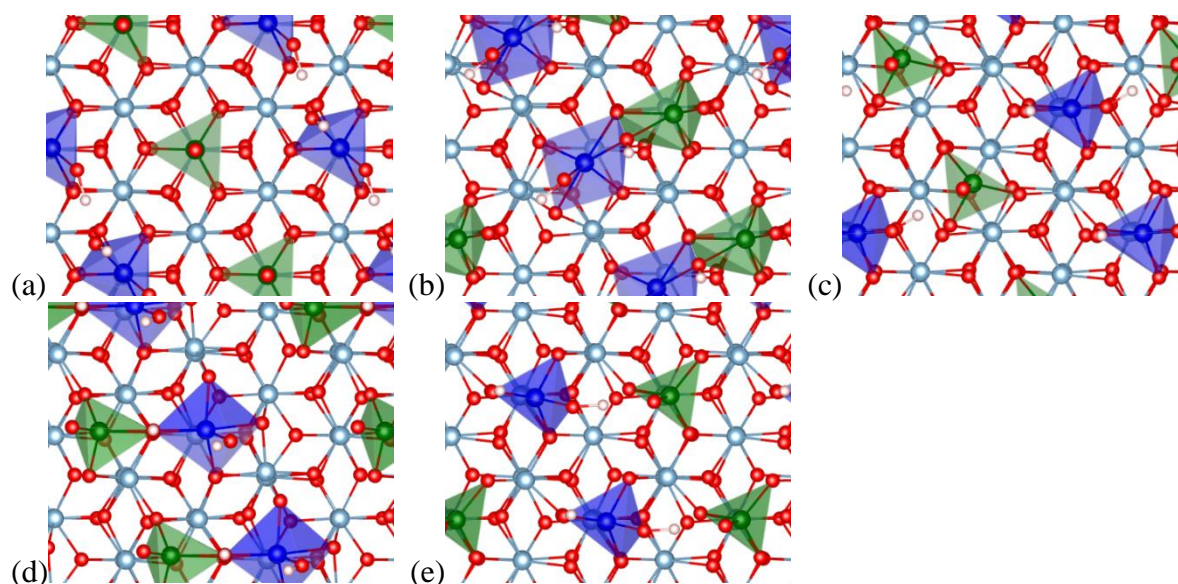


Figure 5.14: Top (0001) views of: (a) $W_{A1}V_{A2}-O_{A2}(OH)_{2A1}$; (b) $W_{A1}V_{B1}-O_{B1}(OH)_{2A1}$; (c) $W_{B1}V_{A1}-O_{A1}(OH)_{2B1}$; (d) $W_{A2}V_{B1}-O_{B1}(OH)_{2A2}$; (e) $W_{B1}V_{A2}-O_{A2}(OH)_{2B1}$.

In a final configuration set, the coordination environment includes two additional O atoms and one hydroxyl group on the surface; details are in **Table 5.11** and **Figure 5.15**. These terminal ligands are expected to nominally fully oxidize both surface cations. As in the previous case, one O atom is selectively adsorbed onto the V atom, while the other O and hydroxyl group are adsorbed onto W. The monomer is the most stable configuration, followed by a polymer configuration (which in fact relaxes into a monomer-like structure). This is a slight departure from the above examples, but because the cations in the polymer case appear to relax far from the nominal A and B sites, the site-dependent characteristics cannot be judged. The more stable of the two dimer configurations retains contact between edges of the V and W coordination environments. Despite the additional electron from the coordinating O (instead of OH), the W valences do not change substantially from the above case; some increase slightly, while others decrease relative to the $W-(OH)_2$ structures.

V valences are also only slightly affected, although the V=O bonds are somewhat shorter as compared to the W-(OH)₂ cases.

	$W_{A1}V_{A2}-O_{A12}(OH)_{A1}$	$W_{A1}V_{B1}-O_{A1B1}(OH)_{A1}$	$W_{B1}V_{A1}-O_{A1B1}(OH)_{B1}$	$W_{A2}V_{B1}-O_{A2B1}(OH)_{A2}$	$W_{B1}V_{A2}-O_{A2B1}(OH)_{B1}$
Relative energy (eV)	0.00	1.47	1.55	1.57	1.12
W-O coordination (Å)	1.73 , 1.86, 1.92 , 1.96, 2.01	1.82, 1.86, 1.90 , 1.97 , 2.06, 2.14	1.74 , 1.83, 1.91 , 1.95, 2.02	1.79, 1.87, 1.89 , 2.00, 2.00 , 2.28	1.73 , 1.86, 1.86, 1.91 , 2.16
Q _B (W)	2.94	2.95	2.89	2.94	2.91
BVS(W)	5.33	5.16	5.45	5.21	5.41
V-O coordination (Å)	1.61 , 1.78, 1.79, 1.80	1.60 , 1.78, 1.86, 1.86 , 2.39	1.61 , 1.77, 1.79, 1.81	1.60 , 1.82, 1.82, 1.90 , 2.30	1.61 , 1.76, 1.78, 1.84
Q _B (V)	2.15	2.21	2.12	2.21	2.23
BVS(V)	4.72	4.58	4.69	4.48	4.69

Table 5.11: Structural and chemical information for $\frac{1}{4}$ ML V and $\frac{1}{4}$ ML W structures on the (0001) sapphire surface with two additional O and one OH ligands. Values as defined previously.

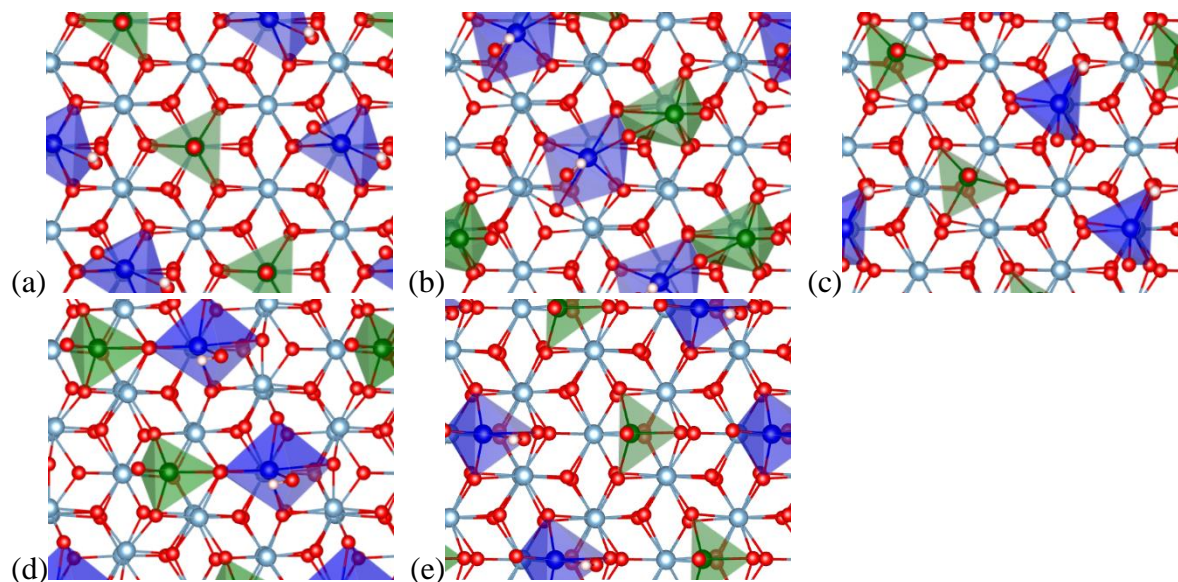


Figure 5.15: Top (0001) views of: (a) $W_{A1}V_{A2}-O_{A12}(OH)_{A1}$; (b) $W_{A1}V_{B1}-O_{A1B1}(OH)_{A1}$; (c) $W_{B1}V_{A1}-O_{A1B1}(OH)_{B1}$; (d) $W_{A2}V_{B1}-O_{A2B1}(OH)_{A2}$; (e) $W_{B1}V_{A2}-O_{A2B1}(OH)_{B1}$.

5.3.4 0.25 ML V + 0.25 ML W / O-terminated α -Al₂O₃: NH₃ adsorption

The adsorption of NH₃ onto the W coordination polyhedron was tested for selected low-energy monomer and dimer cases with V=O, W-(OH)₂ or V=O, W-O,OH coordination environments. NH₃ molecules were initially placed near the hydroxyl group, as was done for the V-only surfaces, and the full structures were allowed to relax. Results for the V-O, W-O,OH cases are given in **Table 5.12** and **Figure 5.16**. Despite the differences in structure, the ammonia adsorption energy is almost exactly the same between the two structures, at about 0.5 eV. The coordination structure and valences of V and W barely change with the addition of ammonia. The structures tell why: NH₃ interacts weakly with these W surface sites, forming a ~1.6 Å H - - - N hydrogen bond with the hydroxyl group. This is in stark contrast to the V-only cases, where the NH₃ either removes the hydroxyl H to become NH₄⁺ ($E_{\text{NH}_3\text{-ads}} = 1.3$ eV) or coordinates with the metal cation ($E_{\text{NH}_3\text{-ads}} = 0.8$ eV).

	W _{A1} V _{A2} -O _{A12} (OH) _{A1} -(NH ₃) _{A1}	W _{A1} V _{B1} -O _{A1B1} (OH) _{A1} -(NH ₃) _{A1}
Relative energy (eV)	0.00	1.47
$E_{\text{NH}_3\text{-ads}}$	-0.51	-0.51
W-O coordination (Å)	1.74 , 1.87, 1.88 , 1.99, 1.99	1.83, 1.85 , 1.86, 2.00 , 2.09, 2.14
Q _B (W)	2.92	2.96
BVS(W)	5.33	5.17
V-O coordination (Å)	1.62 , 1.78, 1.79, 1.80	1.61 , 1.77, 1.85 , 1.85, 2.38
Q _B (V)	2.14	2.22
BVS(V)	4.72	4.60
H _{OH} coord. (Å)	1.03	1.04
Q _B (H)	1.00	1.00

Table 5.12: Structural and chemical information for ¼ ML V and ¼ ML W structures on the (0001) sapphire surface with two additional O and one OH ligands as well as one adsorbed NH₃ molecule. Values as defined previously.

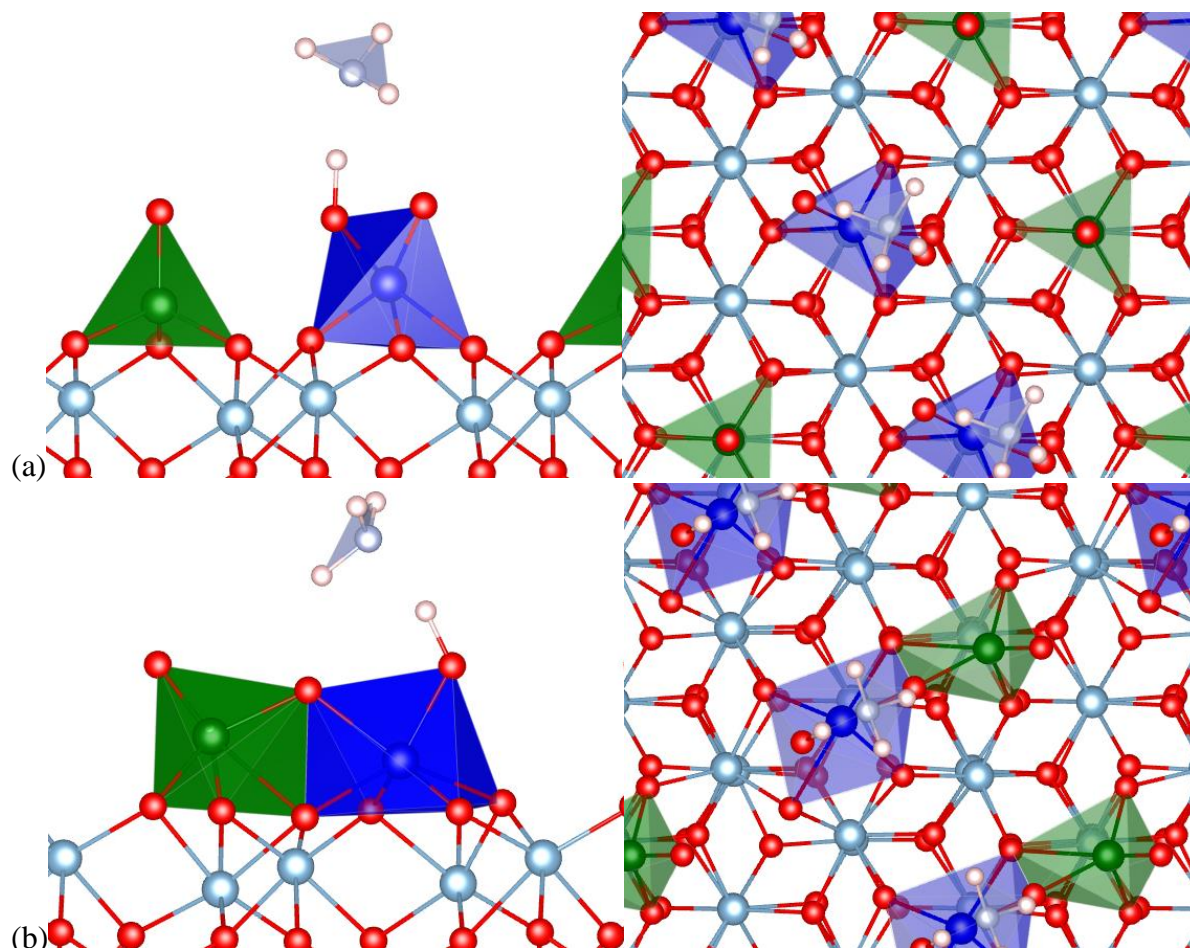


Figure 5.16: Side (1 1 -2 0) (left) and top (0001) (right) views of relaxed structures of NH₃ adsorbed on: (a) W_{A1}V_{A2}-O_{A12}(OH)_{A1} and (b) W_{A1}V_{B1}-O_{A1B1}(OH)_{A1}-(NH₃)_{A1}.

In the V=O, W-(OH)₂ structures, there exist two different hydroxyl sites which may be ideal for NH₃ adsorption. An NH₃ molecule was placed near one site or the other on the most stable monomer, dimer, and polymer configurations with V=O, W-(OH)₂ terminations. Two relaxed structures (originally, monomers and polymers) with two different NH₃ adsorption states are shown here in **Table 5.13** and **Figure 5.17** to highlight significant differences in NH₃ adsorption for these different surface geometries. As before, a monomer case is the most stable for this stoichiometry. In one geometry, NH₃ relaxes to a geometry with two hydrogen bonds forming, one

between N and a surface hydroxyl H (1.6 Å), and the other between an ammonia H and a hydroxyl O (2.1 Å). In the other, NH₃ takes on an umbrella-like formation, with the only surface interaction being a similar 2.1 Å H - - - O hydrogen bond. Remarkably close behind in stability (~0.5 eV) from the lowest-energy monomer structure is a polymer case (which actually relaxes to a V-W dimer) with a relatively high NH₃ adsorption energy. While in the monomer case, NH₃ interacts via hydrogen bonding with the hydroxyl group, the ammonia in this dimer case abstracts an H atom into a NH₄⁺ species. This results in the strongest NH₃ adsorption energy seen thus far in this study (1.69 eV). The interaction distances between the three H atoms in a plane parallel with the surface and the nearby tungstyl or vanadyl oxygen atoms are 1.6 – 1.8 Å long, with the shortest being for the W=O - - - H interaction. However, there are only subtle changes in the valence of the cations, a slight oxidation of W and reduction of V, due to this event. The other adsorption configuration shows a strong hydrogen bonding interaction of 1.6 Å between N and a hydroxyl H.

	W _{A1} V _{A2} -O _{A2} (OH) _{2A1} ⁻ (NH ₃) _{A1} Site 1	W _{A1} V _{A2} ⁻ O _{A2} (OH) _{2A1} -(NH ₃) _{A1} Site 2	W _{A2} V _{B1} ⁻ O _{B1} (OH) _{2A2} -(NH ₃) _{A2} Site 1	W _{A2} V _{B1} ⁻ O _{B1} (OH) _{2A2} -(NH ₃) _{A2} Site 2
Relative energy (eV)	0.00	0.36	0.48	1.41
$E_{\text{NH}_3\text{-ads}}$	-0.56	-0.20	-1.69	-0.76
W-O coordination (Å)	1.82, 1.86, 1.90 , 1.92, 1.92	1.82, 1.87, 1.89 , 1.91, 1.96	1.77 , 1.80, 1.89, 2.12, 2.13, 2.16	1.79, 1.87, 1.90 , 2.01, 2.10, 2.11
Q _B (W)	2.92	2.91	2.93	2.94
BVS(W)	5.30	5.20	5.24	5.16
V-O coordination (Å)	1.62 , 1.79, 1.79, 1.80	1.61 , 1.79, 1.79, 1.80	1.69 , 1.72, 1.77, 2.01 , 2.13	1.64 , 1.72, 1.79, 2.02 , 2.21
Q _B (V)	2.13	2.13	2.20	2.20
BVS(V)	4.63	4.66	4.52	4.55

Table 5.13: Structural and chemical information for ¼ ML V and ¼ ML W structures on the (0001) sapphire surface with one additional O and two OH ligands as well as one adsorbed NH₃ molecule. Values as defined previously.

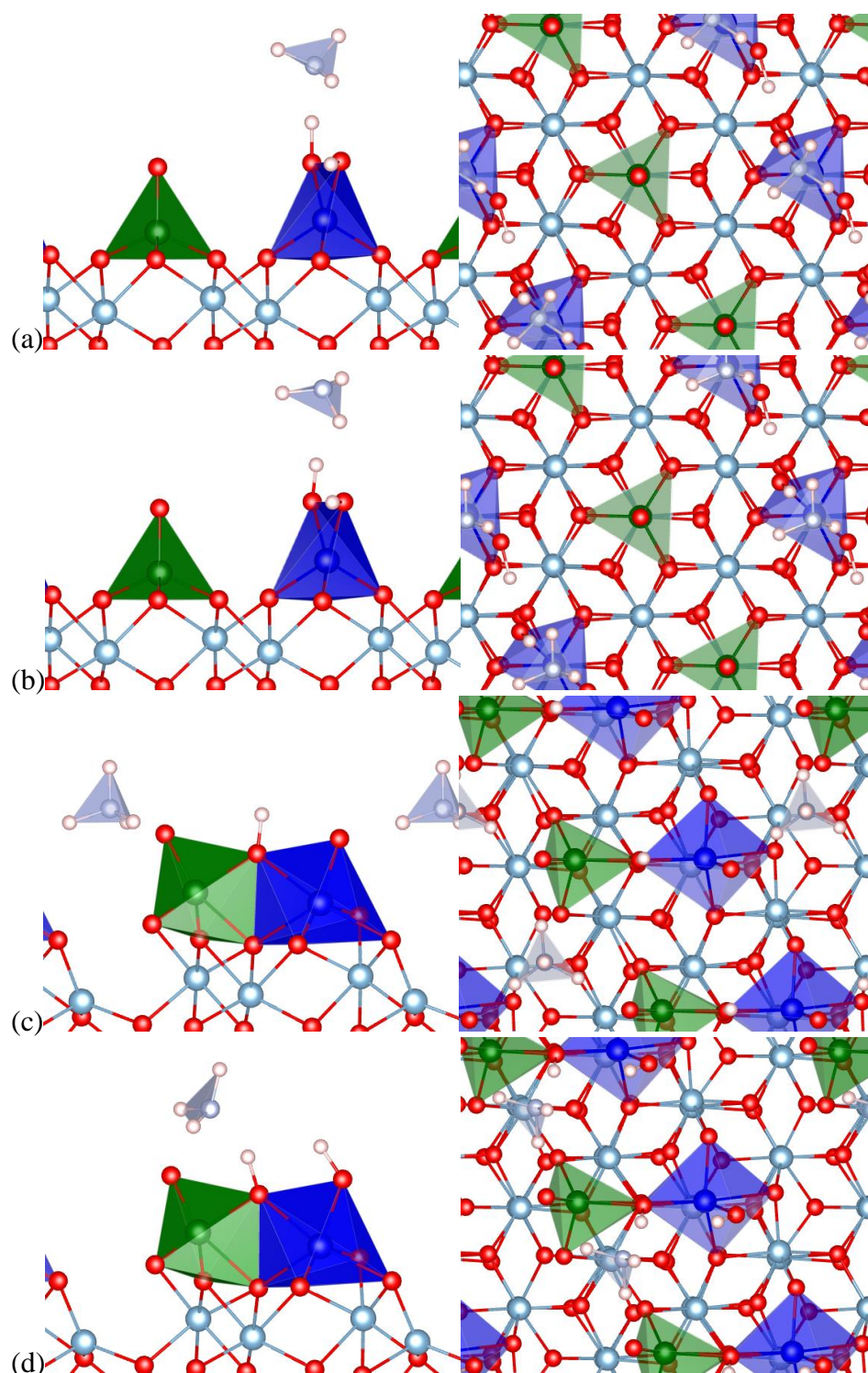


Figure 5.17: Side $(1\ 1\ -2\ 0)$ (left) and top (0001) (right) views of relaxed structures of NH_3 adsorbed on: (a,b) $\text{W}_{\text{A}1}\text{V}_{\text{A}2}\text{-O}_{\text{A}2}(\text{OH})_{2\text{A}1}$ and (c,d) $\text{W}_{\text{A}2}\text{V}_{\text{B}1}\text{-O}_{\text{B}1}(\text{OH})_{2\text{A}2}$.

From these cases, we select the lowest-energy structures from each cationic configuration to investigate differences between N - - - H hydrogen bonding and H abstraction to a NH_4^+ species. **Figure 5.18** shows charge density difference maps for the selected cases ($\text{W}_{\text{A1}}\text{V}_{\text{A2}}\text{-O}_{\text{A2}}(\text{OH})_{2\text{A1}}$ and $\text{W}_{\text{A2}}\text{V}_{\text{B1}}\text{-O}_{\text{B1}}(\text{OH})_{2\text{A2}}$), and **Figure 5.19** shows the PDOS of the NH_n ($n = 3$ or 4) adsorbate as well as the changes in PDOS of V and W upon NH_3 adsorption. In the monomer case ($\text{W}_{\text{A1}}\text{V}_{\text{A2}}\text{-O}_{\text{A2}}(\text{OH})_{2\text{A1}}$), charge difference maps show small perturbations around the V and W coordination environments, although most of the changes are localized on the W hydroxyls. In the PDOS, there is a subtle rearrangement of the sharp V and W states just above E_{F} . Prior to NH_3 adsorption, the greatest proportion of W states sit directly above E_{F} , with the V states slightly higher; however, upon adsorption, the order reverses. There is also an NH_3 state present at about 4 eV below E_{F} , likely due to hybridization of the NH_3 lone pair with the cation $d - \text{O } 2p$ band. The effects of NH_3 adsorption are more drastic on the polymer (relaxed to dimer) structure. Prior to adsorption, W and V share a narrow band just above E_{F} . When NH_3 adsorbs and abstracts a proton from a tungsten hydroxyl group to become NH_4^+ , the W states above E_{F} all but vanish, and the V features flatten and split. Although the V valence does not change significantly, the change in its charge density could be attributed to a lengthening of the vanadyl bond from 1.60 to 1.69 Å as the O interacts with the ammonium ion. From **Figure 5.18**, it is clear that the abstraction of a proton and strong interactions with the resulting NH_4^+ cation lead to substantial changes in the surface structure.

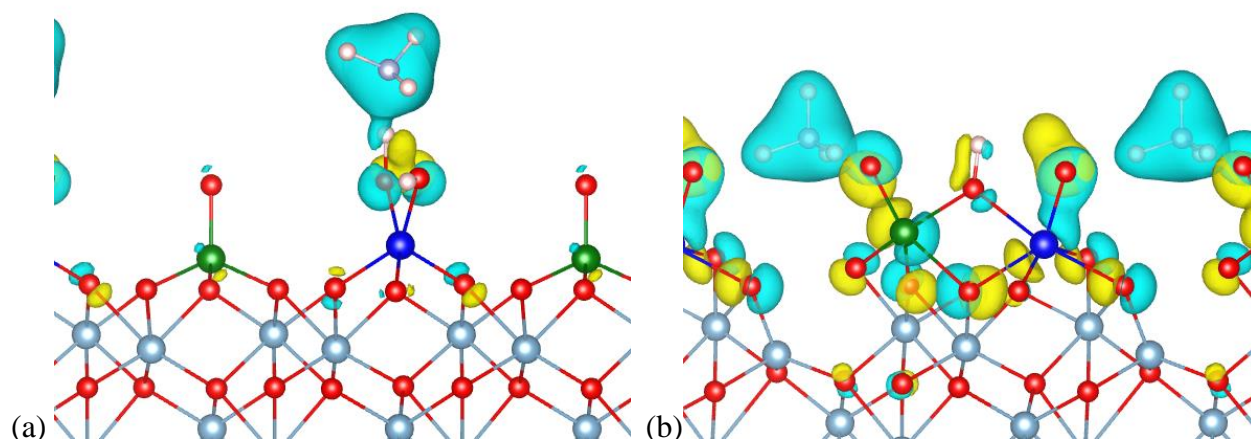


Figure 5.18: Charge density difference maps for NH_3 adsorption onto the (a) $\text{W}_{\text{A1}}\text{V}_{\text{A2}}\text{-O}_{\text{A2}}(\text{OH})_{2\text{A1}}$ and (b) $\text{W}_{\text{A2}}\text{V}_{\text{B1}}\text{-O}_{\text{B1}}(\text{OH})_{2\text{A2}}$ structures. Isosurface values are the same in both cases. Blue regions indicate increased charge density upon NH_3 adsorption, while yellow regions indicate decreased charge density.

5.3.5 0.5 ML V / O-terminated $\alpha\text{-Fe}_2\text{O}_3$ (0001)

Hematite is chosen as an alternate substrate for comparison with sapphire due to its similar structure but drastically different chemical properties. While sapphire is strongly ionic, the bonds between Fe and O ions are somewhat more covalent. Fe^{3+} cations are also much more reducible than Al^{3+} , with the capability to reduce to Fe^{2+} . Spin-polarized calculations were used to accommodate for antiferromagnetic ordering in hematite. The hematite slab, which contains as many atoms as the sapphire slab, was initialized at the lowest energy spin state[147]. We have investigated adsorption of W, V, and other species onto 1x1 hematite unit cells using similar methods and models[126, 129, 130, 231, 232], but here we calculate structures for V and V-W monomers, dimers, and polymers for comparison with the above results for sapphire.

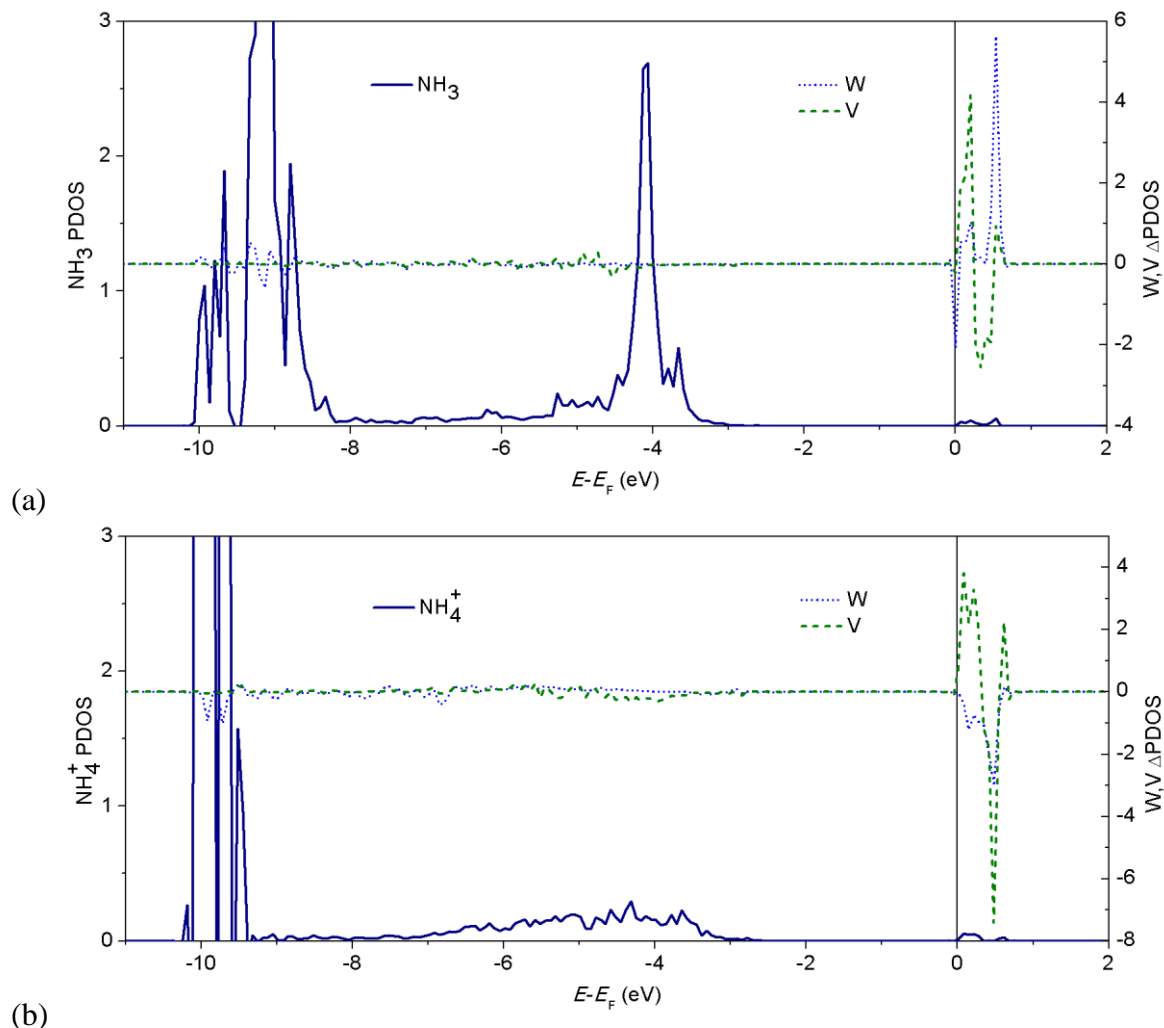


Figure 5.19: NH_n PDOS and W,V difference PDOS for the relaxed structure of NH_3 adsorbed on the (a) $\text{W}_{\text{A1}}\text{V}_{\text{A2}}\text{-O}_{\text{A2}}(\text{OH})_{2\text{A1}}$ monomer structure and (b) $\text{W}_{\text{A2}}\text{V}_{\text{B1}}\text{-O}_{\text{B1}}(\text{OH})_{2\text{A2}}$ structure (which relaxed to a dimer from a polymer configuration). W,V difference PDOS indicate the change in V,W PDOS after NH_3 adsorption and subsequent relaxation. NH_n PDOS are truncated for clarity.

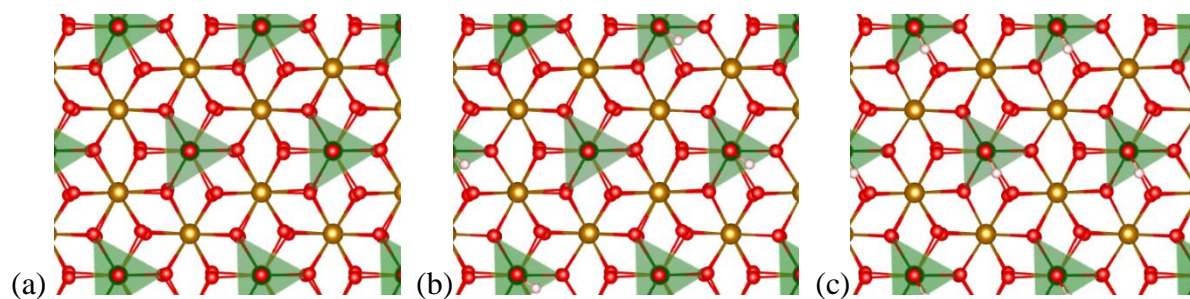


Figure 5.20: Top (0001) views of the hematite-supported monomer structures (a) $\text{V}_{\text{A12}}\text{-O}_{\text{A12}}$; (b) $\text{V}_{\text{A12}}\text{-O}_{\text{A1}}(\text{OH})_{\text{A2}}$; and (c) $\text{V}_{\text{A12}}\text{-(OH)}_{\text{A12}}$. Colors as defined before, with Fe atoms as large gold circles.

	$V_{A12}-(OH)_{A12}$	$V_{A12}-O_{A1}(OH)_{A2}$	$V_{A12}-O_{A12}$
$\Delta E_{+\frac{1}{2}H_2}$	--	-0.88	-1.20
V_I-O coordination (Å)	1.73, 1.73, 1.73, 1.80	1.62 , 1.80, 1.80, 1.80	1.61 , 1.81, 1.81, 1.81
$Q_B(V_I)$	2.12	2.09	2.07
$BVS(V_I)$	4.52	4.59	4.60
$V_{II}-O$ coordination (Å)	1.73, 1.73, 1.73, 1.80	1.72, 1.74, 1.74, 1.78	1.61 , 1.81, 1.81, 1.81
$Q_B(V_{II})$	2.12	2.15	2.07
$BVS(V_{II})$	4.52	4.57	4.60
Fe_C-O coordination (Å)	2.02, 2.02, 2.03, 2.03, 2.03, 2.04	I: 1.95, 1.95, 2.01, 2.06, 2.07, 2.08 II: 1.94, 2.01, 2.02, 2.03, 2.04, 2.04	1.93, 1.93, 1.93, 2.09, 2.09, 2.09
BVS_{FeC}	2.86	I: 2.90 II: 2.93	3.03
Fe_B-O coordination (Å)	1.95, 1.96, 1.96, 2.16, 2.17, 2.20	I: 1.95, 1.95, 1.97, 2.08, 2.16, 2.18 II: 1.96, 1.97, 1.98, 2.08, 2.09, 2.21	1.97, 1.97, 1.97, 2.09, 2.09, 2.09
BVS_{FeB}	2.64	I: 2.74 II: 2.72	2.83

Table 5.14: Structural and chemical information for $\frac{1}{2}$ ML V monomer structures on the (0001) hematite surface. Values as defined previously.

V was placed on the surface of a hematite (0001) surface supercell for several cases analogous to the sapphire calculations shown above. Results for the monomer case are shown in **Table 5.14**, and the structures are depicted in **Figure 5.20**. Compared to sapphire, there are significant differences in V-O bond lengths, particularly for the hydroxylated V. These differences indicate a substantial difference in the valence: the vanadyl-terminated cases are somewhat less oxidized than their counterparts on sapphire, while the hydroxylated cases are significantly more oxidized than those on sapphire. The difference in BVS between the vanadyl and hydroxylated cases is nearly insignificant, but in both cases the BVS values are closer to those expected for V^{5+} . Another

notable difference is observed in the reduction chemistry: the $\Delta E_{+\frac{1}{2}H_2}$ values are much more exothermic than on sapphire, with the first reduction step slightly more exothermic than the second (-1.20 vs. -0.88 eV). This suggests that in the presence of hydrogen, the surface vanadyl ligands would be more likely to convert to hydroxyl ligands. However, the consequence is not V reduction, but in fact a slight reduction of the near-surface Fe^{3+} cations (which have a calculated BVS of 2.91 in the DFT-calculated bulk). As observed on sapphire, the Fe_C cations closest to the surface are more oxidized (by about 0.2 e) than their Fe_B counterparts sitting slightly lower in the near-surface cation layer.

The electronic structure of the surface vanadium atoms in these three monomer configurations is shown in **Figure 5.21**. For these calculations, an on-site $+U$ correction of 2 eV was applied to the Fe d -orbitals to correct for strong d -electron localization[164]. The V d -states below and above E_F are not significantly different between the purely hydroxyl-terminated surface and the mixed hydroxyl-vanadyl case. The appearance of the vanadyl V-states is also similar between the purely vanadyl-terminated surface and the mixed case, although the Fermi level shifts from the middle of the bandgap to the bottom of the V d -band above E_F .

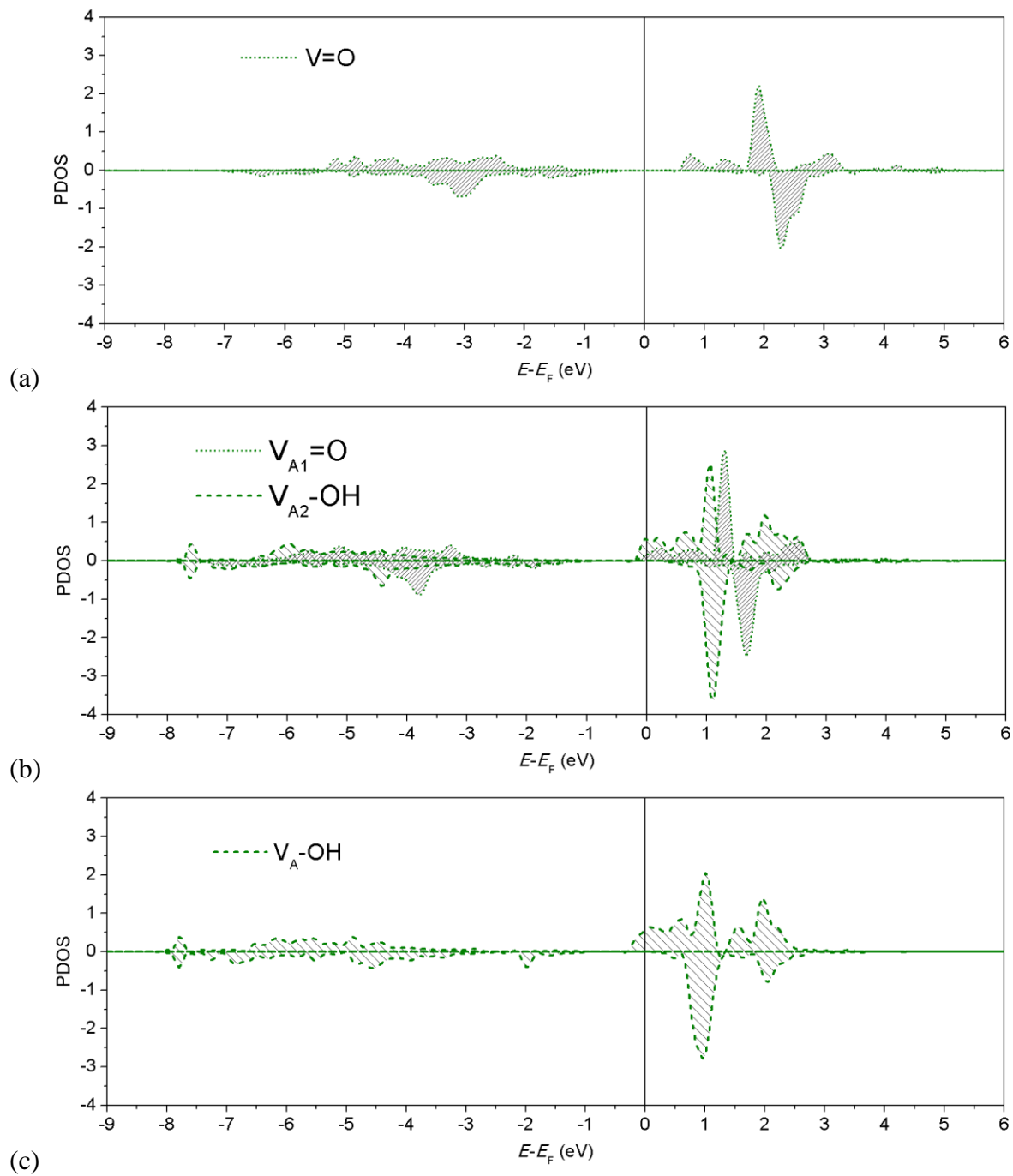


Figure 5.21: Spin-polarized V PDOS for (a) $V_{A12}-O_{A12}$; (b) $V_{A12}-O_{A1}(\text{OH})_{A2}$; (c) $V_{A12}-(\text{OH})_{A12}$. Positive and negative values indicate spin-up and spin-down states, respectively.

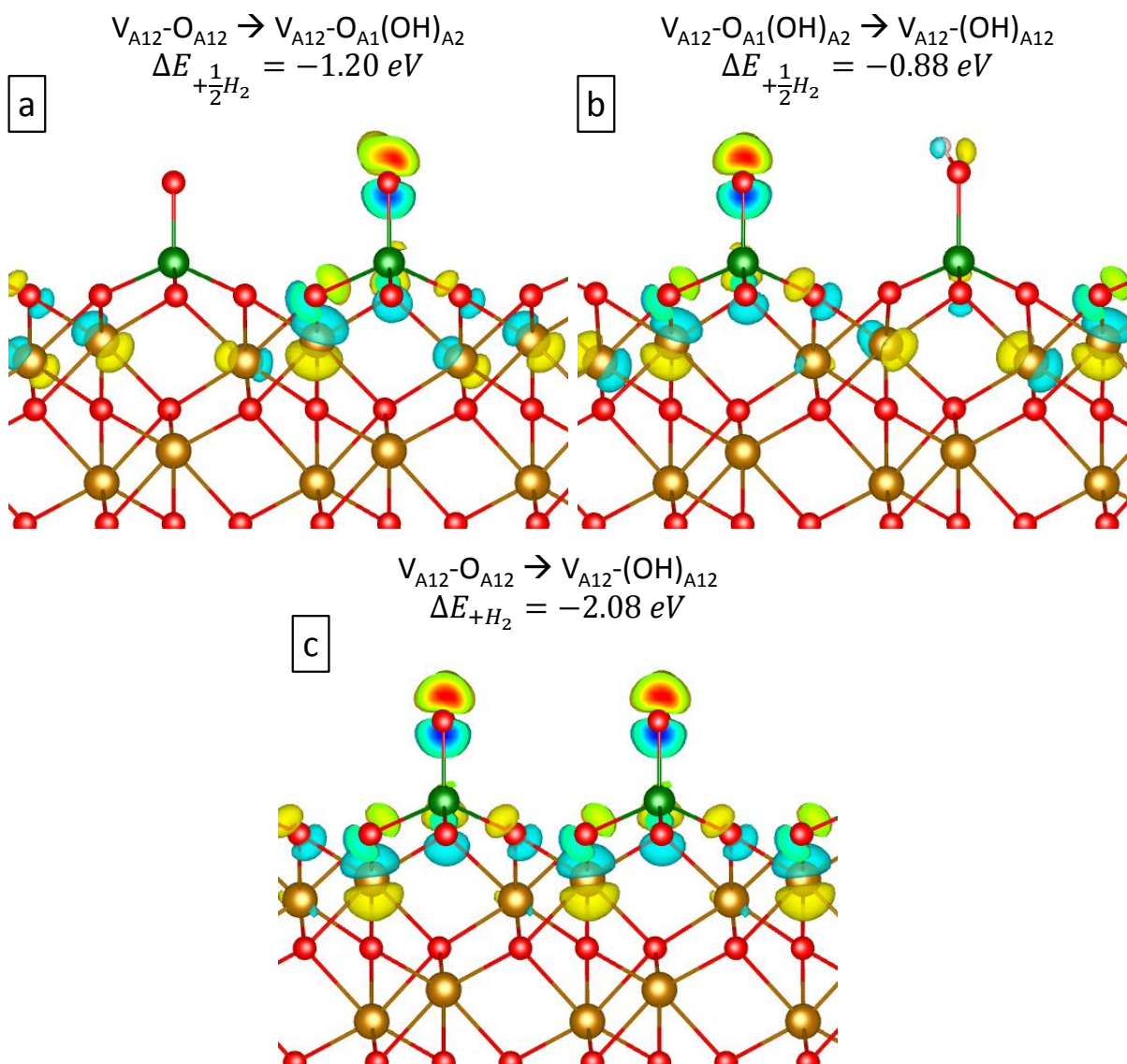


Figure 5.22: Charge difference maps for reactions on the hematite surface: (a) $V_{A12}-O_{A12} \rightarrow V_{A12}-O_{A1}(OH)_{A2}$; (b) $V_{A12}-O_{A1}(OH)_{A2} \rightarrow V_{A12}-(OH)_{A12}$; (c) $V_{A12}-O_{A12} \rightarrow V_{A12}-(OH)_{A12}$. Energies of each reaction are included. Isocharge densities in yellow and red indicate increases in charge density, while blue indicates decreases.

In a similar treatment as shown for sapphire in **Figure 5.5**, **Figure 5.22** shows the effect of sequentially adding hydrogen atoms onto a vanadyl-terminated surface. When adding a hydrogen atom to half of the vanadyl groups, there is a significant distortion of electron density as the cation

and its coordination environment shifts in space. These effects reach well beyond the first coordination shell; significant movements of the near-surface Fe cations are observed. The coordination environment around the remaining vanadyl is mostly unaffected, despite a shift of the Fe cation directly below it. When the second half of the vanadyl groups are hydroxylated, similar charge density perturbations occur around the new hydroxyl group as in the first hydroxylation, with further downward shifts in the subsurface Fe cations. In contrast with observations for sapphire, the charge density associated with sub-surface oxygen atoms is not significantly affected.

Cases with one or two terminal oxygens are detailed in **Table 5.15**, and relaxed structures are shown in **Figure 5.23**. Two isostoichiometric cases with a single bridging oxygen and four with two oxygens are shown. As in the sapphire study, the dimer configuration of the one-oxygen cases and the monomer configuration of the two-oxygen cases have the lowest energies of the two stoichiometries. However, the less stable structures are not as deeply destabilized on hematite (1.14 – 2.00 eV) as they are on sapphire (1.44 – 3.50 eV). Additionally, the dimer and polymer structures do not break apart, remaining in similar positions as their starting configurations.

For the single-oxygen cases, the coordination environment and valence of V is different as compared to the calculations for sapphire. On hematite, V remains near the center of V-O distorted tetrahedra, while on sapphire the A-site V forms five V-O bonds with its surroundings. V is significantly more oxidized in the hematite dimer case than its sapphire counterpart, by 0.35 e and 0.32 e for the A and B site, respectively. For the polymer, however, while the B-site cation is 0.26 e more oxidized on hematite than sapphire, the A-site cation is reduced by 0.39 e .

For the two-oxygen cases, some structural similarities with sapphire are evident. The vanadyl groups in the monomer and dimer cases are 1.61 Å, as they are on sapphire, and the valences are similar. In all the two-oxygen cases, the valences of the hematite-supported V species are similar to, or slightly more reduced than, their sapphire-supported counterparts.

Table 5.16 and **Figure 5.24** show relaxed structures with half the vanadia terminated with hydroxyl groups and half terminated with oxygen, forming vanadyl groups. As was the case for the sapphire structures, some different starting configurations relax into the same final configuration, so only some of the starting coordination structures are reported here. The monomer configuration has the highest stability, followed by the dimers (1.49 – 1.61 eV) and polymers (2.32 – 3.11 eV), which do not separate. Among the polymer configurations, the lowest-energy structure is $V_{A_2B_1}-O_{B_1}(OH)_{A_2}$, in which the V coordination polyhedra only share corners; at least one edge is shared in the other higher-energy configurations. Across the monomer and dimer configurations, the V valences are all very similar, within the range 4.48 – 4.60 e . However, with the exception of the aforementioned $V_{A_2B_1}-O_{B_1}(OH)_{A_2}$ structure, the V atoms in the polymer configurations are substantially more reduced.

	$V_{A1B1}-O_{br}$	$V_{A2B1}-O_{br}$	$V_{A12}-O_{A12}$	$V_{A1B1}-O_{A1B1}$	$V_{A2B1}-O_{A2B1}$	$V_{A2B1}-O_{2br}$
Relative energy (eV)	0.00	1.14	0.00	1.31	1.72	2.00
$V_{I}-O$ coordination (Å)	1.71, 1.74, 1.78 , 1.87	1.74, 1.82, 1.87, 1.92	1.61 , 1.81, 1.81, 1.81	1.61 , 1.79, 1.80, 1.85	1.72 , 1.72, 1.73, 1.77	1.72, 1.72, 1.84 , 1.91, 2.18
$Q_B(V_I)$	2.14	1.98	2.07	2.16	2.18	2.13
BVS(V_I)	4.25	3.53	4.60	4.56	4.70	4.31
$V_{II}-O$ coordination (Å)	1.69, 1.70, 1.90, 1.95	1.73, 1.79 , 1.80, 1.87	1.61 , 1.81, 1.81, 1.81	1.61 , 1.75, 1.78, 1.89	1.60 , 1.83, 1.84, 1.93, 2.23	1.66 , 1.78 , 1.79, 1.80
$Q_B(V_{II})$	2.02	2.00	2.07	2.16	2.15	2.13
BVS(V_{II})	3.95	3.94	4.60	4.62	4.41	4.49

Table 5.15: Structural and chemical information for $\frac{1}{2}$ ML V structures on the (0001) hematite surface with one or two additional oxygen ligands. Values as defined previously.

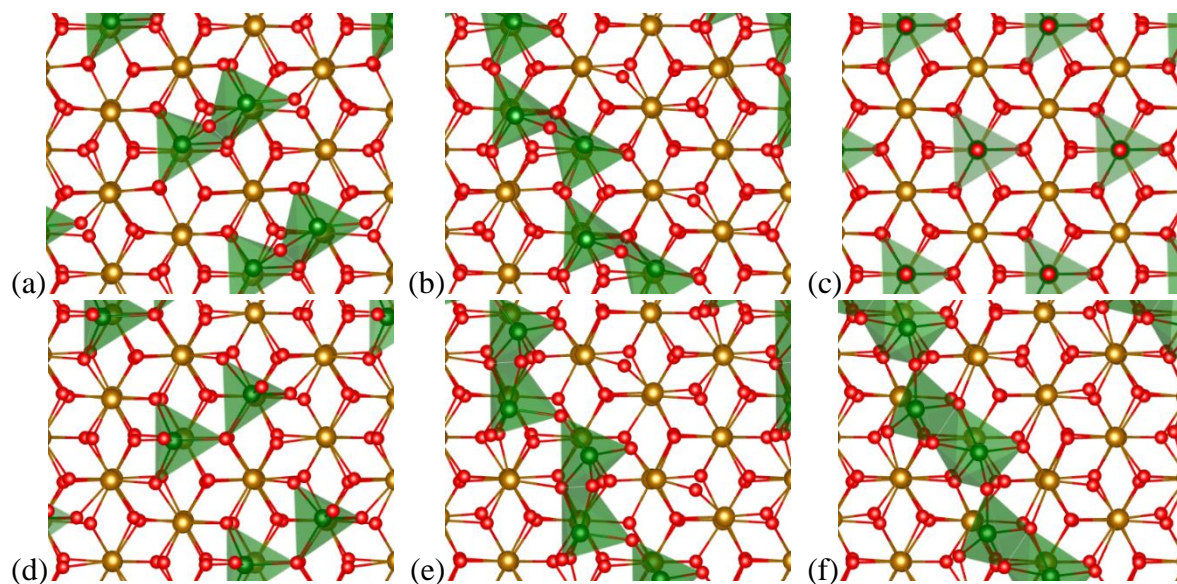


Figure 5.23: Top (0001) views of hematite-supported structures: (a) $V_{A1B1}-O_{br}$; (b) $V_{A2B1}-O_{br}$; (c) $V_{A12}-O_{A12}$; (d) $V_{A1B1}-O_{A1B1}$; (e) $V_{A2B1}-O_{A2B1}$; (f) $V_{A2B1}-O_{2br}$.

	$V_{A12}-O_{A1}(OH)_{A2}$	$V_{A1B1}-O_{A1}(OH)_{B1}$	$V_{A1B1}-O_{br}(OH)_{A1}$	$V_{A2B1}-O_{A2}(OH)_{B1}$	$V_{A2B1}-O_{B1}(OH)_{A2}$	$V_{A2B1}-O_{br}(OH)_{B1}$	$V_{A2B1}-O_{br}(OH)_{A2}$
Relative energy (eV)	0.00	1.57	1.49	2.62	2.32	3.11	2.88
V_I-O coordination (Å)	1.62 , 1.80, 1.80, 1.80	1.62 , 1.77, 1.79, 1.87	1.73, 1.75, 1.76, 1.77	1.69 , 1.72, 1.78, 1.83	1.68, 1.76, 1.77 , 1.78	1.71, 1.74 , 1.81, 1.81	1.74, 1.77, 1.93, 1.97 , 2.00
$Q_B(V_I)$	2.09	2.18	2.21	2.14	2.20	2.10	2.06
BVS(V_I)	4.59	4.53	4.48	4.49	4.58	4.26	3.95
$V_{II}-O$ coordination (Å)	1.72, 1.74, 1.74, 1.78	1.67, 1.73, 1.79 , 1.83	1.62 , 1.74, 1.80, 1.89	1.76, 1.79 , 1.80, 1.97, 2.09	1.61 , 1.79, 1.80, 1.80	1.69, 1.80 , 1.95 , 2.00, 2.03	1.74 , 1.75, 1.81, 1.98 , 2.20
$Q_B(V_{II})$	2.15	2.15	2.17	2.10	2.16	2.04	2.04
BVS(V_{II})	4.57	4.51	4.58	4.00	4.65	3.89	4.04

Table 5.16: Structural and chemical information for $\frac{1}{2}$ ML V structures on the (0001) hematite surface with one additional oxygen and one hydroxyl ligands. Values as defined previously.

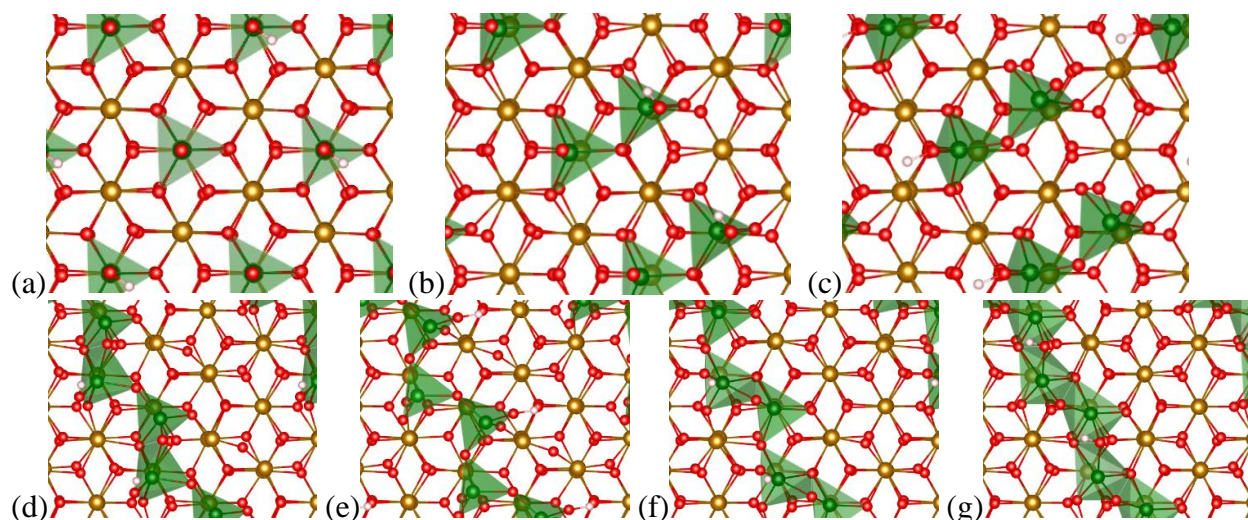


Figure 5.24: Top (0001) views of hematite-supported structures: (a) $V_{A12}-O_{A1}(OH)_{A2}$; (b) $V_{A1B1}-O_{A1}(OH)_{B1}$; (c) $V_{A1B1}-O_{br}(OH)_{A1}$; (d) $V_{A2B1}-O_{A2}(OH)_{B1}$; (e) $V_{A2B1}-O_{B1}(OH)_{A2}$; (f) $V_{A2B1}-O_{br}(OH)_{B1}$; (g) $V_{A2B1}-O_{br}(OH)_{A2}$.

Table 5.17 and **Figure 5.25** show results for hematite surfaces with one hydroxyl group terminating each V atom in the starting configuration. Two additional columns detail dimer and polymer cases with a bridging O atom in addition to the two hydroxyl groups. The stability (as well as the valence of V) decrease in the order of monomer > dimer > polymer for the structures without an additional bridging O. The dimers and polymers remain intact as corner-sharing distorted tetrahedra, with slight movements of V away from the surface A and B sites. As expected, the addition of a bridging O increases the valence of V in the dimer and polymer cases, but the dimer structure relaxes into dispersed monomers.

	$V_{A12}-(OH)_{A12}$	$V_{A1B1}-(OH)_{A1B1}$	$V_{A2B1}-(OH)_{A2B1}$	$V_{A1B1}-O_{br}(OH)_{A1B1}$	$V_{A2B1}-O_{br}(OH)_{A2B1}$
Relative energy (eV)	0.00	1.91	3.53	0.00	1.21
V_I -O coordination (Å)	1.73, 1.73, 1.73, 1.80	1.71, 1.72, 1.80 , 1.82	1.70, 1.82, 1.82 , 1.83	1.73, 1.75, 1.75, 1.76	1.73, 1.76, 1.82, 1.99 , 2.11
$Q_B(V_I)$	2.12	2.17	2.05	2.16	2.15
BVS(V_I)	4.52	4.37	4.01	4.53	4.10
V_{II} -O coordination (Å)	1.73, 1.73, 1.73, 1.80	1.68, 1.73, 1.80 , 1.84	1.72, 1.82 , 1.84, 1.87	1.63 , 1.77, 1.78 , 1.83	1.69 , 1.76, 1.78 , 2.06 , 2.22, 2.33
$Q_B(V_{II})$	2.12	2.14	1.99	2.19	2.20
BVS(V_{II})	4.52	4.41	3.79	4.60	4.36

Table 5.17: Structural and chemical information for $\frac{1}{2}$ ML V structures on the (0001) hematite surface with two additional hydroxyl ligands. Values as defined previously.

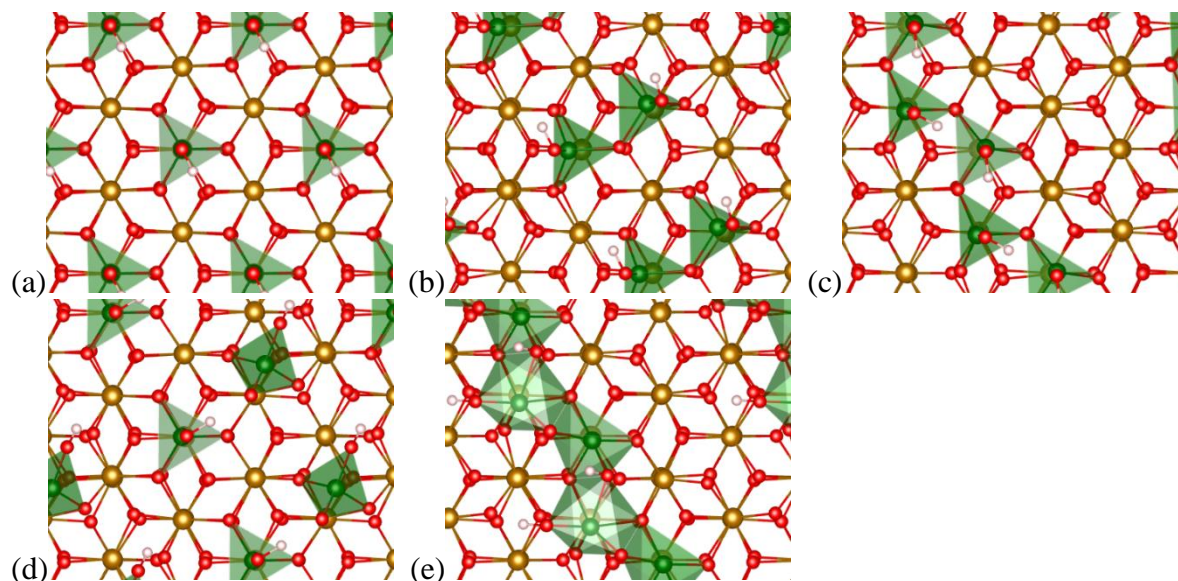


Figure 5.25: Top (0001) views of hematite-supported structures: (a) $V_{A12}-(OH)_{A12}$; (b) $V_{A1B1}-(OH)_{A1B1}$; (c) $V_{A2B1}-(OH)_{A2B1}$; (d) $V_{A1B1}-O_{br}(OH)_{A1B1}$; (e) $V_{A2B1}-O_{br}(OH)_{A2B1}$.

5.3.6 0.5 ML V / O-terminated $\alpha\text{-Fe}_2\text{O}_3$ (0001): NH_3 adsorption

The most stable monomer, dimer, and polymer configurations for the structures with one additional oxygen and hydroxyl group were investigated for NH_3 adsorption onto the hydroxyl. Results are shown in **Table 5.18**, and the relaxed structures are shown in **Figure 5.26**. In the monomer and dimer cases, there is practically no interaction between NH_3 and the surface; the structures are mostly unchanged. However, for the polymer case, there is a very strong interaction as the hydroxyl proton is removed, yielding an NH_4^+ species which sit between polymer rows. These ammonium cations interact with the remaining vanadyl groups, with H - - O hydrogen bond distances of 1.7 – 2.0 Å. The strongest interaction is with the substrate as a 1.6 Å hydrogen bond is formed with a surface O atom.

The effect of NH_3 adsorption on the electronic states of the polymer surface is shown in **Figure 5.27**. On the clean polymer surface, the spin-up states of the upper V *d*-band are somewhat filled

(about twice more than for the hydroxylated V than the vanadyl-terminated V). Upon ammonia adsorption, there is very little change in the V PDOS. Slight shifts in the V *d*-bands result in a reduction of the total occupied fraction of the band by more than half. The ammonium ion shows no states higher than 8 eV below E_F .

	$V_{A12}-O_{A1}(OH)_{A2}-(NH_3)_{A2}$	$V_{A1B1}-O_{br}(OH)_{A1}-(NH_3)_{A1}$	$V_{A2B1}-O_{B1}(OH)_{A2}-(NH_3)_{A2}$
Diff (eV)	0.00	1.50	0.68
E_{NH_3-ads}	0.02	0.03	-1.62
V_I -O coordination (Å)	1.62 , 1.80, 1.80, 1.80	1.73, 1.75, 1.75, 1.78	1.64 , 1.72, 1.80, 1.83
$Q_B(V_I)$	2.09	2.21	2.18
BVS(V_I)	4.59	4.46	4.71
V_{II} -O coordination (Å)	1.73, 1.73, 1.74, 1.78	1.62 , 1.74, 1.79, 1.89	1.64 , 1.77, 1.77, 1.78
$Q_B(V_{II})$	2.17	2.16	2.18
BVS(V_{II})	4.58	4.58	4.72

Table 5.18: Structural and chemical information for $\frac{1}{2}$ ML V structures on the (0001) hematite surface with one additional oxygen and one hydroxyl ligands, as well as one adsorbed NH_3 molecule. Values as defined previously.

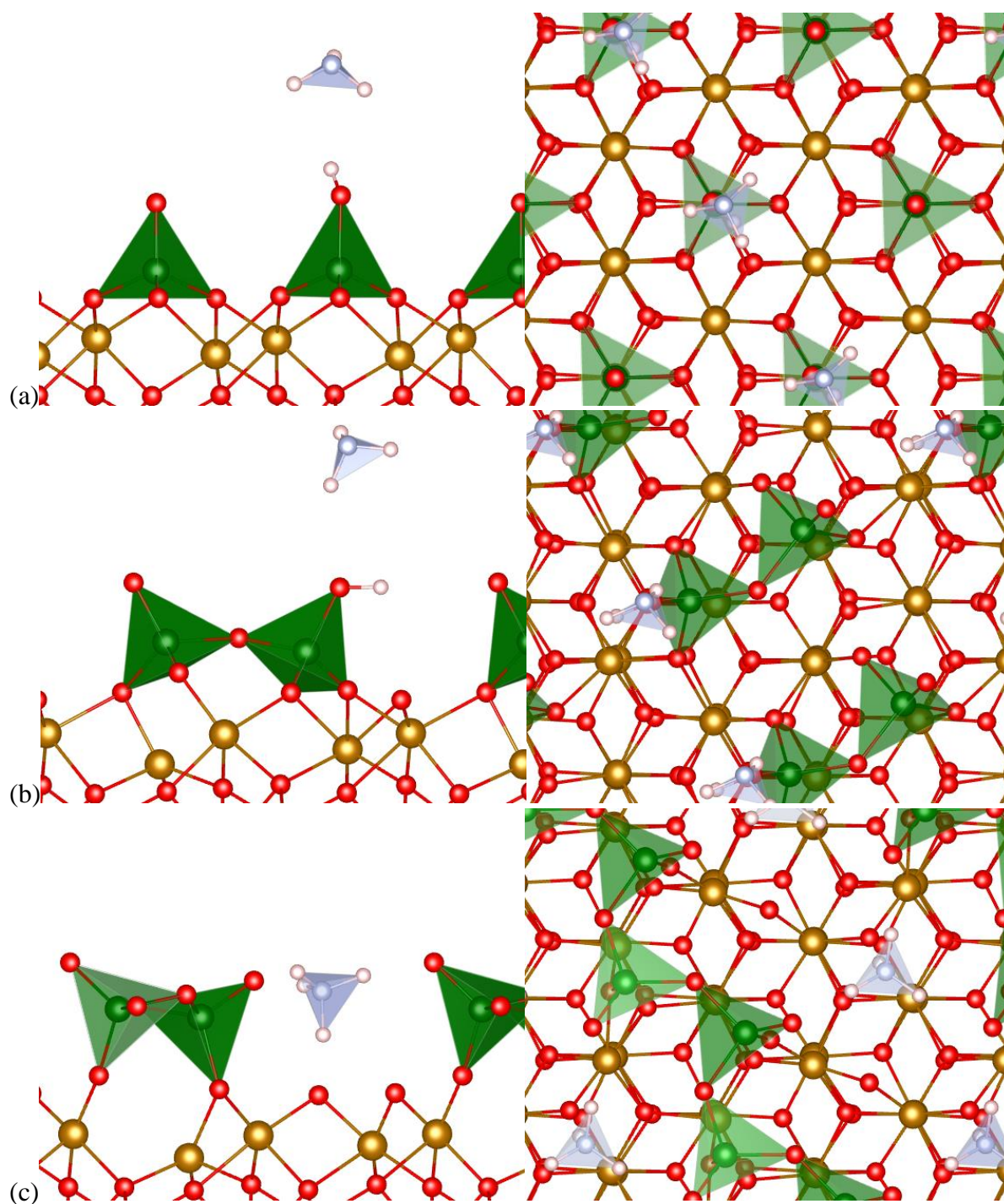


Figure 5.26: Side (1 1 -2 0) (left) and top (0001) (right) views of relaxed structures of NH₃ adsorbed on: (a) V_{A12}-O_{A1}(OH)_{A2}, (b) V_{A1B1}-O_{br}(OH)_{A1}, and (c) V_{A2B1}-O_{B1}(OH)_{A2}.

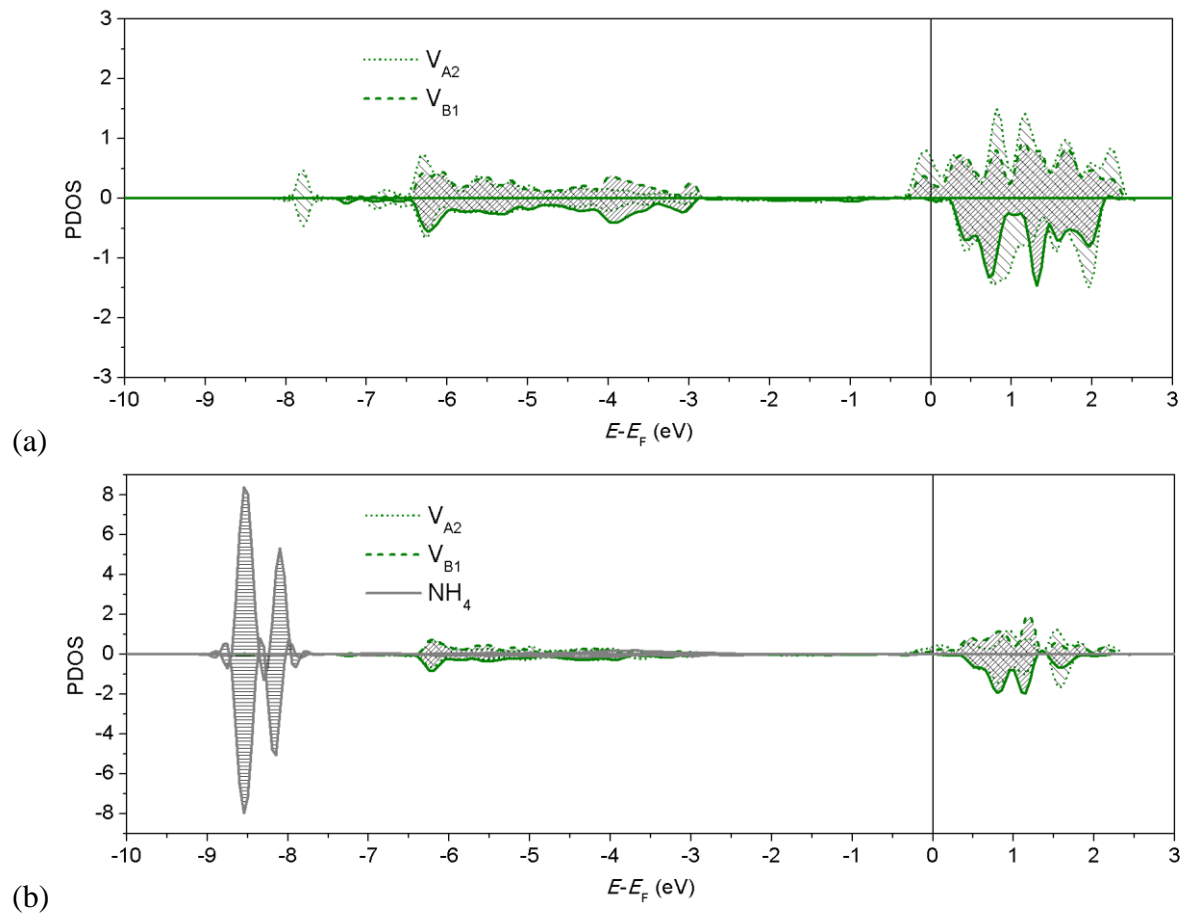


Figure 5.27: Spin-polarized V PDOS for hematite-supported structures: (a) $V_{A2B1}-O_{B1}(OH)_{A2}$, (b) $V_{A2B1}-O_{B1}(OH)_{A2}-(NH_3)_{A2}$. Positive and negative values indicate spin-up and spin-down states, respectively.

5.4 Discussion

5.4.1 Effect of W on V chemistry

The effect of W on sapphire-supported V was investigated by replacing half the adsorbed V with W for a nominal coverage of $\frac{1}{4}$ ML of each. The addition of W partially stabilizes the dimer and polymer structures, reducing the relative energy of these structures vs. $\frac{1}{2}$ ML V alone. While the dimer and polymer structures never reach lower energies than those for the monomers in this work, it is possible that W could stabilize catalyst oligomers on real catalyst supports with more complex surface structures.

The first step of the NO-SCR reaction has been proposed to be the adsorption of NH_3 onto a Brønsted acid site, forming an NH_4^+ cation and thereby “activating” a nearby redox site[17]. We find that the adsorption of NH_3 depends strongly on the catalyst structure. For the V-only case, two kinds of NH_3 adsorption were observed, showing two types of acidity for V: Brønsted and Lewis with NH_3 adsorption energies of $-1.17 - -1.34$ eV and -0.81 eV, respectively. The structures showing Brønsted acidity were V monomers, whereas dimers consisting of corner-sharing distorted tetrahedra showed Lewis acidity. In the mixed V-W structures, however, Lewis-like interactions between the metals and NH_3 were not observed. Different H-bonded structures (OH - - - N, O - - - H) were observed with NH_3 adsorption energies in the range of $-0.51 - -0.76$ eV. Brønsted-like adsorption was observed for a V-W dimer configuration with the two cation coordination polyhedra sharing an edge. The NH_3 adsorption energy for this case, -1.69 eV, suggests that NH_3 interacts much more strongly with the mixed W-V structures than with V alone.

We note that in the cases in which the ammonium cation is formed, there are no NH_4^+ states near the system Fermi level (either above or below E_F). The lack of filled donor states or unfilled

acceptor states near E_F suggests that the ammonium cation is very stable and may not be reactive in the geometries studied. However, the strong adsorption energy of NH_3 corresponding with its protonation to NH_4^+ , which is strengthened by the presence of W, suggests that this is a particularly favorable interaction over real V-W catalysts.

5.4.2 Substrate effects on V chemistry

Analysis of the coordination environments of V on the O-terminated (0001) surfaces of hematite and sapphire show that the dimer and polymer structures are more likely to remain intact on hematite. From a simple structural perspective, this is somewhat surprising, as the lateral lattice parameter of the hematite cell ($a = 5.01 \text{ \AA}$) is 5.3% larger than that of sapphire ($a = 4.76 \text{ \AA}$). The dimers and chains might be more likely to “stretch apart” on the hematite surface, but this is not the case. Instead, this phenomenon can be attributed to the chemical “flexibility” of hematite due to its greater reducibility and the greater degree of covalency in the Fe-O interactions. As discussed below, Bader charge analysis shows that the oxygen atoms bridging V with the substrate have a lesser degree of ionicity on hematite, suggesting a larger range of possible configurations which allow for local distortions at the surface.

Experimental evidence suggests that the effect of the substrate on catalytic behavior is highly dependent on the bond between the catalyst metal and the oxygen atoms in the oxide substrate[24]. While the BVS of all cations on the hematite substrate are slightly underpredicted due to the overprediction of the hematite lattice parameter (as discussed in **Chapter 3**), the differences in coordination-dependent BVS between the sapphire- and hematite-supported cases can be ascribed to the degree of charge transfer between the substrate anions and cations and the charge available to the metal atoms adsorbed on the surface. We therefore look at the Bader charges on the oxygen

atoms in the V coordination environment in **Table 5.19**. For the terminal oxygen atoms (O_t), constituting the vanadyl or hydroxyl oxygens, there is very little dependence on the substrate. However, a large difference is observed for the substrate oxygens (O_s) which coordinate with V and the substrate ($V-O-M_S$, $M_S = Al$ or Fe). In sapphire, the Bader partition of each coordinating substrate oxygen atom contains about 0.4 more electrons per atom than for hematite. This is attributed to the extremely ionic nature of Al^{3+} . Negative charge will thus be localized at the O atoms for sapphire, whereas it will be more covalently shared between Fe and O atoms in hematite. Thus, in sapphire, fewer O states will be available to receive charge from a surface species such as V. In hematite, on the other hand, V can share charge with the available states in O, resulting in a more positive nominal oxidation state according to BVS.

	$V_{Al_2-(OH)_{Al_2}}$	$V_{Al_2-O_{Al_1}(OH)_{Al_2}}$	$V_{Al_2-O_{Al_2}}$
V_I coordinating O_t	-0.62, -0.61	-0.68, -0.68	-1.45, -1.44
V_I coordinating O_s	-1.52, -1.06	-1.50, -1.08	-1.46, -1.04
V_{II} coordinating O_t	-0.62, -0.61	-1.50, -1.41	-1.46, -1.44
V_{II} coordinating O_s	-1.52, -1.06	-1.41, -1.03	-1.47, -1.04

Vanadyl, Hydroxyl, Surface

Table 5.19: Bader charges on O atoms in the V-O coordination environment for 0.5 ML V monomers. The first value in each cell is that for V supported on sapphire, followed that for hematite. Values corresponding to vanadyl groups are shown in red; hydroxyl, blue; and V-O- M_S “surface” oxygens, green.

There are clear differences in the effect of reduction on vanadium species supported on sapphire vs. hematite. As shown in **Tables 5.2** and **5.14**, the reduction of monomeric V supported on hematite is much more strongly exothermic than that on sapphire. However, the local coordination environment of the hydroxylated V species has much shorter V-O bonds on hematite vs. sapphire.

This leads to a calculated valence that is much closer to the expected value for V^{5+} than V^{4+} , despite V sitting at the center of a distorted tetrahedron with one hydroxyl group and three oxygens bridging to the support surface. Analysis of **Figures 5.5** and **5.22** provide an explanation. A reduction event from $V=O$ to $V-OH$ on either surface leads to a shift in the surface oxygen atoms towards V. To compensate for this shift in charge, the sapphire surface requires significant movements of charge through the near-surface lattice, as shown by the significant lobes of charge density shift around deeper oxygen layers in **Figure 5.5(a)**. On hematite, however, these charge shifts are mitigated by shifts in the topmost Fe^{3+} layers, below which no charge shifts are observed. The differences can also be viewed through the near-surface substrate cation coordination environments, given in **Tables 5.2** and **5.14**. Within their coordination environments, the difference between the shortest and longest Al-O bond for near-surface Al atoms in the sapphire-supported V monomer cases are 0.08 for Al_C and 0.19 for Al_B . For hematite-supported V monomers, the ranges in Fe-O bond lengths are 0.16 for Fe_C and 0.25 for Fe_B . Altogether, the hematite surface is better able to accommodate structural changes due to exposure to reactive environments such as H_2 . The dissociative adsorption of H_2 is therefore more strongly favored on hematite than sapphire by about 1.8 eV per H_2 molecule.

Regarding the NH_3 adsorption, the cases studied herein for hematite-supported V show weak interactions with V monomers and dimers, but a very strong interaction with the polymer configuration terminated with one hydroxyl group and one additional oxygen, forming a vanadyl group. The adsorption of NH_3 on this surface is very exothermic (-1.62 eV per NH_3) and results in significant changes to the coordination structure of V as a result. The hydroxylated V gives up its proton to NH_3 , forming an NH_4^+ cation and a somewhat stretched vanadyl group. The other $V=O$

bond stretches as well, from 1.61 to 1.64 Å, due to the positive charge of NH_4^+ . The valence of each vanadium atom is very close to that expected for V^{5+} . In contrast, for the Brønsted-like interaction on sapphire-supported V, the vanadyl groups are extended much further (1.66 – 1.70 Å), resulting in a somewhat lower measured valence. Significant distortions in the surface hematite lattice (as shown in **Figure 5.26**) might allow the V polyhedra to move into better positions to coordinate, reducing the overall energy of adsorption.

5.5 Conclusions

Using density functional theory, several configurations of dispersed V were investigated on the (0001) surface of 2×1 α - Al_2O_3 slab. The effect of two changes on the V environment, the addition of W and the use of a α - Fe_2O_3 substrate, were investigated in order to probe the effect of co-catalysts and substrate chemistry. Dispersed V monomers were found to be the most stable configurations in most cases, although the addition of W or the use of a hematite substrate improved the stability of dimer or polymer phases with bridged catalyst coordination polyhedra. Substrate-dependent differences in the chemical behavior of V were observed, particularly the much stronger dissociative chemisorption of H_2 on hematite vs. sapphire, which can be attributed to the chemical and structural “flexibility” of the more covalently bonded hematite surface. Both the addition of W and the use of a hematite substrate improved the adsorption of NH_3 onto Brønsted acid sites, yielding NH_4^+ and simulating the first step in the NO-SCR reaction.

This work only covers the O-terminated surface of (0001)-oriented sapphire and hematite crystals. As discussed in **Chapter 3** and **Chapter 4**, the Al- or Fe-terminated (0001) single crystal surfaces might be more stable under realistic conditions. However, realistic oxide catalyst surfaces would

be far more complex than any single crystal termination, and modeling the myriad of crystal terminations and defect sites is beyond the scope of this work. Using model systems, the results covered in this chapter yield insight towards the atomic-scale nature of V-W synergy and the effect of oxide support chemistry.

6. Conclusions: Cation-Cation Interactions on Oxide Catalyst Surfaces

6.1 Summary

In this work, the structure and chemical behavior of V and W supported on two oxide substrates (α -Al₂O₃ and α -Fe₂O₃) were investigated by the methods of surface and interface science. The goal of this approach is to provide fundamental physical understanding of catalyst behavior by simplifying the material geometry, allowing a more thorough and precise characterization of the atomic-scale structure of catalytically active phases. Of particular interest is the synergistic interaction between V and W in several reactions, particularly the selective catalytic reaction of nitric oxide (NO-SCR) with ammonia. The influence of the oxide substrate was also investigated by using two different materials with almost identical structures but drastically different chemical properties. This work builds from several years of experimental research on model catalysts in the Bedzyk group[32-35, 66, 129-131, 207, 213] while contributing new perspective to the structure and chemistry of these materials via theoretical tools. The salient points of this work are summarized as follows:

1. Reduction-oxidation reaction cycles on single crystal model catalyst surfaces can cause measurable, reversible structural changes which accompany chemical state shifts. These structural changes range from ligand exchange with a flowing gas to $>1 \text{ \AA}$ lateral movements of surface cations.
2. In the vicinity of another reducible cation, such as a surface V⁵⁺ species or substrate Fe³⁺, W⁶⁺ may reduce under relatively mild reducing conditions (350 – 400 °C in dilute H₂). This reduction

makes available W *d*-states which could increase the Brønsted acidity of W sites, thereby improving catalyst performance for certain reactions.

3. The adsorption of molecules such as NH₃ depends strongly on both the chemistry and the local structure of the catalyst site. In particular, NH₃ adsorption on oxide-supported VO_x (with subsequent protonation to NH₄⁺ over a Brønsted acid site) is stabilized by the presence of W or the use of a reducible oxide substrate.

These conclusions are derived from both experimental studies and theoretical calculations. First-principles electronic structure modeling is a powerful tool for the observation and quantification of electronic states available for catalytic reactions, but without experimental validation of the structures, results must be taken with substantial skepticism. In **Chapter 3** and **Chapter 4**, DFT calculations on model surfaces result in relaxed structures which are consistent with experimental data from XSW, XPS, and XAFS. These structures are a jumping-off point to more detailed theoretical investigations in **Chapter 5** which provide deeper insight into the chemical physics of heterogeneous catalysis at oxide-reactant interfaces.

This work informs the design of catalysts by revealing physical relationships between neighboring cations, namely those of W and V or Fe, in multi-component oxide catalysts. In particular, it is shown in **Chapter 4** that the interaction of V⁴⁺ and W⁶⁺ cations results in a spontaneous charge transfer which slightly reduces W⁶⁺ to W^{(6-δ)+} as indicated by the opening of partially filled W *d*-states at the Fermi level, an effect that may enhance the Brønsted acidity of the W sites. For the design of highly active acid catalysts for more sustainable chemistry, the interaction between metal cations associated with Brønsted acid sites (e.g. W⁶⁺, Mo⁶⁺) and co-reductants (e.g. V⁵⁺, Fe³⁺) and the subsequent effect on the *d* orbitals must be understood. Similar approaches have been used to

engineer multi-component metal[6] and oxide[233] catalysts with improved properties over their substituent materials. This finding for acid catalysts could inform broader investigations of cation-cation interactions at oxide surfaces, with the formation of *d*-states above the valence band in acid catalyst species such as W^{6+} or Mo^{6+} as a search criterion for new acid catalysts.

6.2 Future directions in surface and interface studies of oxide catalysts

6.2.1 *In situ* and *operando* studies of model catalysts

In this work, the interaction of V and W were studied in light of the NO_x -SCR reaction with NH_3 . However, all experimental work focused on the redox behavior upon reaction with O_2 and H_2 . In order to better understand the interaction between V, W, and the substrate under real SCR conditions, the adsorption of NH_3 and NO must be experimentally studied. This would require the construction of new sample cells with tolerance to NH_3 and NO. Many components of our current sample cell setup are made of Cu, which is vulnerable to reaction with NH_3 and NO in the presence of water. Sample cells composed of Al might be better suited for such reactions. The use of different probe molecules by the Bedzyk group is not unprecedented; structural and chemical changes in $VO_x / \alpha-TiO_2$ (110) due to reaction with cyclohexane have been reported by our group[35].

A more ambitious implementation of this idea is to perform *operando* measurements in which the sample reactivity is measured simultaneously with structural and spectroscopic measurements. Reaction products could be measured using on-line mass spectrometry or gas chromatography, yielding information about the activity, selectivity, and kinetics of a reaction. By this approach, the effects of catalyst composition and stoichiometry on catalyst performance could be directly correlated with structural and spectroscopic evidence. While reaction kinetics on single crystal

surfaces are accessible to experimental study in small reactors[234, 235], the potential of *operando* surface X-ray scattering and spectroscopy remains to be seen. The low reactive surface area of a catalyst-coated single would result in low concentrations of reaction products. Side reactions could occur on the relatively large internal surface area of an X-ray penetrable reaction cell composed of several materials, precluding the unambiguous assignment of reactivity to the sample. However, one can imagine *in situ* single crystal studies being compared to *operando* studies on powder catalysts of similar composition. Spectroscopies such as XAFS may be used to bridge atomic scale structural conclusions from *in situ* studies on model single crystal catalysts to reactivity data on more realistic systems. As evinced by the results in **Chapter 3**, however, this requires preliminary characterization to confirm that the single crystals and powder catalysts are actually behaving similarly under similar chemical conditions.

6.2.2 Simulation of the V/W/TiO₂ surface

DFT-relaxed structures of V and W on sapphire and hematite (0001) surfaces show good agreement with experimental results. With several publications by the Bedzyk group on the structure and chemistry of V and W deposited on the α -TiO₂ (rutile) (110) surface[32-35], it would be useful to find relaxed models for our experimental data. This could refine our interpretations of XSW and XPS results while enabling future theoretical work on molecular adsorption and reactivity of these surfaces. Additionally, recent work on mixed V-W deposition on rutile[36] highlights uncertainties about the location of catalyst cations with respect to the substrate surface due to the modulo- d_H ambiguity inherent to XSW-derived atomic positions. Using DFT, unambiguous structural models could be found for V, W, and mixed V-W on the rutile (110)

surface to help answer questions involving multi-layer stacking and the co-reduction of V and W on this substrate.

6.2.3 Reaction pathway calculation and *ab initio* thermodynamics

With the *in situ* atomic-scale characterization tools well known to the Bedzyk group, as well as improvements in simultaneous *in situ* X-ray scattering and spectroscopy, future experiment-theory collaborations could yield accurate models for more complex reactions on oxide surfaces. **Chapter 5** deals with the first step of the NO-SCR reaction: the adsorption of NH₃ onto the catalyst surface. However, several studies report the calculation of complete catalytic pathways, from products to reactants. In most cases these are calculated over metal crystal surfaces, owing to their structural simplicity and the relative ease of calculating structures and energetics for several possible transition states[236, 237]. Such studies are few and far between for oxide surfaces, owing to the complicated redox chemistry of many oxide catalysts and significant corresponding structural shifts (see e.g. **Chapter 3** and Ref. [238]). Knowing the atomic-scale surface structure at different reaction steps via *in situ* experiments could pare down the number of different structures that would need to be calculated and improve confidence in the assignment of reaction pathways. Alternatively, these systems may be studied by *ab initio* thermodynamics[59, 239], although such a treatment would require more accurate molecular adsorption energies, especially for molecules such as NO. As discussed in **Appendix A**, there are several exchange-correlation approximations available for use with plane-wave DFT as implemented in VASP. Modern exchange-correlation functionals such as meta-GGA might yield more accurate calculations of ground-state energies and weakly interacting structures such as those that involve van der Waals interactions.

6.2.4 Structural characterization of real catalysts: zeolites

Many catalysts used in industry for fuel refining and environmental applications consist of metals or metal oxides supported by zeolites. These silicate materials often contain a significant fraction of lattice Al substituting for Si which provides reactive acid sites, and the zeolite framework can be impregnated with other catalytically active species[5]. Zeolites are also highly selective catalysts because of their microporous structure which can be tuned to allow or exclude different molecules from entering and traveling through the pores. Despite their industrial use for several decades, many questions remain regarding the atomic-scale structure of zeolites and their catalytically active additives. For example, the atomic position of Cu atoms supported in the SSZ-13 zeolite is critical to the NO_x-SCR activity of the catalyst. *In situ* spectroscopic evidence[240, 241] and high-temperature XRD[242] provide clues as to the Cu configuration relative to the zeolite lattice under reaction conditions, but so far there are no precise measurements of the Cu position under relevant reaction conditions. Synchrotron methods such as XSW[243] and resonant anomalous X-ray diffraction could yield accurate measurements of cation positions under appropriate reaction conditions for Cu-SSZ-13 and other zeolite systems.

References

1. Malthus, T.R., *An Essay on the Principle of Population*. 1798, J. Johnson: London.
2. United Nations Secretariat, D.o.E.a.S.A., Population Division, *The World at Six Billion*. 1999.
3. Erisman, J.W., Sutton, M.A., Galloway, J., Klimont, Z., and Winiwarter, W., *How a century of ammonia synthesis changed the world*. *Nature Geoscience*, 2008. **1**(10): p. 636-639.
4. Haber, F., *Verfahren zur synthetischen Darstellung von Ammoniak aus den Elementen*. 1908: Germany.
5. Chorkendorff, I. and Niemantsverdriet, J.W., *Concepts of Modern Catalysis and Kinetics*. 2nd ed. 2007, Weinheim, Germany: WILEY-VCH Verlag GmbH & Co.
6. Norskov, J.K., Bligaard, T., Rossmeisl, J., and Christensen, C.H., *Towards the computational design of solid catalysts*. *Nature Chemistry*, 2009. **1**(1): p. 37-46.
7. Greeley, J. and Mavrikakis, M., *Alloy catalysts designed from first principles*. *Nature Materials*, 2004. **3**(11): p. 810-815.
8. Sehested, J., Larsen, K., Kustov, A., Frey, A., Johannessen, T., Bligaard, T., Andersson, M., Nørskov, J., and Christensen, C., *Discovery of technical methanation catalysts based on computational screening*. *Topics in Catalysis*, 2007. **45**(1-4): p. 9-13.
9. Du, X., Gao, X., Hu, W., Yu, J., Luo, Z., and Cen, K., *Catalyst Design Based on DFT Calculations: Metal Oxide Catalysts for Gas Phase NO Reduction*. *The Journal of Physical Chemistry C*, 2014. **118**(25): p. 13617-13622.
10. Wilson, K. and Lee, A.F., *Rational design of heterogeneous catalysts for biodiesel synthesis*. *Catalysis Science & Technology*, 2012. **2**(5): p. 884-897.
11. Gunter, P.L.J., Niemantsverdriet, J.W., Ribeiro, F.H., and Somorjai, G.A., *Surface Science Approach to Modeling Supported Catalysts*. *Catalysis Reviews*, 1997. **39**(1-2): p. 77-168.
12. Ertl, G., *Primary steps in catalytic synthesis of ammonia*. *Journal of Vacuum Science & Technology A*, 1983. **1**(2): p. 1247-1253.
13. Poelman, H., Silversmit, G., Poelman, D., Marin, G.B., and Sels, B.S., *Deposition and characterisation of vanadium oxide thin films: Linking single crystal and supported catalyst*. *Catalysis Today*, 2009. **142**(3-4): p. 125-131.

14. Gabriëlsson, P. and Pedersen, H.G., *Flue Gases from Stationary Sources*, in *Handbook of Heterogeneous Catalysis*. 2008, Wiley-VCH Verlag GmbH & Co. KGaA.
15. Bosch, *Formation and control of nitrogen oxides*. *Catalysis Today*, 1988. **2**(4): p. 369-379.
16. Weckhuysen, B.M. and Keller, D.E., *Chemistry, spectroscopy and the role of supported vanadium oxides in heterogeneous catalysis*. *Catalysis Today*, 2003. **78**(1-4): p. 25-46.
17. Topsøe, N.-Y., *Mechanism of the Selective Catalytic Reduction of Nitric Oxide by Ammonia Elucidated by in Situ On-Line Fourier Transform Infrared Spectroscopy*. *Science*, 1994. **265**(5176): p. 1217-1219.
18. Baran, R., Onfroy, T., Grzybek, T., and Dzwigaj, S., *Influence of the nature and environment of vanadium in VSiBEA zeolite on selective catalytic reduction of NO with ammonia*. *Applied Catalysis B: Environmental*, 2013. **136-137**(0): p. 186-192.
19. Tang, F., Zhuang, K., Yang, F., Yang, L., Xu, B., Qiu, J., and Fan, Y., *Effect of Dispersion State and Surface Properties of Supported Vanadia on the Activity of V₂O₅/TiO₂ Catalysts for the Selective Catalytic Reduction of NO by NH₃*. *Chinese Journal of Catalysis*, 2012. **33**(4-6): p. 933-940.
20. Wachs, I.E., *Recent conceptual advances in the catalysis science of mixed metal oxide catalytic materials*. *Catalysis Today*, 2005. **100**(1-2): p. 79-94.
21. Amiridis, M.D., Wachs, I.E., Deo, G., Jehng, J.-M., and Kim, D.S., *Reactivity of V₂O₅ Catalysts for the Selective Catalytic Reduction of NO by NH₃: Influence of Vanadia Loading, H₂O, and SO₂*. *Journal of Catalysis*, 1996. **161**(1): p. 247-253.
22. Wu, Z., Kim, H.-S., Stair, P.C., Rugmini, S., and Jackson, S.D., *On the Structure of Vanadium Oxide Supported on Aluminas: UV and Visible Raman Spectroscopy, UV-Visible Diffuse Reflectance Spectroscopy, and Temperature-Programmed Reduction Studies*. *The Journal of Physical Chemistry B*, 2005. **109**(7): p. 2793-2800.
23. Wu, Z., Stair, P.C., Rugmini, S., and Jackson, S.D., *Raman spectroscopic study of V/ γ -Al₂O₃ catalysts: quantification of surface vanadia species and their structure reduced by hydrogen*. *Journal of Physical Chemistry C*, 2007. **111**(44): p. 16460-16469.
24. Deo, G. and Wachs, I.E., *Reactivity of Supported Vanadium Oxide Catalysts: The Partial Oxidation of Methanol*. *Journal of Catalysis*, 1994. **146**(2): p. 323-334.
25. Oudenhuijzen, M.K., van Bokhoven, J.A., Ramaker, D.E., and Koningsberger, D.C., *Theoretical Study on Pt Particle Adsorbate Bonding: Influence of Support Ionicity and Implications for Catalysis*. *The Journal of Physical Chemistry B*, 2004. **108**(52): p. 20247-20254.

26. Fievez, T., De Proft, F., Geerlings, P., Weckhuysen, B.M., and Havenith, R.W.A., *Conceptual chemistry approach towards the support effect in supported vanadium oxides: Valence bond calculations on the ionicity of vanadium catalysts*. *Catalysis Today*, 2011. **177**(1): p. 3-11.
27. Tian, H., Ross, E.I., and Wachs, I.E., *Quantitative Determination of the Speciation of Surface Vanadium Oxides and Their Catalytic Activity*. *The Journal of Physical Chemistry B*, 2006. **110**(19): p. 9593-9600.
28. Busca, G., Lietti, L., Ramis, G., and Berti, F., *Chemical and mechanistic aspects of the selective catalytic reduction of NO_x by ammonia over oxide catalysts: A review*. *Applied Catalysis B: Environmental*, 1998. **18**(1-2): p. 1-36.
29. Broclawik, E., Góra, A., and Najbar, M., *The role of tungsten in formation of active sites for NO SCR on the V-W-O catalyst surface — quantum chemical modeling (DFT)*. *Journal of Molecular Catalysis A: Chemical*, 2001. **166**(1): p. 31-38.
30. Sun, C., Dong, L., Yu, W., Liu, L., Li, H., Gao, F., Dong, L., and Chen, Y., *Promotion effect of tungsten oxide on SCR of NO with NH₃ for the V₂O₅-WO₃/Ti_{0.5}Sn_{0.5}O₂ catalyst: Experiments combined with DFT calculations*. *Journal of Molecular Catalysis A: Chemical*, 2011. **346**(1-2): p. 29-38.
31. Kompio, P.G.W.A., Brückner, A., Hipler, F., Auer, G., Löffler, E., and Grünert, W., *A new view on the relations between tungsten and vanadium in V₂O₅WO₃/TiO₂ catalysts for the selective reduction of NO with NH₃*. *Journal of Catalysis*, 2012. **286**(0): p. 237-247.
32. Kim, C.-Y., Elam, J.W., Pellin, M.J., Goswami, D.K., Christensen, S.T., Hersam, M.C., Stair, P.C., and Bedzyk, M.J., *Imaging of Atomic Layer Deposited (ALD) Tungsten Monolayers on α -TiO₂(110) by X-ray Standing Wave Fourier Inversion*. *The Journal of Physical Chemistry B*, 2006. **110**(25): p. 12616-12620.
33. Kim, C.-Y., Elam, J.W., Stair, P.C., and Bedzyk, M.J., *Redox Driven Crystalline Coherent-Incoherent Transformation for a 2 ML VO_x Film Grown on α -TiO₂(110)*. *The Journal of Physical Chemistry C*, 2010. **114**(46): p. 19723-19726.
34. Feng, Z., Cheng, L., Kim, C.-Y., Elam, J.W., Zhang, Z., Curtiss, L.A., Zapol, P., and Bedzyk, M.J., *Atomic-Scale Study of Ambient-Pressure Redox-Induced Changes for an Oxide-Supported Submonolayer Catalyst: VO_x/ α -TiO₂(110)*. *The Journal of Physical Chemistry Letters*, 2012. **3**(19): p. 2845-2850.
35. Feng, Z., Lu, J., Feng, H., Stair, P.C., Elam, J.W., and Bedzyk, M.J., *Catalysts Transform While Molecules React: An Atomic-Scale View*. *The Journal of Physical Chemistry Letters*, 2012. **4**(2): p. 285-291.

36. Feng, Z., McBriarty, M.E., Mane, A.U., Lu, J., Stair, P.C., Elam, J.W., and Bedzyk, M.J., *Redox-Driven Atomic-Scale Changes in Mixed Catalysts: VO_x / WO_x / α -TiO₂ (110)*. submitted.
37. Newnham E, E. and Haan Y. M, D.E., *Refinement of the α Al₂O₃, Ti₂O₃, V₂O₃ and Cr₂O₃ structures*, in *Zeitschrift für Kristallographie - Crystalline Materials*. 1962. p. 235.
38. Noguera, C., *Polar oxide surfaces*. *Journal of Physics-Condensed Matter*, 2000. **12**(31): p. R367-R410.
39. Bora, D.K., Braun, A., and Constable, E.C., "*In rust we trust*". *Hematite - the prospective inorganic backbone for artificial photosynthesis*. *Energy & Environmental Science*, 2013. **6**(2): p. 407-425.
40. Hellman, A. and Pala, R.G.S., *First-Principles Study of Photoinduced Water-Splitting on Fe₂O₃*. *The Journal of Physical Chemistry C*, 2011. **115**(26): p. 12901-12907.
41. Baltrusaitis, J., Hu, Y.-S., McFarland, E.W., and Hellman, A., *Photoelectrochemical Hydrogen Production on α -Fe₂O₃ (0001): Insights from Theory and Experiments*. *ChemSusChem*, 2014. **7**(1): p. 162-171.
42. Široký, K., Jirešová, J., and Hudec, L., *Iron oxide thin film gas sensor*. *Thin Solid Films*, 1994. **245**(1-2): p. 211-214.
43. Al-Abadleh, H.A. and Grassian, V.H., *Oxide surfaces as environmental interfaces*. *Surface Science Reports*, 2003. **52**(3-4): p. 63-161.
44. Catalano, J.G., Park, C., Fenter, P., and Zhang, Z., *Simultaneous inner- and outer-sphere arsenate adsorption on corundum and hematite*. *Geochimica et Cosmochimica Acta*, 2008. **72**(8): p. 1986-2004.
45. Mason, S.E., Iceman, C.R., Tanwar, K.S., Trainor, T.P., and Chaka, A.M., *Pb(II) Adsorption on Isostructural Hydrated Alumina and Hematite (0001) Surfaces: A DFT Study*†. *The Journal of Physical Chemistry C*, 2009. **113**(6): p. 2159-2170.
46. Ponce, F.A. and Bour, D.P., *Nitride-based semiconductors for blue and green light-emitting devices*. *Nature*, 1997. **386**(6623): p. 351-359.
47. Bullis, K. *Cheap and Nearly Unbreakable Sapphire Screens Come into View*. 2014 [cited 2014 August 19]; Available from: <http://www.technologyreview.com/news/529401/cheap-and-nearly-unbreakable-sapphire-screens-come-into-view/>.
48. Trueba, M. and Trasatti, S.P., *gamma-Alumina as a support for catalysts: A review of fundamental aspects*. *European Journal of Inorganic Chemistry*, 2005(17): p. 3393-3403.

49. Wischert, R., Laurent, P., Coperet, C., Delbecq, F., and Sautet, P., *gamma-Alumina: The Essential and Unexpected Role of Water for the Structure, Stability, and Reactivity of "Defect" Sites*. Journal of the American Chemical Society, 2012. **134**(35): p. 14430-14449.
50. Ealet, B., Elyakhloufi, M.H., Gillet, E., and Ricci, M., *Electronic and crystallographic structure of γ -alumina thin films*. Thin Solid Films, 1994. **250**(1–2): p. 92-100.
51. Tasker, P.W., *Stability of ionic-crystal surfaces*. Journal of Physics C-Solid State Physics, 1979. **12**(22): p. 4977-4984.
52. Gautier-Soyer, M., Renaud, G., Barbier, A., and Guénard, P., *Determination of the α - $\text{Al}_2\text{O}_3(0001)$ Surface Relaxation and Termination by Measurements of Crystal Truncation Rods*. Surface Review and Letters, 1998. **05**(01): p. 321-324.
53. Eng, P.J., Trainor, T.P., Brown Jr., G.E., Waychunas, G.A., Newville, M., Sutton, S.R., and Rivers, M.L., *Structure of the Hydrated α - $\text{Al}_2\text{O}_3(0001)$ Surface*. Science, 2000. **288**(5468): p. 1029-1033.
54. Wang, X.G., Weiss, W., Shaikhutdinov, S.K., Ritter, M., Petersen, M., Wagner, F., Schlögl, R., and Scheffler, M., *The Hematite (α - Fe_2O_3) (0001) Surface: Evidence for Domains of Distinct Chemistry*. Physical Review Letters, 1998. **81**(5): p. 1038-1041.
55. Shaikhutdinov, S.K. and Weiss, W., *Oxygen pressure dependence of the α - $\text{Fe}_2\text{O}_3(0001)$ surface structure*. Surface Science, 1999. **432**(3): p. L627-L634.
56. Thevuthasan, S., Kim, Y.J., Yi, S.I., Chambers, S.A., Morais, J., Denecke, R., Fadley, C.S., Liu, P., Kendelewicz, T., and Brown Jr, G.E., *Surface structure of MBE-grown α - $\text{Fe}_2\text{O}_3(0001)$ by intermediate-energy X-ray photoelectron diffraction*. Surface Science, 1999. **425**(2–3): p. 276-286.
57. Bergermayer, W., Schweiger, H., and Wimmer, E., *Ab initio thermodynamics of oxide surfaces: O_2 on $\text{Fe}_2\text{O}_3(0001)$* . Physical Review B, 2004. **69**(19): p. 195409.
58. Lemire, C., Bertarione, S., Zecchina, A., Scarano, D., Chaka, A., Shaikhutdinov, S., and Freund, H.J., *Ferryl ($\text{Fe}=\text{O}$) Termination of the Hematite α - $\text{Fe}_2\text{O}_3(0001)$ Surface*. Physical Review Letters, 2005. **94**(16): p. 166101.
59. Rohrbach, A., Hafner, J., and Kresse, G., *Ab initio study of the (0001) surfaces of hematite and chromia: Influence of strong electronic correlations*. Physical Review B, 2004. **70**.
60. Barbier, A., Stierle, A., Kasper, N., Guittet, M.J., and Jupille, J., *Surface termination of hematite at environmental oxygen pressures: Experimental surface phase diagram*. Physical Review B, 2007. **75**(23): p. 4.

61. Kim, C.Y., Escudro, A.A., Bedzyk, M.J., Liu, L., and Stair, P.C., *X-ray scattering study of the stoichiometric recovery of the alpha-Fe₂O₃(0001) surface*. *Surface Science*, 2004. **572**(2-3): p. 239-246.
62. Trainor, T.P., Chaka, A.M., Eng, P.J., Newville, M., Waychunas, G.A., Catalano, J.G., and Brown, G.E., *Structure and reactivity of the hydrated hematite (0001) surface*. *Surface Science*, 2004. **573**(2): p. 204-224.
63. Yamamoto, S., Kendelewicz, T., Newberg, J.T., Ketteler, G., Starr, D.E., Mysak, E.R., Andersson, K.J., Ogasawara, H., Bluhm, H., Salmeron, M., Brown, G.E., and Nilsson, A., *Water Adsorption on alpha-Fe₂O₃(0001) at near Ambient Conditions*. *The Journal of Physical Chemistry C*, 2010. **114**(5): p. 2256-2266.
64. Vattuone, L., Savio, L., and Rocca, M., *Bridging the structure gap: Chemistry of nanostructured surfaces at well-defined defects*. *Surface Science Reports*, 2008. **63**(3): p. 101-168.
65. Batyrev, I., Alavi, A., and W. Finnis, M., *Abinitio calculations on the Al₂O₃(0001) surface*. *Faraday Discussions*, 1999. **114**(0): p. 33-43.
66. Feng, Z., Kim, C.-Y., Elam, J.W., Ma, Q., Zhang, Z., and Bedzyk, M.J., *Direct Atomic-Scale Observation of Redox-Induced Cation Dynamics in an Oxide-Supported Monolayer Catalyst: W₂O₇/alpha-Fe₂O₃(0001)*. *Journal of the American Chemical Society*, 2009. **131**(51): p. 18200-18201.
67. Escudro, A.A., *X-Ray Standing Wave Imaging of Metal Atoms on Semiconductor and Oxide Surfaces*, in *Materials Science and Engineering*. 2005, Northwestern University.
68. Emery, J.D., *Synchrotron X-ray Studies of Pristine, Intercalated, and Functionalized Epitaxial Graphene on SiC(0001)*, in *Materials Science and Engineering*. 2013, Northwestern University.
69. Als-Nielsen, J. and McMorrow, D., *Elements of Modern X-Ray Physics*. 1st ed. 2001, West Sussex PO19 1UD, England: John Wiley & Sons Ltd.
70. Darwin, C.G., XXXIV. *The theory of X-ray reflexion*. *Philosophical Magazine Series 6*, 1914. **27**(158): p. 315-333.
71. Ewald, P.P., *Zur Begründung der Kristalloptik*. *Annalen der Physik*, 1917. **359**(24): p. 557-597.
72. von Laue, M., *Röntgenstrahl-Interferenzen*, in *Physik und Chemie und ihre Anwendungen in Einzeldarstellungen*. 1941, Akademische verlagsgesellschaft: Frankfurt.

73. Batterman, B.W. and Cole, H., *Dynamical Diffraction of X Rays by Perfect Crystals*. Reviews of Modern Physics, 1964. **36**(3): p. 681-717.
74. Golovchenko, J.A., Patel, J.R., Kaplan, D.R., Cowan, P.L., and Bedzyk, M.J., *Solution to the Surface Registration Problem Using X-Ray Standing Waves*. Physical Review Letters, 1982. **49**(8): p. 560-563.
75. Cheng, L., Fenter, P., Bedzyk, M.J., and Sturchio, N.C., *Fourier-Expansion Solution of Atom Distributions in a Crystal Using X-Ray Standing Waves*. Physical Review Letters, 2003. **90**(25): p. 255503.
76. Bedzyk, M.J. and Materlik, G., *Two-beam dynamical diffraction solution of the phase problem: A determination with x-ray standing-wave fields*. Physical Review B, 1985. **32**(10): p. 6456-6463.
77. Bedzyk, M. and Materlik, G., *X-ray standing wave analysis for bromine chemisorbed on germanium*. Surface Science, 1985. **152-153, Part 1**(0): p. 10-16.
78. Feng, Z., *Atomic-Scale Studies of Oxides Supported Catalysts by X-ray and Imaging Methods*, in *Materials Science and Engineering*. 2011, Northwestern University: Evanston, Illinois.
79. Lin, J.-C., *Atomic-Scale Studies of the Self-Assembly of Pi-Conjugated Molecules on Silicon Surfaces*, in *Materials Science and Engineering*. 2009, Northwestern University: Evanston, Illinois.
80. Cheng, L., *Atomic-scale study of ion incorporation at calcite surface using synchrotron X-ray methods*, in *Materials Science and Engineering*. 1998, Northwestern University: Evanston, Illinois.
81. DuMond, J.W.M., *Theory of the Use of More Than Two Successive X-Ray Crystal Reflections to Obtain Increased Resolving Power*. Physical Review, 1937. **52**(8): p. 872-883.
82. Krause, M.O., *Atomic radiative and radiationless yields for K and L shells*. Journal of Physical and Chemical Reference Data, 1979. **8**(2): p. 307-327.
83. Salmeron, M. and Schlögl, R., *Ambient pressure photoelectron spectroscopy: A new tool for surface science and nanotechnology*. Surface Science Reports, 2008. **63**(4): p. 169-199.
84. Ohno, M. and van Riessen, G.A., *Hole-lifetime width: a comparison between theory and experiment*. Journal of Electron Spectroscopy and Related Phenomena, 2003. **128**(1): p. 1-31.

85. Nelin, C.J., Bagus, P.S., Brown, M.A., Sterrer, M., and Freund, H.-J., *Analysis of the Broadening of X-ray Photoelectron Spectroscopy Peaks for Ionic Crystals*. *Angewandte Chemie International Edition*, 2011. **50**(43): p. 10174-10177.
86. Bagus, P.S., Ilton, E.S., and Nelin, C.J., *The interpretation of XPS spectra: Insights into materials properties*. *Surface Science Reports*, 2013. **68**(2): p. 273-304.
87. Bunker, G., *Introduction to XAFS: A Practical Guide to X-ray Absorption Fine Structure Spectroscopy*. 2010, Cambridge CB2 8RU, UK: Cambridge University Press.
88. Newville, M. *Fundamentals of XAFS*. 2004 7/23/2004 [cited 2014 7/16]; 1.7:[Available from: http://xafs.org/Tutorials?action=AttachFile&do=get&target=Newville_xas_fundamentals.pdf].
89. Sayers, D.E., Stern, E.A., and Lytle, F.W., *New Technique for Investigating Noncrystalline Structures: Fourier Analysis of the Extended X-Ray—Absorption Fine Structure*. *Physical Review Letters*, 1971. **27**(18): p. 1204-1207.
90. Stern, E.A., *Theory of the extended x-ray-absorption fine structure*. *Physical Review B*, 1974. **10**(8): p. 3027-3037.
91. Lee, P.A. and Pendry, J.B., *Theory of the extended x-ray absorption fine structure*. *Physical Review B*, 1975. **11**(8): p. 2795-2811.
92. Rehr, J.J. and Albers, R.C., *Theoretical approaches to x-ray absorption fine structure*. *Reviews of Modern Physics*, 2000. **72**(3): p. 621-654.
93. Rehr, J.J., Kas, J.J., Prange, M.P., Sorini, A.P., Takimoto, Y., and Vila, F., *Ab initio theory and calculations of X-ray spectra*. *Comptes Rendus Physique*, 2009. **10**(6): p. 548-559.
94. Rehr, J.J., Kas, J.J., Vila, F.D., Prange, M.P., and Jorissen, K., *Parameter-free calculations of X-ray spectra with FEFF9*. *Physical Chemistry Chemical Physics*, 2010. **12**(21): p. 5503-5513.
95. Ravel, B. and Newville, M., *ATHENA, ARTEMIS, HEPHAESTUS: data analysis for X-ray absorption spectroscopy using IFEFFIT*. *Journal of Synchrotron Radiation*, 2005. **12**(4): p. 537-541.
96. Samori, P., *Scanning probe microscopies beyond imaging*. *Journal of Materials Chemistry*, 2004. **14**(9): p. 1353-1366.
97. Giessibl, F.J., *Advances in atomic force microscopy*. *Reviews of Modern Physics*, 2003. **75**(3): p. 949-983.

98. George, S.M., *Atomic Layer Deposition: An Overview*. Chemical Reviews, 2009. **110**(1): p. 111-131.
99. George, S.M., Ott, A.W., and Klaus, J.W., *Surface Chemistry for Atomic Layer Growth*. The Journal of Physical Chemistry, 1996. **100**(31): p. 13121-13131.
100. Parsons, G.N., George, S.M., and Knez, M., *Progress and future directions for atomic layer deposition and ALD-based chemistry*. MRS Bulletin, 2011. **36**(11): p. 865-871.
101. Puurunen, R.L., *Surface chemistry of atomic layer deposition: A case study for the trimethylaluminum/water process*. Journal of Applied Physics, 2005. **97**(12): p. 52.
102. Elam, J.W., Nelson, C.E., Grubbs, R.K., and George, S.M., *Nucleation and growth during tungsten atomic layer deposition on SiO₂ surfaces*. Thin Solid Films, 2001. **386**(1): p. 41-52.
103. Martin, R.M., *Electronic Structure: Basic Theory and Practical Methods*. 2004, University Press, Cambridge, United Kingdom: Cambridge University Press.
104. Hohenberg, P. and Kohn, W., *Inhomogeneous Electron Gas*. Physical Review, 1964. **136**(3B): p. B864-B871.
105. Kohn, W. and Sham, L.J., *Self-Consistent Equations Including Exchange and Correlation Effects*. Physical Review, 1965. **140**(4A): p. A1133-A1138.
106. Perdew, J.P., *Climbing the ladder of density functional approximations*. Mrs Bulletin, 2013. **38**(9): p. 743-750.
107. Perdew, J.P. and Schmidt, K., *Jacob's ladder of density functional approximations for the exchange-correlation energy*, in *Density Functional Theory and Its Application to Materials*, V. VanDoren, C. VanAlsenoy, and P. Geerlings, Editors. 2001, Amer Inst Physics: Melville. p. 1-20.
108. Kresse, G. and Furthmüller, J., *Efficient iterative schemes for ab initio total-energy calculations using a plane-wave basis set*. Physical Review B, 1996. **54**(16): p. 11169-11186.
109. Kresse, G. and Furthmüller, J., *Efficiency of ab-initio total energy calculations for metals and semiconductors using a plane-wave basis set*. Computational Materials Science, 1996. **6**(1): p. 15-50.
110. Kresse, G. and Hafner, J., *Ab initio molecular-dynamics simulation of the liquid-metal–amorphous-semiconductor transition in germanium*. Physical Review B, 1994. **49**(20): p. 14251-14269.

111. Kresse, G. and Hafner, J., *Ab initio molecular dynamics for liquid metals*. Physical Review B, 1993. **47**(1): p. 558-561.
112. Blöchl, P.E., *Projector augmented-wave method*. Physical Review B, 1994. **50**(24): p. 17953-17979.
113. Perdew, J.P., Chevary, J.A., Vosko, S.H., Jackson, K.A., Pederson, M.R., Singh, D.J., and Fiolhais, C., *Atoms, molecules, solids, and surfaces: Applications of the generalized gradient approximation for exchange and correlation*. Physical Review B, 1992. **46**(11): p. 6671-6687.
114. Pulay, P., *Convergence acceleration of iterative sequences. the case of scf iteration*. Chemical Physics Letters, 1980. **73**(2): p. 393-398.
115. Monkhorst, H.J. and Pack, J.D., *Special points for Brillouin-zone integrations*. Physical Review B, 1976. **13**(12): p. 5188-5192.
116. Henkelman, G., Arnaldsson, A., and Jónsson, H., *A fast and robust algorithm for Bader decomposition of charge density*. Computational Materials Science, 2006. **36**(3): p. 354-360.
117. Bader, R.F.W., *Atoms in molecules: a quantum theory*. 1990, Oxford: Clarendon Press.
118. Grabowski, S.J., *Hydrogen bonding strength—measures based on geometric and topological parameters*. Journal of Physical Organic Chemistry, 2004. **17**(1): p. 18-31.
119. Brown, I.D., *Recent Developments in the Methods and Applications of the Bond Valence Model*. Chemical Reviews, 2009. **109**(12): p. 6858-6919.
120. Brown, I.D. and Altermatt, D., *Bond-valence parameters obtained from a systematic analysis of the inorganic crystal-structure database*. Acta Crystallographica Section B-Structural Science, 1985. **41**(AUG): p. 244-247.
121. Enterkin, J.A., Becerra-Toledo, A.E., Poeppelmeier, K.R., and Marks, L.D., *A chemical approach to understanding oxide surfaces*. Surface Science, 2012. **606**(3-4): p. 344-355.
122. Enterkin, J.A., Subramanian, A.K., Russell, B.C., Castell, M.R., Poeppelmeier, K.R., and Marks, L.D., *A homologous series of structures on the surface of SrTiO₃(110)*. Nat Mater, 2010. **9**(3): p. 245-248.
123. Hu, S.-Z. and Zhou, Z.-H., *The correlation between metal oxidation state and bond valence parameters for M—O bonds (M = V, Fe and Cu). A simple method to search for the metal oxidation-state independent parameter pairs*, in *Zeitschrift für Kristallographie/International journal for structural, physical, and chemical aspects of crystalline materials*. 2004. p. 614.

124. Hong Qi-Ming, Z.Z.-H., Hu Sheng-Zhi, *Study on the Bond Valence Parameters for Tungsten-oxygen Bonds*. Acta Chimica Sinica, 2004. **62**(18): p. 1733-1737.
125. Allmann, R., *Beziehungen zwischen Bindungslängen und Bindungsstärken in Oxidstrukturen*. Monatshefte für Chemie / Chemical Monthly, 1975. **106**(3): p. 779-793.
126. McBriarty, M.E., Bedzyk, M.J., and Ellis, D.E., *Structure and properties of a model oxide-supported catalyst under redox conditions: $WO_x/\alpha\text{-Fe}_2O_3$ (0001)*. Surface Science, 2012. **606**(17–18): p. 1367-1381.
127. Heinrich, V.E. and Cox, P.A., *The Surface Science of Metal Oxides*. 1994: Cambridge University Press.
128. Weiss, W. and Ranke, W., *Surface chemistry and catalysis on well-defined epitaxial iron-oxide layers*. Progress in Surface Science, 2002. **70**(1–3): p. 1-151.
129. Jin, J., Ma, X., Kim, C.Y., Ellis, D.E., and Bedzyk, M.J., *Adsorption of V on a hematite (0001) surface and its oxidation: Monolayer coverage*. Surface Science, 2007. **601**(19): p. 4571-4581.
130. Jin, J., Ma, X., Kim, C.Y., Ellis, D.E., and Bedzyk, M.J., *Adsorption of V on a hematite (0001) surface and its oxidation: Submonolayer coverage*. Surface Science, 2007. **601**(14): p. 3082-3098.
131. Kim, C.-Y., Escudro, A.A., Stair, P.C., and Bedzyk, M.J., *Atomic-Scale View of Redox-Induced Reversible Changes to a Metal-Oxide Catalytic Surface: $VO_x/\alpha\text{-Fe}_2O_3$ (0001)*. The Journal of Physical Chemistry C, 2007. **111**(5): p. 1874-1877.
132. Soled, S.L., McVicker, G.B., Murrell, L.L., Sherman, L.G., Dispenziere Jr, N.C., Hsu, S.L., and Waldman, D., *Comparison of the acidities of $WO_3Al_2O_3$ and ultrastable faujasite catalysts*. Journal of Catalysis, 1988. **111**(2): p. 286-295.
133. Lietti, L., Alemany, J.L., Forzatti, P., Busca, G., Ramis, G., Giamello, E., and Bregani, F., *Reactivity of $V_2O_5\text{-}WO_3/TiO_2$ catalysts in the selective catalytic reduction of nitric oxide by ammonia*. Catalysis Today, 1996. **29**(1–4): p. 143-148.
134. Ferretto, L. and Glisenti, A., *Study of the surface acidity of an hematite powder*. Journal of Molecular Catalysis A: Chemical, 2002. **187**(1): p. 119-128.
135. Boahene, P.E., Soni, K.K., Dalai, A.K., and Adjaye, J., *Application of different pore diameter SBA-15 supports for heavy gas oil hydrotreatment using FeW catalyst*. Applied Catalysis A: General, 2011. **402**(1–2): p. 31-40.

136. Boahene, P.E., Soni, K.K., Dalai, A.K., and Adjaye, J., *Hydroprocessing of heavy gas oils using FeW/SBA-15 catalysts: Experimentals, optimization of metals loading, and kinetics study*. Catalysis Today, 2013. **207**(0): p. 101-111.
137. Hoffmann, M.R., Martin, S.T., Choi, W., and Bahnemann, D.W., *Environmental Applications of Semiconductor Photocatalysis*. Chemical Reviews, 1995. **95**(1): p. 69-96.
138. Gondal, M.A., Sayeed, M.N., and Alarfaj, A., *Activity comparison of Fe₂O₃, NiO, WO₃, TiO₂ semiconductor catalysts in phenol degradation by laser enhanced photo-catalytic process*. Chemical Physics Letters, 2007. **445**(4-6): p. 325-330.
139. Wang, H., Deutsch, T., and Turner, J.A., *Direct Water Splitting under Visible Light with Nanostructured Hematite and WO₃ Photoanodes and a GaInP₂ Photocathode*. Journal of The Electrochemical Society, 2008. **155**(5): p. F91-F96.
140. Chen, Z., Jaramillo, T.F., Deutsch, T.G., Kleiman-Shwarsctein, A., Forman, A.J., Gaillard, N., Garland, R., Takanabe, K., Heske, C., Sunkara, M., McFarland, E.W., Domen, K., Miller, E.L., Turner, J.A., and Dinh, H.N., *Accelerating materials development for photoelectrochemical hydrogen production: Standards for methods, definitions, and reporting protocols*. Journal of Materials Research, 2010. **25**(01): p. 3-16.
141. Hsiao, P.-T., Chen, L.-C., Li, T.-L., and Teng, H., *Vapor treatment of nanocrystalline WO₃ photoanodes for enhanced photoelectrochemical performance in the decomposition of water*. Journal of Materials Chemistry, 2011. **21**(48): p. 19402-19409.
142. Gondal, M.A., Hameed, A., Yamani, Z.H., and Suwaiyan, A., *Laser induced photo-catalytic oxidation/splitting of water over α -Fe₂O₃, WO₃, TiO₂ and NiO catalysts: activity comparison*. Chemical Physics Letters, 2004. **385**(1-2): p. 111-115.
143. Bi, D. and Xu, Y., *Synergism between Fe₂O₃ and WO₃ particles: Photocatalytic activity enhancement and reaction mechanism*. Journal of Molecular Catalysis A: Chemical, 2013. **367**(0): p. 103-107.
144. Bi, D. and Xu, Y., *Improved Photocatalytic Activity of WO₃ through Clustered Fe₂O₃ for Organic Degradation in the Presence of H₂O₂*. Langmuir, 2011. **27**(15): p. 9359-9366.
145. Kurth, S. and Perdew, J.P., *Role of the exchange-correlation energy: Nature's glue*. International Journal of Quantum Chemistry, 2000. **77**(5): p. 814-818.
146. Ernzerhof, M., Perdew, J.P., and Burke, K., *Coupling-constant dependence of atomization energies*. International Journal of Quantum Chemistry, 1997. **64**(3): p. 285-295.
147. Cava, C.E., Roman, L.S., and Persson, C., *Effects of native defects on the structural and magnetic properties of hematite α -Fe₂O₃*. Physical Review B, 2013. **88**(4): p. 045136.

148. Ellis, D.E. and Guenzburger, D., *The Discrete Variational Method in Density Functional Theory and its Applications to Large Molecules and Solid-State Systems*, in *Advances in Quantum Chemistry*, J.R.S.M.C.Z. Per-Olov Löwdin and B. Erkki, Editors. 1999, Academic Press. p. 51-141.
149. Williams, A.R., deGroot, R.A., and Sommers, C.B., *Generalization of Slater's transition state concept*. The Journal of Chemical Physics, 1975. **63**(2): p. 628-631.
150. Aizawa, M., Morikawa, Y., Namai, Y., Morikawa, H., and Iwasawa, Y., *Oxygen Vacancy Promoting Catalytic Dehydration of Formic Acid on TiO₂(110) by in Situ Scanning Tunneling Microscopic Observation*. The Journal of Physical Chemistry B, 2005. **109**(40): p. 18831-18838.
151. Polarz, S., Strunk, J., Ischenko, V., van den Berg, M.W.E., Hinrichsen, O., Muhler, M., and Driess, M., *On the Role of Oxygen Defects in the Catalytic Performance of Zinc Oxide*. Angewandte Chemie International Edition, 2006. **45**(18): p. 2965-2969.
152. Nguyen, M.-T., Seriani, N., and Gebauer, R., *Defective α -Fe₂O₃(0001): An ab Initio Study*. ChemPhysChem, 2014: p. n/a-n/a.
153. Aidhy, D.S. and Wolverton, C., *First-principles prediction of phase stability and crystal structures in Li-Zn and Na-Zn mixed-metal borohydrides*. Physical Review B, 2011. **83**(14): p. 8.
154. Ghosh, G., *Phase stability and cohesive properties of Au-Sn intermetallics: A first-principles study*. Journal of Materials Research, 2008. **23**(5): p. 1398-1416.
155. Cahn, J.W. and Carter, W.C., *Crystal shapes and phase equilibria: A common mathematical basis*. Metallurgical and Materials Transactions a-Physical Metallurgy and Materials Science, 1996. **27**(6): p. 1431-1440.
156. Cohen, A.J., Mori-Sanchez, P., and Yang, W.T., *Insights into current limitations of density functional theory*. Science, 2008. **321**(5890): p. 792-794.
157. Cohen, A.J., Mori-Sanchez, P., and Yang, W.T., *Challenges for Density Functional Theory*. Chemical Reviews, 2012. **112**(1): p. 289-320.
158. Rollmann, G., Rohrbach, A., Entel, P., and Hafner, J., *First-principles calculation of the structure and magnetic phases of hematite*. Physical Review B, 2004. **69**(16): p. 165107.
159. Svane, A. and Gunnarsson, O., *Transition-metal oxides in the self-interaction-corrected density-functional formalism*. Physical Review Letters, 1990. **65**(9): p. 1148-1151.
160. Punkkinen, M.P.J., Kokko, K., Hergert, W., and Vayrynen, I.J., *Fe₂O₃ within the LSDA+U approach*. Journal of Physics-Condensed Matter, 1999. **11**(11): p. 2341-2349.

161. Anisimov, V.I., Zaanen, J., and Andersen, O.K., *Band theory and Mott insulators: Hubbard U instead of Stoner I*. Physical Review B, 1991. **44**(3): p. 943-954.
162. Terakura, K., Oguchi, T., Williams, A.R., and Kübler, J., *Band theory of insulating transition-metal monoxides: Band-structure calculations*. Physical Review B, 1984. **30**(8): p. 4734-4747.
163. Perdew, J.P. and Zunger, A., *Self-interaction correction to density-functional approximations for many-electron systems*. Physical Review B, 1981. **23**(10): p. 5048-5079.
164. Dudarev, S.L., Botton, G.A., Savrasov, S.Y., Humphreys, C.J., and Sutton, A.P., *Electron-energy-loss spectra and the structural stability of nickel oxide: An LSDA+U study*. Physical Review B, 1998. **57**(3): p. 1505-1509.
165. Himmetoglu, B., Floris, A., de Gironcoli, S., and Cococcioni, M., *Hubbard-corrected DFT energy functionals: The LDA+U description of correlated systems*. International Journal of Quantum Chemistry, 2014. **114**(1): p. 14-49.
166. Mosey, N.J., Liao, P., and Carter, E.A., *Rotationally invariant ab initio evaluation of Coulomb and exchange parameters for DFT+U calculations*. The Journal of Chemical Physics, 2008. **129**(1): p. -.
167. Sechrist, Z.A., Fabreguette, F.H., Heintz, O., Phung, T.M., Johnson, D.C., and George, S.M., *Optimization and Structural Characterization of W/Al₂O₃ Nanolaminates Grown Using Atomic Layer Deposition Techniques*. Chemistry of Materials, 2005. **17**(13): p. 3475-3485.
168. Karuppanan, S. and Kijung, Y., *Growth and characterization of stoichiometric tungsten oxide nanorods by thermal evaporation and subsequent annealing*. Nanotechnology, 2007. **18**(39): p. 395604.
169. Sun, M., Xu, N., Cao, Y.W., Yao, J.N., and Wang, E.G., *Nanocrystalline tungsten oxide thin film: Preparation, microstructure, and photochromic behavior*. Journal of Materials Research, 2000. **15**(4): p. 927-933.
170. Chernyshova, I.V., Hochella Jr, M.F., and Madden, A.S., *Size-dependent structural transformations of hematite nanoparticles. I. Phase transition*. Physical Chemistry Chemical Physics, 2007. **9**(14): p. 1736-1750.
171. Salvati, L., Makovsky, L.E., Stencel, J.M., Brown, F.R., and Hercules, D.M., *Surface spectroscopic study of tungsten-alumina catalysts using x-ray photoelectron, ion scattering, and Raman spectroscopies*. The Journal of Physical Chemistry, 1981. **85**(24): p. 3700-3707.
172. Diehl, R., Brandt, G., and Salje, E., *Crystal-structure of triclinic WO₃*. Acta Crystallographica Section B-Structural Science, 1978. **34**(APR): p. 1105-1111.

173. Hilbrig, F., Goebel, H.E., Knoezinger, H., Schmelz, H., and Lengeler, B., *X-ray absorption spectroscopy study of the titania- and alumina-supported tungsten oxide system*. The Journal of Physical Chemistry, 1991. **95**(18): p. 6973-6978.
174. Balerna, A., Bernieri, E., Burattini, E., Kuzmin, A., Lusic, A., Purans, J., and Cikmach, P., *EXAFS studies of MeO_3-x ($Me = W, Mo, Re, Ir$) crystalline and amorphous oxides*. Nuclear Instruments and Methods in Physics Research Section A: Accelerators, Spectrometers, Detectors and Associated Equipment, 1991. **308**(1-2): p. 234-239.
175. Valigi, M., Gazzoli, D., Pettiti, I., Mattei, G., Colonna, S., De Rossi, S., and Ferraris, G., *WO_x/ZrO₂ catalysts: Part 1. Preparation, bulk and surface characterization*. Applied Catalysis A: General, 2002. **231**(1-2): p. 159-172.
176. Yamazoe, S., Hitomi, Y., Shishido, T., and Tanaka, T., *XAFS Study of Tungsten L1- and L3-Edges: Structural Analysis of WO₃ Species Loaded on TiO₂ as a Catalyst for Photo-oxidation of NH₃*. The Journal of Physical Chemistry C, 2008. **112**(17): p. 6869-6879.
177. Carrier, X., Marceau, E., Carabineiro, H., Rodriguez-Gonzalez, V., and Che, M., *EXAFS spectroscopy as a tool to probe metal-support interaction and surface molecular structures in oxide-supported catalysts: application to Al₂O₃-supported Ni(ii) complexes and ZrO₂-supported tungstates*. Physical Chemistry Chemical Physics, 2009. **11**(35): p. 7527-7539.
178. Ravel, B. *EXAFS Modeling (Feffit / Artemis / SixPack) FAQ*. 2010 2010-02-25 [cited 2014 2014-07-15]; Available from: <http://cars9.uchicago.edu/ifeffit/FAQ/FeffitModeling>.
179. Li, G.G., Bridges, F., and Booth, C.H., *X-ray-absorption fine-structure standards: A comparison of experiment and theory*. Physical Review B, 1995. **52**(9): p. 6332-6348.
180. Crüsemann, R., Bökman, F., Fritzsche, V., and Bertagnolli, H., *A multiple scattering EXAFS study of organometallic compounds: W(CO)₆ and (1,3,5-trimethylbenzene)W(CO)₃*. Chemical Physics, 1995. **194**(1): p. 81-90.
181. Richardson, A.D., Hedberg, K., and Lucier, G.M., *Gas-Phase Molecular Structures of Third Row Transition-Metal Hexafluorides WF₆, ReF₆, OsF₆, IrF₆, and PtF₆. An Electron-Diffraction and ab Initio Study*. Inorganic Chemistry, 2000. **39**(13): p. 2787-2793.
182. Walczak, J. and Rychłowska-Himmel, I., *Phase equilibria in the systems Fe₂O₃-WO₃ and FeVO₄-WO₃*. Thermochemica Acta, 1993. **221**(1): p. 115-121.
183. Khodakov, A., Olthof, B., Bell, A.T., and Iglesia, E., *Structure and Catalytic Properties of Supported Vanadium Oxides: Support Effects on Oxidative Dehydrogenation Reactions*. Journal of Catalysis, 1999. **181**(2): p. 205-216.

184. Magg, N., Boonchuan, I., Giorgi, J.B., Schroeder, T., Bäumer, M., Döbler, J., Wu, Z., Kondratenko, E., Cherian, M., Baerns, M., Stair, P.C., Sauer, J., and Freund, H.-J., *Vibrational spectra of alumina- and silica-supported vanadia revisited: An experimental and theoretical model catalyst study*. Journal of Catalysis, 2004. **226**: p. 88-100.
185. Dinse, A., Ozarowski, A., Hess, C., Schomäcker, R., and Dinse, K.-P., *Potential of High-Frequency EPR for Investigation of Supported Vanadium Oxide Catalysts*. The Journal of Physical Chemistry C, 2008. **112**(45): p. 17664-17671.
186. Wegener, S.L., Kim, H., Marks, T.J., and Stair, P.C., *Precursor Nuclearity Effects in Supported Vanadium Oxides Prepared by Organometallic Grafting*. The Journal of Physical Chemistry Letters, 2011. **2**(3): p. 170-175.
187. Cheng, L., Ferguson, G.A., Zygmunt, S.A., and Curtiss, L.A., *Structure–activity relationships for propane oxidative dehydrogenation by anatase-supported vanadium oxide monomers and dimers*. Journal of Catalysis, 2013. **302**(0): p. 31-36.
188. Weckhuysen, B.M., Jehng, J.M., and Wachs, I.E., *In situ Raman spectroscopy of supported transition metal oxide catalysts: O-18(2)-O-16(2) isotopic labeling studies*. Journal of Physical Chemistry B, 2000. **104**(31): p. 7382-7387.
189. Magg, N., Giorgi, J.B., Schroeder, T., Bäumer, M., and Freund, H.-J., *Model Catalyst Studies on Vanadia Particles Deposited onto a Thin-Film Alumina Support. 1. Structural Characterization*. The Journal of Physical Chemistry B, 2002. **106**(34): p. 8756-8761.
190. Keller, D.E., de Groot, F.M.F., Koningsberger, D.C., and Weckhuysen, B.M., *VO₄ Upside Down: A New Molecular Structure for Supported VO₄ Catalysts*. The Journal of Physical Chemistry B, 2005. **109**(20): p. 10223-10233.
191. Gijzeman, O.L.J., van Lingen, J.N.J., van Lenthe, J.H., Tinnemans, S.J., Keller, D.E., and Weckhuysen, B.M., *A new model for the molecular structure of supported vanadium oxide catalysts*. Chemical Physics Letters, 2004. **397**(1–3): p. 277-281.
192. Wegener, S.L., Marks, T.J., and Stair, P.C., *Design Strategies for the Molecular Level Synthesis of Supported Catalysts*. Accounts of Chemical Research, 2011. **45**(2): p. 206-214.
193. Kudla, R.J., Subramanian, S., Chattha, M.S., and Hoost, T.E., *Effect of Tungsten Oxide Addition on the Catalytic Activity of γ -Al₂O₃ for NO_x Reduction from Fuel-Lean Gas Mixtures*. Industrial & Engineering Chemistry Research, 1996. **35**(12): p. 4394-4397.
194. Barton, D., Soled, S., and Iglesia, E., *Solid acid catalysts based on supported tungsten oxides*. Topics in Catalysis, 1998. **6**(1-4): p. 87-99.

195. Baertsch, C.D., Komala, K.T., Chua, Y.-H., and Iglesia, E., *Genesis of Brønsted Acid Sites during Dehydration of 2-Butanol on Tungsten Oxide Catalysts*. *Journal of Catalysis*, 2002. **205**(1): p. 44-57.
196. Iglesia, E., Barton, D.G., Soled, S.L., Miseo, S., Baumgartner, J.E., Gates, W.E., Fuentes, G.A., and Meitzner, G.D., *Selective isomerization of alkanes on supported tungsten oxide acids*, in *Studies in Surface Science and Catalysis*, W.N.D.E.I. Joe W. Hightower and T.B. Alexis, Editors. 1996, Elsevier. p. 533-542.
197. Vermaire, D.C. and van Berge, P.C., *The preparation of WO₃TiO₂ and Wo₃Al₂O₃ and characterization by temperature-programmed reduction*. *Journal of Catalysis*, 1989. **116**(2): p. 309-317.
198. Fiedor, J.N., Proctor, A., Houalla, M., and Hercules, D.M., *Study of the reduction behavior of W/TiO₂ catalysts by XPS using curve fitting, deconvolution and factor analysis*. *Surface and Interface Analysis*, 1995. **23**(4): p. 204-212.
199. Bertinchamps, F., Grégoire, C., and Gaigneaux, E.M., *Systematic investigation of supported transition metal oxide based formulations for the catalytic oxidative elimination of (chloro)-aromatics: Part II: Influence of the nature and addition protocol of secondary phases to VO_x/TiO₂*. *Applied Catalysis B: Environmental*, 2006. **66**(1-2): p. 10-22.
200. Schmitt, C., Giebeler, L., Schierholz, R., Endres, S., Fasel, C., Vogel, H., and Fuess, H., *Characterization of V-W and Mo-W Mixed Oxide Catalysts for the Selective Oxidation of Acrolein to Acrylic Acid*, in *Zeitschrift für Physikalische Chemie*. 2007. p. 1525.
201. Wang, Y., Wang, S., Zhou, S., Xu, J., Ye, J., Gu, S., Zhang, R., and Ren, Q., *Effects of sapphire substrate annealing on ZnO epitaxial films grown by MOCVD*. *Applied Surface Science*, 2006. **253**(4): p. 1745-1747.
202. Elam, J.W., Groner, M.D., and George, S.M., *Viscous flow reactor with quartz crystal microbalance for thin film growth by atomic layer deposition*. *Review of Scientific Instruments*, 2002. **73**(8): p. 2981-2987.
203. Badot, J.C., Ribes, S., Yousfi, E.B., Vivier, V., Pereira-Ramos, J.P., Baffier, N., and Lincot, D., *Atomic layer epitaxy of vanadium oxide thin films and electrochemical behavior in presence of lithium ions*. *Electrochemical and Solid State Letters*, 2000. **3**(10): p. 485-488.
204. Klug, J.A., *Synchrotron X-ray Studies of Epitaxial Ferroelectric Thin Films and Nanostructures*, in *Physics and Astronomy*. 2010, Northwestern University.
205. Bedzyk, M.J. and Cheng, L., *X-ray standing wave studies of minerals and mineral surfaces: principles and applications*, in *Reviews in Mineralogy and Geochemistry*, P.A. Fenter, et al., Editors. 2002, Mineralogical Society of America: Washington, D.C., USA. p. 221-266.

206. Walko, D.A., Sakata, O., Lyman, P.F., Lee, T.L., Tinkham, B.P., Okasinski, J.S., Zhang, Z., and Bedzyk, M.J., *Surface and interface studies at APS endstation 5ID-C*, in *Synchrotron Radiation Instrumentation*, T. Warwick, et al., Editors. 2004, Amer Inst Physics: Melville. p. 1166-1169.
207. Kim, C.-Y., Klug, J.A., Stair, P.C., and Bedzyk, M.J., *Hydration and Reduction of Molecular Beam Epitaxy Grown VOx/ α -Fe₂O₃(0001): Ambient Pressure Study*. The Journal of Physical Chemistry C, 2009. **113**(4): p. 1406-1410.
208. Tielsch, B.J. and Fulghum, J.E., *Differential Charging in XPS. Part I: Demonstration of Lateral Charging in a Bulk Insulator Using Imaging XPS*. Surface and Interface Analysis, 1996. **24**(1): p. 28-33.
209. Leftheriotis, G., Papaefthimiou, S., Yianoulis, P., Siokou, A., and Kefalas, D., *Structural and electrochemical properties of opaque sol-gel deposited WO₃ layers*. Applied Surface Science, 2003. **218**(1-4): p. 276-281.
210. Wagner, C.D., Riggs, W.M., Davis, L.E., and Moulder, J.F., *Handbook of X-ray Photoelectron Spectroscopy*. 1 ed. 1979: Perkin-Elmer Corporation (Physical Electronics).
211. Silversmit, G., Depla, D., Poelman, H., Marin, G.B., and De Gryse, R., *Determination of the V2p XPS binding energies for different vanadium oxidation states (V⁵⁺ to V⁰⁺)*. Journal of Electron Spectroscopy and Related Phenomena, 2004. **135**(2-3): p. 167-175.
212. Mendialdua, J., Casanova, R., and Barbaux, Y., *XPS studies of V₂O₅, V₆O₁₃, VO₂ and V₂O₃*. Journal of Electron Spectroscopy and Related Phenomena, 1995. **71**(3): p. 249-261.
213. Kim, C.-Y. and Bedzyk, M.J., *Study of growth and oxidation of vanadium films on α -Fe₂O₃(0001)*. Thin Solid Films, 2006. **515**(4): p. 2015-2020.
214. Warwick, M.E.A., Roberts, A.J., Slade, R.C.T., and Binions, R., *Electric field assisted chemical vapour deposition - a new method for the preparation of highly porous supercapacitor electrodes*. Journal of Materials Chemistry A, 2014.
215. Horsley, J.A., Wachs, I.E., Brown, J.M., Via, G.H., and Hardcastle, F.D., *Structure of surface tungsten oxide species in the tungsten trioxide/alumina supported oxide system from x-ray absorption near-edge spectroscopy and Raman spectroscopy*. The Journal of Physical Chemistry, 1987. **91**(15): p. 4014-4020.
216. Dumesic, J.A., Topsøe, N.Y., Topsøe, H., Chen, Y., and Slabiak, T., *Kinetics of Selective Catalytic Reduction of Nitric Oxide by Ammonia over Vanadia/Titania*. Journal of Catalysis, 1996. **163**(2): p. 409-417.

217. Anstrom, M., Dumesic, J.A., and Topsoe, N.Y., *Theoretical insight into the nature of ammonia adsorption on vanadia-based catalysts for SCR reaction*. Catalysis Letters, 2002. **78**(1-4): p. 281-289.
218. Anstrom, M., Topsøe, N.-Y., and Dumesic, J.A., *Density functional theory studies of mechanistic aspects of the SCR reaction on vanadium oxide catalysts*. Journal of Catalysis, 2003. **213**(2): p. 115-125.
219. Soyer, S., Uzun, A., Senkan, S., and Onal, I., *A quantum chemical study of nitric oxide reduction by ammonia (SCR reaction) on V₂O₅ catalyst surface*. Catalysis Today, 2006. **118**(3-4): p. 268-278.
220. Johnson, A.M., Quezada, B.R., Marks, L.D., and Stair, P.C., *Influence of the Metal Oxide Substrate Structure on Vanadium Oxide Monomer Formation*. Topics in Catalysis, 2014. **57**(1-4): p. 177-187.
221. Kim, H., Ferguson, G.A., Cheng, L., Zygmunt, S.A., Stair, P.C., and Curtiss, L.A., *Structure-Specific Reactivity of Alumina-Supported Monomeric Vanadium Oxide Species*. The Journal of Physical Chemistry C, 2011. **116**(4): p. 2927-2932.
222. Kim, H.-S., Zygmunt, S.A., Stair, P.C., Zapol, P., and Curtiss, L.A., *Monomeric Vanadium Oxide on a θ -Al₂O₃ Support: A Combined Experimental/Theoretical Study*. The Journal of Physical Chemistry C, 2009. **113**(20): p. 8836-8843.
223. van Lingen, J.N.J., Gijzeman, O.L.J., Weckhuysen, B.M., and van Lenthe, J.H., *On the umbrella model for supported vanadium oxide catalysts*. Journal of Catalysis, 2006. **239**(1): p. 34-41.
224. Keller, D.E., Visser, T., Soulimani, F., Koningsberger, D.C., and Weckhuysen, B.M., *Hydration effects on the molecular structure of silica-supported vanadium oxide catalysts: A combined IR, Raman, UV-vis and EXAFS study*. Vibrational Spectroscopy, 2007. **43**(1): p. 140-151.
225. Uzunova, E.L., Gohl, F., Kresse, G., and Hafner, J., *Application of Hybrid Functionals to the Modeling of NO Adsorption on Cu-SAPO-34 and Co-SAPO-34: A Periodic DFT Study*. Journal of Physical Chemistry C, 2009. **113**(13): p. 5274-5291.
226. Bilić, A., Reimers, J.R., Hush, N.S., and Hafner, J., *Adsorption of ammonia on the gold (111) surface*. The Journal of Chemical Physics, 2002. **116**(20): p. 8981-8987.
227. Busca, G., *FT-IR study of the surface chemistry of anatase-supported vanadium oxide monolayer catalysts*. Langmuir, 1986. **2**(5): p. 577-582.

228. Tsyganenko, A.A., Pozdnyakov, D.V., and Filimonov, V.N., *Infrared study of surface species arising from ammonia adsorption on oxide surfaces*. Journal of Molecular Structure, 1975. **29**(2): p. 299-318.
229. Brese, N.E. and Okeeffe, M., *Bond-valence parameters for solids*. Acta Crystallographica Section B-Structural Science, 1991. **47**: p. 192-197.
230. Yao, H., Chen, Y., Wei, Y., Zhao, Z., Liu, Z., and Xu, C., *A periodic DFT study of ammonia adsorption on the V2O5 (001), V2O5 (010) and V2O5 (100) surfaces: Lewis versus Brönsted acid sites*. Surface Science, 2012. **606**(21–22): p. 1739-1748.
231. Yin, S. and Ellis, D.E., *H2O adsorption and dissociation on defective hematite (001) surfaces: A DFT study*. Surface Science, 2008. **602**(12): p. 2047-2054.
232. Yin, S., Ma, X., and Ellis, D.E., *Initial stages of H2O adsorption and hydroxylation of Fe-terminated α -Fe2O3(001) surface*. Surface Science, 2007. **601**(12): p. 2426-2437.
233. Suntivich, J., May, K.J., Gasteiger, H.A., Goodenough, J.B., and Shao-Horn, Y., *A Perovskite Oxide Optimized for Oxygen Evolution Catalysis from Molecular Orbital Principles*. Science, 2011. **334**(6061): p. 1383-1385.
234. Martynova, Y., Liu, B.H., McBriarty, M.E., Groot, I.M.N., Bedzyk, M.J., Shaikhutdinov, S., and Freund, H.J., *CO oxidation over ZnO films on Pt(111) at near-atmospheric pressures*. Journal of Catalysis, 2013. **301**(0): p. 227-232.
235. Pan, Q., Liu, B.H., McBriarty, M.E., Martynova, Y., Groot, I.M.N., Wang, S., Bedzyk, M.J., Shaikhutdinov, S., and Freund, H.J., *Reactivity of Ultra-Thin ZnO Films Supported by Ag(111) and Cu(111): A Comparison to ZnO/Pt(111)*. Catalysis Letters, 2014. **144**(4): p. 648-655.
236. Behrens, M., Studt, F., Kasatkin, I., Kühl, S., Hävecker, M., Abild-Pedersen, F., Zander, S., Girgsdies, F., Kurr, P., Knief, B.-L., Tovar, M., Fischer, R.W., Nørskov, J.K., and Schlögl, R., *The Active Site of Methanol Synthesis over Cu/ZnO/Al2O3 Industrial Catalysts*. Science, 2012. **336**(6083): p. 893-897.
237. Gokhale, A.A., Dumesic, J.A., and Mavrikakis, M., *On the Mechanism of Low-Temperature Water Gas Shift Reaction on Copper*. Journal of the American Chemical Society, 2008. **130**(4): p. 1402-1414.
238. Yao, H., Chen, Y., Zhao, Z., Wei, Y., Liu, Z., Zhai, D., Liu, B., and Xu, C., *Periodic DFT study on mechanism of selective catalytic reduction of NO via NH3 and O2 over the V2O5 (001) surface: Competitive sites and pathways*. Journal of Catalysis, 2013. **305**(0): p. 67-75.

239. Reuter, K. and Scheffler, M., *Composition, structure, and stability of RuO₂(110) as a function of oxygen pressure*. Physical Review B, 2002. **65**(3): p. 11.
240. Kwak, J.H., Zhu, H.Y., Lee, J.H., Peden, C.H.F., and Szanyi, J., *Two different cationic positions in Cu-SSZ-13?* Chemical Communications, 2012. **48**(39): p. 4758-4760.
241. Gao, F., Walter, E.D., Karp, E.M., Luo, J., Tonkyn, R.G., Kwak, J.H., Szanyi, J., and Peden, C.H.F., *Structure–activity relationships in NH₃-SCR over Cu-SSZ-13 as probed by reaction kinetics and EPR studies*. Journal of Catalysis, 2013. **300**(0): p. 20-29.
242. Fickel, D.W. and Lobo, R.F., *Copper Coordination in Cu-SSZ-13 and Cu-SSZ-16 Investigated by Variable-Temperature XRD*. The Journal of Physical Chemistry C, 2009. **114**(3): p. 1633-1640.
243. Van Bokhoven, J.A., Lee, T.L., Drakopoulos, M., Lamberti, C., Thiess, S., and Zegenhagen, J., *Determining the aluminium occupancy on the active T-sites in zeolites using X-ray standing waves*. Nature Materials, 2008. **7**(7): p. 551-555.

Appendix A: Introduction to DFT Calculations in VASP

First-principles methods are very complementary to X-ray scattering measurements of crystalline materials, as both provide details about the atomic-scale structure of a periodic unit of matter. In particular, density functional theory (DFT) with a plane-wave basis set is widely used to simulate crystal bulk structures and surfaces. Low-energy structures can be relaxed from starting guesses, yielding calculated bond lengths and symmetries or coordination environments for XSW-derived atomic positions. Additional information such as the electronic or chemical properties of the surface can be calculated for the prediction of surface chemical processes.

The goal of this Appendix is to demonstrate how to set up, run, and analyze DFT calculations using the popular Vienna Ab-Initio Simulation Package (VASP)[1-6]. In particular, I will focus on how to model the structure of surfaces and interfaces such as those which we study in the Bedzyk group. For more information, please refer to the comprehensive [VASP guide](#) which is freely available online. References to the VASP manual will be included as hyperlinks (notated by underlined blue text) in the electronic form of this document.

Getting started

In order to run VASP calculations, some knowledge of UNIX shell commands is necessary. A few fundamental commands are listed below. These commands are useful on any UNIX system, including the SPEC-running instruments in the Northwestern X-ray lab and at the Advanced Photon Source.

<code>pwd</code>	Displays current working directory
<code>ls</code>	Lists the files available in working directory
<code>cd target</code>	Change directory to the <code>target</code> directory
<code>cd ..</code>	Change directory to parent directory
<code>man command</code>	Look at manual for <code>command</code>

<code>vi file</code>	Use the <code>vi</code> or <code>vim</code> text editor to view the contents of <code>file</code>
<code>touch file</code>	Create <code>file</code>
<code>ssh host</code>	Connect to <code>host</code> using a secure shell
<code>sftp host</code>	Connect to <code>host</code> for file transfer
<code>top</code>	View active processes on the computer

Additionally, some useful commands and characters for text editing in `vi` or `vim` are given below.

[arrow keys]	Navigate around the file
[ctrl]+f	Go forward one page
[ctrl]+b	Go back one page
[shift]+G	Go to the end of the document
i	Insert text
dd	Delete a line
y	Yank (copy) a line
ma	Mark a line as “a”
y'a	Yank lines from the cursor to line “a”
p	Insert (“put”) a line or lines that had been yanked or deleted
:number	Go to line number
:split file	Open another file in the same pane, e.g. to yank lines from file
:q	Quit the text editor
:wq	Quit and save changes
:q!	Quit and do not save changes
#	Indicates a commented line to VASP

VASP calculations are run on a server which can be accessed via SSH and SFTP. On Mac and Linux operating systems, this can be done through a terminal window. For Windows, tools such as [BitVise SSH Client](#) can be downloaded for communicating via SSH and SFTP. It may also be convenient to use a Linux operating system running in virtualization software such as [Oracle VM VirtualBox](#) for manipulating files in a UNIX environment.

The input files: INCAR, POTCAR, POSCAR, and KPOINTS

It is assumed that a working version of VASP is compiled on the server which will be used. Prof. Ellis can direct you to a server and help set you up with an account and scripts for running VASP. The next step is to set up a working directory. Each structure you calculate should have its own directory with an identifiable name, as the output files (OUTCAR, DOSCAR, CHGCAR, etc.) will not be named uniquely for each structure. The working directory must contain the following four input files: [INCAR](#) defines the starting options for a calculation; [POTCAR](#) contains the data for the pseudopotentials that will be used in the calculation; [POSCAR](#) defines the size and shape of the periodic cell and includes the coordinates of the atoms in the cell; and [KPOINTS](#) defines the size of the k -point mesh that will be used in the calculation. In order to avoid subtle formatting issues, it is recommended to modify existing input files instead of composing them from scratch.

INCAR

Several options define the size, scope, and details of a VASP calculation. Those that are not included in an INCAR file are automatically set to default values. The contents of a typical INCAR file for an atomic relaxation in spin-polarized mode are shown below, followed by an INCAR file for a density of states (DOS) calculation with fixed atomic positions.

SYSTEM = VA_OHA/Fe2O3 ionic relaxation

Start parameters for this run:

NPAR = 2 parallelization option
 ICHARG = 1 initial charge density option
 ISTART = 1 initial wavefunctions option

Electronic Relaxation:

PREC = Medium precision of calculation
 NELM = 300 max number of electronic steps
 NELMIN = 6 min number of electronic steps
 EDIFF = 1E-03 energy stopping criterion for electronic iterations
 EDIFFG = -1E-03 force stopping criterion for geometric

iterations

LREAL = A real-space projection
 ALGO=Very Fast choose algorithm
 NSIM=4 parallelization option
 ISPIN=2 spin-polarization option
 MAGMOM= 3.0 2*-3.0 2*3.0 2*-3.0 15*0 initial magnetic moment
 AMIX=0.2 electronic mixing parameters
 BMIX=0.0001
 AMIX_MAG=0.5 magnetic mixing parameters
 BMIX_MAG=0.0001

Ionic Relaxation:

ISYM = 0 turns symmetry calculation on or off
 ISIF = 2 geometrical relaxation mode
 NSW = 60 max number of geometry steps
 IBRION = 2 ionic relaxation method
 POTIM = .1 time step for geometrical optimization

DOS related values:

ISMEAR = 0 smearing method
 SIGMA = .200 broadening in eV

WRITING OPTION:

LCHARG = TRUE CHGCAR file is saved

SYSTEM = VA_OHA/Fe2O3 DOS calculation

Start parameters for this run:

NPAR = 1 parallelization option
 ICHARG = 11 initial charge density option
 ISTART = 1 initial wavefunctions option

Electronic Relaxation:

PREC = Medium precision of calculation
 NELM = 300 max number of electronic steps
 NELMIN = 6 min number of electronic steps
 EDIFF = 1E-03 energy stopping criterion for electronic iterations
 EDIFFG = -1E-03 force stopping criterion for geometric

iterations

LREAL = A real-space projection
 ALGO=Very Fast choose algorithm
 NSIM=4 parallelization option
 ISPIN=2 spin-polarization option
 MAGMOM= 3.0 2*-3.0 2*3.0 2*-3.0 15*0 initial magnetic moment
 AMIX=0.2 electronic mixing parameters
 BMIX=0.0001
 AMIX_MAG=0.5 magnetic mixing parameters
 BMIX_MAG=0.0001

Ionic Relaxation:

NSW = 0 max number of geometry steps

DOS related values:

ISMEAR = 5 smearing method
 SIGMA = .200 broadening in eV

WRITING OPTION:

LCHARG = TRUE CHGCAR file is saved
 LWAVE = FALSE WAVECAR file is not saved
 LORBIT = 1
 EMIN = -25
 EMAX = 15
 NEDOS = 601
 RWIGS = 0.9 1.6 0.8 0.7

The choice of many of these options depends on the size of the supercell or the server to be used and should be discussed with Prof. Ellis. Here, I'll mention a few important parameters that you'll probably tweak for your calculations. Relevant pages from the VASP Guide are included as hyperlinks.

[NPAR](#): This determines the degree of parallelization to be used on multi-core computers for band structure calculations. $NPAR = 1$ means that each band is calculated by all cores simultaneously. Distributing multiple bands over multiple cores, i.e. $NPAR > 1$, makes more efficient use of the cores' computing power but requires more memory. For ionic relaxations on multi-core machines, $NPAR = 2$ is a good choice. Site-projected atomic DOS calculations require that $NPAR = 1$ in many versions of VASP.

[ICHARG](#): This tells VASP how to initialize the charge density for a calculation. By default, if there is no charge density file present, then VASP will calculate it as a superposition of the pseudopotential atomic charge densities or from orbitals projected from the WAVECAR file. $ICHARG = 1$ uses the existing CHGCAR file as a starting point for the calculation. $ICHARG = 11$ fixes the input charge density for DOS and band structure calculations.

[ISTART](#): This determines whether the wavefunctions from the WAVECAR file are read in ($ISTART = 1$) or not ($ISTART = 0$). If a structure becomes stuck in an unstable state during ionic relaxation, then it may help to freshly initialize the wavefunctions using $ISTART = 0$.

[EDIFF](#), [EDIFFG](#): These define the stopping conditions for the electronic and ionic relaxations. If the total free energy change becomes less than $EDIFF$, then the electronic iterations of an ionic relaxation step will stop. Regardless of the $EDIFF$ value, the number of electronic iterations will be no fewer than $NELMIN$ and no more than $NELM$. $EDIFFG$ similarly defines the free energy step between ionic iterations at which the ionic relaxation will stop. However, if $EDIFFG$ is negative, then it defines the force on all atoms at which the relaxation will stop.

LREAL: This selects whether real-space or reciprocal-space projection operators are used. For large cells, including surface supercells, `LREAL = TRUE` or `LREAL = A` (automated optimization of real-space projection operators) should be selected. The `PREC` tag selects the degree of precision of the projection; for our purposes, `Medium` is sufficient, and `Low` can be used for initial structural relaxations of large slabs. For cells with fewer than 20 atoms, such as bulk unit cells, reciprocal-space projections (`LREAL = FALSE`) may be more efficient.

ISPIN: This selects whether spin polarization is used (`ISPIN = 2`) or not (`ISPIN = 1`). For calculations on many transition metal oxides (including hematite), spin polarization is necessary. Two sets of wavefunctions are calculated, one for each spin state. Both the total charge density and the spin density are given in the `CHGCAR` file, and the spin-polarized DOS is output to the `DOSCAR` file.

MAGMOM: This defines the magnetic moments on all the atoms in the `POSCAR` file, in order. In the example above, the magnetic moments are shown for an antiferromagnetic hematite slab with 8 Fe^{3+} ions, 12 O^{2-} ions, and a V atom atop the surface.

ISYM: This parameter can be set so that VASP automatically determines what symmetry elements are present in the supercell. Symmetry (`ISYM = 1` or `2`) can be used to run the calculation more quickly by symmetrizing the charge density, forces on the ions, and stress tensor. However, if symmetry elements are included, atomic motions that break the symmetry of the supercell are not allowed. To account for this, most calculations of unknown surface structures should be run with `ISYM = 0`, which disables the symmetry calculation.

ISIF: For most slab calculations, the lattice parameters are fixed to enforce bulk-like boundary conditions. The forces on the ions are calculated, and the ions are allowed to relax (aside from those

which are fixed – see the POSCAR discussion below). This corresponds to the default value of `ISIF = 2`. When calculating a bulk unit cell to determine the optimal lattice constant, different values of `ISIF` should be used, namely `ISIF = 6` for relaxation of the cell shape and volume without allowing the ion positions to relax.

[NSW](#): This sets the number of ionic relaxation steps before the VASP run will complete, assuming that the `EDIFFG` condition is not satisfied first. While this number is arbitrary, it may be useful if you have queued jobs and don't want to spend too long on any one calculation. I typically use `NSW = 60` for the initial ionic relaxation and `NSW = 120` for further, finer runs.

[IBRION](#): This defines the method by which ions are moved in response to the calculated forces at the end of the electronic relaxation iterations in each ionic relaxation step. For structural relaxations, I use `IBRION = 1` (quasi-Newtonian) or `IBRION = 2` (conjugate-gradient) algorithms. The quasi-Newtonian movements are calculated more quickly, but the choice of too large of a `POTIM` value (see below) can lead to large displacements of ions, putting the system into an unstable state from which a reasonable configuration may not be recovered. On the other hand, the conjugate-gradient method provides a smoother relaxation, but without allowing large displacements, the structure may relax into a metastable state. `POTIM` scales the amount by which each ion is moved by the calculated force. For coarse relaxations, I use `POTIM = 0.1` or `0.2` and then reduce this value for finer convergence of the forces. While the VASP manual suggests a value of `POTIM = 0.5`, surface slabs have more degrees of freedom and therefore require more delicate relaxation parameters.

[ISMEAR](#): As VASP calculates the ground state (0 K) electronic structure, some artificial smearing is introduced to smoothen the band structure. The `ISMEAR` parameter offers several different smearing

schemes, and the SIGMA parameter gives the degree of smearing (in eV). For structural relaxations, ISMEAR = 0 (Gaussian smearing) is typically used. The choice of ISMEAR is more critical for DOS calculations. I use a 5th-order Methfessel-Paxton smearing (ISMEAR = 5) with SIGMA = 0.1 for Al₂O₃ substrates or SIGMA = 0.2 for Fe₂O₃.

LORBIT: This tag determines how the output wavefunctions are projected into the DOS output files (DOSCAR, PROCAR, and PROOUT). The radii of the Wigner-Seitz spheres into which the site-selected wavefunctions are projected are given in the RWIGS line. For ionic relaxations, the default value LORBIT = 0 is typically used. For DOS calculations, LORBIT = 1 yields an orbital-decomposed projection of the wavefunction character of each band into the PROCAR file as well as site-selected partial DOS (PDOS) saved into DOSCAR. If the line RWIGS is not given in INCAR, the Wigner-Seitz radii are read in from each pseudopotential entry in POTCAR. However, the Wigner-Seitz radii (in Å) can be specified for a particular system. These can be tuned empirically by matching the site-projected electron occupations at the end of the OUTCAR file with the expected values (e.g. O should have a charge of -2) while the sum of the Wigner-Seitz integrated electrons should be roughly correct. The total enclosed Wigner-Seitz volume should also be close to the supercell volume. For oxide systems, the Wigner-Seitz radii of oxygen may be much larger than that of the oxidized cations.

EMIN, EMAX, NEDOS: EMIN and EMAX define the energy range (in eV) over which DOS data will be calculated, with the Fermi level typically near 0. NEDOS defines the number of energy points in DOSCAR. Thus, the energy step size for outputted DOSCAR data is $\frac{(EMAX-EMIN)}{NEDOS-1}$.

POTCAR

The POTCAR file can be assembled from the set of functionals provided by VASP for each element. Prof. Ellis can direct you to the atomic POTCAR library on each server; it is referred to here as `/potcar_dir`. A POTCAR file can be assembled manually by creating the POTCAR file in the working directory, using the `vi` command `:split /potcar_dir/element/POTCAR` to open the atomic POTCAR for `element`, and then using `yank (y)` and `put (p)` commands to copy over the contents of the atomic POTCAR file. It can be done more simply by the following command:

```
cat /potcar_dir/element1/POTCAR /potcar_dir/element2/POTCAR >POTCAR
```

Note that the order of pseudopotentials in the POTCAR file should match those in the POSCAR and INCAR files. That is, if the order of atoms in POTCAR is Fe, O, W, H, then the POSCAR file should contain Fe, then O, then W, and finally H atomic coordinates. Similarly, the INCAR lines MAGMOM and RWIGS should follow the same order. The choice of pseudopotentials will be discussed below.

POSCAR

The starting configuration of atoms is included in the [POSCAR](#) file. An example POSCAR file is given below for a fully relaxed structure which corresponds to the example files mentioned above, with one A-site OH-terminated W atom on an O-terminated 1x1 α -Fe₂O₃ slab.

```

01dec08 Fe2O3 surface slab
1.0000000000000000
5.0064096000000000 0.0000000000000000 0.0000000000000000
-2.5032066300000000 4.3356770000000000 0.0000000000000000
0.0000000000000000 0.0000000000000000 25.0000000000000000
Fe O W H
7 13 1 1
Selective dynamics
Direct
0.3333317800000017 0.6666650800000014 0.0124710999999991 F F F
0.9999974799999976 0.9999990100000034 0.0798906899999992 F F F
0.6666650900000022 0.3333312999999976 0.1048318599999973 F F F
0.3334810811236429 0.6670661471640385 0.1708071759158919 T T T
0.9999390170822759 0.0000093483247709 0.1956355287048166 T T T
0.6694450880090362 0.3320008606894154 0.2651339343089623 T T T
0.3273274172255321 0.6591577552677926 0.2819440826535809 T T T
0.3567982799999996 0.3333547499999980 0.0461765000000014 F F F
0.6666404599999964 0.0234398600000034 0.0461765599999993 F F F
0.9765542900000028 0.6431985600000019 0.0461768600000028 F F F
0.3098834600000018 0.9999819100000025 0.1385502099999982 F F F
0.0000134900000006 0.3099021700000009 0.1385497500000028 F F F
0.6900975100000011 0.6901156400000019 0.1385498599999977 F F F
0.0226732125625943 0.6714120251100745 0.2325833319135099 T T T
0.3282710808511147 0.3466861533349534 0.2331766698078316 T T T
0.6509629747966795 0.9782581902173371 0.2332886081183316 T T T
0.9976348175688619 0.3189330422547997 0.3325915116417645 T T T
0.6624004838091339 0.6482473534320699 0.3309654047070128 T T T
0.3289177509584301 0.9865599424332773 0.3345230241083723 T T T
0.9613775611886371 0.9605447516502711 0.4356028850390206 T T T
0.9900861429147152 0.9819618848305128 0.3590595079532306 T T T
0.1186014567585621 0.1204624498527347 0.4581451848021618 T T T

```

At the top of the POSCAR file is a comment line, followed by a scaling factor by which the lattice parameters are multiplied. This is followed by three lines that define the lattice vectors. In this case, we have a hexagonal cell, with the a and b directions defined by a relaxed bulk unit cell and the c direction set at 25 Å. Next, the atomic species making up the file are given, followed by the corresponding number of each species (here, 7 Fe, 13 O, 1 W, and 1 H). The choice of “Selective dynamics” means that each atom can be fixed or allowed to move along each lattice vector. These are chosen as T or F (movement allowed or fixed, respectively) tags at the end of the entry for each

atom. The following line, “Direct”, states that the given atomic positions are in fractional coordinates along the defined lattice vectors. Finally, the atomic positions are listed.

For the slab defined by the POSCAR file shown above, several atoms (3 Fe and 6 O) are fixed in place to enforce bulk-like boundary conditions. These positions, along with the lattice parameters, were derived from a relaxed bulk unit cell. Note that the difference between the highest and lowest atoms in the slab is about 0.45, indicating that there is about 13 Å of vacuum space between the top and bottom of the periodic slabs.

KPOINTS

The KPOINTS file defines the k -point mesh that will be used. While the k -point mesh can be explicitly defined, it is usually calculated by the method of Monkhorst and Pack[7] based on an input mesh size.

The contents of an example KPOINTS file for a 1x1 α -Al₂O₃ or α -Fe₂O₃ slab supercell are given below.

```
Monkhorst      specifies that the Monkhorst-Pack scheme will be used
0              number of kpoints (0 turns on automatic generation)
Gamma         sets origin of the k-point mesh at the gamma point
4 4 1         defines the number of divisions of the mesh along reciprocal
              lattice vectors
0. 0. 0.      offset of the k-mesh
```

In most slab cases, only the fourth line needs to be modified. A coarser k -point mesh is sufficient for structural relaxations. For DOS and band structure calculations, one might test a few different k -point meshes (e.g. 6 6 1 or 8 8 1) to check if the DOS is affected. However, a finer k -mesh increases the memory requirements and calculation time substantially. In tall ($c > 20$ Å) slabs, the number of k -point divisions in the c^* direction doesn't need to be greater than 1.

Choice of functional

DFT is a powerful tool for materials science, but its physical accuracy is limited by the approximations that go into an efficient calculation. As mentioned in **Chapter 2**, the choice of the approximate exchange-correlation (XC) functional of the electron density depends on the materials to be studied and the desired balance of physical accuracy and computational efficiency. The XC energy E_{xc} must be included in a DFT calculation to accurately predict the ground-state electron density and related properties such as bond lengths[8]; without accounting for E_{xc} , lattice parameters are predicted to be far too large. Surface electronic properties would also be completely bogus as the energy to extract an electron from the surface would be severely underpredicted. The choice of an appropriate XC functional is therefore critically important for surface structure determination and the prediction of surface chemical effects. The different flavors of XC functionals are discussed below, and specific functionals are referred to in the provided references.

John Perdew, a leader in the development of XC functionals, considers the increasing degrees of complexity of XC functionals as hierarchical rungs on a “Jacob’s ladder” from the Hartree approximation, which neglects E_{xc} entirely, to an as-yet hypothetical “perfectly accurate” account of the exchange-correlation energy[9, 10]. The first rung is the local density approximation (LDA), described in **Equation 2.29**. The LDA E_{xc} is a functional of the electron density $n(\mathbf{r})$ as calculated for a homogeneous electron gas of the same density. (The local spin density approximation, LSDA, is similar, with separate contributions from the spin-up and spin-down densities; this can be generalized to the other approximations discussed below.) The next rung up is the generalized gradient approximation (GGA), in which the gradient of the electron density $\nabla n(\mathbf{r})$ is taken into account as well as $n(\mathbf{r})$. LDA tends to over-bind atoms in solid lattices, resulting in smaller than expected lattice

parameters, while GGA slightly under-binds, yielding the opposite effect[6]. GGA provides much more accurate results for chemical phenomena such as atomization energies[11, 12] and molecular adsorption at surfaces[13], among other properties[14, 15], making it the standard for calculations of surface chemical phenomena and heterogeneous catalysis. However, GGA suffers from intrinsic errors at surfaces which lead to inaccurate defect formation energies in metals and adhesion energies at weak metal-oxide interfaces[16]; schemes to correct this error have been developed[17]. The GGA approach is further augmented to the third rung, meta-GGA, by including a somewhat less localized contribution from the orbital kinetic energy density $\tau_{\sigma}(\mathbf{r})$ or the Laplacian $\nabla^2 n(\mathbf{r})$ in addition to the local and nearly-local contributions included in GGA. Without adding too much computational cost, the meta-GGA approach yields more accurate lattice parameters and surface energies than GGA or LDA[15] and gives better predictions for hydrogen-bonded structures[18] and van der Waals interactions[19]. The approaches described above are usually non-empirical, derived completely from first principles.

Hybrid functionals, which include some degree of exact exchange, make up the fourth rung of Perdew's ladder. The exchange energy E_x can be calculated using Hartree-Fock-like methods and mixed in with exchange and correlation components calculated from functionals from the first three rungs. While the exact exchange calculation is computationally expensive, hybrid functionals offer significant improvements over GGA in the calculation of molecular bond lengths and atomization energies[20], lattice parameters[21], and semiconductor or insulator bandgaps[22]. However, they are semi-empirical, requiring at least one tunable parameter (e.g. the degree of exact exchange mixing with GGA-calculated exchange). The fifth (and currently highest) rung uses the random phase approximation (RPA), which gives a nearly-exact treatment of long-range exchange-correlation effects and shows excellent predictive properties across a range of materials, including those with van der Waals interactions such as graphite[23, 24].

For oxides and oxide surfaces, GGA is widely used. In the Ellis group, we typically use pseudopotentials which explicitly account for only the chemically active valence and near-valence electrons. The projector augmented wave (PAW) method[5], which smoothens out the high-energy wavefunctions near the pseudopotential core, is used to reduce the required plane-wave cutoff energy (see Georg Kresse's presentation, [“The PAW and US-PP database”](#), for a primer on VASP pseudopotentials). Libraries including pseudopotentials for all atoms using this PAW-GGA approach can be found in Prof. Ellis's files on our servers. Two of the most common GGA functionals are PW91[12] and PBE[11]. For many applications, such as the calculation of bulk lattice constants and mechanical properties, these approaches are nearly interchangeable. However, PBE has been found to be somewhat more accurate than PW91 in the calculation of the aforementioned intrinsic surface energy error[25]. In future work, the use of meta-GGA functionals may be preferred to improve the treatment of long-range interactions of surface species, such as hydrogen bonds or van der Waals effects.

Within a given PAW-GGA framework, there are several pseudopotentials to choose from for each atom. Pseudopotentials are selected as a tradeoff between accuracy and computational intensity. For example, a standard PAW-PBE pseudopotential for Al has a maximum plane-wave energy of 240.300 eV, but a high energy variant (labeled as Al_h in the pseudopotential directory) has a higher cutoff energy of 294.838 eV. For each of these pseudopotentials, wavefunctions for only the three valence electrons ($3s^23p^1$) are used in the DFT calculation. For some atoms, pseudopotentials can be selected with more or fewer valence electrons available for calculation. In the work reported in this dissertation, I used the extended pseudopotentials W_{pv} and V_{pv} for tungsten and vanadium, which include wavefunctions for the p^6 near-valence shell in addition to the s and d valence electrons.

In many transition metal oxides and rare earth oxides with partially filled d or f valence shells, strong electron correlation effects require the use of further corrections, as discussed in **Section 3.2.2.9**. A classic case is that of NiO, for which an underestimation of Coulomb repulsion between localized d electrons leads to an unrealistic broadening of their density of states. This leads to a severely underpredicted bandgap, or even the prediction of a metallic state, by traditional local (spin) density approximation (L(S)DA) calculations[26]. The addition of an on-site $+U$ term aims to correct this error by simulating Coulomb repulsion in the d orbital[27-29]. This is frequently implemented in VASP by the method of Dudarev *et al.*[29], which penalizes partial occupation of bands, forcing the electron density into more localized states. The $+U$ value, i.e. the size of the energy penalty, can be chosen empirically and applied to particular orbitals of particular elements in the calculation, although some methods have been developed to calculate $+U$ values *ab initio*[30]. Additionally, Hartree-Fock calculations can be performed, and this exact exchange energy is taken into account in hybrid functionals such as the popular B3LYP functional.

In summary, care must be taken in choosing the appropriate functional for a particular materials system. The type of material (metal, semiconductor, oxide), interatomic interactions (ionic, covalent, van der Waals), and other special considerations (e.g. strongly correlated electrons) must all be taken into account when determining a theoretical scheme. It is helpful to run simulations on known material systems similar to those of interest that can be compared to literature values for lattice parameters, bulk moduli, band structure, adsorption energies, or surface energies.

Composing the slab

Plane-wave VASP calculations use periodic boundary conditions in three dimensions. To calculate surface structures, a slab must be constructed with a large distance (~ 10 Å) between the top and bottom

sides to avoid interactions between periodic surfaces. Slabs can be asymmetric, with one termination fixed to enforce bulk-like boundary conditions and the other side allowed to relax. Alternatively, for centrosymmetric crystals, some researchers prefer symmetric slabs with both terminations identical and allowed to relax.

Initial surface structures can be composed by “chemical intuition”. Starting from a bulk-like termination, adsorbates or ligands can be added with starting configurations and interaction distances informed by experiment. If these interaction distances are too close or too long, the forces on the atoms will be strongly attractive or repulsive, resulting in extreme ionic movements into unrealistic or unstable positions. At the start of a VASP calculation, the nearest-neighbor distances for each atom are calculated, providing a quick “sanity check” about the position of surface ligands.

Running VASP and achieving convergence

A VASP calculation, or run, is initiated by running the appropriate script from a UNIX terminal. VASP runs consist of series of iterations of electronic and ionic structure convergence which continue. The calculation begins with an “educated guess” of the structure as described above. For a bulk cell calculation, the initial structure can come from X-ray diffraction data. Due to the approximations used in DFT, the cell may converge to a lattice parameter slightly larger or smaller than the experimental values. Bulk cells can be converged relatively quickly, especially if there are symmetry elements present (which are automatically detected by VASP and utilized in the calculation). Once the structure, potentials, and other information are read in from the input files, the calculation begins by generating test wavefunctions (typically for free atoms) and iteratively relaxing the electronic states until a low-energy charge density has been converged. Forces on the atoms are then calculated, and the atoms are moved according to the selected algorithm. After each ionic relaxation, the new atomic coordinates are

saved in the [CONTCAR](#) file, and information about the calculation is saved in the OUTCAR file. These will be discussed in more detail below.

Converging a surface slab supercell is much more computationally intensive than a bulk cell. At the surface, the symmetry is broken, so there are fewer symmetry elements to utilize; in fact, it is recommended to turn off symmetry elements completely ($ISYM = 0$) when converging surface structures to allow for symmetry-breaking lateral movements across the surface. Bond lengths and angles can change significantly through a VASP run, and bonds can be made or broken as atoms and ligands migrate. Long structural relaxations with hundreds of ionic iterations are sometimes necessary to converge to the lowest-energy surface. With a myriad of possible surface configurations, it is difficult to know whether the relaxed structure is in fact that of the lowest energy for a particular stoichiometry.

Ionic relaxation using a conjugate-gradient algorithm gives a smoother transition from the initial configuration to the final relaxed state. While this often results in convergence after fewer ionic relaxation iterations, it can also prevent the system from relaxing into unexpected low-energy structures. Additionally, there is a bug in VASP that occasionally kills conjugate-gradient relaxation calculations with the following error message:

```
ZBRENT: fatal error in bracketing
please rerun with smaller EDIFF, or copy CONTCAR to POSCAR and
continue
```

One solution to this problem is setting $NSW = 19$, although it's not clear why this works.

If further VASP runs will be performed for a system, then the next calculation can be set up by replacing the old POSCAR file with CONTCAR. It is also useful to save INCAR and OUTCAR files corresponding to the completed run for future reference. A simple script called `upcar` which updates these files and can be found in Prof. Ellis's scripts.

The output files: WAVECAR, CONTCAR, OUTCAR, CHGCAR, DOSCAR

During a VASP run and upon its conclusion, data is written to several output files. Before sufficient convergence is achieved, these files can be used to continue the calculation in a new VASP run. When a structure is satisfactorily converged, this data can be interpreted to learn about the structural, chemical, and electronic properties of the system.

WAVECAR

All wavefunctions used in a VASP calculation are stored in [WAVECAR](#). This is a very useful file for continuing calculations, as otherwise the initial wavefunctions will be calculated from CHGCAR or initialized randomly. WAVECAR is also necessary for band-projected charge density calculations as described below. For calculations on large ensembles of atoms or with fine k -point meshes, this file can grow to several gigabytes. It therefore might be desirable in some cases to not save any data into WAVECAR by setting `LWAVE = FALSE` in INCAR.

CONTCAR

The CONTCAR file tracks the relaxed structure of the ions and is identical in format to POSCAR. At the end of a VASP run, the CONTCAR file can be copied to POSCAR as described above.

OUTCAR

Details of VASP calculations are saved into OUTCAR throughout a VASP run. The beginning of OUTCAR documents details from all the input files, including values from INCAR, default values for parameters not specified in INCAR, and some basic information about the pseudopotentials used. A nearest neighbor table is calculated, providing interatomic spacings up to some cutoff length that depends on the atom. The results of symmetry calculations are documented, as is the calculation of the k -mesh.

After these initial calculations, the electronic relaxation iterations begin. Details from each calculation are shown, including all components of the total supercell energy. Calculation times are also listed and can be used to diagnose computational bottlenecks. At the end of each step, the total free energy is given as `TOTEN`. In order to track the energy convergence of a VASP run, one can use the following command in the directory of the `OUTCAR` file:

```
grep TOTEN OUTCAR
```

to see how the total supercell energy changes with electronic iterations.

After the electronic structure is converged, VASP outputs the energies and occupations of each calculated band at each k -point. Due to Pauli exclusion, the maximum occupancy of each band is 2 for non-spin-polarized calculations and 1 for spin-polarized calculations. Finally, the Coulomb forces on each ionic core are calculated. A rule of thumb is to converge the force on each relaxing atom within $0.02 \text{ eV} / \text{\AA}$ for each lattice direction. The forces on non-relaxing atoms may inevitably be much higher due to constraints imposed to enforce bulk-like boundary conditions against a vacuum surface. The free energy of the ion-relaxed electron system is then displayed. If another ionic relaxation step follows, then the atoms are allowed to relax in response to the calculated forces, and a new electronic relaxation begins.

Once force convergence is achieved (or `NSW` is reached), the total charge is calculated within Wigner-Seitz spheres of each atom and shown in `OUTCAR`. In spin-polarized calculations, the magnetic moment is given for each atom as well. The VASP run concludes with a log of the total time and memory use of the run.

CHGCAR

Charge density information is stored in [CHGCAR](#). This can be used as an input for further VASP runs, or after satisfactory convergence is achieved, the charge density can be analyzed. The Bader charge can be partitioned from CHGCAR using a [shell script developed by Henkelman *et al.*](#) [31] Additionally, charge density isosurfaces and slices can be visualized by software such as [VESTA](#) or [XCrySDen](#). For spin-polarized calculations, a spin density array is given after the charge density array. Charge density differences between two structures can be calculated using the `chgdiff.pl` tool, [also available from the Henkelman group](#).

Charge densities corresponding to particular bands or regions of the density of states can be calculated by setting `LPARD = TRUE` in INCAR. Bands can be selected explicitly using the `IBAND` tag, and the integration over certain k -points can be set using `KPUSE`. Perhaps the simplest way to visualize the charge density corresponding to a certain band in the DOS is by setting the `EINT` tag to the desired range of energies. To run VASP with `LPARD = TRUE`, `WAVECAR` and `CHGCAR` files must be provided along the standard input files. As VASP is only re-projecting the charge density, the calculation is very quick. The partial charge density is output to the file `PARCHG`.

DOSCAR

Densities of states, including the total DOS and atom-projected partial DOS (PDOS), are output to [DOSCAR](#). At the beginning of the file, the total DOS is given, as well as the integrated DOS. Because of the contribution of bands below `EMIN`, the first entry in DOSCAR might be very large. If `RWIGS` is set in INCAR, then the atom- and orbital- (s -, p -, d -)projected PDOS for each atom are given after the total DOS. In the case of spin-polarized calculations, DOSCAR will include both spin-up and spin-down components for the total DOS as well as each projected PDOS. DOSCAR data is split into its atomic

constituents using the `dan_split.pl` script written by Dr. Daniel Wells and available on Prof. Ellis's servers. Atomic PDOS can be selected for summation into an ensemble PDOS using the `dan_sumdos.pl` script. This is particularly useful for looking at adsorbed molecules or total contributions from symmetric groups of atoms (e.g. oxygen layers in oxides).

References

1. Kresse, G. and Furthmüller, J., *Efficient iterative schemes for ab initio total-energy calculations using a plane-wave basis set*. Physical Review B, 1996. **54**(16): p. 11169-11186.
2. Kresse, G. and Furthmüller, J., *Efficiency of ab-initio total energy calculations for metals and semiconductors using a plane-wave basis set*. Computational Materials Science, 1996. **6**(1): p. 15-50.
3. Kresse, G. and Hafner, J., *Ab initio molecular-dynamics simulation of the liquid-metal–amorphous-semiconductor transition in germanium*. Physical Review B, 1994. **49**(20): p. 14251-14269.
4. Kresse, G. and Hafner, J., *Ab initio molecular dynamics for liquid metals*. Physical Review B, 1993. **47**(1): p. 558-561.
5. Blöchl, P.E., *Projector augmented-wave method*. Physical Review B, 1994. **50**(24): p. 17953-17979.
6. Hafner, J., *Ab-initio simulations of materials using VASP: Density-functional theory and beyond*. Journal of Computational Chemistry, 2008. **29**(13): p. 2044-2078.
7. Monkhorst, H.J. and Pack, J.D., *Special points for Brillouin-zone integrations*. Physical Review B, 1976. **13**(12): p. 5188-5192.
8. Kurth, S. and Perdew, J.P., *Role of the exchange–correlation energy: Nature's glue*. International Journal of Quantum Chemistry, 2000. **77**(5): p. 814-818.
9. Perdew, J.P. and Schmidt, K., *Jacob's ladder of density functional approximations for the exchange-correlation energy*, in *Density Functional Theory and Its Application to Materials*, V. VanDoren, C. VanAlsenoy, and P. Geerlings, Editors. 2001, Amer Inst Physics: Melville. p. 1-20.
10. Perdew, J.P., *Climbing the ladder of density functional approximations*. Mrs Bulletin, 2013. **38**(9): p. 743-750.
11. Perdew, J.P., Burke, K., and Ernzerhof, M., *Generalized Gradient Approximation Made Simple*. Physical Review Letters, 1996. **77**(18): p. 3865-3868.

12. Perdew, J.P., Chevary, J.A., Vosko, S.H., Jackson, K.A., Pederson, M.R., Singh, D.J., and Fiolhais, C., *Atoms, molecules, solids, and surfaces: Applications of the generalized gradient approximation for exchange and correlation*. Physical Review B, 1992. **46**(11): p. 6671-6687.
13. Ford, D.C., Xu, Y., and Mavrikakis, M., *Atomic and molecular adsorption on Pt(111)*. Surface Science, 2005. **587**(3): p. 159-174.
14. Marlo, M. and Milman, V., *Density-functional study of bulk and surface properties of titanium nitride using different exchange-correlation functionals*. Physical Review B, 2000. **62**(4): p. 2899-2907.
15. Staroverov, V.N., Scuseria, G.E., Tao, J., and Perdew, J.P., *Tests of a ladder of density functionals for bulk solids and surfaces*. Physical Review B, 2004. **69**(7): p. 11.
16. Mattsson, A.E. and Jennison, D.R., *Computing accurate surface energies and the importance of electron self-energy in metal/metal-oxide adhesion*. Surface Science, 2002. **520**(1–2): p. L611-L618.
17. Mattsson, T.R. and Mattsson, A.E., *Calculating the vacancy formation energy in metals: Pt, Pd, and Mo*. Physical Review B, 2002. **66**(21): p. 214110.
18. Tao, J.M., Perdew, J.P., Staroverov, V.N., and Scuseria, G.E., *Climbing the density functional ladder: Nonempirical meta-generalized gradient approximation designed for molecules and solids*. Physical Review Letters, 2003. **91**(14): p. 4.
19. Sun, J., Haunschild, R., Xiao, B., Bulik, I.W., Scuseria, G.E., and Perdew, J.P., *Semilocal and hybrid meta-generalized gradient approximations based on the understanding of the kinetic-energy-density dependence*. The Journal of Chemical Physics, 2013. **138**(4): p. -.
20. Paier, J., Hirschl, R., Marsman, M., and Kresse, G., *The Perdew–Burke–Ernzerhof exchange-correlation functional applied to the G2-1 test set using a plane-wave basis set*. The Journal of Chemical Physics, 2005. **122**(23): p. -.
21. Paier, J., Marsman, M., and Kresse, G., *Why does the B3LYP hybrid functional fail for metals?* The Journal of Chemical Physics, 2007. **127**(2): p. -.
22. Paier, J., Marsman, M., Hummer, K., Kresse, G., Gerber, I.C., and Ángyán, J.G., *Screened hybrid density functionals applied to solids*. The Journal of Chemical Physics, 2006. **124**(15): p. -.
23. Harl, J. and Kresse, G., *Accurate Bulk Properties from Approximate Many-Body Techniques*. Physical Review Letters, 2009. **103**(5): p. 056401.
24. Harl, J., Schimka, L., and Kresse, G., *Assessing the quality of the random phase approximation for lattice constants and atomization energies of solids*. Physical Review B, 2010. **81**(11): p. 115126.

25. Mattsson, A.E., Armiento, R., Schultz, P.A., and Mattsson, T.R., *Nonequivalence of the generalized gradient approximations PBE and PW91*. Physical Review B, 2006. **73**(19): p. 195123.
26. Terakura, K., Oguchi, T., Williams, A.R., and Kübler, J., *Band theory of insulating transition-metal monoxides: Band-structure calculations*. Physical Review B, 1984. **30**(8): p. 4734-4747.
27. Anisimov, V.I., Solovyev, I.V., Korotin, M.A., Czyżyk, M.T., and Sawatzky, G.A., *Density-functional theory and NiO photoemission spectra*. Physical Review B, 1993. **48**(23): p. 16929-16934.
28. Anisimov, V.I., Zaanen, J., and Andersen, O.K., *Band theory and Mott insulators: Hubbard U instead of Stoner I*. Physical Review B, 1991. **44**(3): p. 943-954.
29. Dudarev, S.L., Botton, G.A., Savrasov, S.Y., Humphreys, C.J., and Sutton, A.P., *Electron-energy-loss spectra and the structural stability of nickel oxide: An LSDA+U study*. Physical Review B, 1998. **57**(3): p. 1505-1509.
30. Mosey, N.J., Liao, P., and Carter, E.A., *Rotationally invariant ab initio evaluation of Coulomb and exchange parameters for DFT+U calculations*. The Journal of Chemical Physics, 2008. **129**(1): p. -.
31. Henkelman, G., Arnaldsson, A., and Jónsson, H., *A fast and robust algorithm for Bader decomposition of charge density*. Computational Materials Science, 2006. **36**(3): p. 354-360.

Appendix B: XSW Measurements on α -Al₂O₃ Substrates

Chapter 4 includes the first report, to our knowledge, of XSW measurements which involve the generation of short-period XSWs from a α -Al₂O₃ single crystal substrate. Short-period XSWs have been generated from thin films grown on aluminum oxide[1], and long-period XSWs from total external reflection of the α -Al₂O₃ surface have been used for studies of environmental interfaces[2-5]. Additionally, XSWs and subsequent optical luminescence patterns generated in an α -Al₂O₃ single crystal were analyzed by X-ray holography, and the positions of light elements in the bulk were reconstructed[6]. Considering the technical relevance of sapphire as a substrate for optical devices[7], the lack of short-period (Bragg-reflection) XSW studies on the surfaces of α -Al₂O₃ is somewhat surprising. However, the consequences of dynamical diffraction theory for crystals composed of light elements present some unique challenges for sapphire XSW studies and tools for interpreting experimental results. Here, I discuss these challenges and considerations for XSW on sapphire in light of previous work on α -Fe₂O₃ (hematite), a crystal with more conventional diffractive properties. As a starting point, calculated (006) rocking curves are shown for sapphire and hematite at a beam energy of 13 keV in **Figure B.1**.

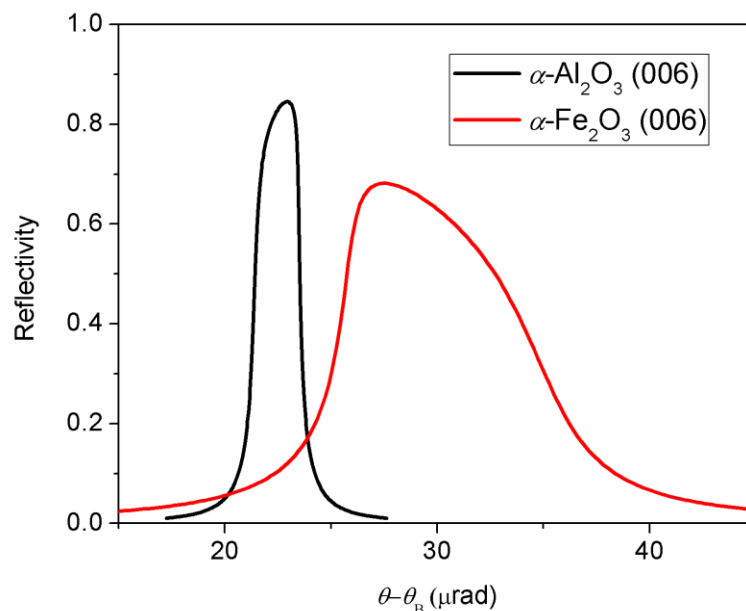


Figure B.1: Comparison of α -Al₂O₃ and α -Fe₂O₃ (006) rocking curves at a beam energy of 13 keV. Crystal angles are shown relative to the Bragg angle θ_B . Rocking curves were calculated using SWAMv4.2.

As discussed in **Chapter 2**, the XSW effect involves a translation of the XSW antinodes to the diffraction plane from a position $\frac{1}{2}d_H$ away from the diffraction plane as the crystal is rocked from low to high angle across the $H = hkl$ Bragg reflection. The diffraction plane is defined as the plane of highest effective electron density, at which the real part of the H^{th} Fourier component of the scattering density is maximized[8]. For the hematite (006) reflection, the diffraction plane sits at the middle of the Fe bilayer (see **Figure B.2**). The Fe atoms are not coplanar – in the (006) direction, they are separated by about $0.10 \cdot d_{006}$. However, the electron density of this staggered Fe₂ layer ($Z_{\text{total}} = 2 \cdot Z_{\text{Fe}} = 52$) is high enough to significantly outweigh that of the O₃ planes ($Z_{\text{total}} = 24$) which sit $\frac{1}{2}d_{006}$ away from the center of the Fe₂ layer. In sapphire, this is not the case. The Al₂ planes are similarly staggered (by $0.08 \cdot d_{006}$), but the total electron density of the Al₂ plane ($z_{\text{total}} = 26$) is similar to that of the O₃ plane. This effect is amplified by the high ionicity of sapphire, by which Al and O atoms should be considered as Al³⁺

and O^{2-} ions; consequences of this effect are discussed below. Thus, the high electron density planes in sapphire are actually the O_3 planes, and so the XSW antinodes travel from the Al_2 plane to the O_3 plane as the crystal angle is increased, as shown in **Figure B.2**. The movement of XSW antinodes for the (006) reflection is therefore offset by half a phase relative to that of hematite.

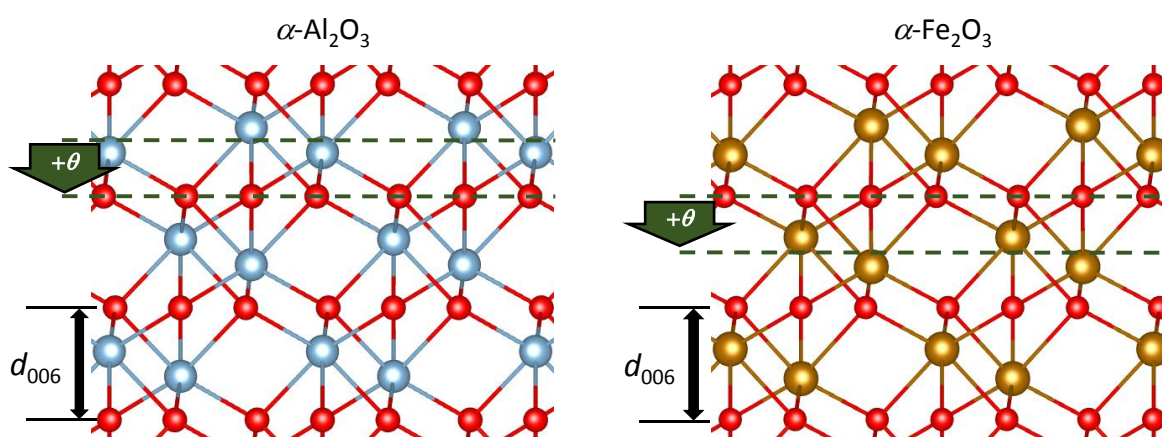


Figure B.2: Comparison of the crystal structures and dynamical diffraction effects through the (006) reflection condition for sapphire (left) and hematite (right). The initial (low-angle) and final (high-angle) positions of the XSW antinodes are shown as green dashed lines, and the green arrow indicates the movement of the XSW antinodes as the crystal angle relative to the incident beam is increased. O atoms are shown in red; Al, blue; and Fe, gold.

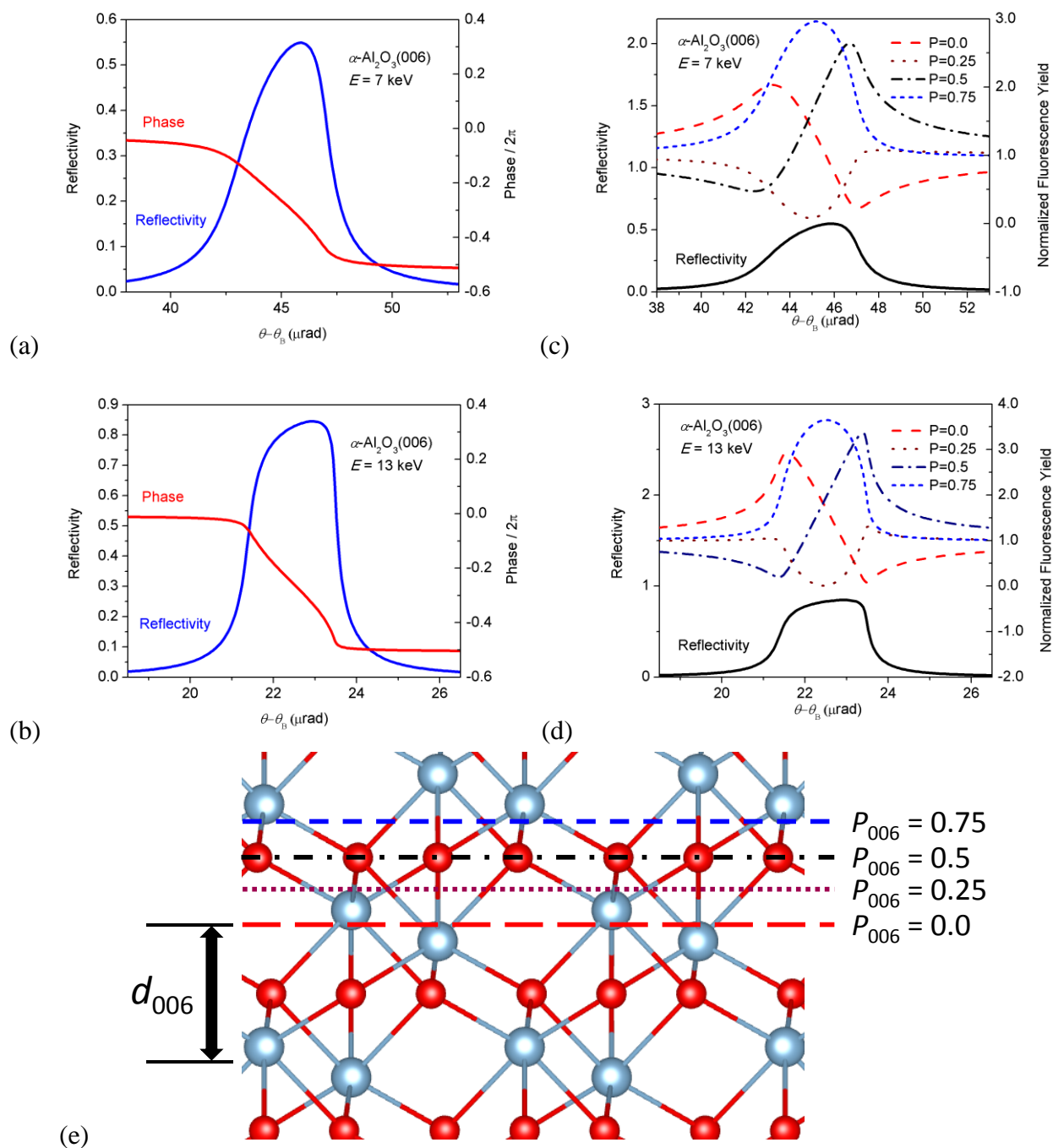


Figure B.3: Calculated $\alpha\text{-Al}_2\text{O}_3$ (006) rocking curves and reflected wave phases (a,b) as well as fluorescence yields ($f_{006} = 1$) for different coherent positions P_{006} relative to the center of the Al_2 plane (c,d). Incident X-ray energies are 7 keV (a,c) and 13 keV (b,d). Crystal angles are shown relative to the Bragg angle θ_B . Calculations were performed using SWAMv4.2 software. (e) Coherent positions P_{006} are shown superposed over the $\alpha\text{-Al}_2\text{O}_3$ crystal structure. O and Al atoms are small red and large light blue circles, respectively.

Calculated α -Al₂O₃ (006) rocking curves are shown in **Figure B.3** for X-ray energies of 7 and 13 keV, along with the expected XSW fluorescence yields expected for perfectly coherent ($f_{006} = 1$) surface species with the given (006) coherent positions P_{006} . $P_{006} = 0$ is defined as the center of the staggered Al₂ plane; $P_{006} = 0.5$ therefore corresponds to a position on the bulk oxygen plane. The movement of the XSW antinodes from the metal plane to the oxygen plane with increasing crystal angle leads to an unusual shape for the (006) rocking curve. Although the Al₂ plane has a lower overall electron density than the O₃ plane, the X-ray absorption of Al is greater than that of O. For most crystals studied by XSW, including hematite, the high-angle side of the rocking curve is attenuated, as the X-ray absorption is higher on these planes. This effect can be exaggerated by tuning the X-ray energy to just above an absorption edge of an atom in the absorbing plane[9]. For sapphire, however, the X-ray absorption is higher on the low-angle side of the rocking curve. The 7 keV rocking curves show much more attenuation on the low-angle side due to stronger absorption of lower energy X-rays.

The extreme ionic nature of sapphire draws into question the assumption that the structure factor can be calculated using atomic form factors derived from neutral atoms. Form factors are calculated as a function of $k = \frac{\sin \theta}{\lambda}$, where θ is the scattering angle and λ is the X-ray wavelength, by the method and parameters in Ref. [10]. As pointed out by G. Campbell and shown in **Figure B.4**, form factors calculated for neutral Al⁰ and O⁰ deviate substantially from those calculated for Al³⁺ and O²⁻ at low k but become very close above $k = 0.3 \text{ \AA}^{-1}$. The value of k at a scattering condition can be calculated via Bragg's law, such that for a crystal reflection at $H = hkl$,

$$k_H = \frac{\sin \theta_H}{\lambda} = \frac{1}{2d_H} \quad (\text{B.1})$$

For sapphire, $k_{006} = 0.231 \text{ \AA}^{-1}$, which is indicated in **Figure B.4**. At this value, form factors are 8.7128, 8.7157, 5.1110, and 5.2735 for Al^0 , Al^{3+} , O^0 , and O^{2-} , respectively. While the atomic and ionic form factors are nearly identical, the $\sim 3\%$ difference in the O form factor is especially significant because of the similar electron densities of the O_3 and staggered Al_2 planes. This leads to substantial changes to the calculated sapphire rocking curve. **Figure B.5** shows that the use of ionic form factors in the structure factor calculation results in a broader and more intense rocking curve vs. neutral atom form factors. Differences in calculated parameters for the sapphire (006) reflection at 13 keV are detailed in **Table B.1**. The use of ionic form factors significantly improved the quality of XSW fits and were used for XSW analysis in **Chapter 4**.

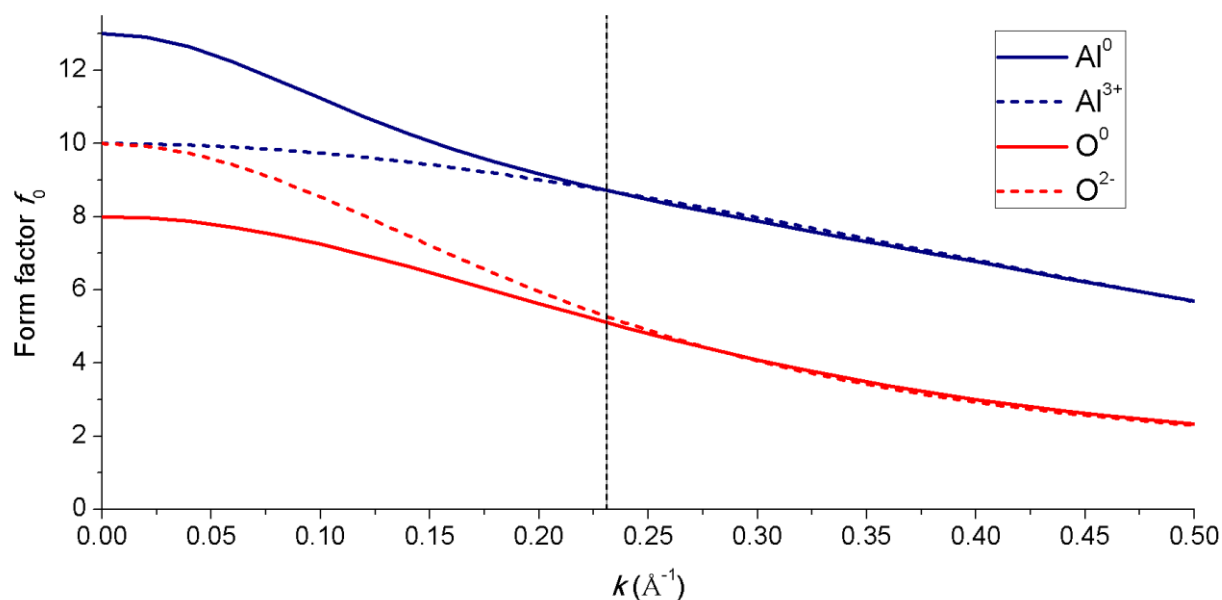


Figure B.4: Atomic and ionic form factors for Al and O as functions of $k = \frac{\sin \theta}{\lambda}$. The dashed vertical black line corresponds to k_{006} for $\alpha\text{-Al}_2\text{O}_3$.

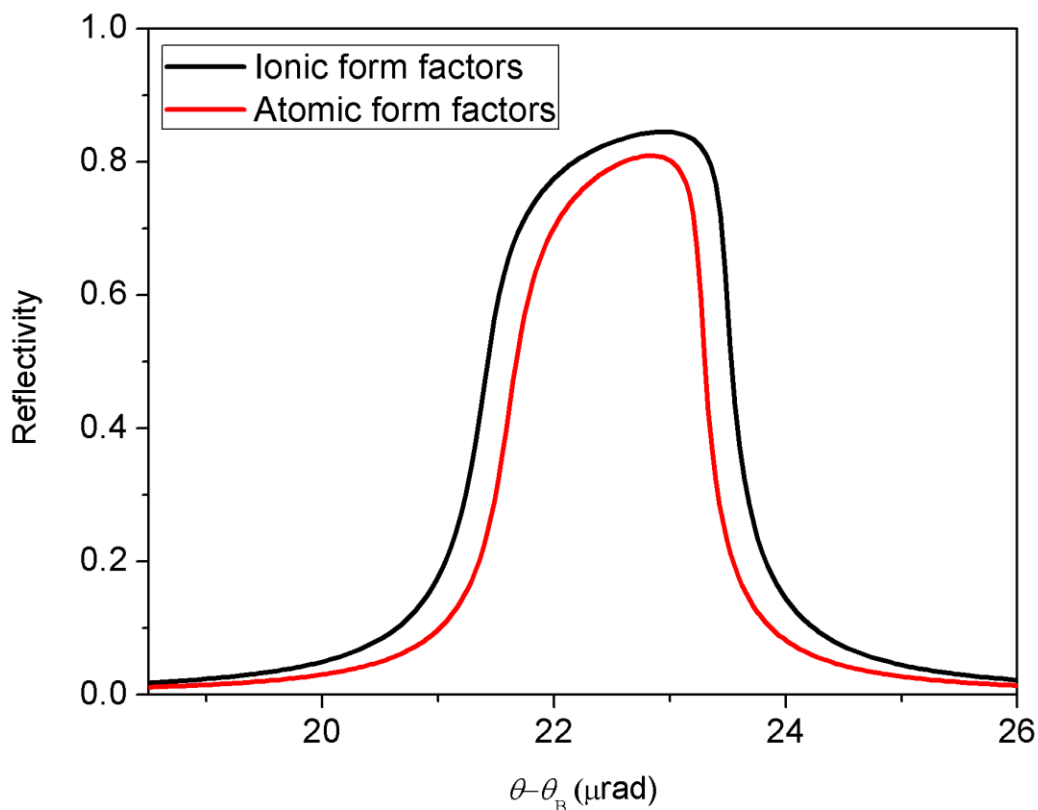


Figure B.5: Sapphire (006) rocking curves at 13 keV beam energy calculated using ionic (Al^{3+} , O^{2-}) and atomic (Al^0 , O^0) form factors. The use of ionic (Al^{3+} , O^{2-}) form factors in the structure factor calculation results in a broader and more intense rocking curve.

As **Figures B.1, B.3, and B.5** reveal, the intrinsic rocking curves for sapphire are extremely narrow. In previous studies using natural hematite or rutile crystals, very small beam sizes ($\sim 100 \mu\text{m} \times 100 \mu\text{m}$) were required to “pick” a particular crystallite. Nearby mosaic crystallites would diffract at slightly different angles, broadening the measured rocking curve and preventing accurate XSW analysis. Fortunately, synthetic sapphire substrates of very high crystal quality and purity are available. Crystals from Rubicon Technology, Inc. were used for the XSW measurements reported in **Chapter 4**, and the high crystal quality allowed the use of relatively large beam sizes (on the order of 1 mm x 1 mm) for XSW measurements. With nearly perfect crystals, the primary experimental limitations become the

quality of the beamline instrumentation and the angular width of the incident beam. Mini-steppers on the crystal rotation axis were used to achieve a minimum angular movement of ~ 0.03 millidegrees, and care was taken to dampen vibrations that might have traveled through the gas lines to the Be dome mini-chamber in which the sample was mounted.

	Atomic form factors	Ionic form factors
d -spacing (\AA)	2.165783	
Bragg angle (degrees)	12.7196	
F_0	$301.478 + 1.33886i$	$301.471 + 1.33886i$
$F_{006} (=F_{00-6})$	$-11.0374 + 0.650248i$	$-13.8932 + 0.650248i$
Phase ($\pm \mathbf{H}/2\pi$)	-0.009366	-0.007444
Darwin width (μrad)	1.652395	2.075670
$\theta - \theta_B$ (μrad)	22.441186	22.440638
Penetration depth (off-Bragg) (μm)	78.0689	
Penetration depth (at reflection) (μm)	8.43246	6.85522
Refractive index $n = 1 - \delta - \beta i$	$1 - 4.81984 \cdot 10^{-6} - 2.14049i \cdot 10^{-8}$	$1 - 4.81973 \cdot 10^{-6} - 2.14049i \cdot 10^{-8}$
Critical angle (mrad)	3.104785	3.104747

Table B.1: Selected calculated parameters of the $\alpha\text{-Al}_2\text{O}_3$ (006) reflection at an incident beam energy of 13 keV. Calculations were performed using SWAMv4.2. The use of ionic form factors results in a larger structure factor, wider Darwin width, and shorter X-ray penetration depth at the reflection condition.

The $\alpha\text{-Al}_2\text{O}_3$ (006) rocking curve is much narrower than any of the first-order Si reflections typically used in X-ray monochromators (111, 220, and 004). Since the experimentally measured rocking curve is a convolution of the sample reflectivity with the optical emission function, the features of a traditional single optic would “wash out” those of the $\alpha\text{-Al}_2\text{O}_3$ (006) reflection. In this case, XSW features in the

fluorescence yield would be very difficult to resolve. However, by detuning the angle between two crystals from the peak reflection condition, the angular width of the resulting beam can be made very small[11]. At the beamline, two channel-cut Si (220) monochromator crystals were mounted as shown in **Figure B.6**. The emission function from each of the two channel-cuts is shown as a filled rocking curve plot after each step in the optics (going from right to left, as one typically views the beamline components). The emission function of the first Si(220) channel-cut is represented by the filled blue curve. The emission function of the second Si(220) channel-cut, shown as the red curve, is identical to that of the first. The total emission function of the optics is calculated by multiplying the two functions together, and thus if the second optic is tuned to its maximum reflectivity, the total emission function will resemble the square of that of a single channel-cut. If the angle of the second channel-cut is detuned slightly from its peak intensity, then the emission function resembles the purple curve, which is much narrower than either peak. By this approach, the measured α -Al₂O₃ (006) reflectivity will not be totally dominated by the features of the optics, and insightful XSW measurements can be performed.

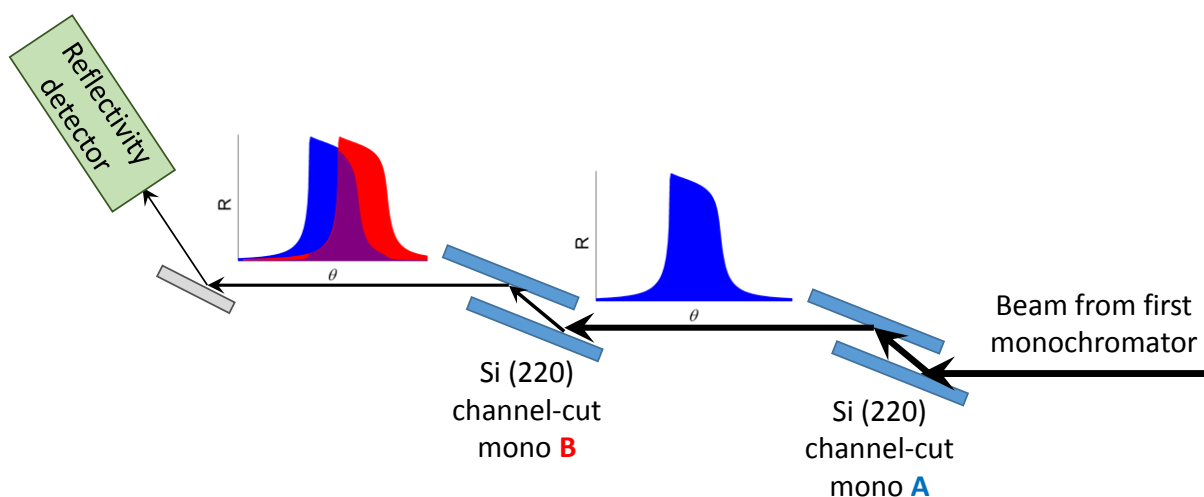


Figure B.6: Schematic of the optics setup for α -Al₂O₃ (006) XSW measurements. Filled curves (Si(220) rocking curves at 7 keV) represent the approximate emission functions of the optics after each channel-cut postmonochromator, with the blue contribution from Mono A and the red from Mono B. Mono B is detuned slightly from its emission peak, and the purple curve is the resulting product of the emission functions of Monos A and B.

In the XSW experiments reported in **Chapter 4**, the first channel-cut was detuned to 80% of its output intensity to reject harmonics coming through the upstream monochromator, and the second channel-cut was detuned to 15 – 30% of its output intensity in order to minimize the width of the measured α -Al₂O₃ (006) rocking curve. However, the measured rocking curves were still 3 – 5 times wider than the theoretical rocking curve. In order to account for this broadening in the rocking curve fit, a Gaussian smear was applied to the emission function of the optics in SWAM. The detuning of the second channel-cut crystal was explicitly taken into account in the fitting, although each channel-cut was approximated as only one crystal reflection, not two. The fits also did not include any contribution from the upstream monochromator (diamond (111) at beamline 33-ID-D and Si(111) at beamline 5-ID-C).

XSW experiments were also performed at the α -Al₂O₃ (104), (113), and (012) reflections for the samples described in **Chapter 4**. However, satisfactory XSW fits could not be performed for these reflections. In many cases, the fluorescence detector dead time was not correctly reported to saved data files, preventing proper dead time correction of the data. This correction is significant, as the dead time was roughly 20 – 30% due to strong diffuse scattering at these off-normal geometries in which the polarization direction of the beam points into the crystal bulk. As no significant asymmetries were observed in the fluorescence yields collected for these cases, it is possible that there is no measurable coherent fraction of the surface species of interest in these directions. However, it is also possible that coherent fractions exist at positions near those directly between the high electron density planes and the planes $\frac{1}{2}d_H$ away from them; these would be analogous to coherent fractions $P_{006} = 0.25$ or 0.75 , as shown in **Figure B.3**. Without accurate correction for the fluorescence detector dead time, this data cannot be confidently interpreted.

References

1. Kazimirov, A., Scherb, G., Zegenhagen, J., Lee, T.L., Bedzyk, M.J., Kelly, M.K., Angerer, H., and Ambacher, O., *Polarity determination of a GaN thin film on sapphire (0001) with x-ray standing waves*. Journal of Applied Physics, 1998. **84**(3): p. 1703-1705.
2. Templeton, A.S., Trainor, T.P., Traina, S.J., Spormann, A.M., and Brown, G.E., *Pb(II) distributions at biofilm-metal oxide interfaces*. Proceedings of the National Academy of Sciences of the United States of America, 2001. **98**(21): p. 11897-11902.
3. Trainor, T.P., Templeton, A.S., Brown, G.E., and Parks, G.A., *Application of the long-period X-ray standing wave technique to the analysis of surface reactivity: Pb(II) sorption at alpha-Al₂O₃/aqueous solution interfaces in the presence and absence of Se(VI)*. Langmuir, 2002. **18**(15): p. 5782-5791.
4. Yoon, T.H., Trainor, T.P., Eng, P.J., Bargar, J.R., and Brown, G.E., *Trace metal ion partitioning at polymer film-metal oxide interfaces: Long-period X-ray standing wave study*. Langmuir, 2005. **21**(10): p. 4503-4511.
5. Wang, Y.G., Michel, F.M., Levard, C., Choi, Y., Eng, P.J., and Brown, G.E., *Competitive Sorption of Pb(II) and Zn(II) on Polyacrylic Acid-Coated Hydrated Aluminum-Oxide Surfaces*. Environmental Science & Technology, 2013. **47**(21): p. 12131-12139.
6. Hayashi, K., Hayashi, T., Shishido, T., Matsubara, E., Makino, H., Yao, T., and Matsushita, T., *Application of x-ray excited optical luminescence to x-ray standing wave method and atomic resolution holography*. Physical Review B, 2007. **76**(1): p. 6.
7. Ponce, F.A. and Bour, D.P., *Nitride-based semiconductors for blue and green light-emitting devices*. Nature, 1997. **386**(6623): p. 351-359.
8. Bedzyk, M.J. and Materlik, G., *Two-beam dynamical diffraction solution of the phase problem: A determination with x-ray standing-wave fields*. Physical Review B, 1985. **32**(10): p. 6456-6463.
9. Bedzyk, M.J., Materlik, G., and Kovalchuk, M.V., *X-ray-standing-wave—modulated electron emission near absorption edges in centrosymmetric and noncentrosymmetric crystals*. Physical Review B, 1984. **30**(5): p. 2453-2461.
10. Waasmaier, D. and Kirfel, A., *New analytical scattering-factor functions for free atoms and ions*. Acta Crystallographica Section A, 1995. **51**(3): p. 416-431.
11. DuMond, J.W.M., *Theory of the Use of More Than Two Successive X-Ray Crystal Reflections to Obtain Increased Resolving Power*. Physical Review, 1937. **52**(8): p. 872-883.